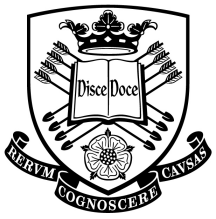

The University Of Sheffield.

ADDITIVE MANUFACTURING OF TUNGSTEN

via Selective Laser Melting and Electron Beam Melting

Jonathan Wright

January 8, 2020

A thesis submitted in partial fulfilment of the requirements for the degree of Doctor of Philosophy

The University of Sheffield
Department of Materials Science and Engineering

SUPERVISOR:
Professor Iain Todd

E-MAIL:
Jon.simon.wright@gmail.com

ABSTRACT

This thesis explores powder bed Additive Layer Manufacturing (ALM) of pure tungsten. Two ALM processes were investigated; Selective Laser Melting (SLM) and Electron Beam Melting (EBM). An optimal experimental design approach was adopted to investigate the effect of process parameters on parts produced.

Analysis of the SLM process was carried out using a Response Surface Methodology (RSM). The beam power in SLM significantly effected porosity; a laser power of at least 400 Watts was required to produce near dense parts (0.23% porosity). A valid response model could not be fitted to the SLM experimental data. Cracks propagated throughout SLM components as the porosity was reduced. This was attributed to stress imparted during processing and an operating temperature below the Ductile to Brittle Transition Temperature (DBTT).

An Arcam EBM system was modified in order to reduce the build volume, allowing small volume materials development. A RSM was adopted to model the effects of EBM process parameters on defects within parts. Specifically, hatch spacing, beam current, and beam speed were investigated and shown to all have a significant effect on porosity and geometric accuracy. Second order models were generated to fit the experiential data, representing the response well ($R^2 = 99\%$ and $R^2 = 93\%$) a minimum porosity of 0.04% was achieved.

The properties of EBM tungsten were characterised; three point bending and Weibull analysis was used to determine characteristic strength (340 MPa). Hardness and modulus was measured via nanoidentation was found to vary as a function of the position within samples. This was attributed to residual stress imparted during processing. EBSD revealed a strong [111] texture. This was attributed to the angle of thermal gradients in the melt pool.

ACKNOWLEDGEMENTS

Firstly, I thank my supervisor Professor Iain Todd for giving me this opportunity and for his support and guidance throughout. I feel extremely lucky that Iain has allowed me access to the latest in additive manufacturing equipment and the freedom to spend countless hours experimenting with it.

I must also express my gratitude to Professor Neil Hopkinson, I was privileged that Neil introduced me to additive manufacturing processes during my final year masters project, developing my interest in the field.

This project would also not have been possible without funding from Culham Centre for Fusion Energy (CCFE), in particular I thank my supervisor my Dr Mike Porton. I have thoroughly enjoyed all my time spent at CCFE learning about the fascinating research that takes place there.

Thanks must go to the staff at Renishaw PLC (Stone), in particular Ravi Aswathanarayanaswamy, for allowing use of the AM400 SLM system.

The past four years would not have been the same without my colleagues in particular Everth Hernandez Nava, Sam Tammas-Williams, Phil Mahoney, James Hunt, Laura Asensio. A special mention must also go to Chris Smith, not only has his expertise in the field of Electron Beam Melting (EBM) been invaluable but I must thank him for the gym sessions, bike rides, his optimism, good humour and friendship.

I am grateful to my partner Amber for her love, support, and reassurance throughout.

Last but not least I thank my parents and sister for a lifetime of support and encouragement, for providing the opportunities and education, and allowing me to peruse my interests. I dedicate this thesis to them and my partner.

Jonathan Wright

CONTENTS

NOMENCLATURE

α	Thermal diffusivity	
β	Shape parameter (Weibull modulus)	
δ	Displacement	m
ϵ	Strain	Pa
η	Absorptance	
η	Scale parameter	
λ	Thermal conductivity	
$\lambda(t)$	Failure rate function	
μ	Poisson's Ratio	
ρ	Density	Kg/m^3
σ	Stress	Pa
τ_i	Interaction time	s
A	Absorptivity	
a	Linear Thermal Expansion Coefficient	$strain/K$
A_c	Indentation contact area	m^2
A_s	Spot area	m^2
b	Current compensation constant	
C_p	Specific heat capacity	$J/Kg/K$
C_e	Turning point function constant	
c_l	Longitudinal wave velocity	m/s
c_t	Transverse wave velocity	m/s
d	Beam diameter	m
d	Distance	m
E	Young's modulus	Pa
E_{F2}	Turning point function constant	
E_F	Turning point function constant	
E_f	Exponent Factor	
$F(t)$	Cumulative density function	
$f(t)$	Weibull distribution function	
G	Shear modulus	Pa

H	Hardness	Pa
h	Hatch spacing	m
h^*	Normalised hatch spacing	
h_c	Indentation depth	m
I_x	Second moment of area about the x axis	$N.m$
I_0	Reference current	A
l	Layer thickness	m
l^*	Normalised layer thickness	
L_0	Reference line length	mm
m	Mass	Kg
M_0	Multiplication factor	
M_z	Bending moment	$N.m$
P	Beam power	W
p	Load	N
P^*	Normalised beam power	
P_A	Power density	W/m^2
P_e	Effective power	W
p_{max}	Maximum load	N
Pd	Point distance	m
Q	Volumetric energy density	J/m^3
Q^*	Normalised energy density	
Q_{SP}	Spot energy	J
$R(t)$	Reliability function	
r_B	Beam radius	m
S_f	Speed factor	
T	Temperature	K
t	Time	s
T_0	Initial temperature	K
t_e	Exposure time	s
T_m	Melting temperature	K
t_t	Traverse time	s
v	Velocity	m/s
v^*	Normalised velocity	

v_0	Reference velocity	m/s
v_t	Traverse velocity	m/s
X	Distance in the x dimension	m
Y	Distance in the y dimension	m
Z	Distance in the z dimension	m
Z_f	Thickness factor	
Z_{max}	Maximum vertical distance over which the thickness function is applied	m
q''	Heat flux	W/m^2

ABBREVIATIONS

ABF Arcam Build Files

ALM Additive Layer Manufacturing

AM Additive Manufacturing

ANOVA Analysis of Variance

BCC Body-Centered Cubic

CAD Computer Aided Design

CCFE Culham Centre for Fusion Energy

CFC Carbon Fibre Composite

DBTT Ductile to Brittle Transition Temperature

DED Direct Energy Deposition

DEMO DEMOnstration Power Station

DOE Design of Experiments

EBAM Electron Beam Additive Manufacturing

EBM Electron Beam Melting

EBSD Electron Backscatter Diffraction

EDM Electrical Discharge Machining

FEA Finite Element Analysis

FFF Free-form Fabrication

TGM Thermal Gradient Mechanism

ISE Indentation Size Effect

ITER International Thermonuclear Experimental Reactor

LOF Lack of Fusion

LSM Least Squares Methods

MCF Magnetic Confinement Fusion

PFC Plasma Facing Component

PPE Personal Protective Equipment

PRS Powder Recovery System

RBV Reduced Build Volume

RP Rapid Prototyping

RSM Response Surface Methodology

RT Rapid Tooling

SBT Small Build Tank

SFF Solid Free-form Fabrication

SLA Stereolithography

SLM Selective laser Melting

SLS Selective Laser Sintering

WLMD Wire Laser Metal Deposition

LIST OF FIGURES

LIST OF TABLES

INTRODUCTION

In recent years Additive Layer Manufacturing (ALM) has undergone a rapid development; a technology which was for many years reserved for prototyping applications can now be used to produce high quality engineering components. ALM offers an array of advantages to engineers when compared to other manufacturing routes such as unrivalled design freedom and lack of product specific tooling. Much of the recent research efforts have been focused on the development of new material specific process parameters, there is however still a long list of common engineering materials for which ALM processes have not been fully investigated. One such material is the element tungsten.

Tungsten is the material of choice for a number of industrial applications due to its unique combination of properties. These properties however also result in many manufacturing challenges when considering well established fabrication methods. ALM can therefore open the opportunity to create complex optimised structures with relative ease. There has been to date limited work carried out on the development of ALM processing of tungsten.

This study aims to asses the feasibility of ALM processing of tungsten via Electron Beam Melting (EBM) and Selective Laser Melting (SLM). Statistical experimental design is used to determine optimal process parameters whilst minimising experimental effort. The occurrence of defects in the material produced will be used as a measure.

This work was funded by Culham Centre for Fusion Energy (CCFE), the UK's national nuclear fusion research laboratory. Tungsten's unique set of properties mean it is of particular interest in magnetic confinement fusion. Tungsten is the chosen plasma facing material for the next generation of Tokamak reactor the International Thermonuclear Experimental Reactor or ITER.

1 LITERATURE REVIEW

1.1 ADDITIVE LAYER MANUFACTURING

Broadly speaking Additive Manufacturing (AM) involves the joining of thin layers of material to build up a three dimensional component. Many different terms are used when referring to AM processes. Additive Layer Manufacturing (ALM) Rapid Prototyping (RP), Rapid Tooling (RT), Free-form Fabrication (FFF), Solid Free-form Fabrication (SFF), and 3D Printing are some of the commonly used terms. For simplicity ALM will be used throughout this document.

1.1.1 Stereolithography and the birth of ALM

ALM was first introduced in 1986 via a patent granted to Chuck Hall labelled 'Apparatus for production of three-dimensional objects by stereolithography' [1]. This led to the first commercial machine, released by 3D systems the following year. The process that this new machine used was called Stereolithography (SLA).

Figure 1.1 shows a schematic of the SLA process as depicted in the patent granted to Chuck Hall. The SLA process consists of an ultraviolet laser which selectively scans to initiate a curing reaction in a thin layer of polymer resin atop a platform. The platform is then lowered allowing another layer of the liquid resin to be deposited on top of the previous layer and the laser curing process is repeated. Scanning of the laser on each layer is driven by a Computer Aided Design (CAD) file which defines the area that will be cured, this includes supports which fix any overhanging areas to the build platform. After the process is completed supports are removed manually and then the product is placed in an oven to solidify any areas that had not fully cured.

This process has seen limited commercial application due to the fact that exposure to sunlight causes further curing in applicable materials leading to a deterioration in mechanical properties over time[2]. Thus the SLA process has been reserved for prototyping applications only and as a result the process is often associated with the term rapid prototyping (RP) [3].

1.1.2 ALM Processes and Hardware

Chuck Hall's invention of SLA has since birthed a wide range of ALM processes and hardware. ALM systems vary significantly between how layers are deposited, how material is consolidated, and which materials are used. Table 1.1 on page 7 has been assembled to provide an overview of ALM processes, materials, and manufacturers currently available though this should not be taken as a fully comprehensive list.

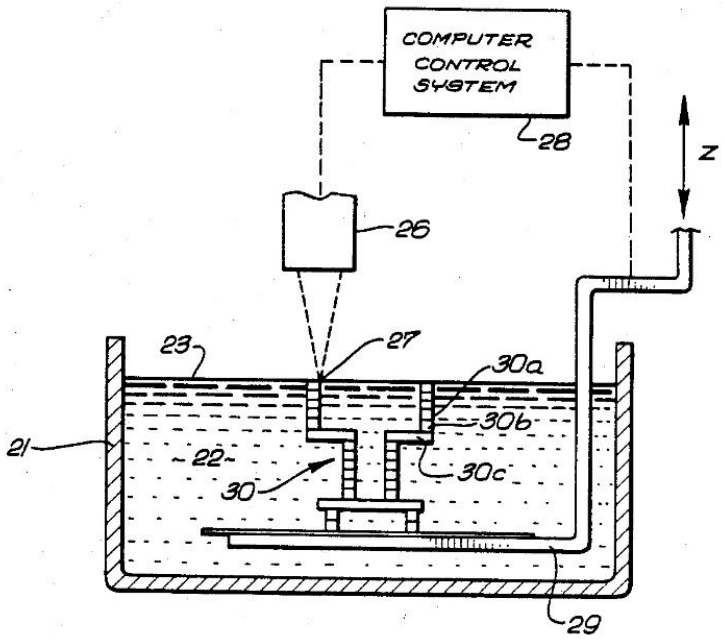

Figure 1.1: Schematic Diagram of the SLA Process. Diagram taken from 'Apparatus for production of three-dimensional objects by Stereolithography' Patent application [1]

1.1.3 The benefits and limitations of additive layer manufacturing

A layer based approach to manufacturing can allow for the creation of extremely complex geometries which would be difficult, or even impossible, to produce using traditional methods (such as casting, moulding, machining, and forming). This geometrical freedom has the potential to allow engineers to focus on optimising a component for its intended application by removing many of the manufacturing considerations that would otherwise need to be taken into account such as re-entrant features required for casting.

This design freedom offered by ALM is sometimes overstated as manufacturing considerations are still necessary; there are minimum limits on feature size due to the resolution of the process. Additionally, component orientation will affect the build time and dictate whether there are any overhanging surfaces that need to be supported. Another consideration which should be made with ALM process is the surface finish of parts which can be poor, this has implications for the mechanical properties in particular the fatigue life [4].

An advantage of the ALM approach is the fact that no additional tooling is required for new components. This tool-less approach results in shorter lead times and reduced cost for new products [5].

ALM processes are low waste, the majority of the feedstock material can be recycled, leading to cost savings, as well as environmental advantages. There needs to be consideration to the disposal of feedstock materials, in particular metal powders, must be removed with care to eliminate negative environmental effects. Feedstock material can be expensive and users of ALM systems are often constrained to purchasing material supplied by the system manufacturer.

Table 1.1: An overview of ALM processes and hardware (adapted from [6])

Type of Process	Process	Acronym	Material Family	Supplier
Photopolymerisation	Sterolithography	SLA	Plastic	3D Systems formlabs DWS Systems
	Digital light Processing	DLP	Plastic	EnvisionTEC B9Creations
	Continuous Digital Light Processing	CDLP	Plastic	carbon3D EnvisionTEC
Material Extrusion	Fused Deposition Modeling	FDM	Plastic Composite	Stratasys Ultimaker MakerBot
Material Jetting	Material Jetting	MJ	Plastics	Stratasys 3DSystems
	NanoParticle Jetting	NPJ	Metal	XJET
	Drop On Demand	DOD	Wax	Solidscape
Binder Jetting	Binder Jetting	BJ	Sand Metal	ExOne Desktop Metal 3D Systems voxeljet
Powder Bed Fusion	Multi Jet Fusion	MJF	Plastic	HP
	Selective Laser Sintering	SLS	Plastic	EOS 3D Systems
	Selective Laser Melting	SLM DMLS	Metal	EOS 3D Systems Renishaw SLM Solutions Concept Laser Aconity
	Electron Beam Melting	EBM	Metal	Arcam Freemelt
Direct Energy Deposition	Laser Engineering Net Shape	LENS	Metal	OPTOMEC
	Electron Beam Additive Manufacturing	EBAM	Metal	Sciaky

1.2 TYPES OF ALM PROCESSES

ALM processes can be roughly categorised by the feedstock material as follows:

- Powder based
- Solid deposition
- Liquid based

This subsection will discuss these processes.

1.2.1 Powder Based Processes

As a result of the materials used in early ALM processes e.g. SLA, parts manufactured had limited functional value. The development of ALM processes in recent years has led to a number of systems which are capable of processing functional materials. One of the most promising is powder bed ALM.

Powder bed processes have been developed for a wide variety of polymers, metals, and ceramics. The first powder bed process was initially patented in 1979 but was not fully realised until the late 1980s [7]; this was a polymer based process known as Selective Laser Sintering (SLS).

A schematic diagram of a generic powder bed ALM system is shown in Figure 1.2[8]. Powder bed systems consist of a rake or wiper which collects powdered material from a hopper and deposits a thin layer on a substrate. A heat source (most commonly a laser) then selectively consolidates the powder layer. Following selective melting of the powder the substrate will lower (typically by between 20 and 100μm) and a new layer of powder is deposited by the wiper. The steps of powder deposition, selective melting, and the lowering of the substrate, are repeated until the desired part is complete.

Since the development of the first powder bed process, the technology has evolved from sintering of plastics, to sintering metals and eventually to fully melting metals, known as Selective Laser Melting (SLM). Systems with an electron beam as the power source have also been developed, this process is known as Electron Beam Melting (EBM). SLM and EBM systems can fully melt powder particles producing components with density in excess of 99% and with mechanical properties comparable to bulk [9].

Selective Laser Melting

The SLM process can vary depending on the manufacturer of the apparatus used. Variations include differing inert atmospheres, the mechanism by which powder is stored and deposited, and the type of laser used. The type of laser used can have a significant effect on the process as the wavelength will affect the energy which is absorbed by the powder feedstock material, CO_2, Nd:YAG fiber and Yb:YAG fiber lasers are typically used in SLM systems. In the early days of SLM development CO_2 lasers were adapted from SLS processes however now more commonly Yb:YAG lasers are used due to the higher energy absorption of metallic powders at infrared wavelengths [10].

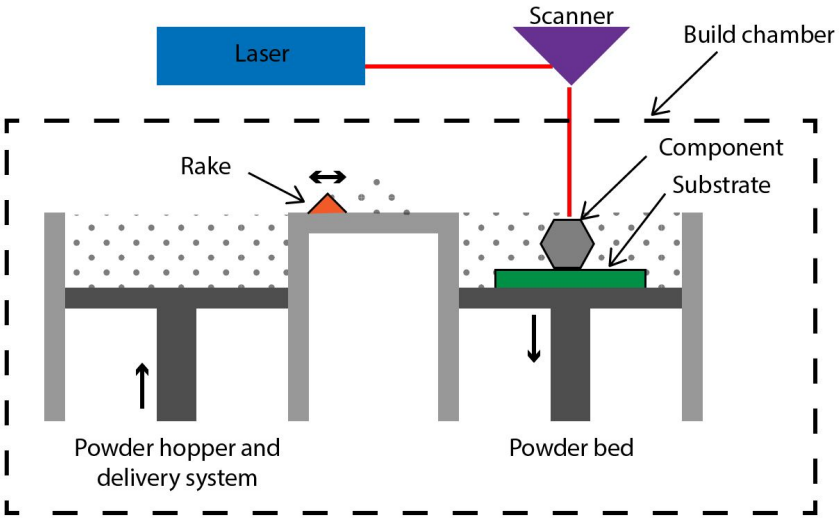

Figure 1.2: Generic Schematic Diagram of a powder bed Process. Adapted from [8]

In recent years the range of available SLM systems and their capabilities increased and a number of trends can be observed. Build volumes are becoming larger, lasers are becoming more powerful, higher preheat temperatures are achievable, and atmospheres with lower impurity levels present. One example of the current capabilities of SLM systems are Aconity3D who offer [11]:

- A large cylindrical build volume with 400mm diameter and 400mm height
- Lasers which deliver powers of up to 1000W.
- A vacuum atmosphere down to a pressure of 1mBar
- Preheating temperatures of up to 1200°C

The larger build volumes available in the current generation of ALM systems allow for the production of large components, providing the potential for the application of ALM to components that could not previously be manufactured [12]. Additionally larger build volumes can add economies of scale to batch production. Higher laser powers can enable faster build speeds, processing of a wider range of materials and higher build quality [13]. A higher quality atmosphere can reduce impurities in particular oxygen and nitrogen in components, it can also act to reduce defects [14, 15, 16]. High preheating temperatures can, reduce residual stress, alter microstructure, improve strength and ductility, and enable processing of alloys which are prone to cracking [17, 18]. High preheat temperatures can increase the adsorption of impurities and can have a negative impact on mechanical properties so increased preheat temperatures should be considered in tandem with low impurity atmospheres[19].

Energy density, non dimensional numbers and laser interaction parameters

The majority of SLM systems operate using a hatching scan strategy. Hatching consists of a back and forth raster pattern. Variable laser parameters

used during processing via hatching are beam velocity (v), hatch spacing (h), layer thickness (l), and beam power (P). Where hatch spacing (also known as hatch offset) is the distance between successive scan lines. These parameters in combination with the absorptance of the powder (η) to laser radiation define the applied energy density, the volumetric energy density (Q) can be calculated using Equation 1.

$$Q = \eta \frac{P}{vhl} \tag{1}$$

Some SLM systems such as those produced by Renishaw PLC use a modulated or 'pulsed' laser. Systems with modulated lasers typically operate with a square like wave or on/off laser profile. During the on phase the laser emits a pulse at a given point on the powder bed, during the off phase the scanning system moves along the hatch line to the next point. The time for which the laser is on is referred to as the exposure time (t_e) and the distance between points is known as the point distance (Pd). The time during which the laser is off and moving between points will be defined as the traverse time or t_t and the beam velocity between these points v_t.

It follows that in order to calculate the volumetric energy density for a modulated laser system the effective beam velocity v_e is calculated as

$$v_e = \frac{Pd}{t_e + t_t} \tag{2}$$

where

$$t_t = \frac{Pd}{v_t} \tag{3}$$

We must also account for the fact that the laser is off during the traversing between points. The average effective laser power P_e can be calculated as

$$P_e = P \frac{t_e}{t_e + t_t} \tag{4}$$

Substituting into Equation 1 and rearranging it can be shown that for a modulated laser system

$$Q = \eta \frac{P.Pd}{t_e.hl} \tag{5}$$

The volumetric energy density applied during heating must be tailored to each material based on its properties, specific heat capacity, latent heat, and melting point. If insufficient energy is applied to the layer, molten particles will not sufficiently wet the surface of the preceding layer, a process known as balling [20, 21]. If too much volumetric energy is applied the keyhole effect may occur, where the beam penetrates deep into the part creating porous voids under cooling [22]. An additional consideration when applying excess energy to the powder layer is vaporisation. Any vaporised material will condense on the inner surfaces of the system, this is a particular concern if the condensation occurs on the glass window through which the laser passes as it can absorb much of the radiation delivered by the laser as the build continues.

The SLM process and powder bed ALM processes in general are complex, it is therefore difficult to reliably calculate the ideal parameters and energy density directly from material properties [23].

Energy density calculations are not time dependent and therefore do not account for the rate at which energy is applied to the powder bed, this is crucial as the rate of heat input to the system is dependent on the rate of heat loss. This is particularly important to consider when comparing continuous laser systems to modulated systems as for a given set of parameters the rate of energy input for a modulated system will be lower. This is due to the travel time between points where the laser is off, this travel time reduces the effective velocity and power input to the system.

Accurately defining and calibrating system parameters and their associated errors for each system is difficult. No standards currently exist for the collaboration of ALM systems with each manufacturer carrying this out to their own specifications. The ability for a user to measure the accuracy of this calibration is limited as it would require full access to the systems hardware and software as well as additional expertise and measurement systems. These issues in particular mean that numerical models such as energy density calculations can not be reliably used and they are typically only implemented for relative comparisons.[24]

Much of the research into ALM is focussed on establishing optimised process parameters for a vast range of materials via experimental methods. Work has also been carried out on computational modelling of the process through methods such as finite element analysis (FEA), however reliable models do not yet exist for selection of parameters and such models would be computationally expensive [21, 25, 26]. Key challenges in modelling powder ALM processes include but are not limited to:

- The random nature of powder spreading over the build platform [27].
- The interaction of the laser with the layer [27].
- Differences in the process and hardware across the wide range of systems available.
- Changing or often complex part geometry which results in a variation in thermal behaviour throughout the build [28].

As a result of these difficulties in producing accurate numerical models for selective laser melting empirical and physically based process maps have been developed in order to compare parameter data across ALM systems [29]. Normalised processing diagrams developed by Thomas et al can be used to visualise the difference in processing parameters between materials and systems [29]. This method used dimensionless groups in order to normalise parameters and is based on dimensionless groups developed by Ion et al [30] which are commonly used for comparisons in laser bean welding. Dimensionless groups for additive manufacturing are defined as follows in Equations 6-10.

$$P^* = \frac{Aq}{r_b \lambda (t_m - t_0)} \tag{6}$$

$$v^* = \frac{v r_b}{\alpha} \tag{7}$$

$$l* = \frac{2l}{r_B} \tag{8}$$

$$Q* = \frac{q*}{v * l*} \tag{9}$$

$$h* = \frac{h}{r_B} \tag{10}$$

Where P^*, v^*, l^*, Q^* and h^* are the normalised laser power, velocity, layer thickness, energy density and hatch spacing respectively. A plot comparing parameters across a range of alloys and AM systems as presented by Thomas et al is included in Figure 1.3 [29]. This technique provides a method for visualising parameter data across the literature and can help to provide an insight into processing regions for alloys which can help with early parameter selection and development minimising experimental effort.

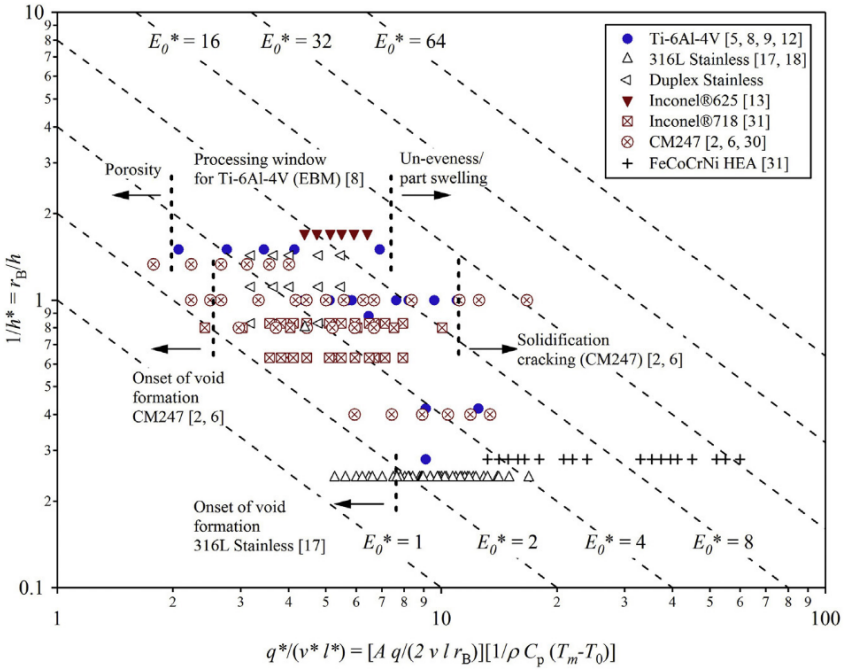

Figure 1.3: Normalised processing map for AM of a range of alloy systems constructed using equations 6-10 and parameters gathered from literature [29]

Mukherjee et al identified three important non dimensional numbers in additive manufacturing, these are the Peclet number, the Maragoni number, and the Fourier number[31]. using these dimentionless numbers the authours concluded that:

- High Peclet numbers in ALM indicate convective heat transfer is the main mechanism for heat transfer in the molten pool[31].
- High Maragoni numbers in ALM indicates large velocities in the molten pool which increases the size and aspect ratio of molten material, which can help to reduce porosity. At very high Maragoni number may lead to instability which can increase defects[31].

- High Fourier numbers in ALM indicates a rapid cooling rate and high ratio of temperature gradient to solidification rate[31].

Suder and Williams define three important laser interaction parameters which unlike energy density calculations take into consideration the diameter of the beam [32]. The interaction of a laser with a surface is given by the interaction time, the size of the beam and the power density [32]. Suder and williams define the power density q_P as:

$$P_A = \frac{P}{A_s} \tag{11}$$

Where A_s is the area of the laser spot on the surface and P is the beam power. The interaction time τ_i is given as:

$$\tau_i = \frac{d}{v} \tag{12}$$

Where d is the beam diameter and v is the beam velocity. The energy delivered by the laser to a specific spot in the surface Q_{SP} in the case of a square beam profile can be given as:

$$Q_{SP} = P.\tau_i \tag{13}$$

For small beam diameters the assumption of a square beam profile is sufficient.

Suder and Williams conclude that the depth of penetration is controlled by the specific point energy and the power density. The width of a weld is controlled by interaction time[32].

Electron Beam Melting

EBM is a process developed by Arcam AB. EBM is in many ways the same as SLM, however the difference in heat source leads to a number of notable variations in the processes.

A key advantage of the EBM process is speed, the electron beam is controlled by a series of magnetic lenses which can focus and deflect the beam almost instantaneously. Laser systems on the other hand use a series of mirrors which are controlled by small electric motors, the speed at which the laser can move across the surface is therefore limited by the inertia of this system. This is particularly important for complex parts such as lattice structures where in laser systems time taken for the beam to traverse between melt areas becomes a significant factor in total build time. In addition to the speed advantages of the electron beam deflection, EBM systems can maintain larger melt pools than SLM systems and so use higher powers, speeds, and hatch offsets which can further increase the speed of melting [9]. The larger meltpools in EBM along with fast scan speeds, large powder size distributions, and relatively thick layers (typically 70µm compared to 30µm in SLM) also produce a rougher surface [9] [33].

The range of powders available for manufacture via EBM are lower than that available for laser processing due to considerations of electrical conductivity; powders in EBM must be able to dissipate the charge applied by

the beam. The vast majority of EBM research effort is focused on titanium and its alloys in particular Ti6Al4V [34]. This is in part to the wide ranging applications for this alloy notably within the biomedical [35] and aerospace industries [36].

The local nature of melting during laser processing leads to high thermal gradients and rapid solidification. Contraction of the melt pool during solidification creates residual stresses in parts[37]. Stress in SLM parts often then needs to be removed through post process heat treatment however this can lead to distortion and cracking of parts in process[38]. EBM takes place at an elevated temperature and therefore can eliminate the need for heat treatment through in process annealing and the reduction of thermal gradients[39]. The high beam speed and power achievable with an electron gun allows the beam to rapidly scan the build area heating the substrate and each layer of powder to maintain an elevated build temperature. Authors have reported the use of electrical resistance heaters in SLM systems to try to reduce residual stresses [40] [17], however few commercial systems feature heating systems and these are often a modification made for research purposes.

ARCAM EBM systems are aimed at industrial production and therefore present some challenges for research and development. The greatest of these challenges is as a result of the large scale of the build tanks which tend to be increasing over time to meet the demands of the industrial setting. These large build volumes allow for cost savings in industrial settings but result in increased costs and practical difficulties for small scale R&D. Due to the volume of powder required to run these systems which requires a large initial raw material cost and specialised handling and processing equipment which often isn't justifiable for as yet unproven materials. A PhD Thesis by Francisco Medina attempted to address this issue through the development of an in house systems with a small build 120mm diameter build volume [41].

Powder Direct Energy Deposition

Another notable category of powder based processes is direct energy deposition (DED) also known as 'blown powder'. A schematic of the DED process is provided in Figure 1.4. In DED powder is propelled through a nozzle onto the component surface where heat source simultaneously melts the powder. This deposition is repeated layer by layer in order to fabricate components, typically a laser is used as a heat source in a process known as 'Laser Engineered Net Shaping '(LENS) or 'Laser Metal Deposition' (LMD)[42]. DED systems use one of two different mechanisms to selectively deposit material; either the deposition head remains stationary and the component moves or vice versa. The benefits and drawbacks of each system will vary and should be evaluated for each product on a case by case basis [8].

DED can produce fully dense parts and uses layer thickness's as small as 0.1mm and up to several millimetres in thickness, allowing for high deposition rates whilst also providing an accurate surface where necessary. A key advantage of DED is that the process lends itself well to scaling when compared to powder bed systems allowing for processing of large parts. In addition DED allows a high degree of grain structure control. This process also has the advantage over other powder bed systems in that dissimilar materials can be used at the same time with the addition of a second nozzle[43]. This technique can also be used to control alloy composition in process[44].

The DED process lends itself well to the repairing of wear in functional parts and this is its primary industrial use[45].

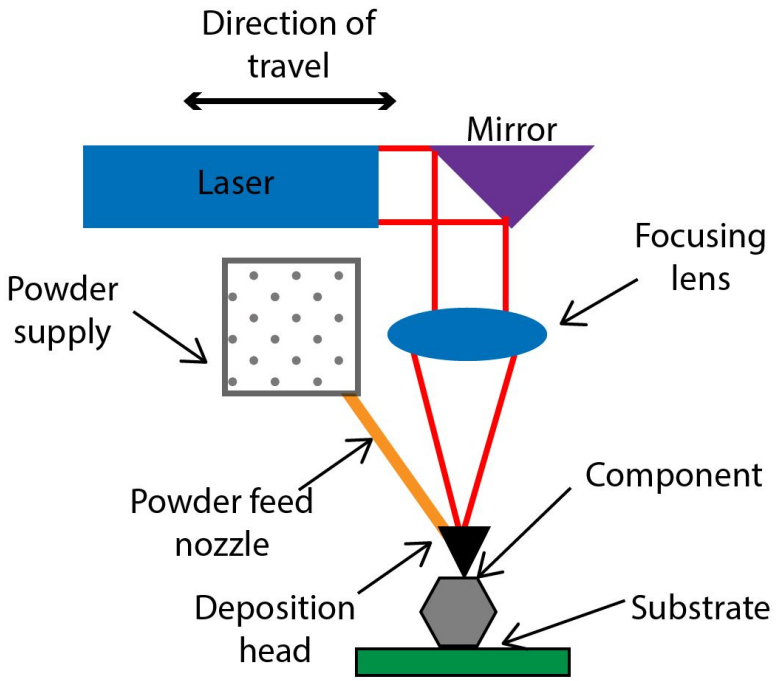

Figure 1.4: Generic Schematic Diagram of the DED Process. Adapted from [8]

1.2.2 Solid Deposition

Solid deposition techniques can be categorised as a DED process however wire feed material is used and deposited with the use of a heat source typically a laser 'Wire Laser Metal Deposition' (wLMD) or an electron beam 'Electron Beam Additive Manufacturing' (EBAM). Wire feed systems are suitable for high deposition rates and therefore normally accommodate large build volumes. Solid deposition however has relatively poor dimensional accuracy and parts will often need extensive post process machining. This poor dimensionality accuracy means that the same level of component complexity available in powder bed processes is not achievable. Solid deposition has been shown to produce strongly anisotropic mechanical properties, producing significantly lower tensile strength in the build direction[46]. A schematic diagram of a wire feed solid deposition system is included in 1.5

Despite the negatives, solid based processes have their place in commercial production with the ability to create components with complex geometry when compared to conventional methods at high deposition rates and with large build volumes.

The relative cost of solid based processes are low when compared to powder based processes as a result of the differences in feedstock production[46].

1.2.3 Liquid Based Processes

Liquid based processes typically take one of two forms: photo polymer reactions, such as stereolithography, or droplet deposition mechanisms, such as

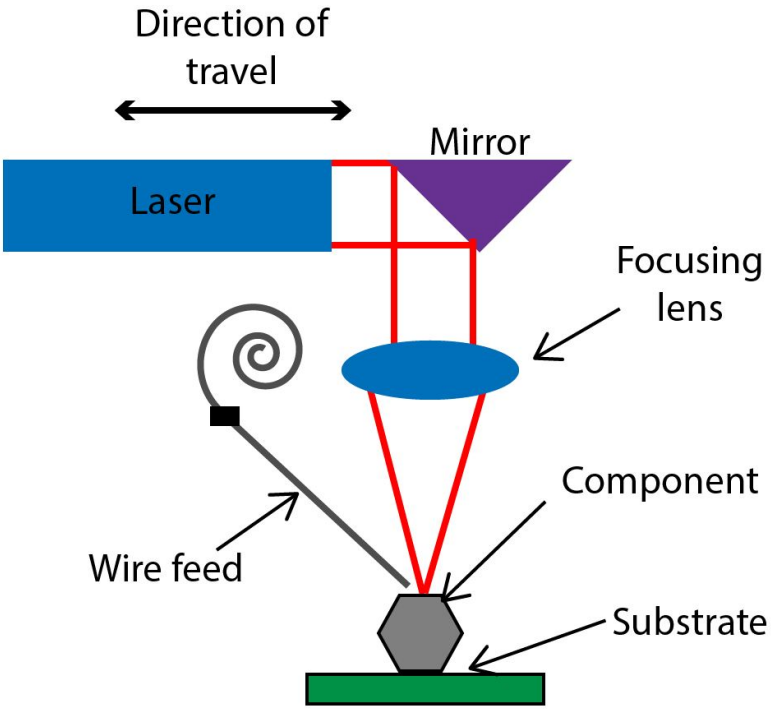

Figure 1.5: Generic Schematic Diagram of wire feed processes. Adapted from [8]

inkjets. Liquid based methods are capable of producing a good surface finish, however the materials available, and their resulting mechanical properties, are unsuitable for most applications. As a result, liquid based processes are reserved mainly for prototyping, or applications where aesthetics are the primary concern. Liquid based processes will not be explored further in this review.

1.2.4 Defects in AM formation mechanisms

Components produced via powder bed ALM contain defects. Categories identified from the reviewed literature can be summarised as follows:

- **Porosity** - Voids within the material.
- **Balling** - When melted powder does not wet the underlying surface and solidifies into spheres, creating a rough surface.
- **Residual stress** - Stresses which remain in the material after processing.
- **Cracking** - Fractures in the material as a result of stresses imparted during processing.
- **Warping** - A change in geometry, typically as a result of thermal stresses.
- **De-lamination** - Separation of successive layers due to incomplete bonding.
- **Swelling** - Surface tension effects lead to expanding of the top surface.

Process variables can influence the type, size, and frequency of these defects.

Porosity should be minimised in parts which undergo stress bearing applications as porosity directly reduces the mechanical strength, fatigue life and elongation to failure [47, 48]. In some applications porosity can be desirable such as biomedical implants where it can enable bonding to bone [49]. Sources of porosity in ALM components have been identified as powder induced or process induced. Powder induced porosity stems from gas bubbles within atomised powder, this gas remains trapped in material after re-solidification [50].

Process induced porosity stems from the effects of processing itself. It can be as a result of insufficient energy input, excessive energy input, component geometry, powder morphology, insufficient overlap (between layers or hatches), balling, swelling, key holing or surface tension effects [51, 52, 53, 28, 50] . Porosity which occurs due to insufficient melting of powder are typicality referred to as Lack of fusion (LOF) defects. LOF typically occur due to insufficient energy input or overlap [54, 51]. In severe cases lack of fusion can lead to separation of layers known as de-lamination.

The effect of the fluid dynamics of molten material plays an important role in consolidation of powder. At the length scales of the molten pool, surface tension is the dominant force acting on it. Similarly coalescing and reshaping of molten material happens on a much shorter time-scale and powder begins to coalesce before it is fully molten [50]. Molten powder will coalesce with the nearest material, the direction of which may not be downwards towards the preceding layer. In this way defects can propagate over multiple layers. As the dominant force is surface tension molten material will tend to assume a spherical shape. Molten material may not sufficiently wet the surface and can solidify into balls, this is known as balling [55]. Balling can in turn lead to porosity, increase surface roughness and interfere with powder deposition [56].

Powder bed ALM processes apply high energy over a small area to allow for rapid melting and solidification. The result of this is high temperature gradients and corresponding residual stresses which can accumulate over a number of layers [57, 58]. This stress remains in the parts after processing and heat treatment is often used to stress relieve parts [59]. Residual stresses can sometimes build up to a point where crack propagation occurs in parts during processing [51]. Similarly built up thermal stresses can lead to parts deforming during processing, known as warping. The elevated build temperatures in EBM and some SLM systems can help to reduce thermal stresses and even stress relieve parts during processing, reducing the occurrence of cracks and warping [60].

1.3 TUNGSTEN

1.3.1 Production from Ore

Tungsten has an average abundance of approximately one part per million on earth. Mineral deposits consist of much higher concentrations of 0.1 to 2 percent. Tungsten exists naturally as two mineral groups Wolframite ($(Fe,Mn)WO_4$) and Scheelite ($CaWO_4$). The Wolframite group is further divided based on the manganese and iron content. Ferberite is iron tungstate which contains a manganese content up to 20 percent. Huebenerite is man-

ganese tungstate that contains up to 20 percent iron content. Wolframite is used to label those minerals that contain between 20 and 80 percent of both iron and manganese tungstate [61].

Due to the low concentration of tungsten in mineral deposits, a large volume of gangue material must be separated from the ore. This processing typically takes place close to mines and is carried out in two steps comminution and concentration.

Comminution acts to crush and grind material to reduce the particle size such that particles can be sorted. Concentration acts to sort particles based on their composition. A range of methods are used for this such as gravity, flotation, magnetic, and electrostatic separation. Concentrates typically reach a concentration of 65-75% for trade [61].

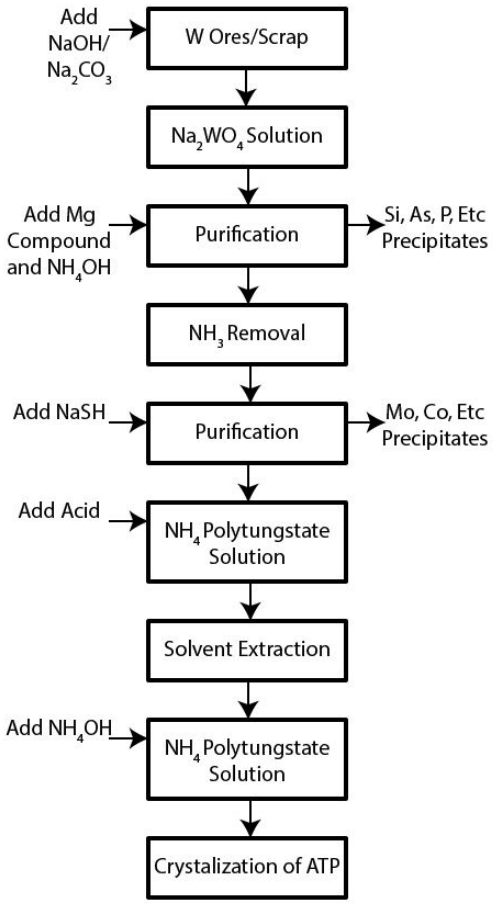

Figure 1.6: A general flow diagram for the hydrometallurgy of tungsten [62]

An overview of the modern hydrometallurgical process for tungsten is provided in figure 1.6 [62]. Firstly digestion of the minerals is carried out using sodium hydroxide or sodium carbonate. Contaminants are removed from the resulting solution using precipitation methods to remove impurities such as silicon, arsenic, phosphorus, and molybdenum.

$$(Fe, Mn)WO_4 + 2NaOH \rightarrow Na_2WO_4 + (Fe, Mn)(OH)_2$$

$$CaWO_4 + Na_2CO_3 \rightarrow Na_2WO_4 + CaCO_3$$

Ion exchange is carried out to separate sodium. Modern techniques extract tungsten from an acidic solution by amines dissolved in an organic solvent.

$$10(R_3NH)^+ + 5SO_4^{2-} + 2HW_6O_{21}^{5-} + 10Na^+ \rightarrow 2(R_3NH)_5HW_6O_{21} + 5Na_2SO_4$$

$$(R_3NH)_5HW_6O_{21} + 14NH_4OH \rightarrow 12(NH_4)_5HW_6O_{21} + 5(R_3NH)OH$$

$$2(NH_4)_5HW_6O_{21} + 14NH_4OH \rightarrow 12(NH_4)_2WO_4 + 8H_2O$$

The concentrated ammonium tungstate solution is crystallised via evaporation to form ammonium paratungstate (ATP) crystals.

$$12(NH_4)_2WO_4 \rightarrow (NH_4)_{10}H_2W_{12}O_{42}4H_2O + 2H_2O + 14NH_3$$

Decomposition of ATP occurs with increasing temperature to the range of $400 - 900^oC$ to form tungsten trioxide (WO_3) and tungsten blue oxide (WO_{3-x}) [62]

Hydrogen reduction of these tungsten oxides is then used to form tungsten powder. By adjusting the reduction parameters such as temperature and humidity the powder characteristics such as grain size and distribution can be controlled. Thus commercially available tungsten powders are produced in mean size ranges of 0.1-100μm [61]. Subsequent powder such as plasma spheroidisation can be used to achieve a more desirable morphology.

1.3.2 Physical Properties

Tungsten exists in three known crystal states (α, β, and γ). α-tungsten is the only stable structure, β and γ-tungsten form α-tungsten when heated to $\geqslant 700^oC$. α-tungsten has a Body-Centered Cubic (BCC) structure. Tungsten behaves close to isotropically with an anisotropy coefficient at 24^oC of $A = 1.010$. The elastic properties at 20^oC are given below [61].

Youngs modulus, E (GPa)	390-410
Shear modulus, G (GPa)	156-177
Bulk modulus, K (GPa)	305-310
Poisons Ratio, μ	0.280-0.30

At 20^oC tungsten has a thermal expansion coefficient, α of $4.4x10^{-6}K^{-1}$[61] and thermal conductivity $175W.m^{-1}.K{-}1$ [63]. Tungsten's melting point lies at the highest of any element at 3422 ± 15^oC [61]. Density also lies amongst the highest at $19.25g/cm^3$ with a temperature of 25^oC. Primary recrystallisation temperatures have been reported in the range of $900 - 1700^oC$ [64] [65] [66] [67]. At low temperatures tungsten's behaviour is brittle. The Ductile to Brittle Transition Temperature (DBTT) lies in the range $200 - 300^oC$ and is heavily dependent on its mechanical, microstructure, and chemical states [61]. As a BCC metal tungsten has a preferred solidification orientation of [100] parallel to the long axis of columnar grains [68].

Tungsten has the lowest vapour pressure of any element [69]. This property along with its high melting point and ability to be drawn into fine wire lead to its first commercial application as lamp filaments at the start of the twentieth century [67]. Tungsten's unique combination of properties lead to it being the material of choice in a number of other applications. Its thermal properties lead to its use in high temperature environments, such as high temperature furnaces where it is used in heating elements and for shielding [70]. High density brings about the use of tungsten as X-ray shielding, gyroscope rotors, and as counter balance weights.

Tungsten has become the material of choice for plasma facing components in nuclear fusion experiments such as the International Thermonuclear Experimental Reactor (ITER) due to good thermal conductivity, low splutteringing yield, and a short activation decay time [71]. The application of nuclear fusion is discussed further in Section 1.4

1.3.3 Deformation Mechanisms

Deformation mechanisms in tungsten are slip, twinning and cleavage. Slip occurs in the most densely packed [111] direction and in the {110} and {122} planes. At elevated temperatures slip in the 111 plane also occurs. Slip is the most dominant deformation mechanism in tungsten.

Twinning occurs only in high purity tungsten twins form on the {112} planes in the [111] direction.

The usual cleavage plane is {110} but may also occur in {112}.

1.3.4 The origin of tungsten's lack of ductility

There are two known causes for tungsten's lack of ductility, a lack of close packed planes and poor grain boundary cohesion [72]. Tungsten due to its BCC structure is close packed along the <111> direction and its plastic deformation is dependant on the mobility of the $\frac{1}{2} < 111 >$ screw dislocation [73]. These dislocations spread over three planes and have a very high Peierls stress. This three-dimensional dislocation structure is difficult to move through slip and is the main factor which limits the deformation of tungsten. The second reason for tungsten's lack of ductility is poor grain boundary cohesion [72]. Inter granular fracture is the prominent failure mode in tungsten, and it can be worsened by the presence of impurities [74].

1.3.5 The effect of Impurities on the properties of tungsten

Interstitial atoms such as oxygen, carbon, hydrogen, nitrogen potassium, phosphorus, and nickel have low solubility in tungsten at room temperature ($< 0.1\mu g/g$) [61]. At melting temperature however the solubility increases to around $1000\mu g/g$. This results in segregation of impurities to the grain boundaries during cooling. Studies have demonstrated that the concentration of impurities at grain boundaries increase inter-granular fracture and result in embrittlement [75] [74].

The analysis of impurities in tungsten and their distribution requires complex sample preparation and analysis techniques such as auger spectroscopy and secondary ion mass spectroscopy. This is one explanation for the lack of a detailed understanding of the effects of impurities. In general, the re-

ported mechanical properties of tungsten have changed in the past 50 years as impurity levels have decreased. It is not possible to define absolute values for mechanical properties as the type, concentration and location of impurities cannot be precisely defined [61].

1.3.6 Oxidation

Tungsten's oxidation states range form 2− to 6+. Its most common oxidation state is +6, the oxide which forms in oxygen or air is tungstic oxide (WO_3) [76]. The oxidation of tungsten is heavily dependent on temperature and oxygen partial pressure. Oxidation of tungsten begins at room temperature and the thickness of the oxide layer increases with temperature. The rate of oxidation between room temperature and 200°C is slow but increases rapidly above this [61]. Between 327°C and 750°C protective oxide films are formed and the rate of oxidation is limited by diffusion. Above 750°C sublimation begins to occur, the sublimation rate is equal to the oxidation rate above 1300°C and the surface remains free from oxides. Tungsten powder reacts with oxygen like bulk where grain sizes are greater than one micron. In high temperature applications processing of tungsten inert atmospheres is required to prevent rapid oxidation [61].

As discussed previously, oxygen has a low solubility in tungsten at room temperature and solubility increases with temperature. Oxides which are adsorbed into a solid solution at temperature segregate to grain boundaries during cooling causing embrittlement. JR Stephens systematically investigated the effects of oxygen additions to tungsten in 1963. Stephens prepared samples with oxygen content between 4 and 50ppm and subjected the samples to tensile and bend testing [77]. At 4ppm the DBTT was measured at 232°C (450°F). Increasing the oxygen content to 10ppm, 30ppm and 50ppm increased the DBTT to 287°C, 448°C and 548°C respectively. Stephens also found that at increased oxygen content the yield and tensile strength decreased. Yield strength reduced by around 50 percent and tensile strength reduced by 30 percent over the range tested [77]. Small increases in oxygen content lead to large increases in DBTT and therefore oxygen in tungsten should be kept to a minimum. The exact concentration of oxygen should be determined for each application based on the required mechanical properties required and the operating temperature.

1.3.7 Thermomechanical processing

Thermomechanical processing is considered necessary in order to produce ductile tungsten and to reduce the DBTT. This phenomenon is in conflict with the effect of deformation on most ductile materials which exhibit a work hardening, where an increase in dislocation density leads to an increase in strength and decrease in ductility.

The effect of deformation on tungsten's mechanical properties was first recorded systematically in 1963 [78]. In this study the DBTT was found to decrease to 82°C at a rolling reduction of 73% and at temperature of 1150 to 1450°C. Subsequent studies have been carried out since this first report, the results of these studies can be summarised as the DBTT decreases as working temperature and grain size decreases [72] [79]. Additionally, these effects of working the material are found to be some extent reduced if subsequent annealing is carried out. For example, Reiser et al [80] showed

that annealing rolled tungsten at 200°C for one hour increased the DBTT from 375°C to 675°C.

Many of the studies into the ductalisation of tungsten via thermomechanical processing have proposed mechanisms by which this process occurs. These theories were summarised by Ren et al as follows [72]:

1. Thermomechanical processing increases density, removing porosity which may act as locations of stress concentrations.

2. Thermomechanical processing results in a lamellar microstructure with elongated grains. The high angle grain boundaries resulting from this deformed microstructure facilitate the movement of dislocations across grain boundaries.

3. Low temperature thermomechanical processing increases the fraction of edge and mixed dislocations. These dislocations have higher mobility and improve the low temperature fracture toughness.

4. Thermomechanical processing increases the dislocation density decreasing the energy necessary for dislocation migration.

5. Texture helps to control cleavage planes and the orientation of crack front propagation.

6. Average grain size decreases as deformation ratio increases leading to an increase in fracture toughness.

7. Thermomechanical processing increases the density of grain boundaries therefore reducing the average concentration of impurities at grain boundaries.

It is not yet clear to what extent these factors influence the effects of thermomechanical working of tungsten and further experimental work needs to be carried out in order to establish a causal link between these factors and experimentally measured ductility [72].

1.3.8 Nanocrystalline tungsten

Mechanical properties of metal alloys have previously been improved through the creation of nanocrystalline microstructures [81]. This approach has been seen as promising as a method for improving tungsten's ductility. Two approaches are considered for creating Nanocrystalline materials, top down and bottom up. The top down approach refers to the creation of a nanocrystalline microstructure via techniques which involve severe plastic deformation [82]. This technique have been shown to increase compression strength and decrease the DBTT. It is however difficult to scale up top down processes and the geometric freedom is very limited, these processes therefore are not likely to have commercial importance [82]. Bottom up approaches involve sintering of nano sized powders with the inclusion of grain growth inhibitor such as metal carbides or oxides. There are limited reports on the mechanical properties of nanocrystalline tungsten manufacture using bottom up processes and no data has as of yet suggested that grain refinement alone can improve ductility [72].

1.3.9 Production

Tungsten components are typically manufactured through the powder metallurgy route of compacting and sintering. In order to obtain dense material subsequent cold forming (rolling, swaging, and forging) is required. This processing results in an anisotropic microstructure and grains are often highly elongated [83]. Mechanical properties can be highly dependent on the microstructure; ductility, and strength have also been shown to increase with rolling induced deformation [84] [85]. When compared to ductile metals, shaping tungsten is challenging and should be carried out between the DBTT and the recrystallisation temperature. Tungsten can be machined, (drilled, turned, milled, etc.) however this is difficult, requires expertise, and close adherence to ideal conditions. Structures with greater complexity can be formed by Electrical Discharge Machining (EDM) [61] overcoming some of these difficulties.

1.3.10 Tungsten Alloys

Alloying tungsten has been considered as a means of improving the chemical, physical and mechanical properties. A huge number of alloys have been investigated but relatively few have been recognised as technically important [61].

Much of the research effort has been focused on addressing the issues of high DBTT and poor fabricability [61]. Tungsten's brittle behaviour stems from two factors, a lack of close packed planes and poor cohesion of grain boundaries. As a result, alloying elements generally aim to perform either one of the following; remove impurities or increase dislocation mobility [72]. Tungsten-rhenium alloys have been the most effective method for improving ductility through the promotion of additional slip planes and have gained much importance in this regard.

Another key area of alloy research is as a means to improve high temperature tensile and creep strength. Dispersion strengthening and precipitation hardening have been the most effective ways of achieving this [61].

Tungsten-Rhenium alloys

In 1955 Geach and Hughes first demonstrated that additions of rhenium could improve the workability of tungsten, their method involved cold rolling the alloy and measuring the reduction before fracture. The tungsten-rhenium alloy (35at.%) achieved an 11% reduction whilst the pure tungsten sample failed at the beginning of the rolling process prior to any reduction [86].

Following this initial finding Klopp et al conducted a more complete set of mechanical tests (three point bend, tensile, and creep) on arc melted and electron beam melted alloys [87]. Klopp et al showed that additions of rhenium as low as 1% could significantly decrease the DBTT, with greater improvements shown near the solubility limit of 27 wt% [87]. These authours also found that the creep strength was maximised with additions of 6-8% rhenium [88]. Subsequent studies have therefore focussed on rhenium concentrations of 6-8% to achieve ductility whilst maximising strength. Additions of around 27% were used to achieve maximise ductility. Another effect of rhenium again first reported by Klopp et al is a grain refining effect and an increase in the recrystallization temperature [87]. Grain size itself has been shown to significantly affect the DBTT of both tungsten and tungsten-rhenium alloys [89]. These early studies were all performed with

the use of thermal mechanical processing which is a factor that must be considered. More recent studies have performed similar tests with as sintered W-Re and have shown a strong solid solution softening effect [90].

For the application of fusion, rhenium must be limited as its transmutation products result in long lived radioactive waste [91]. A tungsten first wall is expected to trans-mutate to tungsten-rhenium at a rate of around 3at.% over a five year life of the first wall [91]. The thermal conductivity of tungsten is significantly reduced by only small additions of rhenium [92], an important consideration for such applications.

The main drawbacks of rhenium as a method for improving ductility are its relative rarity and cost. The effects of increased strength and ductility with solid solution alloying is unexpected and found a number of BCC alloys [92]. The cause of this effect has been attributed to scavenging of impurities (in particular oxygen), improving grain boundary cohesion and directly modifying the mechanical response [72]. Whilst these factors may have an influence, the main effect appears to be as a result of solid solution softening which increases the low temperature mobility of screw dislocations [93, 72].

Other Solid solution alloys

Due to the beneficial effect rhenium additions have on tungsten there has been significant research into other solid solution alloys. Molybdenum, niobium, tantalum and vanadium are the only elements that are fully miscible with tungsten [94]. Rhenium, titanium, technetium, iridium, hafnium, rhodium and osmium show limited solubility.

Iridium, hafnium and rhodium have limited solubility in tungsten at 2-4%. Additions of these elements have shown some promising effects on tungsten such as Tungsten-iridium which has been shown to have similar effects on tungsten as Rhenium [95]. However studies on these particular elements along with technetium and osmium are somewhat limited as they are rare elements and are not likely to offer cost advantages over Rhenium [72].

Alloying with tantalum or vanadium has not been shown to have an effect on ductility [96]. Titanium has been shown to improve toughness and strength although tungsten-titanium alloys still behave in a brittle manner [97]. Recent research into tungsten-molybdenum alloys up to 30 wt.% did not show improvements in terms of ductility [98].

In summary promising novel solid solution alloys for tungsten are lacking and much of the research effort remains focused on tungsten-rhenium.

Dispersion strengthened alloys

Dispersed phases in tungsten are typically metal oxides, carbides, nitrides and borides; usually prepared by compacting and sintering due to the lack of stability of the dispersed phases at tungsten's melting temperature [61].

OXIDE DISPERSED Thorium dioxide also known as thoria is an ideal dispersoid as it is insoluble in tungsten and is stable at high temperature. Additions of 0.5-4 wt.% significantly restrict grain coarsening during sintering, producing a fine grained microstructure [61]. Thoria particles locate at grain boundaries thus impede grain boundary mobility [61]. Thoria increases the recrystallisation temperature, strength and creep resistance of

tungsten. It has also been shown that additions of rhenium and iridium can improve ductility in thoriated tungsten.

The most common use for tungsten thoria is as electrodes in tungsten inert gas (TIG) welding. This is in the most part due to the fact that thoria lowered the electronic work function, enhancing thermionic emission, therefore creating a more stable arc [61, 99].

Other oxide dispersed alloys of yttrium, lanthanum, zirconium, hafnium and cerium behave similarly to thoria but provide different emission characteristics depending on temperature [61].

CARBIDE DISPERSED Alloys with dispersed carbides are produced by heat treatment of super saturated solid solutions. Binary tungsten carbide alloys show some strengthening effect in the temperature range 200 - 427°C but have little effect at higher temperatures, this is due tungsten carbide particles coarsening rapidly above those temperatures [76].

Of the elements in groups IV, V and VI hafnium carbide has the greatest high temperature stability [76]. Alloying with HfC increases the DBTT by around 100°C as rolled but decreases slightly as recrystallized. Strength improvements up to ninefold can be achieved with optimum hafnium carbide composition of 0.35at.% . The strength properties of HfC and the ductility of the W-Re system can be combined. W-Re-HfC cannot be produced via powder metallurgy techniques due to hafnium's high affinity to oxygen and is typically produced via arc melting. W-Re-HfC have the highest strength of any man made alloys at at temperatures greater than 2000K [61].

Other carbides have been investigated such as TaC NbC and ZrC and have been found to be as effective as HfC. However above a temperature of 1649°C they do not maintain the same strength properties as HfC alloys due to the coarsening of the carbide precipitates at this temperature [76].

OTHER DISPERSION STRENGTHENED ALLOYS Boron can exist simultaneously as a substitutional and interstitial impurity in tungsten at low concentrations. Small additions of boron can produce a rapid increase in strength [100]. The strengthening effect of borides however such as HfB and ZrB has been shown to be less effective than that of carbides [76]. The addition of nitrides causes embrittlement, and typically results in cracking during fabrication. The addition of HfN to W-Re alloys for example has been shown to cause a loss of ductility with no strength benefit [76].

Tungsten Heavy alloys

The term heavy alloy is typically used to refer to alloys containing large amounts of tungsten with an either nickel-copper or nickel iron matrix.

These alloys are typically designed to utilise the thermal properties of tungsten and its high density. Often used for counterweights and inertial components such as in gyroscopes or flywheels or as electrodes for resistance welding [76].

1.3.11 ALM of Tungsten

There has been significant investigation into the SLM of tungsten powders. Appendix B provides a tabulated summary of the process parameters extracted literature to date.

SLM of tungsten powder was first reported by Zhang et al [101] in 2012 producing samples with a relative density of 82%. The following year it was shown by Deprez et al that SLM could be used to manufacture collimators from tungsten with sufficient geometric accuracy for use in magnetic resonance imaging (MRI) [102]. The authors did not report the parameters or SLM system used to produce the collimator but did report a relative density of 89.9% and dimensional accuracy ranged from -260 to $+650\mu m$. Zhou et al reported an investigation into SLM tungsten using a Renishaw AM250 system fitted with a 200*W* laser. Zhou et al reported an achieved density 82.9% and attributed the low density to the balling effect [20] and oxide contamination [55].

Nie et al have published two papers on the ALM of tungsten using a femtosecond laser, capable of delivering a high peak power of up to 125MW for relatively short pulse durations of 400*fs* [103] [104]. The authors demonstrated that this novel technique could be used to control grain sizes in samples.

Wang et al investigated SLM of tungsten using a Renishaw AM 400 system, specifically the authors investigated the impact of the powder morphology on densification. It was shown that plasma spheroidisation increases powder packing density and laser absorptivity which in turn leads to increased sample density [105]. A maximum relative density of 96% was achieved. An article available by Sidambe reports the use of a Renishaw SLM 125 system to manufacture tungsten at a optically measured relative density of 98% [106].

Enneti et al reported the importance of laser power on densification for SLM of tungsten using an EOSINT M280 system with laser power between 200 and 300 watts [107]. The authors also investigated the effect of two separate powders with differing size ranges and packing density, though the pacing density was found to have a significant effect at 200W at 300W the difference was found to be insignificant. Leading the authors to conclude that low bulk density powder could be successfully used. In an investigation by Enneti et al using a Concept laser system with a maximum power of 90W, the resulting material density increased with volumetric energy density [108] achiving density in the range 59-75%.

Authors have also investigated SLM of tungsten based alloys. Ivekovic et al investigated the manufacture of tungsten with tantalum mixed in various ratios (1, 5 10 wt%) using two different SLM systems [109]. The addition of tantalum was found to reduce the grain size, however cracks were observed in all samples. The authors reported the use of a heated stage to preheat the system to 400 degrees Celsius in order to reduce cracking however this was not found to reduce the observed cracks and the authors concluded that oxygen content should be minimised in order to prevent a decrease in the DBTT. Gu et all investigated tungsten with the addition of 2.5 wt.% titanium carbide observing unique microstructures and reporting a relative density of 97.8% which was significantly affected by variations in energy density [110]. Uhlmann et al investigated the effect of process parameters on the manufacture of tungsten carbide cobalt using a design of experiments methodology [111]. The authors found that the relative density of material was greater at increased energy density however this lead to the evaporation of cobalt which in turn causes embrittlement of the material and cracks therefore easily spread.

Commercial ventures offering ALM tungsten have recently emerged. This includes M & I Materials who under their brand name WOLFMET are of-

fering high precision SLM tungsten components. A case study on their web page discusses collimators which have been produced and tested with hole sizes of 0.6mm in diameter [112]. M & I materials submitted a patent application in 2016 titled 'Selective Laser Melting of Refractory Metal Powder' which describes an ALM method to process refractory metal powders with a melting point above 2400°C [113]. Prior to this in 2014 Smit RONTGEN a Philips brand announced research into the development of SLM tungsten using custom designed EOS M280 systems. Initial trials were reported to produce a feature resolution down to 100µm with a maximum build volume of 230x230x200mm [114].

To date there have been no reported works on EBM of Tungsten

1.4 TUNGSTEN AS A MATERIAL IN FUSION

Global energy consumption is increasing year on year [115]. Recent predictions suggest this trend will continue with a 30% increase in consumption by the year 2040. This is the equivalent to adding another China and India to current global demand [116].

Human demand for energy is currently fed to a large extent by non-renewable sources such as fossil fuels [115]. Each year the U.S energy information administration releases projection for future energy generation based on current trends. Figure 1.7 shows the current projection until 2050. Renewable energy is projected to be the largest growing energy source meeting the expected rise in demand increasing from 18% to 31%. Despite these increases, in 2050 fossil fuels are expected to remain the dominant fuel source accounting for 68% of electricity generation and over 75% of overall consumption with crude oil consumption continuing to increase year on year. [117] [116].

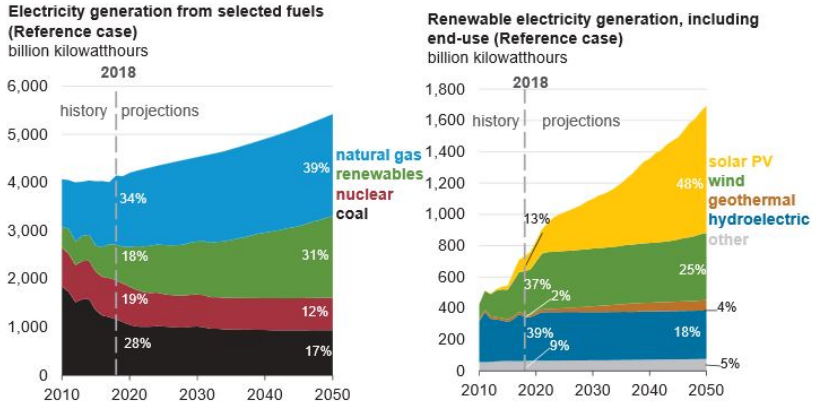

Figure 1.7: Projected rise in global electricity generation by source. Source: U.S Energy Information Administration, Annual Energy Outlook 2019 [117]

The release of CO_2 into the environment as a result of the combustion of fossil fuels is leading to irreversible climate change [118]. The increase over the coming years will only exacerbate this problem with the global average temperature expected to rise between 0.3 and 4.8 degrees Celsius in the current century as a result of the greenhouse effect [119]. This temperature rise is anticipated to cause polar ice melt, sea level rise and super storms [120].

A solution currently being investigated to reduce the impact of global environmental change is nuclear fusion. Fusion has the potential to deliver almost limitless energy without directly producing greenhouse gasses and long lived nuclear waste [121]. Nuclear fusion is the act binding two elements, a process in which mass is not conserved and large amounts of energy are released [122]. The ratio of fuel mass to energy produced is extremely high for fusion reactions, one kilogram of fusion fuel can provide the same energy as 10 million kilograms of fossil fuels [123].

There are a large number of possible fusion reactions. The reaction between the hydrogen isotopes deuterium and tritium is favoured for harnessing fusion energy (Equation 14), this is due to relatively low temperatures required and abundant deuterium fuel source [124]. The deuterium-tritium reaction releases energy in the form of a high energy (14.1MeV) neutron and (3.5MeV) helium particle. Temperatures of 150 million ^{o}C are required for the initiation of the deuterium-tritium reaction [122].

Deuterium is stable and naturally abundant and can be extracted from seawater by electrolysis. Tritium on the other hand is unstable with a half-life of 12.32 years [124]. Tritium can be produced via neutron activation of the isotope litium-6. This typically takes place in nuclear fission reactors but will have to take place in the walls of fusion reactors in a process known as breeding in order to maintain sufficient tritium inventory [124].

$$ {}^{2}_{1}D + {}^{3}_{1}T \rightarrow {}^{4}_{2}He + {}^{1}_{0}n \tag{14} $$

The extremely high temperatures required to initiate the deuterium-tritium reaction are considerably higher than the ionization of the reactants. The reaction therefore must take place in the plasma state and in a vacuum. There are two leading methods for confining this plasma in order to maintain a stable fusion reaction, magnetic confinement (MCF) and inertial confinement (ICF). ICF heats and compresses a fuel target with the use of lasers, creating shockwaves that travel inward through the target. MCF uses magnetic field to contain a hot plasma in a toridal shaped reactor known as a TOKOMAK and is considered the most viable source of reliable fusion energy [125]. The majority of research effort particularly in Europe is dedicated to MCF.

1.4.1 MCF and the TOKOMAK

The limitations of MCF are that net power out cannot be achieved at this time; the maximum achieved power out is 65% of the energy input, meaning energy is lost. This maximum power was achieved by the Joint European Torus (JET), located at CCFE [126] producing a peak power of 16MW in 1997 for an input heating power of 24MW [124] (Figure 1.8). In order to reach higher net power output reactor sizes need to be increased and reactions sustained for longer periods of time.

EUROfusion is a collaboration between a group of EU countries. They defined a roadmap to achieve the realisation of fusion power by 2050. This is a two step process; the first step being the development of a reactor which demonstrates net power out, the second is to produce a demonstration power plant. The former is currently being constructed and is called International Thermonuclear Experimental Reactor (ITER). The latter is known as the demonstration power station (DEMO) [127].

ITER is a project involving China, the European Union, India, Japan, Korea, Russia and the United States. The aims of ITER are as follows:

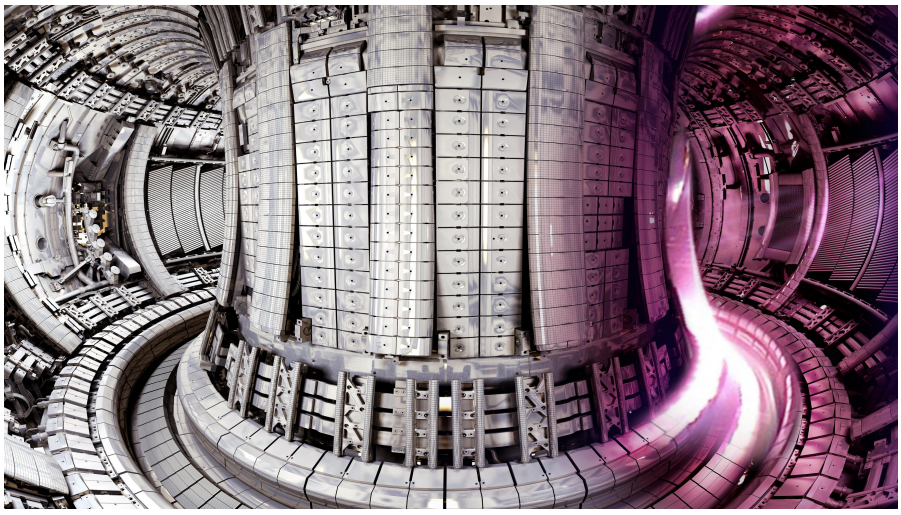

Figure 1.8: A photorealistic render of the TOKOMAK JET []

- Produce 500MW of fusion power from 50MW of heating input power (Energy gain factor of 10).
- Demonstrate the integrated operation of fusion technologies including heating, control, diagnostics and remote maintenance.
- Test tritium breeding with the aim of demonstrating tritium sustainability.
- Demonstrate safety, by demonstrating control of the plasma and fusion reactions and negligible environmental consequences
- Achieve a deuterium tritium plasma that is stable for long periods of time through internal heating.

ITER will remain an experimental device and is not intended to generate electricity. The experience gained in the operation of ITER will inform the construction of DEMO which will include turbines for electicity production. The main aim of DEMO is simply to act as a prototype of a power producing reactor, opening the way for industrial and commercial exploitation [128].

ITER and DEMO are to be based on a TOKAMAK reactor design. A TOKAMAK consist of a vacuum chamber which is in the shape of a torus. A plasma is created and heated within the chamber using a series of heating steps including neutral beam injection, high frequency electromagnetic waves and ohmic heating [129]. Plasma is contained within the chamber using controlled toroidal and poloidal magnetic fields [122]. The charged helium particles from the reaction are contained within the plasma. The neutrons which account for 80% of the reaction energy are uncharged and therefore exit the plasma and collide with the plasma facing components (PFC) on the inside of the vessel. Heat generated from the atomic collisions of these high energy neutrons is extracted from the PFCs using a high pressure coolant [122]. In DEMO This extracted heat energy will then be used to drive turbines for electricity generation [127].

Plasma facing components

The PFCs consist of two components, the divertor and the blanket. The blanket accounts for the majority of the PFCs covering the inside walls of a TOKOMAK and has a number of functions as follows:

1. Breed tritium.
2. Extract heat.
3. Shield components such as the pressure vessel and magnets from neutron irradiation.
4. Provides a low spluttering first wall.

The divertor is typically located at the bottom of a TOKOMAK and consists of a number of segments known as cassettes. The divertor is the only PFC that comes into contact with the plasma. The roles of the divertor are:

1. Remove impurities from the plasma during operation, allowing the reaction to be maintained.
2. Recirculation of fuel
3. Neutron shielding
4. Cooling
5. Minimise production of impurities by limiting plasma wall interactions to a small region.

An image of a divertor cassette is shown in Figure 1.9. The surface of the targets during operation experience exceptionally high heat flux of between 5 and $20MW/m^2$. These high heat fluxes provide very demanding conditions on the plasma facing targets, leading to high erosion rates, high temperatures and thermal stresses.

The considerations that must be made when selecting suitable plasma facing materials are as follows:

- Withstand steady state and transient thermal loading, thermal shock, fatigue, recrystallization and melting. The PFCs are subject to steady state loading of $5 - 20MW/m^2$, transient heat loading can take place up to $10MJ/m^2$ due to plasma disruptions [130] [131]. These transient loads can lead to large temperature gradients and as a result high thermal stresses [132].
- Withstand and operate under neutron induced damage such as irradiation hardening and embrittlement for at least two years. It has previously been determined that a viable power plant will require upwards of 75% utilisation [133]. Maintenance and replacement of the PFCs, in particular the divertor is estimated to take up to six months and therefore components must be able to withstand neutron irradiation for at least 2 years [134]. Utilisation is a key factor for demonstrating viability so a longer operationg period is preferable.
- Be non-hazardous after a period of 100 years due to transmutation as a result of neutron bombardment [135]. This target has been set such that fusion waste will not present a burden for future generations [136].

- Retain minimum tritium fuel. Tritium is absorbed by plasma facing materials as a result of interaction with the ion plasma through implantation and diffusion or migration. Retained tritium must be minimised in order to maintain inventory levels [137].
- Allow passing of high heat flux (high thermal conductivity).
- Be non magnetic
- Be producible and replaceable at a viable and reasonable cost.
- Be plasma compatible. The maximum impurity concentration in the plasma must remain low, particularly for materials with high atomic numbers [138].

These criteria make material selection challenging and no current material meets all these criteria. Carbon fibre composites (CFC) have been implemented in many TOKAMAKs to date as they meet many of these criteria well [139], ITER was also initially intended to feature a CFC first wall [140]. Experimental studies in JET demonstrated that tritium retention was above the acceptable limits, changing to an all metallic beryllium/tungsten first wall reduced tritium retention by at least a factor of ten [141].

Tungsten has a low fuel retention, high thermal conductivity, creep resistance, reasonable cost, and its activation products have a short half-life. Consequently, ITER and DEMO are now expected to feature tungsten as a plasma facing material. Tungsten is currently the most ideal material for this application though it still has its shortcomings. Tungsten is brittle even at elevated temperatures with a high DBTT. Parts of the tungsten PFCs could operate in the brittle regime [142]. ITER designs consist of 54 divertor cassettes. The plasma facing surfaces of the divertor is to be covered in a grid of tungsten 'monoblocks' as shown in Figure 1.9. The monoblocks are actively cooled by high pressure coolant which runs through a copper interlayer. Their small size (Approximately:30x30x12mm) and spacing allows for mismatched thermal expansion and insures that stresses are minimised[143]. The tungsten plasma facing surfaces are to be bonded to a copper inter layer and CuCrZr alloy which acts as a heat sink.

1.5 SUMMARY AND RESEARCH AIMS

Tungsten is uniquely suited to some specific applications due to its incomparable properties. Specifically the application of PFC in magnetic confinement fusion has been discussed where tungsten's thermal, mechanical, activation and fuel retention properties mean it is currently considered as the most viable choice. Challenges exist in manufacturing tungsten components, particularly those with complex geometries. ALM is a novel manufacturing technique which has the potential to enable the production of more complex tungsten components. Specifically the powder bed processes of SLM and EBM can be used to melt metallic powders in a layer by layer manner to build components with a large amount of design freedom and high geometric accuracy.

Investigations into ALM tungsten to date have focused exclusively on SLM. The findings from this literature were outlined in Section 1.3.11 these findings can be briefly summarised as follows:

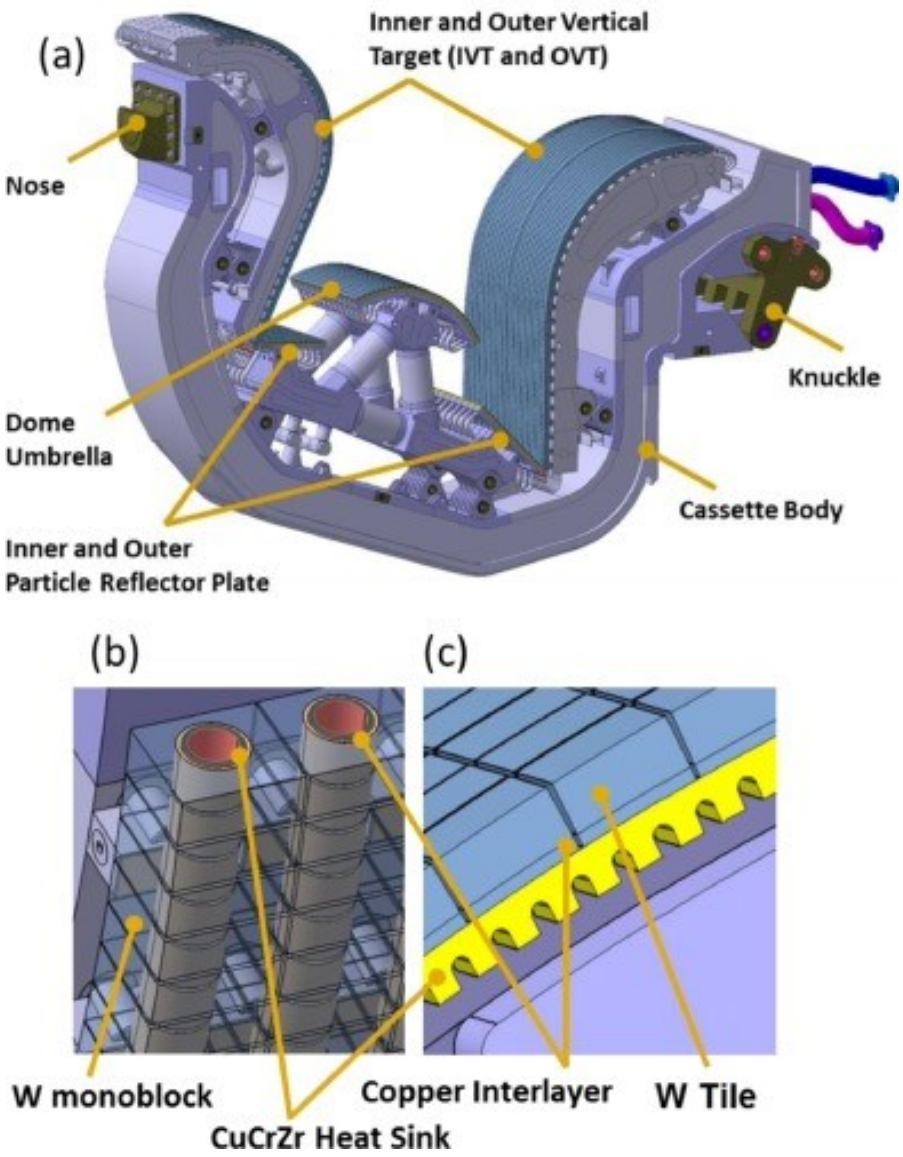

Figure 1.9: An rendering of the proposed divertor cassette design for ITER. (a) A divertor cassette showing plasma targets. (b) Array of tungsten monoblocks which cover the surface of the divertor. (c) A cross section of the plasma facing first wall. ([144])

- Spheroidised powders with high packing density can produce higher sample density. With certain process parameters this effect has been found to be insignificant.
- Optically measured density of up to 98% can be achieved.
- High geometric accuracy can be achieved, with one online article claiming a feature size as small as 100µm

The current literature on tungsten SLM does not fully examine the effects of processing parameters on the material density. The data from the literature on SLM has been collated and tabulated in Appendix B. In order to reveal any trends in this data some of the key variables have been plotted in Figures 1.10 and 1.11 The maximum laser power used in the above mentioned publications has been plotted against the achieved density in Figure

1.10. Regression analysis reveals a significant direct correlation between laser power and density across the available literature. Four of the publications provide significant information to calculate energy density. Figure 1.11 plots the energy density against the maximum achieved sample density and the beam power at the maximum sample density, a strong inverse relationship is found in both cases.

These observations suggest the following:

- Higher power lasers are required to achieve higher density.
- At lower laser powers a higher energy density is required to maximise material density.

It appears that the rate of energy input is an important factor for producing high density ALM tungsten. Energy density itself appears to be a less important factor and the optimum energy density decreases as the power increases. None of the current literature has independently assessed the effects of laser power and energy density on sample density and these observations can only be derived through analysis of the available data as a whole.

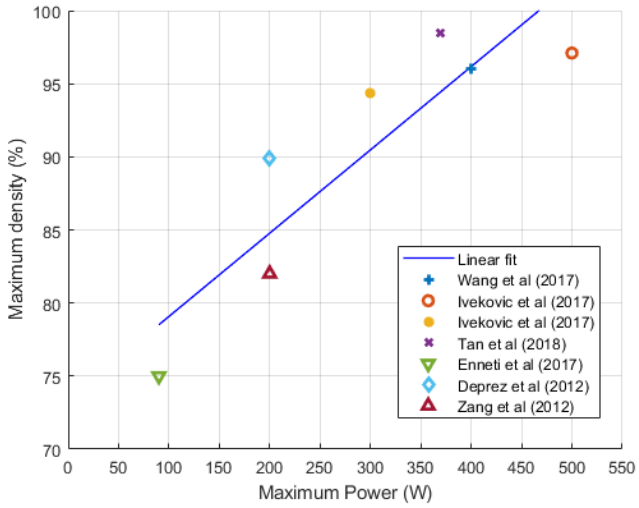

Figure 1.10: The relationship between the maximum beam power and sample density for published data $R^2 = 0.79$ $p - value = 0.002$

The gaps identified in the current literature are as follows. Firstly the current literature has not systematically examined the effect of all ALM process variables on powder consolidation. Though trends across these papers suggest that there are significant correlations between sample density, beam power and energy density.

Secondly EBM has not been investigated as a method for ALM of tungsten. This is likely due to practical difficulties discussed previously in relation to the size of the build volumes in ARCAM EBM systems. Despite these challenges the EBM could offer significant benefits. The EBM process:

- Utilises higher powers of up to 3KW, this is significantly higher than is available in SLM currently which may help to produce higher material density.

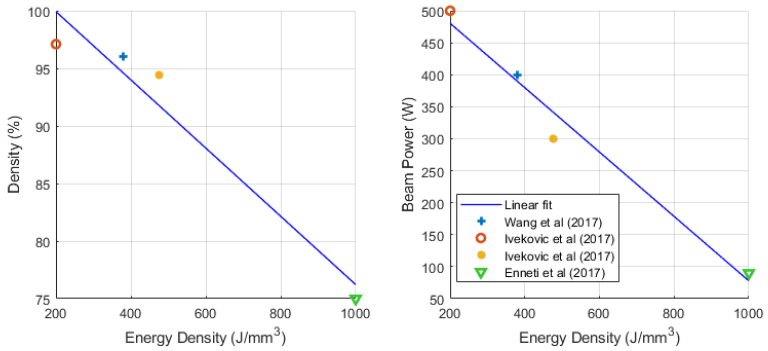

Figure 1.11: Left: The relationship between Energy density and sample density for published data $R^2 = 0.97$ $p-value = 0.013$ at the maximum reported density. Right: The relationship between Energy density and Beam Power for published data at the maximum reported density $R^2 = 0.94$ $p-value = 0.028$

- Takes place in a vacuum which may help prevent oxidation at high temperatures and other impurities. Oxides and impurities which in tungsten could segregate to and weaken grain boundaries, leading to embrittlement.
- Operates with high build temperatures which could reduce thermal stresses and reduce cracking

Thirdly there has been limited investigation into the mechanical properties of ALM tungsten.

The objective of this work will therefore be, to use statistical experimental design to identify the effect of process parameters on tungsten ALM. In order to produce crack free tungsten with a density greater than 98% via ALM. Improving the quality of ALM tungsten is important if this material is to be used for applications such as PFC's. Experimentation will be carried out on both SLM and EBM systems to establish the strengths and limitations of each manufacturing method. The outline for the tasks in order to achieve this are as follows:

- To establish the effect of process parameters on defect formation in SLM of tungsten using statistical design of experiments (DOE). With the aim of identifying an optimum processing region which minimises defects.
- Establish the feasibility of EBM of tungsten.
- If EBM processing can be achieved, investigate the effects of process parameters on defect formation. With the aim of identifying an optimum processing region which minimises defects.
- Characterise key material properties of the ALM tungsten produced.

2 EXPERIMENTAL TECHNIQUES

2.1 TUNGSTEN POWDER

Tungsten powder was supplied by LPW Technology LTD (Cheshire UK) and was used to carry out all experimental builds. The powder was processed using plasma spheroidisation as opposed to plasma atomisation. The powder had a purity of 99.99% and oxygen content below 200ppm . During plasma spheroidisation the raw angular powder passes through a gas plasma, the plasma melts the particles allowing them to reform into spherical powder particles [145]. Spherical particles allow for better flowability which can be advantageous for AM processes [105]. Plasma atomisation is a similar process that uses wire as a raw input material. The advantage of spheroidisation for tungsten is that it allows the raw extracted powder to be directly spheroidised without first producing a wire feedstock [145]. The particle size distribution of the powder was measured via laser diffraction using a Malvern Mastersizer 3000, d10, d50, and d90 were measured at 25.5µm, 32.8µm and 42.1µm respectively. Powder morphology was analysed using a Philips XL30 Scanning Electron Microscope (SEM) shown in Figure 2.1a. Particles were found in most cases to be spherical in shape. The hall flow rate was measured as per ASTM B213-17 at 5.7s/50g [146]. Tap density was measured in accordance with ASTM B212-17 at 14g/cm^3 [147].

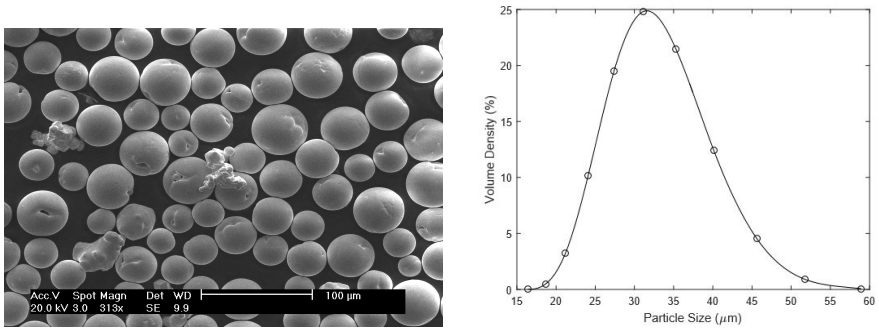

(a) **(b)**

Figure 2.1: Powder morphology: (a) SEM micrograph (b) Powder size distribution as measured by laser diffraction

2.2 CARTESIAN COORDINATE SYSTEM

Through this work a three dimensional Cartesian coordinate system will be used to define positions within the various systems used, and samples produced. Axis lines X, Y, and Z are orientated as follows:

- **Z** - Parallel to the build direction.

- **X** - Perpendicular to the build direction and parallel to the front of the build chamber.

- **y** - Perpendicular to the build direction and parallel to the side of the build chamber.

Figure 2.2 shows a diagram of the coordinate system as arranged for drawings.

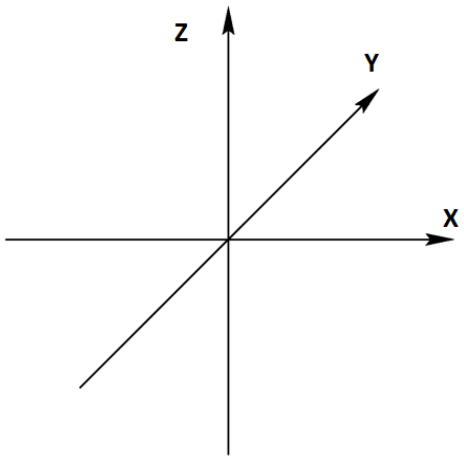

Figure 2.2: Cartesian Coordinate system

2.3 DESIGN OF EXPERIMENTS

A design of experiments (DOE) approach was used in order to investigate the effects of process variables on measured responses. The book 'Design and analysis of experiments' by Douglas Montgomary is recommended for further details on DOE [148]. A response surface methodology (RSM) was used to model responses [149].

There are a number of limitations of a DOE approach which must be taken into consideration when using these methods. Firstly selection of variables requires a knowledge and understanding of the process [148]. The researcher must select a suitable range of each variable in order to observe any effects. Too wide or narrow a range can lead to the appearance that key factors do not affect the process. Additionally the range selected should yield usable results, too wide of a range can lead to a process failing. In reality it is often vary hard to select ideal levels of variables initially and DOE becomes an iterative process [148].

Secondly the DOE process itself can contribute to human error. The core concepts used in DOE such as randomisation and blocking can lead to mistakes when setting parameters for each experiment [148]. Planning should be carried out in order to ensure these potential errors are eliminated. It is suggested that before carrying out experiments trial runs should be conducted in order to establish consistency in the experimental technique [148].

2.4 RENISHAW SLM 125 AND AM 400

2.4.1 System overview SLM 125

The Renishaw SLM 125, is as the name suggests used to manufacture components using the SLM method of ALM within a square 125mm build area. The Renishaw SLM 125 is identical to the earlier MTT SLM 125 system, the rights to which were purchased by Renishaw PLC, after which the machine was re branded. An image of a SLM 125 system is shown in Figure 2.3.

Figure 2.3: Renishaw SLM 125 System

The SLM 125 uses a 200 Watt ytterbium fibre laser focused to a spot diameter of 50µm. The process takes place in an atmosphere of argon which is circulated and filtered during operation to remove contaminants produced. Housed within the upper section of the chamber is the powder hopper, dosing mechanism, wiper, and build platform. In the top of the chamber there is a glass window through which the laser beam passes during operation. The lower part of the build chamber houses the mechanism which moves the build platform and an overflow hopper which is used to collect unprocessed powder.

User control of the SLM 125 is via a touch screen located to the right hand side of the chamber. The user interface allows control of the moving components during set up, clean down, and during operation. The interface also allows the user to monitor the progress of a build along with information from sensors such as temperatures, pressures, and oxygen levels. A chiller sits alongside the machine which maintains the temperature of the optics system at 20°C.

2.4.2 System overview AM 400

A number of experimental builds were carried out using the Renishaw AM 400 system at Renishaw PLC (Stone, UK). The Renishaw AM 400 operates using the same process as the SLM 125 system but the hardware has two key differences. Firstly, the AM 400 uses a 400 Watt laser as opposed to the 200 Watt laser of the SLM 125 system. Secondly the AM 400 houses a 250mm square build platform in comparison to the 125mm platform found in the SLM 125.

Figure 2.4: Renishaw AM 400 System

Reduced Build Volume

Builds on the AM 400 were carried out using the reduced build volume (RBV) shown in Figure 2.5. The RBV fits within the standard 250mm build platform and contains a powder hopper, dosing mechanism, and overflow. The RBV allows for processing of small volumes of powder and is particularly useful for material specific parameter developments. It uses a square substrate with sides of length 78mm and a radius at each corner of 15mm.

2.4.3 Process steps

Before running the system, the hopper is removed from the chamber and filled with powder before reinsertion. A substrate and the rake are inserted and levelled, such that they are parallel with a small gap, to allow the first layer to be deposited. The recoater blade material of the raking system is a 10mm diameter extruded silicone tube which is replaced between each build. The process takes place in a vacuum chamber, upon starting the build process air is removed from the chamber via a vacuum pump to a pressure of 100 mbar, the chamber is then filled with argon until the oxygen level in the chamber reaches a pre defined level; typically between 100ppm

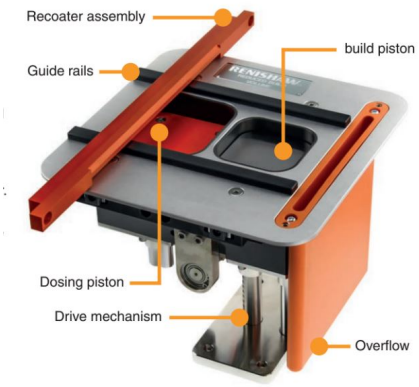

Figure 2.5: CAD Rendering of the RBV

and 1000ppm. The system does not utilise a heated build platform and the substrate at the start of the process is at a room temperature of $18 - 25^{o}$C. During processing of tungsten the substrate temperature was measured at 60^{o}C $\pm 10^{o}$C.

Upon the build starting powder is deposited from the hopper at the rear of the chamber in front of the rake, which then moves forward, depositing a layer of powder atop the substrate. Any excess powder is deposited into the overflow hopper at the front of the chamber. The deposited powder is selectively melted, as determined by a CAD file. The substrate is then lowered by the layer thickness and the steps are repeated until the desired height is reached.

After completion of a build the chamber is opened and all powder brushed into the overflow hopper. Powder collected in the overflow hopper is sieved using a 53µm test sieve to remove any contaminants or large particles before reuse.

2.4.4 Software

Build files were prepared using a combination of Rhino3D and MTT AutoFab software. Rhino3D was used to generate a CAD file with the desired geometry which could then be exported as an STL file to be processed in AutoFab. AutoFab allows the addition of support structures to parts after which the parts can be sliced to the desired layer thickness. The AutoFab software also generates the laser paths for each layer as defined by a series of melt parameters. The slice and laser path data were then exported as an MTT file which was read by the SLM 125.

2.5 ARCAM S12 EBM PROCESS

2.5.1 Hardware Overview

Arcam supply a range of EBM machine models but all are based on the same template. For this work an Arcam S12 system was used. Figure 2.6 shows a schematic of the S12 build chamber and its key components for reference. The components of the Arcam S12 are housed within a vacuum chamber and beam column. Prior to operation, the vacuum chamber is evacuated to

a pressure less than $5x10^{-4}mbar$, and the beam column to a pressure less than $5x10^{-4}mbar$. The beam column houses the electron gun, magnetic focusing, and deflection lenses.

The vacuum chamber contains two powder hoppers, one on either side. A rake controlled by a motor, at the back of the chamber, moves between the two hoppers collecting and depositing thin layers of powder. Powder sensors either side of the build tank detect the amount of powder which is deposited on each layer. This information is used to adjust the movement of the rake to collect more or less powder as required. The build platform moves up and down in the Z direction. After each completed layer the platform is lowered by the layer thickness (typically $70\mu m$), this movement is controlled by a motor mounted below the chamber. Parts are built on top of square stainless substrates, these plates are supplied by Arcam with thickness $10mm$ and side lengths $150mm$, $170mm$, $190mm$, and $210mm$.

A heat shield sits between the build area and the powder hoppers. The heat shield insulates from radiative heat transfer, directing reflected energy back towards the top layer of the build. The heat shield consists of two stainless steel sheets mounted to a pyramidal frame forming a small gap between each sheet minimising conductive heat transfer.

A port hole and window located in the front of the build chamber allows for visual monitoring of the process.

2.5.2 Electron gun

The electron beam used in the S12 operates upto 3kW at 60kV. The electron beam is generated using a tungsten filament as a cathode which operates at a temperature of 2200°C. The filament is replaced approximately every 100 hours of use. A grid cup also known as a bias cup is used between the anode and the cathode to control the beam current and the shape of the beam.

Following acceleration of electrons through the anode the beam passes through a series of electromagnetic lenses which correct astigmatism, focus and deflect the beam. The electromagnetic coils are controlled by Arcam's EBM control software. The electron column is maintained at a temperature below 60°C via a chiller which passes coolant through coils placed over the beam column.

2.5.3 Ancillaries

There are a number of ancillary components of the S12 system that aid its function, These are an electronics cabinet, a chiller, and a helium supply. The electronics cabinet sits alongside the vacuum chamber and houses all the control systems for the beam, motors, powder sensors, thermocouples, vacuum pumps, etc. This section of the S12 also provides a user interface in the form of a PC with a touch screen. The PC uses a version of Windows XP operating system and communicates with the machine via Arcam's EBM control software which is disused in more detail in Section A.5. The chiller is used to maintain the beam column at a set temperature of 60°C. Finally helium is supplied from a gas bottle alongside the machine; the helium flows into the chamber to reduce the accumulation of charge in the powder bed during operation. Additionally it also acts to reduce the cooling time following a build.

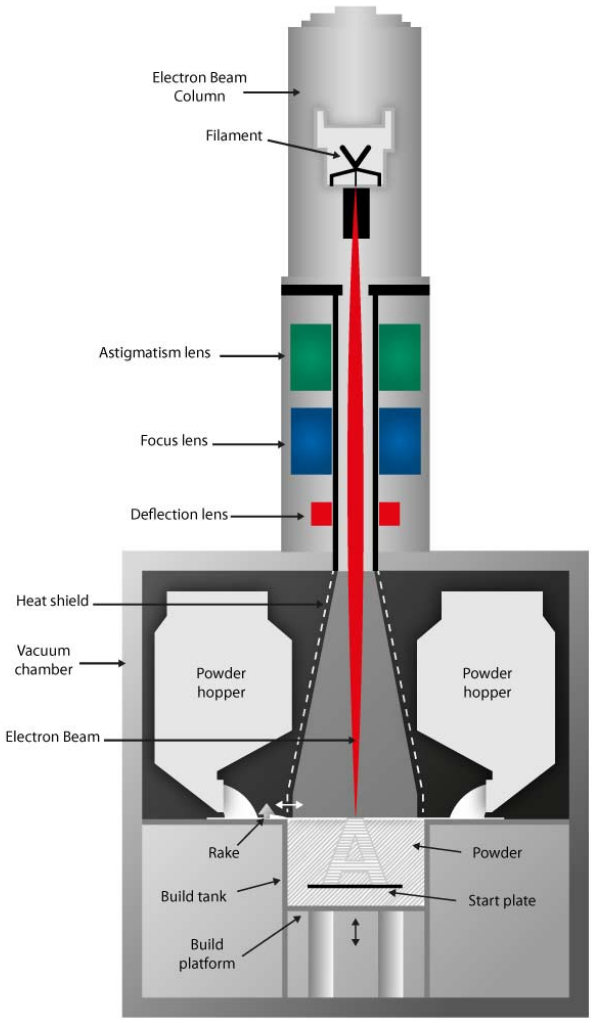

Figure 2.6: Schematic of ARCAM S12 EBM System. Image from arcam.com

2.5.4 Small Build Tank

An in house build tank was developed in order to minimise the required volume of powder. Details of this system are provided in Appendix J.

Tungsten

For the volume of powder that was being processed it was feasible to use manual methods to recycle powder. Powder inside the chamber was collected into a container using a scoop and brush. Sintered powder was removed from parts using a bush. Collected powder was sieved using a 53 µm test sieve before reuse.

Powder Changeover

The following precautions were taken to minimise the cross contamination of powders when switching to processing a different powder types. Every component was removed from the chamber and fully disassembled. All parts were cleaned fully with Isopropyl alcohol and paper cloth. Any consumable components for example rake blades or rope seals were replaced

with new parts before reassembly. Along with cleaning the components, all tools and personal protective equipment (PPE) were cleaned thoroughly. To minimise the risk of contamination when switching powder, this procedure was only carried out once during the course of this work.

Handling equipment

Loaded hoppers and barrels required handling equipment to safely lift and manoeuvre. To move the hoppers a specialised lifting equipment was used. Powder barrels were placed on caster wheels to allow them to be moved easily. To transfer powder between barrels and hoppers a large metallic scoop was used.

2.5.5 S12 Set up procedure

In brief set up procedure for the S12 is as follows:

1. Replace any consumable parts as necessary for example heat shield panels, rake teeth, filaments etc.
2. Load hoppers with powder.
3. Lower build platform and deposit a thick layer of powder on top of the build platform; a layer approximate 30mm in thickness was used for all builds in this work.
4. Mark start plate with a cross at the centre.
5. Place start plate on top of the powder layer with a grounding plate and thermocouple sandwiched between the plate and powder. The plate should be as close to centred in the build platform as possible, minor deviations from the centre are corrected by the software.
6. Open hoppers.
7. Level the plate such that it is parallel to the rake with only a small gap.
8. Clear any powder from the top of the plate and lower to account for thermal expansion (typicaly 0.5 mm).
9. Insert heat shield.
10. Close chamber and start vacuum pumps
11. Once the pressures in the chamber and beam column are below $5x10^{-4}$ and $5x10^{-6}$ mbar respectively turn on the high voltage supply for the beam.
12. Align the beam centre in EBM control with the centre of the plate.

2.6 EBM PROCESSING STEPS

Following the set up procedure a build can be carried out. The EBM process can be summarised as follows:

1. The start plate is heated using a given beam current until a pre determined temperature is reached (1000°C for tungsten), as measured using a thermocouple located underneath the substrate.
2. The rake then deposits a small layer of powder.
3. The entire bed of powder is then preheated.
4. Finally the beam selectively melts a given area of the powder bed as dictated by the inputted CAD file.
5. Build platform drops.
6. Steps 2 to 5 are repeated until the build is complete.

The EBM process consists of four main steps, plate heating, powder deposition, preheat, and melt. These four steps will be discussed here in detail.

2.6.1 Plate Heating

Before any powder is deposited the start plate is heated to a set temperature which will be maintained throughout the build. The start plate is heated by the electron beam which rapidly scans the plate at a given speed and current. To evenly heat the plate a hatch pattern with line order is used. A line order strategy as illustrated in Figure 2.7, allows processing of hatch lines non sequentially. The plate is heated using this hatch strategy for a given number of repetitions after which heating continues with the pattern rotated by 90 degrees. When the start plate reaches a temperature of 350°C the current is reduced for fifteen minutes to slow the heating rate, allowing time for any gasses or moisture that have been released to be removed. The whole start plate heating process, including outgassing, takes approximately 45 minutes.

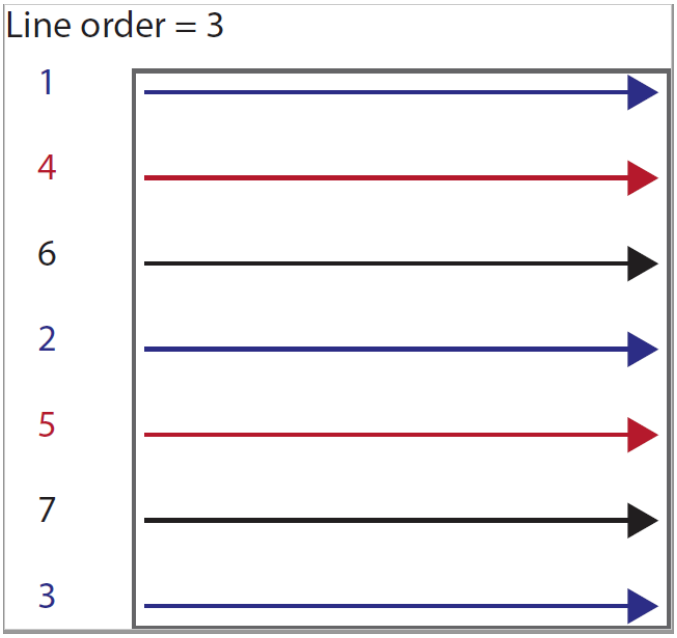

Figure 2.7: Line order example

2.6.2 Powder deposition

The powder deposition step involves the lowering of the build platform by the layer thickness and the depositing of a thin layer of powder. At the outflow of the hoppers a small pile of powder forms into which the rake passes forcing a small amount of powder to flow over the top of the rake. The powder in front of the rake is then passed across the build platform depositing a thin layer of powder. Powder sensors are used to determine the amount of powder moved by the rake. This information is used to adjust subsequent fetching of powder to ensure enough powder is deposited whilst keeping powder use as efficient as possible. To ensure that an even layer of powder is deposited onto the plate the rake typically makes 3 passes

2.6.3 Preheat

The preheating step is an important part of the EBM process. Preheating sinters all the powder on the build area. Sintering of powder is essential as it prevents 'smokes' during the melt step, where the high energy input would rapidly charge powder particles causing them to repel.

The Arcam S12 has a two stage preheat these are referred to as Preheat 1 and Preheat 2. Preheat 1 lightly sinters the powder using a low current. The light sinter provided by Preheat 1 allows the higher energy density to be applied during Preheat 2. Preheat 2 creates a final hard sinter strongly bonding together powder to allow for melting. The Preheat strategy is similar to plate heating using a hatch pattern with line order to give even heating of the layer. Arcam's Auto Calculation can be used during preheating. Auto Calculation aims to balance the total heat input of preheating and melting such that the temperature of the build says constant.

2.6.4 Melt

As in most SLM processes the melt step in EBM consists of contouring and hatching. Hatching is used as a fast method of processing the bulk of a part, whilst contouring melts the part's surface. Contouring uses low beam velocity and current, in order to create small and stable melt pools, which in turn provides the best surface finish. The low velocity required during contouring can result in long build times, however the Arcam EBM system's multibeam technology takes advantage of the rapid deflection of the electron beam in order to maintain several melt pools at once. Images of the process during hatching and contouring steps are shown in Figure 2.8

The contouring step uses a constant speed and current throughout the process the hatching step on the other hand varies these parameters based on the geometry of the part and its thermal history. The current and speed during the melt step are determined through the use of four functions (discussed in Appendix A), these functions help to reduce accumulation of heat in certain areas of the part and allow for maintaining a stable build temperature.

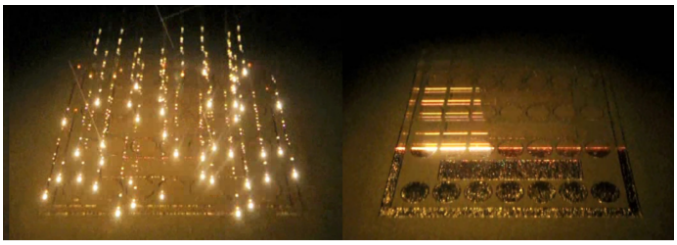

Figure 2.8: Shown Left: Photograph during the contouring melt step. Right: An image taken during the catching melt step.

2.7 HEALTH & SAFTEY

Personal Protective Equipment (PPE) is an important consideration when dealing with powdered materials as they can present risks that are not present in bulk form. There is a risk with all powdered materials of inhalation which can lead to a build up of material in the lungs, causing symptoms of asthma or breathing difficulties. To protect from inhalation a Sundstrom SR100 protective mask was worn whenever in close proximity to powder. Titanium powders present the additional risk of explosion under the right conditions. This risk is mitigated by the large particle size powder (45-105 μm) supplied by ARCAM. Tungsten has the potential to cause a reaction when in contact with skin and can cause damage to organs through repeated exposure, to prevent contact with skin, latex gloves and lab coats were worn whenever handling this powder. Lab coats and gloves were also used when handling Ti6AL4V powder, this material is biocompatible and thus presents a lower risk. The PPE used provides the additional benefit of protecting the powder from contaminants, such as skin particles and fibres from clothing.

An important consideration for EBM of tungsten is X-ray radiation. Due to its high atomic number tungsten has a high output of X-rays under electron beam radiation, as such it is often used as a target in X-ray generation [150]. In EBM this high X-ray output presents a safety risk, ARCAM EBM systems have X-ray shielding but this is qualified using materials which produce lower x-ray outputs such as titanium alloys. Additional precautions must be taken for tungsten to ensure a safe environment. During EBM of tungsten X-ray hotspots around the system were identified using a scintillator probe. A dosemeter was then used to measure and quantify the dose at each hotspot to ensure the dose remained below the legal limit of $6mSv$ per year [151] .

2.8 CHARACTERISATION

2.8.1 Sample Micropreparation

Samples were prepared for optical microscopy, electron microscopy, and nano indentation using the following technique. First, where necessary samples were sectioned using electric discharge machining (EDM). After sectioning samples were mounted in a conductive bakelite compound using a Bueler Simplimet 1000 at a pressure of 290bar at 100°C for 4 minutes. The sample surface was prepared via planar grinding on a Struers Tegramin-20

preperation system using silicon carbide paper of grit sizes ranging from p200 to p2500. Following grinding the surface of samples was polished using a 3µm diamond suspension for 20 minutes. A final polishing step was carried out using colloidal silica for 30 minutes.

2.8.2 Optical Microscopy

Optical images and measurements were taken using CLEMEX microscopy hardware and software. The CLEMEX system consists of a motorised stage which is controlled by the accompanying software. This combination of hardware and software allows for the use of features such as autofocus, image stitching, and high volume analysis.

Defect Measurement

Samples were imaged using a CLEMEX microscope and accompanying software. Images were taken of each sample in a grid pattern at a 100 times magnification with a 20% overlap between images. All samples were imaged in the same session under consistent lighting. The grids of images were stitched using the software packages ImageJ and Matlab.

An ImageJ script and accompanying Matlab code were written to analyse the stiched images in order to measure cracks and porosity. In summary, the function of the script was as follows:

1. Measure melted area of sample via thresholding
2. Measure size and shape of defects via thresholding
3. Distinguish between types of defect
4. Output percentage area of porosity and cracks

Defects were approximated to ellipses and measured as such. In order to distinguish between porosity and cracks it was assumed that a crack had an aspect ratio below 0.1, all other defects were measured as porosity. This image processing method is outlined visually in Figure 2.9. The ImageJ script and Matlab code used for image analysis can be found in full in Appendix D

2.8.3 Electron Microscopy and Backscatter Diffraction

Electron microscopy was carried out using an FEI Inspect F50 fitted with an Oxford Instruments EBSD detector. Observations were typically carried out using a 20kV acceleration voltage, 5mm spot size, and 14mm working distance.

Electron Backscatter Diffraction (EBSD) patterns were acquired and indexed using an Oxford Instruments EBSD Detector along with Channel 5 HKL acquisition software. Indexing, mapping and generation of pole figures was carried out using Channel 5 HKL post processing software.

2.8.4 Nano Indentation

Nanoindentation measurement techniques measure the relationship between indentation load, P, and depth, h, during loading and unloading of an indenter. This is in comparison to conventional indentation techniques which

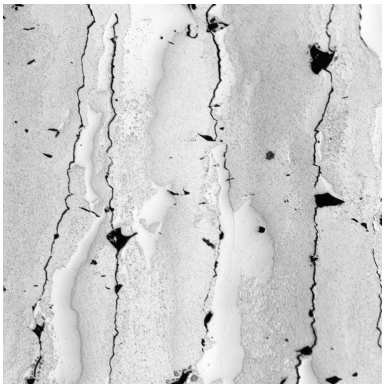

(a) Original sample image

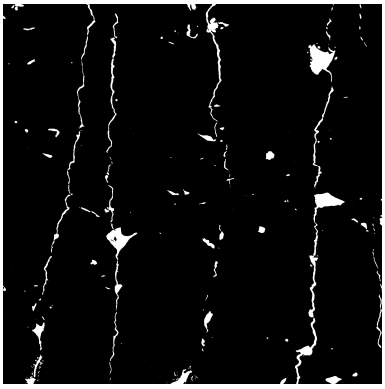

(b) Measure sample area

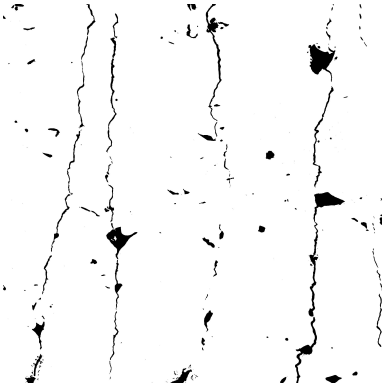

(c) Threshold defects

(d) Measure cracks

(e) Measure porosity

Figure 2.9: Optical image processing method

optically measure the size of the indent in order to measure hardness. As a result of this load displacement measurement Nanoindentation can evaluate other material properties such as Young's modulus and yield stress. From the p-h curve indentation hardness H can be calculated as follows [152]:

$$H = \frac{p_{max}}{A_C} \tag{15}$$

Where p_{max} is the maximum applied force. A_c is the contact area which is a geometrical function of depth h_c. For an ideal Berkovich tip $A_c = 24.5h_c^2$ [152].

Nano Indentation was carried out using a Hysitron TI-Premier platform. Test samples were cleaned thoroughly with isopropanol and compressed air before loading into the system along with fused quartz and polycarbonate calibration samples. Following loading of the samples the system was left for 20 minutes to stabilise and allow for the samples to thermalise.

Prior to testing, calibration was carried out on the X and Y positions of the stage and optics via indenting into the polycarbonate sample. Following the stage calibration the Berkovich tip area function (TAF) was calibrated through indentation of the fused quartz sample. Indentation was performed on the sample in a grid of three by three indents giving a total of nine data sets. The measured indenter response for the calibration indents was compared to the expected values through the systems inbuilt software at a range of loads. The indentation load function used for the TAF calculation is shown in Figure 2.10.

The Load functions used for the indentation of samples is shown in Figure 2.11, in order to obtain hardness and modulus values. The method outlined by Oliver and Pharr was used to calculate hardness and modulus values [152]. For each indent an air indent calibration was performed to correct for any drift in the transducer.

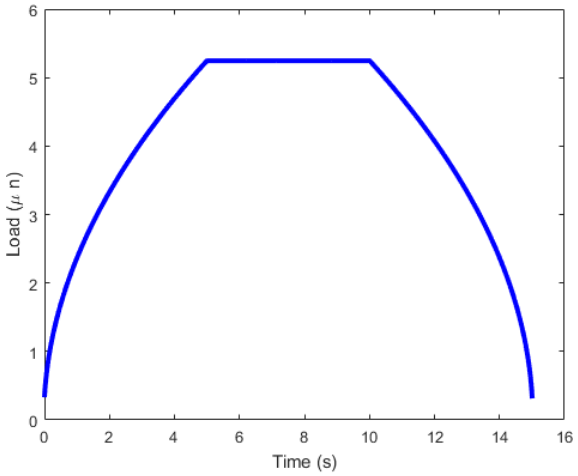

Figure 2.10: Tip area load function used for fused quartz calibration

Measurement of residual stress

As early as 1932 it was demonstrated that the stress state of a material has an influence on indentation hardness measurements [153]. Sines and Carlson [154] later showed that if an applied stress is tensile then the material

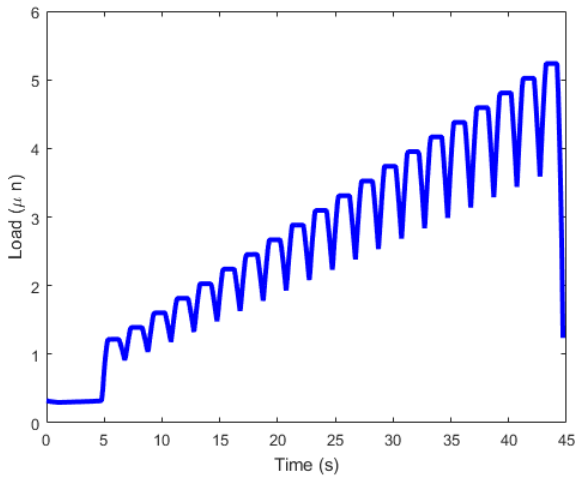

Figure 2.11: Load function used to determine hardness and modulus values

will appear softer and if a residual stress is compressive then the material will appear harder. A result from their work is shown in Figure 2.12. Several methods of measuring residual stress through indentation have been proposed since. The most common of these is the indentation cracking technique for brittle ceramics and glasses [155].

Following this Tsui et al showed that elastic modulus measurements via Nanoindentation were also stress dependent [156]. Figure 2.13 from this work shows the variation in contact area via the Oliver and Pharr method compared to opticaly measured contact areas demonstrating that nanoindentation contact area estimations are not independent of stress. Bolshakov et al confirmed that the Oliver Pharr method is dependent on applied stress [157]. In these studies Bolshakov et al and Tsui et al did not provide a full methodology for determining residual stress [157] [156]. A range of models have since emerged for the estimation of residual stress using nano indentation, a review by Jang et al is recommended for a full review of these techniques [153].

One of the main limitations of these residual stress estimation methods is that they require a stress free reference with identical microstructure which can be difficult to obtain. For this study these models for estimating residual stress and a stress free sample will not be used, the relative differences in hardness and modulus across samples will be presented. This can be used to demonstrate a variation in stress state as demonstrated by Bolshakov et al and Tsui but can not quantify the extent of this stress [157][156].

2.8.5 Ultrasonic Testing

Acoustic transverse and longitudinal wave velocities can be used to determine the Shear and Elastic modulus of solid materials using Equations 16 and 17 [158] [159]. Where c_t is the transverse wave velocity and c_l is the longitudinal velocity.

Shear Modulus

$$G = \rho c_t^2 \tag{16}$$

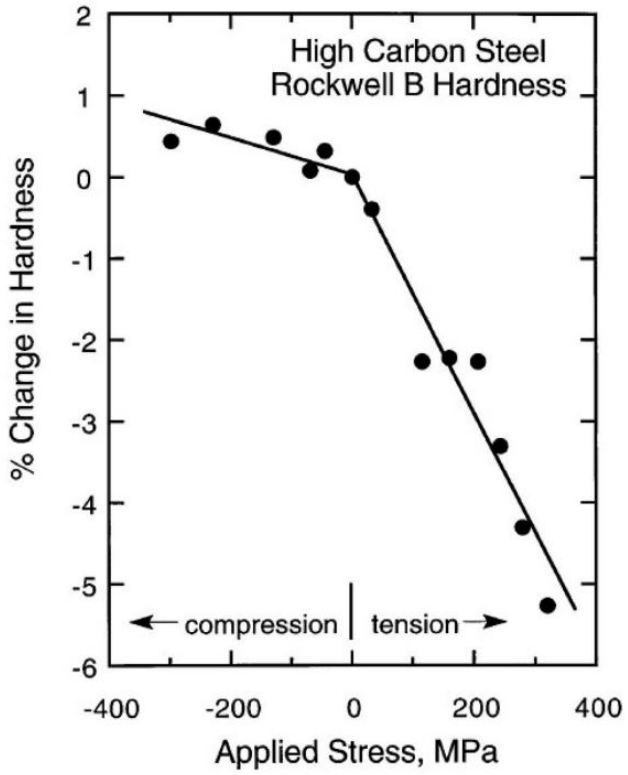

Figure 2.12: The Change in Rockwell B hardness produced by uniaxial stresses in a high carbon steel bar, [153][154]

Young's Modulus

$$E = 4\rho c_t^2 \left(\frac{\frac{3}{4} - (\frac{c_t}{c_l})^2}{1 - (\frac{c_t}{c_l})^2} \right) \tag{17}$$

Poisson's Ratio

$$\mu = \frac{\frac{1}{2} - (\frac{c_t}{c_l})^2}{1 - (\frac{c_t}{c_l})^2} \tag{18}$$

Ultrasonic testing was carried out using Olympus Epoch 600 with longitudinal and transverse wave transducers. A background measurement was taken with each of the transducers before placing transducers on the sample. The Epoch 600 along with the transducers was then used to pass a pulse through a sample and measure the time period for the pulse to return after reflecting of the opposite surface. The thickness of each tested sample was measured using a set of digital vernier callipers to an accuracy of +/-0.01mm and averaged over three measurements. The measured sample thickness and time period were then used to calculate the wave velocities using Equation 19. Samples tested were cuboids which measured 10mmx10mmx5mm with sides cut parallel via EDM. The transducer was placed on the face perpendicular to the 5mm edge.

$$v = \frac{d}{t} \tag{19}$$

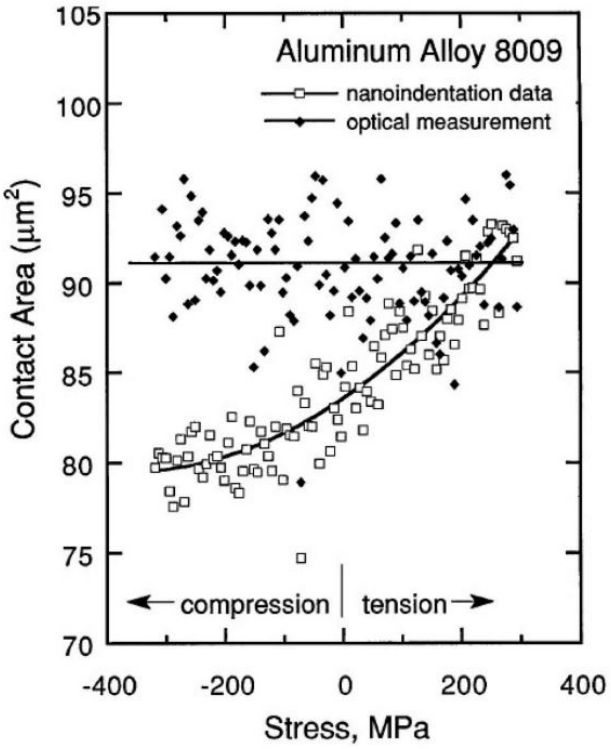

Figure 2.13: Load function used to determine hardness and modulus values

2.8.6 Thermal Characterisation

Tungsten's thermal properties are exploited in many applications and therefore an understanding of them is important. In magnetic confinement fusion PFCs are subjected to high thermal loads during operation and one of the key functions of the PFCs is heat transfer. The operating temperature of the tungsten first wall and divertor in DEMO is predicted to be between 500 and 900°C [160]. It is therefore important to understand the thermal properties within this range such that it can be qualified for use [143]. Laser flash analysis was used to measure thermal conductivity and thermal mechanical analysis was used to measure the thermal expansion coefficient.

Laser Flash Analysis

Thermal diffusivity was measured using an Anter Flashline 3000 in accordance with ASTM E1461-13 [161]. The Laser Flash method first described by Parker et al. [162] consists of a cylindrical test specimen which is subjected on one side to a high intensity laser pulse of short duration. The pulse is absorbed by the front surface of the sample and the corresponding temperature rise on the rear face is measured. The time between the laser pulse and the measured temperature rise along with the sample thickness can be used to calculate the thermal diffusivity. Measurements take place in a heated chamber and can therefore diffusivity can be measured over a range of temperatures; the Anter Flashine system is capable of carrying out measurements between ambient temperature and 1000°C. For measurements over a range of temperatures a heating rate of $5°C/minute$ was used.

Thermal diffusivity (α) along with specific heat (C_p) and density (ρ) can be used to calculate thermal conductivity (λ) according to Equation 20.

$$\lambda = \alpha C_p \rho \tag{20}$$

Specimens for Laser Flash Analysis (LFA) were 12.5 mm in diameter; the thickness of specimens was calculated such that half the maximum temperature on the rear face occurs between 10 and 1000 ms after the pulse. Equation 21 can be used to calculate the specimen thickness (L) for a given value of thermal diffusivity and the time for the temperature to reach half of the maximum ($t_{1/2}$). Given a thermal diffusivity for Tungsten of $6.895e^{-5} m^2/s$, minimum and maximum sample thickness's were calculated at 2.23 and 22.3mm respectively; thus a thickness of 5mm was selected.

$$\alpha = 0.13879 \frac{L^2}{t_{1/2}} \tag{21}$$

Specimens were prepared via EDM to ensure that surfaces were flat and parallel within 0.5% of the thickness, reducing the error in thermal diffusivity measurement to 1% [161]. A graphite spray coating was used on samples to improve the absorption of the laser pulse.

Thermal Mechanical Analysis

The Coefficient of Thermal expansion was measured using a PerkinElmer TMA 4000 thermomechanical analyzer (TMA) in accordance with ASTM E831-14 [163]. TMA measures the expansion of materials via a quartz probe when subjected to a constant heating rate. A heating rate of $5°C/minute$ was selected, the quartz probe applied a constant force of 100mN on the sample throughout the measurements. Samples were cylindrical with diameter and height of 5mm. The TMA was used to collect values for the sample height z and temperature T for temperatures ranging from atmospheric to 600°C which can then be used to calculate mean linear thermal expansion. The least squares regression method was used to produce a linear fit of the data collected; the rate of length change with temperature for the linear fit ($\frac{dL}{dT}$) can be used to calculate the linear coefficient of thermal expansion (α) via Equation 22.

$$\alpha = \frac{1}{z}\frac{dz}{dT} \tag{22}$$

2.9 3-POINT BEND TESTING

2.9.1 Test Procedure

Three point bend tests were carried out in to measure the mechanical strength of produced material, this test method was selected due to the small sample size required and suitability to brittle materials. Three point bend tests were carried out in accordance with BS EN 843-1[164]. This standard is for ceramics but was chosen as the most suitable due to the current lack of a standard for brittle metallics. Tests were conducted using an Instron 4505 Universal mechanical testing machine equipped with a 10kN load cell with

recent UKAS accredited force calibration. The tests were carried out at the National Physical Laboratory (NPL). A semi-articulating flexural strength test rig was fitted to the load cell. Rollers were freely rotating to minimise the effects of frictional forces. Figure L.1 outlines the degrees of freedom of the test rig. The distance between supporting rollers was $20mm$ and the loading roller was centred between the supports. The samples were loaded at a rate of $0.5mm/s$ until failure. All tests were performed at $20(+/-1)^{o}C$. Further information on three-point bend tests are included in Appendix L

3 SELECTIVE LASER MELTING OF TUNGSTEN

3.1 INTRODUCTION

A review of the literature in Chapter 1 identified only a small body of previous work carried out on SLM of tungsten. The work that has been completed previously measured high porosity in samples, but did not involve a full and systematic exploration of process parameters in order to identify optimal conditions.

This chapter will therefore aim to use optimal experimental design to identify the effect of the process variables on the occurrence of defects. By understanding the factors which cause defects we hope to be able to reduce them. The chapter is split into two sections covering each of the two SLM systems investigated, the SLM125 and the AM400. As discussed in the previous chapter these systems are in many ways identical with the key differences being build area and laser power.

A response surface methodology was adopted in order to model the response. A significance level of $p - value = 0.05$ was selected for both sets of experiments to allow for any variation due to uncontrollable factors between and within builds.

3.2 THE EFFECT OF RENISHAW SLM125 PROCESS PARAMETERS ON DEFECTS

3.2.1 Experimental design

An experiment was conducted into the effect of build parameters on the occurrence of defects within samples produced on the SLM125 system. A response surface experimental design was selected investigating four system parameters over three levels. Hatch spacing (h), layer thickness (l), point distance (Pd) and exposure time (t_e) were varied over the levels listed in Table 3.1. The effect of remelting each layer with the same parameters was also investigated. A summary of the parameters investigated and their corresponding levels are summarised in Figure 3.1. A total of six repeats were carried out at the centre point. Sample geometry was selected as 5mm cubes with square pin supports with dimensions 1x1x2mm (Figure 3.1). The centre point for the experimental design was based on the values reported by Zhou et al [55].

3.2.2 Build Layout

The build layout is shown in Figure 3.2. Samples were arranged in an offset grid pattern to ensure they were not up or downstream of one another with respect to the wiper and recirculation system. A total of four builds were conducted, two at a 30µm layer thickness and one at both 20µm and 40µm layer thickness. Samples positions were randomised within each

build. These trials were carried out with power set to the maximum value on the SLM125 system at 200*W*.

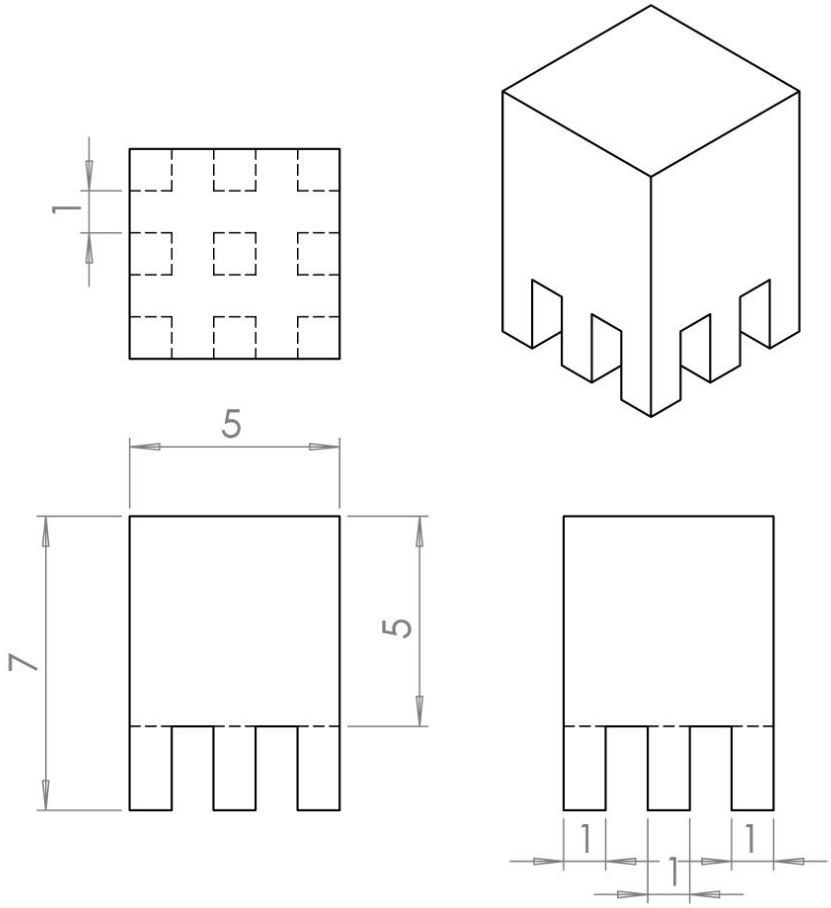

Figure 3.1: Sample geometry built on the SLM125 system. Dimensions given in mm

Following the builds, samples were sectioned centrally parallel to the XZ plane and prepared as described in Section 2.8. Samples were imaged using the Clemex system and porosity measured using ImageJ also discussed in Section 2.8.

3.2.3 Results

Two responses were measured for each sample; percentage porosity and mean size of pores. A full summary of the porosity measurements for each sample is provided in Appendix D. No other defects were observed. Builds with a 40µm layer thickness failed and these results are therefore not included, samples were observed to detach from the substrate and due to this the builds were stopped.

All imaged samples showed a large percentage volume porosity measuring in the range 6.5 to 20.8%. The mean porosity was 11.7% with a standard deviation of 3.2%. The mean area of pores was 2631μm^2 with a standard deviation of 779µm. This equates to an average pore diameter of 58µm.

An ANOVA was carried out on the porosity results to determine if the process parameters and their interactions had a significant effect on the re-

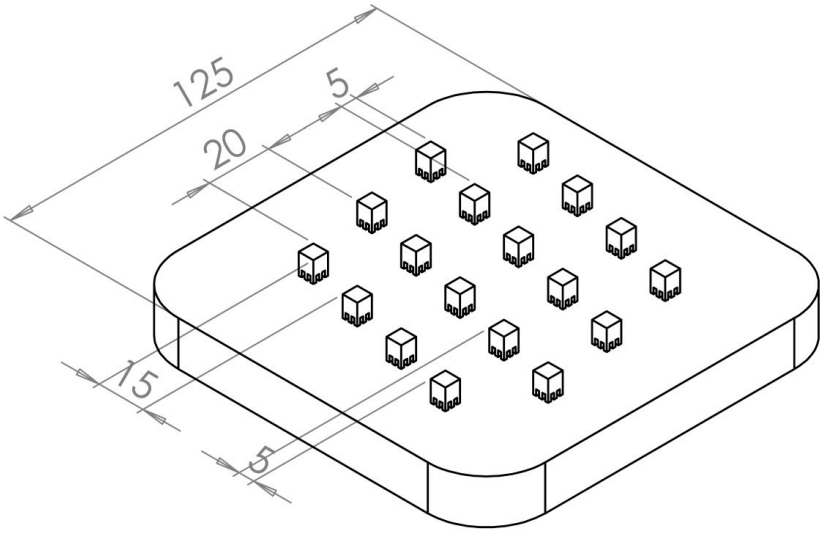

Figure 3.2: Build Layout for samples built on the SLM125 system. Dimensions given in mm

Table 3.1: Parameters investigated on the SLM125 system and their corresponding experimental levels

Parameter	Low	Middle	High
Exposure time (μs)	200	400	600
Hatch offset (μm)	30	50	70
Point distance (μm)	30	50	70
Layer thickness (μm)	20	30	40
Remelting	0		1

sponses. This analysis was carried out using the software package Minitab. ANOVA results are summarised in Appendix D Table D.2. The p-value indicates the significance level of the relationship between each parameter and the response. The coefficient indicates the magnitude and direction of this relationship.

The percentage porosity was found to be significantly effected by the linear terms; point distance ($p-value = 0.021$) and remelting ($p-value = 0.022$). As point distance was increased by 20μm the mean porosity was raised by 2.4%. Remelting on each layer was found to decrease the porosity by an average of 0.93%. Square and interaction terms did not present a significant effect on the porosity percentage ($p-value > 0.05$).

The mean area of pores was found to be significantly effected by the linear term exposure time ($p-value = 0.039$), as exposure time was increased by 200μm the mean was raised by $655\mu m^2$. The square term of exposure time also had a significant effect on the size of pores ($p-value = 0.021$). The size of pores was increased by a mean value of $678\mu m^2$ for each level increase in this term. The interaction terms between exposure time and layer thickness, and layer thickness and remelting also had a significant effect on this response ($p-values : 0.006, 0.003$. Coef:1017, −617).

Second order models were generated to fit the two responses, using a least squares approximation. A summary of the model is provided in Table 3.2. s is the standard deviation of the model. $R^2(adj)$ and $R^2(pred)$ are the

Table 3.2: Response surface regression model summary for the porosity responses. Samples produced on the SLM125 system at a power of 200W. Parameters given in Table 3.1

Response	**s**	R^2	$R^2(adj)$	$R^2(pred)$
Porosity (%)	1.96	78.26%	62.61%	33.12%
Mean pore area (μm)	601	65.48%	40.63%	0.00%

adjusted and predicted R^2 values respectively. An ANOVA was performed comparing models and experimental results; a summary of this analysis is included in Table D.2. ANOVA indicated that the models fit the data well (p-values $<$ 0.001 and 0.013). Regression analysis for the models on the other hand indicated low $R^2(pred)$ values (33.12% and 0.00%), this suggests that the models are an over fit. $R^2(pred)$ is calculated by systematically removing data points and evaluating how well the model can predict them, a low $R^2(pred)$ and high $p-value$ therefore indicates that the model is tailored to fit the data but does not represent the overall response well.

The relationship between the volumetric energy density and porosity is plotted in Figure 3.3. A significant correlation (p-value = 0.00071) was found. As the energy input increases the porosity tends to decrease. There is however a large amount of scatter in this data (Pearson correlation = -0.480). No significant relationship was found between the size of pores and the volumetric energy density (Pearson correlation = 0.114, P-Value = 0.462).

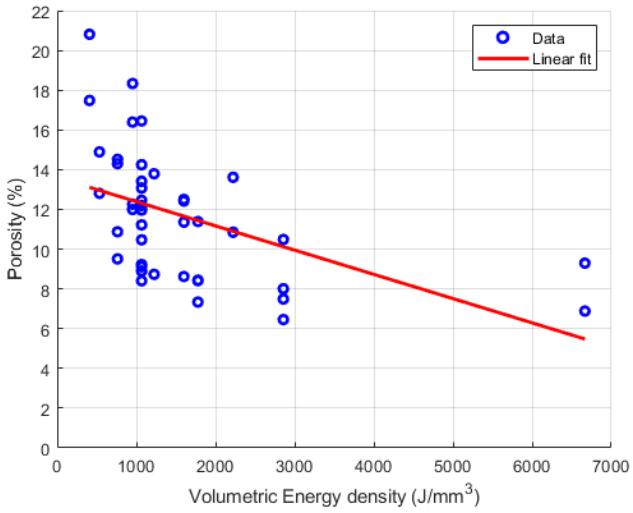

Figure 3.3: The effect of volumetric energy density on porosity with linear fit (p-value = 0.0007 Pearson correlation = -0.480). SLM125 system at a power of 200W. Parameters given in Table 3.1

3.2.4 Discussion

Porosity greater than 6.5% was found in all samples. This high porosity is in agreement with the findings of previous work carried out on laser processing of tungsten powder [20] [55] [102]. Where porosity in the range 10 to 17% was reported. In order for ALM to be considered a viable manufacturing route for tungsten these defects must be eliminated.

Increasing energy density through reduced point distance and multiple repetitions of remelting helped to reduce the volume percentage of porosity. A decrease in point distance by 20µm corresponds to a 2.4% decrease in porosity. At a minimum tested point distance of 30µm, it can only be reduced by a further 20µm, which assuming the response remains linear, would not be sufficient to eliminate the minimum measured 6.5% porosity. Remelting equated to approximately a 1% reduction in porosity, such that seven remelts on each layer would be necessary to remove porosity, assuming again a linear response. These changes are not practical and would result in extremely long build times, other alternatives should therefore be investigated.

Increased energy density significantly reduces the percentage porosity. This suggests that porosity is occurring due to incomplete melting of the powder. Images taken of pores under SEM suggest that this hypothesis is true. Figure 3.4 shows an image of a SLM sample taken by a SEM, powder particles are visible inside the pores.

The response surface generated did not accurately represent the data, it is therefore not possible to use this model to predict optimum parameters minimising the rate of defects ($R^2(pred) = 0,33\%$). The variables that were found to be significant such as remelting and point distance indicate that increased energy density may help to reduce the volume of porosity. Microscopy images which show samples containing powder particles also point towards the conclusion that energy input is too low. The effect of power should therefore be investigated, this will be covered in the next section of this chapter.

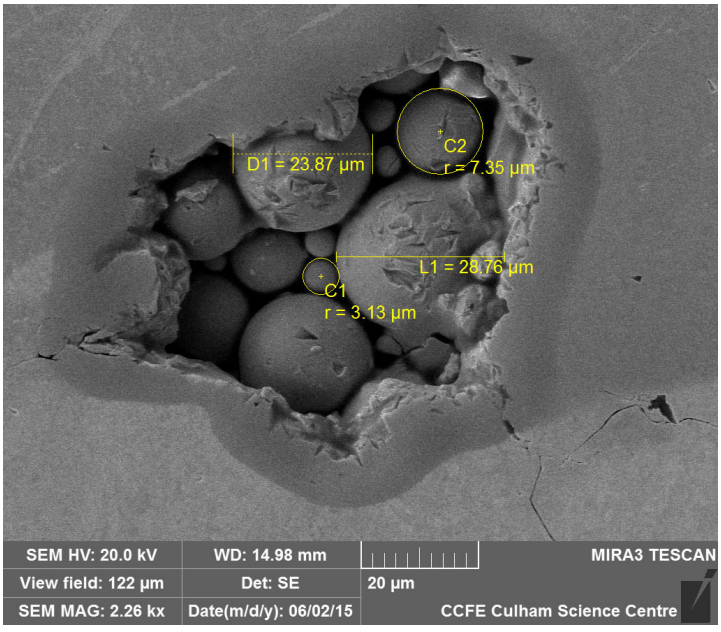

Figure 3.4: SEM image showing a lack of fusion defect with unmelted powder. Melt parameters: $Q = 200W$, $h = 30\mu m$, $Pd = 30\mu m$, $l = 30\mu m$, $t_e = 600\mu s$

Table 3.3: Parameters investigated on the AM400 system and their corresponding experimental levels

Parameter	Low	Middle	High
Exposure time (μs)	200	400	600
Hatch offset (μm)	30	50	70
Point distance (μm)	30	50	70
Power (W)	200	300	400

Table 3.4: Parameter levels used for Design of experiments

3.3 THE EFFECT OF RENISHAW AM400 PROCESS PARAMETERS ON DEFECTS

3.3.1 Experimental Design

Results from the previous section (samples produced on the SLM125 system), suggested that the energy density was too low to fully melt the powder. As a result a set of experiments was carried out on the AM400 system in order to asses the effect of laser power and its interactions with the other process variables.

A similar experimental design methodology was adopted on the 400*W* AM400 system to that of the 200*W* SLM125. A response surface design was carried out investigating four system parameters over three levels. Variables were hatch spacing (h), point distance (Pd), exposure time (t_e) and power (Q); layer thickness was maintained constant at 30μm. Table 3.4 shows the levels used for each parameter. Five Repeats were conducted at the centre point giving a total of thirty samples. The sample order was randomised and samples were divided in to three builds of ten.

3.3.2 Build Layout

Builds were carried out using the reduced build volume (RBV). As discussed previously the RBV fits within the standard 250mm build platform and contains a small powder hopper, dosing mechanism, and overflow container. The RBV allows for processing of small volumes of powder and is particularly useful for parameter development for new materials. It uses a square substrate with sides of length 78mm and a radius at each corner of 15mm.

The samples built were cuboids with dimensions 5x5x7mm, the longer dimension was aligned parallel with the build direction. Samples were built directly onto a steel substrate and were arranged as shown in Figure 3.5. Samples were arranged on the plate such that they were close to the dosing mechanism to ensure that on each layer adequate powder was deposited onto the samples. Samples were also positioned such that in the event of a sample failing or detaching from the substrate it would be unlikely to affect any of the other samples.

Following completion of the builds samples were removed from the substrates and sectioned using EDM. Sample cross sections were mounted, ground, polished, and imaged using the methods previously discussed. Analysis of images of the sample cross sections was carried out using ImageJ and Matlab as outlined in Section 2.8.

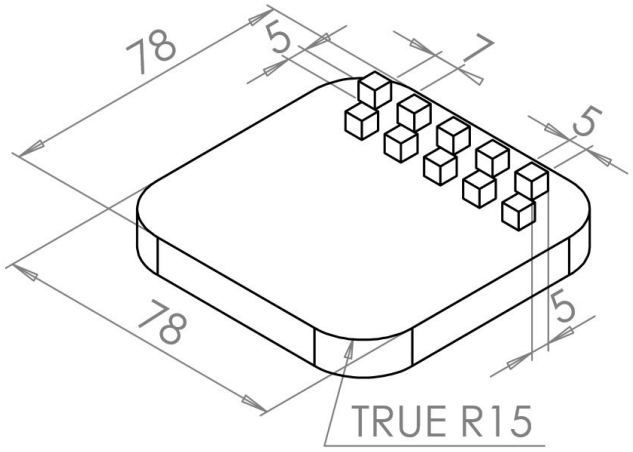

Figure 3.5: Experimental build Layout for builds carried out on th AM400 system - Dimensions given in mm

3.3.3 Results

The defect measurement values and corresponding system parameters are listed in Appendix E. Three measured responses are tabulated; porosity area (%), crack area (%), and defect total (%); where the defect total is the sum of porosity and crack area. All samples completed successfully with the exception of Sample 26 which failed due to what appeared to be large numbers cracks.

All of the samples had some porosity and the majority of samples also showed cracking. Sample 14 shown in Figure 3.6 had the least porosity at 0.52% but also displayed significant cracks. The mean porosity area percentage for all samples was 6.6%, with a standard deviation of 7.8%. The mean crack area percentage was 0.19%, with a standard deviation of 0.21%

It was noted that several samples in the first and third builds displayed large porous areas parallel to the build direction in the same location. This porosity is likely due to insufficient powder dosing at certain points during the build. These areas of porosity remain in the data set however in future builds complete dosing of powder should be ensured.

Porosity

A summary of the ANOVA results for porosity area percentage is included in Appendix E Table E.2. Power showed a significant effect on porosity ($p - Value < 0.001$). An increase in power of $100W$ corresponded on average to a 7.67% decrease in porosity. The square term of power also had a significant effect on porosity ($p - value = 0.009$). The porosity was increased by a mean value of 6.8% for each level increase in this term. All other variables and interactions did not show a significant effect within the range tested($p - Value > 0.05$). No significant effect was found in porosity between builds ($p - value = 0.336$).

The main effects of power on porosity are plotted in Figure 3.7. Power is shown to have a strong inverse relationship on porosity between 200 and 300 Watts, with the mean decreasing from approximately 17% to 2% in this range. A comparison of the sample cross sections at the three power levels is included in Figure 3.8.

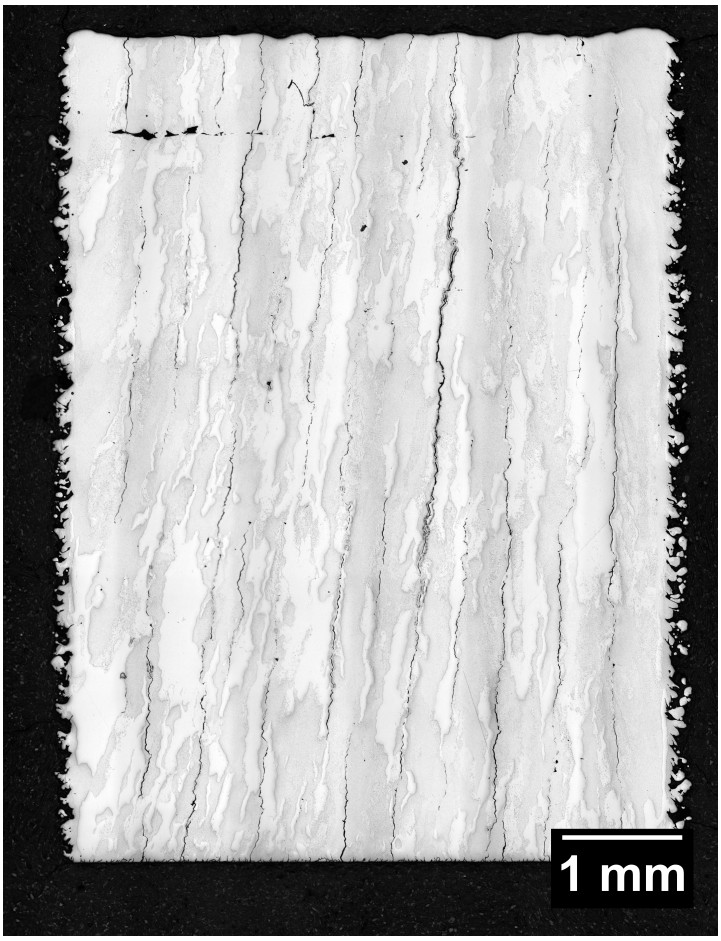

Figure 3.6: A cross section image of Sample 16 which showed the lowest porosity produced via the SLM process. Produced on the Renishaw AM400 with melt Parameters as follows: $Q = 400W$, $h = 70/mum$, $Pd = 70\mu m$, $t_e = 600$, $l = 30$

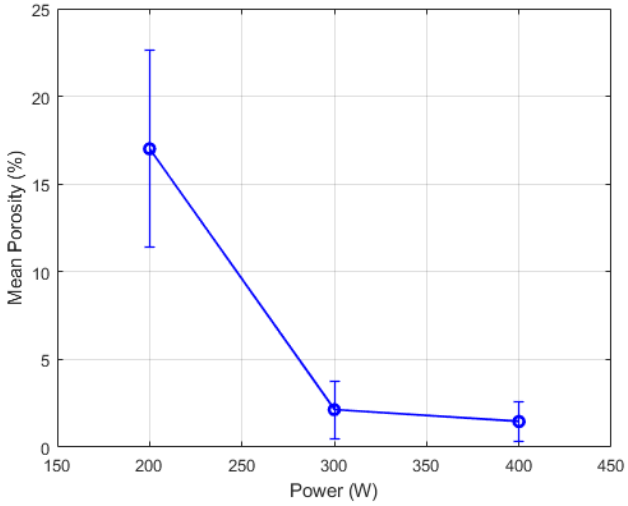

Figure 3.7: Main effects plot for Porosity (%) for beam power 200 to 400W

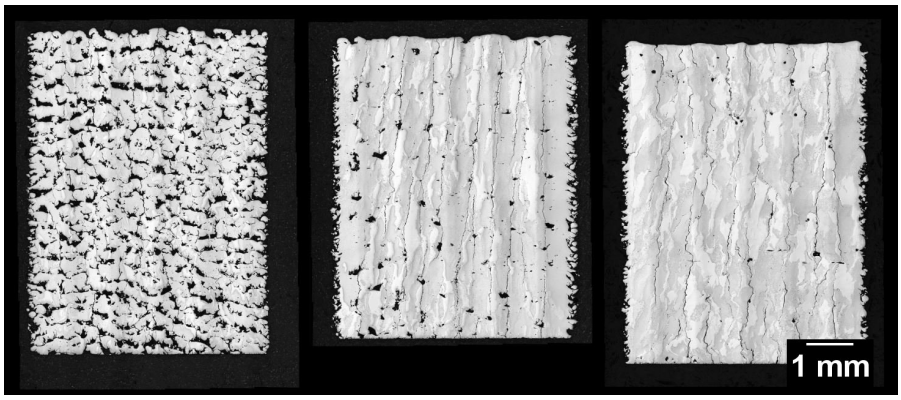

Figure 3.8: A comparison of sample cross sections at varying power from the response surface centre point (h = 50µm, l = 30µm, Pd = 50µm, t=400µs). Left: Q = 200*W* Centre: Q = 300*W* Right: Q = 400*W*

The relationship between volumetric energy density and porosity is shown in figure 3.9. No significant correlation was found between the input energy density and the resulting volume of porosity (p-value = 0.292).

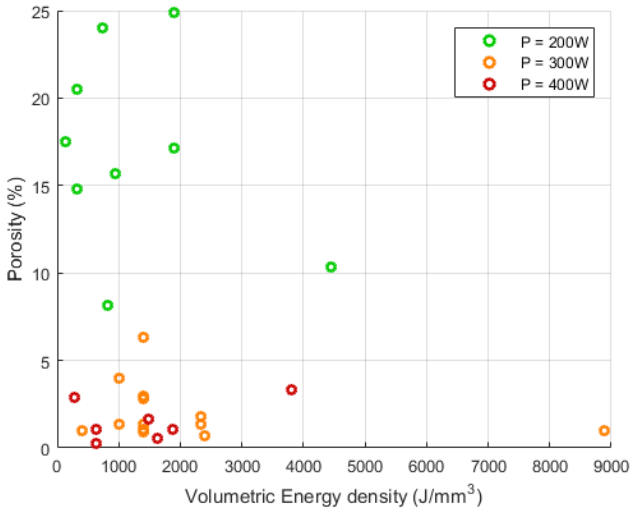

Figure 3.9: A plot of energy density against porosity for samples prepared on the Renishaw AM400 at power between 200W and 400W (Pearson =-0.202, p-value = 0.292)

Crack area

Cracks were found to propagate parallel to build direction along grain boundaries. A summary of the ANOVA results for crack area percentage are listed in Table E.2. Power showed a significant effect on cracks ($p - Value = 0.013$). An increase in power of 100*W* corresponded on average to a 0.14% increase in the crack area percentage. All other variables and interactions did not show a significant effect within the range tested ($p - Value => 0.05$). No significant effect was found on cracks between the three builds ($p - Value = 0.690$).

The main effects of power on cracks are plotted in Figure 3.10. Power is shown to have a direct relationship with crack area.

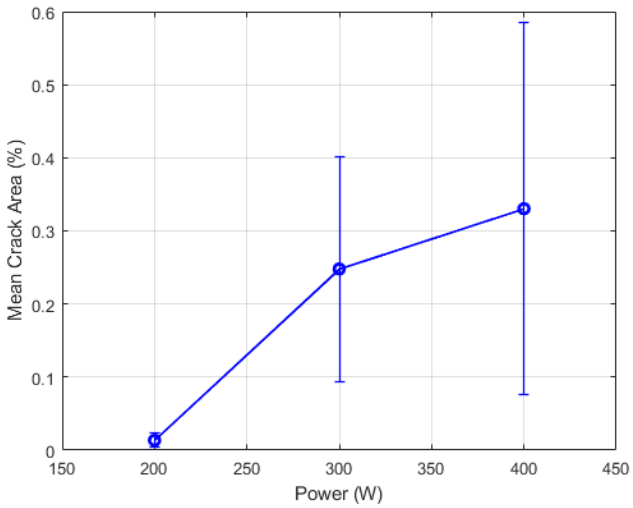

Figure 3.10: Main effects plot for Crack area (%) for beam power 200 to 400W

The relationship between volumetric energy density and the area of cracks is shown in figure 3.11. No significant correlation was found between the input energy density and the resulting volume of cracks (p-value = 0.078).

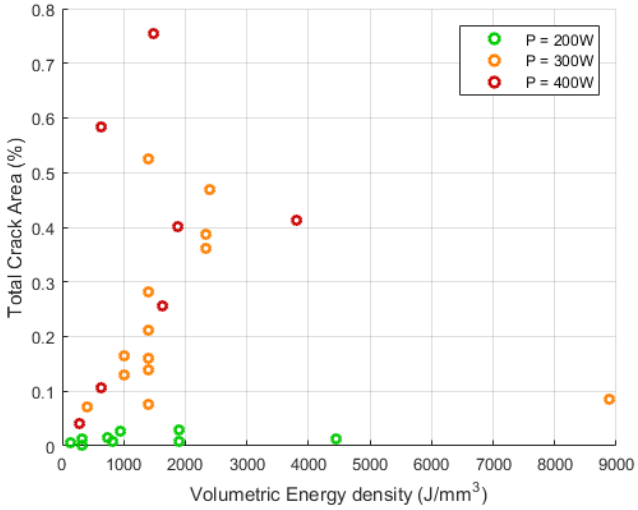

Figure 3.11: A plot of energy density against crack area percentage for samples prepared on the Renishaw AM400 at power between 200W and 400W. (Pearson correlation = 0.688, p-value = 0.078)

3.3.4 Relationship between Cracks and Porosity

A significant inverse relationship was found between the two responses crack area and porosity area potted in Figure 3.12 (p-value = 0.002; Pearson correlation -0.546).

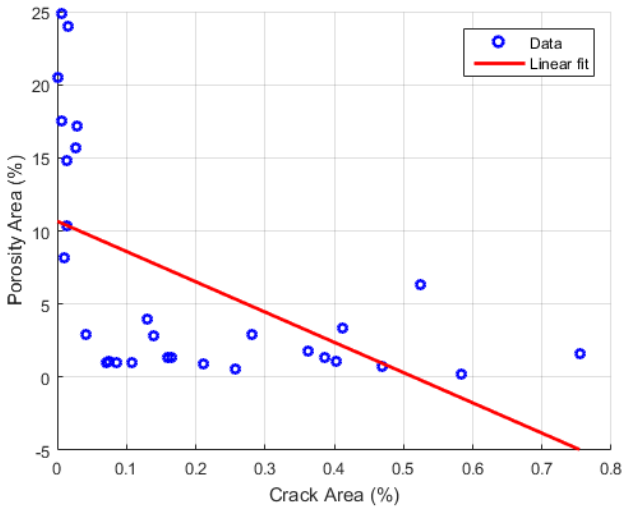

Figure 3.12: Scatter plot of the two responses, crack area percentage against porosity area percentage (p-value = 0.002; Pearson correlation -0.546)

Table 3.5: Regression model summary for the responses porosity area (%) and crack area(%)

Response	**S**	R^2	$R^2(adj)$	$R^2(pred)$
Porosity (%)	3.541	91.24%	79.56%	0.00%
Crack area (%)	0.174	69.65%	29.18%	0.00%

3.3.5 Regression model

Second order models were generated to fit the two responses, using a least squares approximation. A summary of the model is provided in Table 3.5. s is the standard deviation of the model. $R^2(adj)$ and $R^2(pred)$ are the adjusted and predicted R^2 values respectively. An ANOVA was performed comparing models and experimental results; a summary of this analysis is included in Table D.2. ANOVA indicated that the model fit the data well for the porosity response ($p-value < 0.001$). The model fit for the crack response was not significant ($p-value < 0.173$). Regression analysis for the models indicated low $R^2(pred)$ values (0.00% and 0.00%), this suggests that the models are an over fit and cannot accurately replicate the responses.

3.3.6 Discussion

Laser power has a large effect on the occurrence of defects within tungsten samples produced via SLM. Two types of defect were observed in this series of experiments, lack of fusion and cracks. The response surface generated for each type of defect did not accurately represent the data, it is therefore not possible to use this model to predict optimum parameters in order to minimise the rate of defects ($R^2(pred) = 0$). Some strong correlations were found within the data however, which can serve as indicators of considerations which should be made when processing tungsten. For example, increasing power from 200 to 400 Watts significantly reducing lack of fusion defects. The minimum achieved porosity at power of 200W was 8% and at

400W this was reduced to 0.5%. However as power is increased cracks also begin to appear as defects within the samples.

This correlation between beam power and porosity is in agreement with the data analysed from the literature in Chapter 1. Figure 3.13 plots the maximum beam power against the maximum achieved density for all the current literature on SLM tungsten along with that of the current study. A strong correlation is found between Power and density across the literature (p-value = 0.002).

In Chapter 1 a strong inverse correlation was found between energy density input and the resulting sample density across the literature. This was attributed to the fact that at lower laser powers authors tended to use higher energy density and a strong correlation was found between these two inputs.

This hypothesis is confirmed by the results presented in this chapter. It was shown at a laser power of 200W on the SLM125 system increasing energy density can significantly reduce porosity (Figure 3.3). The minimum porosity achieved on the SLM125 system ($Q = 200W$) was achieved at a volumetric energy of 2857J/mm^3. On the 400W AM400 system on the other hand, the maximum density was achieved at only 635J/mm^3 and no significant correlation was found between porosity and energy density. Thus power appears to be the most important factor to consider in producing dense tungsten and low powered systems (<300W) can only, to a limited extent, compensate for the lack of power by increasing energy density.

Suder and Williams demonstrated that penetration depth in laser welding is controlled by two factors, specific point energy and power density [32]. The point energy can be increased by either by increasing the interaction time (slower traverse speeds) or increasing power [32]. Power density can be increased through the implementation of higher beam powers or reduced beam diameter. Increased point energy via variation of speed did not have an effect in this set of experiments. Increasing point energy through increased beam power on the other hand did have an effect on porosity. Similarly increased power density through the use of a 400W laser resulted in lower porosity.

This suggests that in SLM systems with relatively low power the rate at which energy is being applied reaches equilibrium with the rate of heat loss. The energy within the processed material remains bellow that required for sufficient penetration depth of the laser. This manifested in lack of fusion defects as shown in Figure 3.4.

To redress the balance between the rate of heat input and heat loss we must consider conduction as defined by Fourier's law (Equation 23) as the main source of heat loss in the SLM process [165]. In order to increase the peak temperature of the melt pool either the heat flux (q'') must be increased or the temperature gradient (ΔT) decreased. Increasing the heat flux can be achieved by the use of higher beam power as was investigated here or alternatively the beam diameter at the material surface can be reduced. In order to decrease the temperature gradient the ambient temperature must be increased by some method of external heating such as a heated build platform.

Mukherjee et al showed that high marangoni numbers produce larger melt pools and result in a reduction in lack of fusion defects [31]. On the other hand increased power leads to higher fourier numbers as heat is accumulated quickly [31]. Future work could model the effect of build parameters, particularly power, on the melt pool size. Models could be used to

calculate marangoni and fourier numbers. This may give an indication of the melt pool dynamics which lead to lack of fusion defects and cracks [31].

$$q'' = -\lambda \Delta T \tag{23}$$

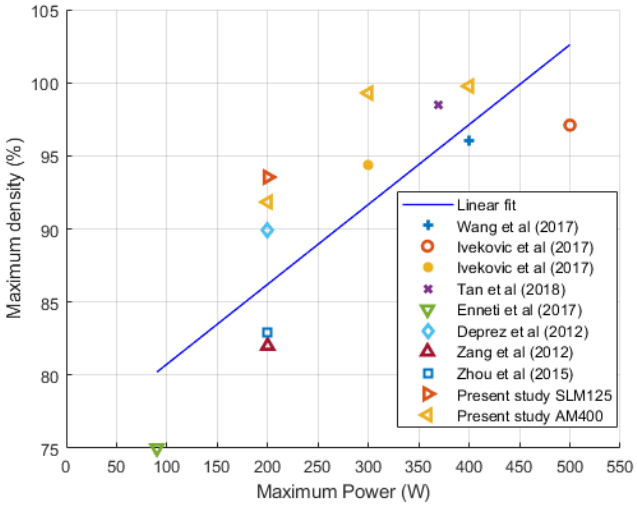

Figure 3.13: p-value = 0.00217

Residual stress has been shown previously to be imparted on components during SLM processing [166]. As the top layer of a sample cools following melting it begins to shrink due to thermal contraction. This shrinking is resisted by the cooler layers below and thus stress is induced. Tungsten is particularly susceptible to cracking under this residual stress due to its high DBTT. Cracking has been observed in processing of other refectories such as molybdenum [167], tantalum [168]. Recently Sidambe et al also observed cracks along tungsten grain boundaries produced via SLM [169].

Tungsten's lack of ductility can be attributed to the poor cohesion of grain boundaries which results in inter-granular fracture being the prominent failure mode [72]. Relatively small increases in impurities can have a significant effect DBTT. In this case total impurity levels in the feedstock material were below 100ppm but the exact levels of impurities were not known and the levels of any impurities after processing are also unknown [77] .

In the case of the Renishaw SLM process there are a number of potential sources of impurities. Oxygen in this process is maintained below 100ppm. Oxidation of tungsten at elevated temperatures is strongly dependent on oxygen partial pressures, but is still susceptible at these pressures, as well as atmospheric temperature and pressure [61]. Another potential source of impurity is the replaceable silicon wiper blades used which tend to erode during use. Other sources of impurities could include, cleaning procedures and equipment or powder recycling apparatus. As powder is recycled and reused these impurities may accumulate in the feedstock material. Impurities in tungsten tend to have decreasing solubility with temperature and will segregate to grain boundaries during cooling which in turn create embrittlement.

Future studies could investigate the effect of powder impurities on cracking. Experimentation with different grades of feedstock powder could be

undertaken and measurements taken of the accumulation of impurities during recycling of powder. The effect of atmosphere should also be considered, SLM systems which operate under vacuum may eliminate the potential for accumulation of oxide impurities.

Cracking occurs in SLM due to the accumulation of stress during processing. Stresses can be reduced through the use of elevated build temperatures. Reducing the temperature difference between the melt pool and the surrounding material leads to reduced cooling rates which in turn lessen the build up of stresses. As discussed previously, current SLM systems for example those made by Aconity3D offer build temperatures as high as 1200°C and the effect of these elevated temperatures on crack formation should be investigated.

Another potential solution to prevent cracking of tungsten during processing is alloying. Additions of rhenium would produce a more ductile material which in turn would be less likely to crack during processing [87]. This could allow for post process heat treatment to relieve residual stress. Tungsten-rhenium alloys may also be more suited for many applications where ductility is desirable. For the application of plasma facing components rhenium additions are not desirable. Alternative options for solid solution alloys are limited for this application due to the need for low activation, irradiation performance and reasonable costs [170, 72].

Similar results to these have been observed in SLM of other refractory elements. Faidel et al conducted a similar experimental design on molybdenum and concluded similarly that power was a key factor for producing dense molybdenum [171]. The 200W laser used by Faidel et al was insufficient to fully fuse powder even with very high energy density of upto $1066 J/mm^3$. Similarly Bajaj et al demonstrated that power was a key factor in molybdenum processing, achieving significantly higher density when laser power was increased from 200*W* to 400*W* [172].

A similar result was found by Zhou et al using tantalum powder, increasing energy through reduced scan speeds had no effect on sample density. However increasing energy density through the use of higher laser powers (300*W* and $434 J/mm^3$) resulted in significantly reduced porosity. At these increased powers the authors found that cracks would appear in samples due to the residual stressed imparted during processing.

Further work needs to be carried out on the development of SLM tungsten if it is to be implemented in demanding applications such as MCF. A more detailed understanding is required on the effect of process parameters and impurity levels on the formation of cracks in order to qualify this process for such applications.

3.4 CHAPTER CONCLUSIONS

Power has been determined to be an important factor in the SLM of tungsten. A 200*W* laser was found to be insufficient to fully melt powder. As power was increased to 400*W* porosity was reduced. However, stress was imparted during the process. Due to tungsten's high DBTT this stress manifested as cracks in samples.

Modifications need to be made to the process in order to prevent the build-up of stress in parts during processing. One option that has been explored by other authors is heated substrates [173].

Another alternative to the heated bed is to investigate EBM as a processing route. The elevated temperatures of EBM can bring temperature above the DBTT and allow stresses to be relieved in the process [39]. This will be investigated in the following four chapters.

4 ELECTRON BEAM MELTING OF TUNGSTEN

4.1 INTRODUCTION

Aa series of experiments were carried out in order to asses the feasibility of processing tungsten powder using the EBM process. Prior to carrying out these experiments the machine and ancillaries were fully cleaned using the method outlined in Section 2.5.4.

The development of tungsten EBM processing discussed in this chapter consists of two main sections. Firstly, an initial trial and error style of development was adopted in order to correct any issues with the machine set-up and to establish suitable process parameters for the plate heating, preheat, and melt steps. The second phase consisted of using a DOE approach to establish optimum melt parameter settings. Development was carried out on the Arcam S12 using an in house small build tank. Details of the modifications made to the S12 system to create a small build tank are given in Appendix J.

4.2 INITIAL TRIALS

4.2.1 Experimental setup

The build layout used for the following experimental builds is shown in Figure 4.1. The build geometry consisted of nine 10mm cubes arranged in a 3 by 3 grid with a spacing of 10mm between each cube. 30Kg of tungsten powder was loaded into the hopper for each build and recycled following each build, as per the method outlined in Section 2.5.4. A layer thickness of 35µm was used for all builds. Initially all melt functions were disabled.

4.2.2 Plate heating

A series of trials were run with the aim to establish suitable parameters for the plate heating stage of the process. For these tests the current was varied in order to reach a steady heating rate and the maximum temperature was varied to establish the temperature at which the powder would sinter together. Prior to the trials, a maximum plate temperature of 1000°C was selected. 1000°C was selected as it was the highest safe operation temperature whilst allowing a safe margin of error to the approximately 1100°C operating limit of the system. By operating at this limit the temperature gradient between the molten powder and the environment is minimised in turn minimising any residual stress. The findings of these plate heating trials can be summarised as follows:

- The powder around the plate loosely sinters at between 900°C and 1000°C.

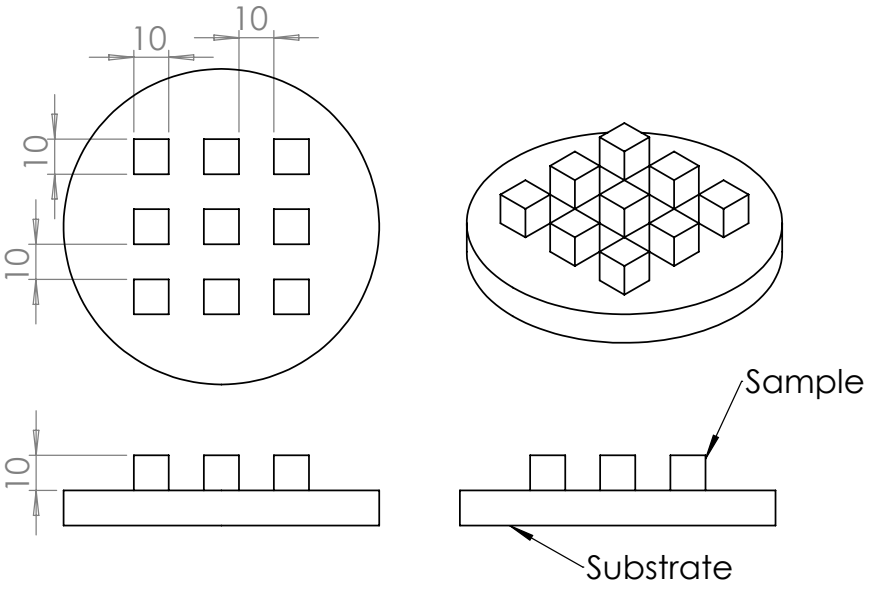

Figure 4.1: The build layout used for the initial development of the EBM process for tungsten powder.

Table 4.1: Plate heating parameters selected for use with tungsten, the SBT, and a 90mm diameter substrate

Parameter	Value
Current (mA)	8.3
Repetitions	12
Speed (mm/s)	3995
Line order	15
Line offset (mm)	1.2

- A current of 9mA would raise the temperature of the plate to around 800°C. This current needs to be incrementally increased to 20mA in order to reach 1000°C.

Following these plate heating trials a plate temperature of 1000°C was selected with beam heating settings as outlined in Table 4.1. The current was manually increased by the operator between 800°C and 1000°C to maintain a steady heating rate. These parameters were kept consistent throughout all the following experimental builds.

4.2.3 Preheat

The energy input during preheat was increased through varying the number of repetitions. The number of repetitions was incrementally increased until the temperature remained stable throughout the build. A summary of the final preheat settings is outlined in Table 4.2.

Table 4.2: Preheat selected for use with tungsten, the SBT, and a 90mm substrate

Parameter	Preheat 1	Preheat 2
Current (mA)	8.3	38
Repetitions	12	30
Speed (mm/s)	3995	14600
Line order	15	15
Line offset (mm)	1.2	1.2

Table 4.3: Initial melt parameters selected for the development of EBM tungsten

Parameter	Value
Current (mA)	7
Speed (mm/s)	140
Hatch offset (mm)	0.25

4.2.4 Melt

Once appropriate preheat and plate heating were established, the melt step was developed. In this subsection are outlined a number of issues that were addressed during these trials in order to establish successful melting of parts.

A standard hatching melt strategy was used, the contouring step was disabled. As a starting point the parameters listed in Table 4.3 were selected. These parameters were approximated based on a combination of standard Arcam parameters for alloys such as Ti6Al4V (to select hatch spacing) and those used in the previous SLM trials based on the energy density relationship (Equation 1).

Supports

An immediate issue that was faced when attempting the melt step was the need for supports. The energy required to melt the firs few layers causes rapid vaporisaion of the surface of substrate bellow. The stresses imparted through this process was found to heavily deform the plates preventing further powder deposition. An example of one of these deformed substrates is shown in Figure 4.2.

Figure 4.2: Image of a substrate following EBM of tungsten powder directly onto the surface.

To address this issue supports were added. Wafer supports were used with a height of 5mm. Wafer supports are built up from single line melts on each layer to create a thin walled structure that can easily be removed. Using

Table 4.4: Wafer Support Parameters

Parameter	Value
Current (mA)	6
Speed (mm/s)	250
Focus offset (mA)	0

Table 4.5: Thickness function settings selected

S_f	Z_f	E_f	Z_{max}
2	0.25	2.2	2

supports acted to minimise the initial energy input preventing damage to the plate. An alternative to using supports would be to change the plate material, this however was not explored . Selected support parameters are listed in Table 4.4.

The Thickness function

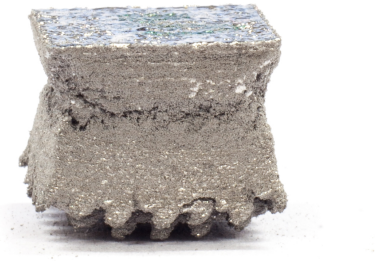

Figure 4.3: A tungsten cuboid built with the use of wafer supports and no melt functions

The addition of supports resulted in successful builds, however this revealed another problem. An image of a sample built using supports is shown in Figure 4.3; it is clear that the resulting build geometry is dramatically different to the input STL files. This can be accounted for in the fact that there is a difference in the rate of heat dissipation between the top and bottom of the part. The thickness function aims to correct for this, and thus a series of trials were run in order to find a set of parameters for the thickness function that would result in accurate sample geometries. Samples were built over a range of thickness and exponent factors listed in Table 4.6 and plotted in Figure 4.4. The resulting samples were assessed qualitatively to determine which of the thickness functions tested produced the most accurate geometry. From this assessment the thickness function used for all future samples is outlined in Table 4.5.

Table 4.6: Thickness function parameters tested during initial trials

Sample	S_f	Z_f	E_f	Z_{max}
1	2	0.25	1.1	4
2	2	0.25	1.1	4
3	4	0.25	1.1	4
4	6	0.25	1.1	4
5	8	0.25	1.1	4
6	2	0.25	2.2	2
7	4	0.25	2.2	2
8	6	0.25	2.2	2
9	8	0.25	2.2	2

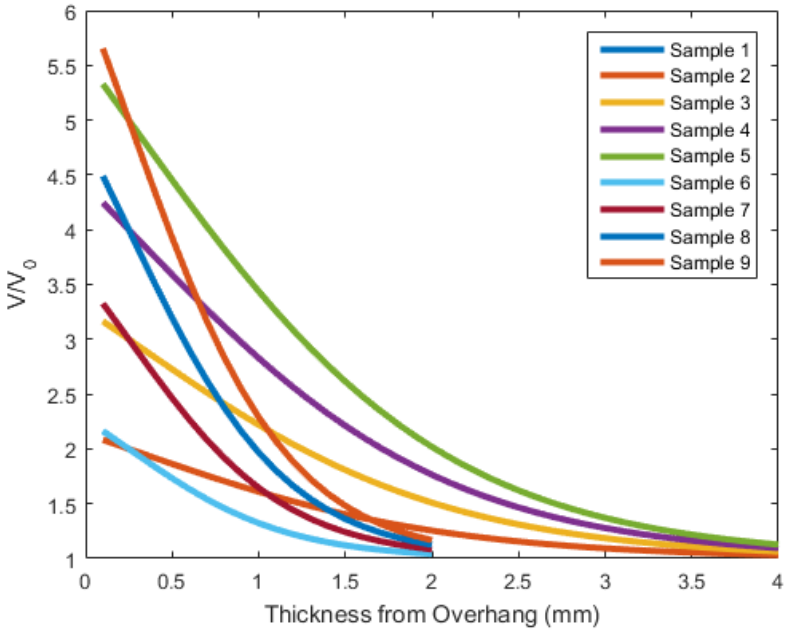

Figure 4.4: Plot of thickness function parameters tested during initial trials

4.2.5 Summary

The findings of the initial trials outlined in this section set a foundation for the development of EBM tungsten. The three main process steps were investigated. Figure 4.5 shows an image of a completed build following this development including sintered powder.

4.3 THE EFFECT OF BUILD PARAMETERS ON DEFECTS

4.3.1 Introduction

The initial development discussed in the previous section acted to identify the process parameters which would result in a successful tungsten build.

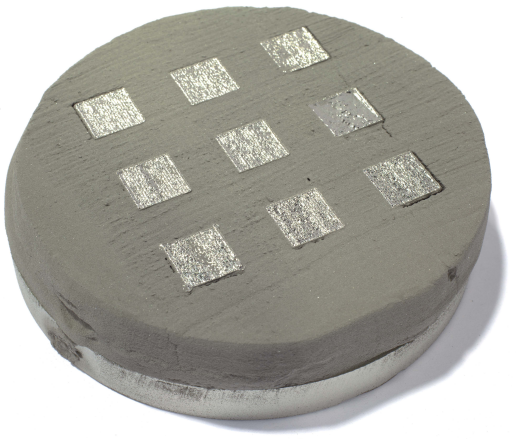

Figure 4.5: Image of an EBM tungsten build following the initial development

In this section the effect of the key process parameters on defects will be investigated.

4.3.2 Experimental Design

A response surface design was selected to investigate the effect of varying beam speed (v), current(I) and hatch offset (h) during melting; these parameters were varied over three levels as listed in Table 4.7. Six repeats were carried out at the centre point giving a total of twenty samples. All other process parameters remained constant; layer thickness and focus offset were maintained at 30µm and 10mA respectively. A hatching scan strategy was used and the pattern was rotated by 90 degrees on each layer. Support, preheat, plate heating, and thickness function parameters used are listed above in Tables 4.4, 4.2, 4.1, and 4.6 respectively.

In order to use the thickness function ,as was deemed necessary during the initial trials, the EBM control software requires that the speed function is enabled. Current was set to the specified value for each sample, the required speed function was then determined from the desired beam speed using linear interpolation. The speed function used for each combination of current and speed is listed in Table F.1.

The design of experiments was carried out over two builds, sample orders were randomised. Each build consisted of fifteen cuboids with height 5mm, width 5mm, and length 9.5mm. Samples were arranged in a five by three grid with a spacing of 10mm in the X direction and 5mm in Y. Wafer supports with a height of 2mm were used to join the samples to the substrate.

Folowing completion of builds each sample was separated from the substrate by hand and supports were removed via planar grinding with 120 grit silicon carbide paper. The samples were then mounted in Bakelite and prepared for optical imaging as outlined in Section 2.8.2. Porosity was then measured using the Clemex optical microscope system discussed in Section 2.8.1. Significance level was set at (p-Value = 0.05) to allow for any external variables which may produce noise in the data.

Table 4.7: Levels for varied melt parameters

Parameter	Low	Middle	High
Current (mA)	5	7	9
Speed (mm/s)	100	140	180
Hatch offset (mm)	0.2	0.25	0.3

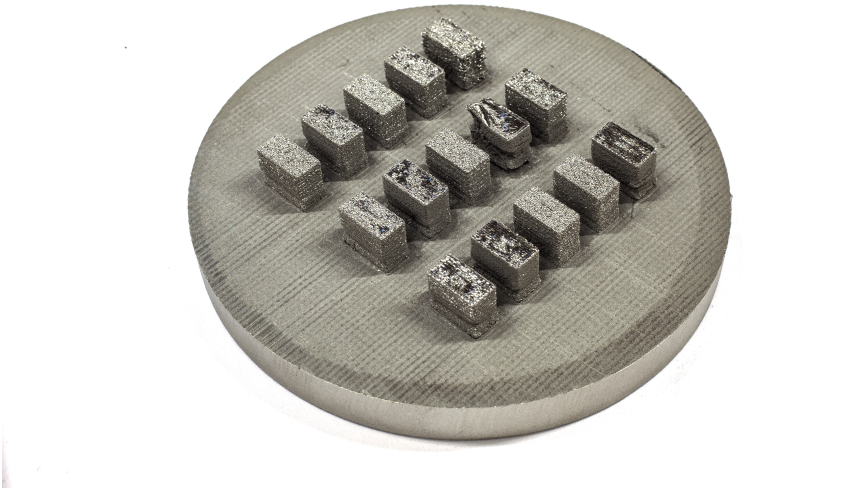

Figure 4.6: An Image of a completed DOE Build

4.3.3 Porosity Results

A full list of porosity results is provided in Appendix F Table F.1. Measured porosity in samples ranged from 0.04 to 11%. The mean porosity was 2.1% with a standard deviation of 3.3%. No cracks were observed in the samples.

The statistical analysis software minitab was used to analyse the results. An ANOVA was performed to asses the significance of each variable with relation to the porosity response, results are shown in Appendix F Table F.2. ANOVA demonstrated that the linear response of the three variables investigated was significant above the 99.9% significance level (p-value < 0.001). The square terms of speed and current were also found to be significant (p-value < 0.001, p-value = 0.009) along with the two way interactions of speed against current, and current against hatch offset(p-value < 0.001, p-value = 0.001). The square factor of hatch spacing and the interaction of speed against hatch spacing were found not to be significant variables (p-value = 0.849, p-value = 0.623). No significant variation was found between the two builds.

Figure 4.9 shows two micrographs compare the effect of beam current on porosity at constant speed and hatch spacing. At 7mA large pores are visible and porosity was measured at 1.29%, increasing the beam current to 9mA reduced porosity to 0.2%.

A second order model was generated via the least squares regression analysis method to fit the porosity response, R^2 values for the model are listed in Table 4.8. $R^2(adj)$ and $R^2(pred)$ are the adjusted and the predicted R^2 values respectively. The second order regression model fitted the data well

Table 4.8: Regression model summary for the porosity response

Standard Deviation	R^2	R^2**(adj)**	R^2**(pred)**
0.472	99.01%	97.90%	92.30%

with an R^2 value representing 99.01% of the variation with a standard deviation of 0.47% porosity. The lack of fit for the model was not significant ($p-value = 0.22$). Figure 4.7 shows a contour plot of the modelled porosity response for the range of current and speed investigated, at a constant hatch offset of 0.25mm. Table F.2 lists the regression coefficients for each of the variables and all interactions.

The porosity was plotted against the volumetric energy density as presented in Figure 4.8. The volumetric energy density was found to have a significant effect on the porosity ($p-value 0.0047$ $R^2 = 0.33$). Over the range of parameters investigated porosity tends to decrease with increasing energy density.

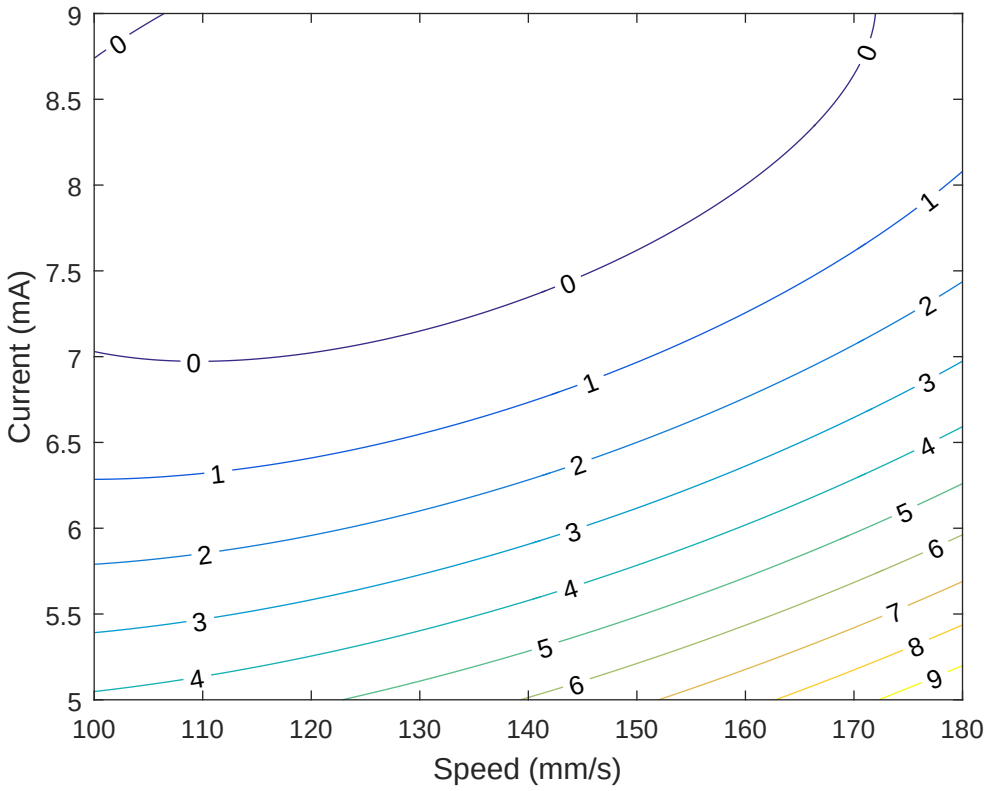

Figure 4.7: Contour plot of the variation in Porosity (%) against speed and current based on the second order response surface regression model (Hatch 0.25mm)

4.3.4 Geometry

Many of the samples demonstrated a poor geometrical accuracy when compared to the input CAD geometry. An example of this distortion is shown

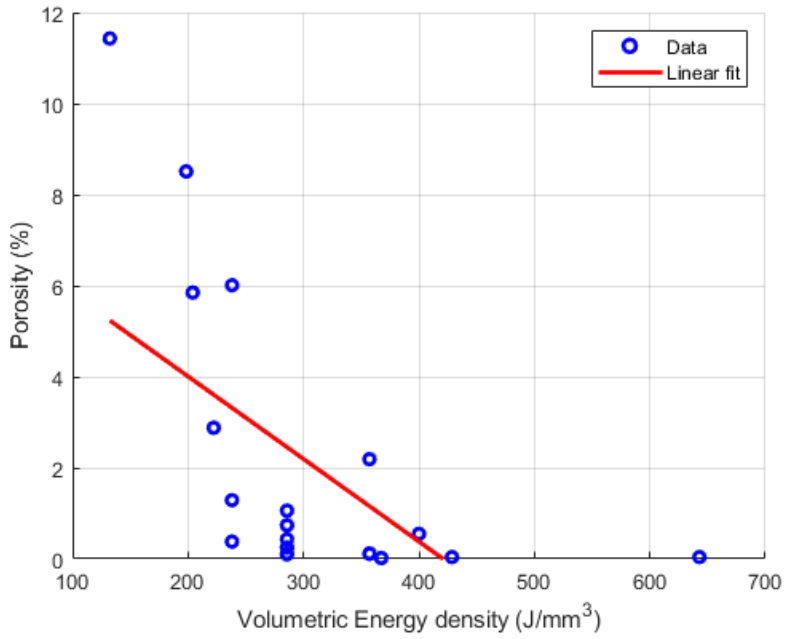

Figure 4.8: The effect of volumetric energy density on porosity with linear fit ($p-value = 0.0047$ $R^2 = 0.33$). Parameters given in Table 4.7

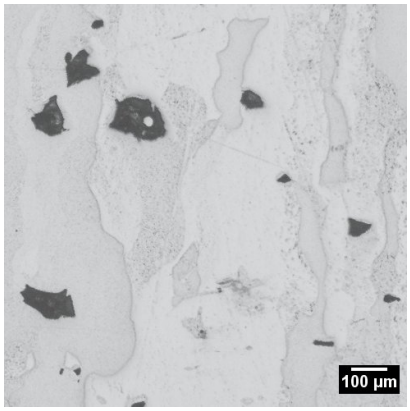

(a) Sample 1 cross section, $I = 7mA$, ($P = 350W$)

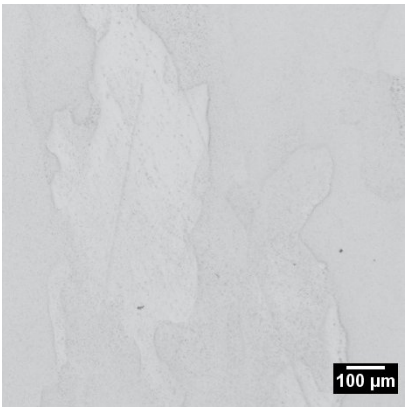

(b) Sample 5 cross section, $I = 9mA$, ($P = 450W$)

Figure 4.9: Comparison of two EBM sample cross sections showing high and low porosity. $v = 140mm/s$, $h = 0.3mm$.

in Figure 4.10. In order to quantify the amount of distortion found in each sample an image analysis routine was developed.

Geometry Image Analysis Routine

Images taken of the sample cross sections were analysed using a Matlab image analysis script. This script compared the cross section of the sample to the input CAD geometry and was used to output the maximum deviation between the two. Prior to analysis the bottom surface of the sample was

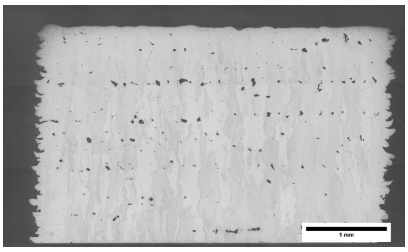

(a) Sample 1 cross section, $I = 7mA$, ($P = 350W$)

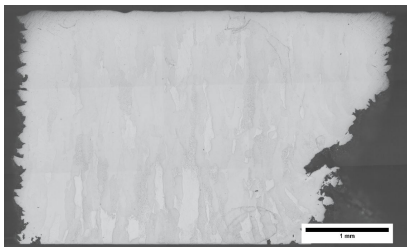

(b) Sample 5 cross section, $I = 9mA$, ($P = 450W$)

Figure 4.10: Comparison of two EBM sample cross sections showing the combination of good geometry with high porosity and poor geometry with low porosity $v = 140mm/s$, $h = 0.3mm$.

aligned horizontally using Adobe Lightroom software. The image analysis script can be summarised in the following steps:

- Load image.
- Threshold to black and white image.
- Fill any closed porosity.
- Smooth edges and find the centroid of the sample.
- Generate the ideal sample geometry with the same centroid.
- Extract the perimeters of the sample and ideal case.
- Measure the distance between the perimeters for each pixel.

This method is outlined visually in Figure 4.11 and the script is included in Appendix I.

Results

The maximum offset for each sample is listed in Appendix F Table F.3. The mean of the measured offsets between CAD geometry and that produced was $438\mu m$ with a standard deviation $119\mu m$

An ANOVA was performed to assess the significance of the relationship between the parameters used and the resulting geometry, the results of which are outlined in Appendix F Table F.4.

The liner terms speed and current were found to have a significant effect on the sample geometry (p-value = 0.006, p-value < 0.001). The interactions between, speed and hatch spacing, and speed and current were found to be significant (p-value = 0.013, p-value = 0.003) . The square term of current had a significant effect (p-value = <0.001). A significant difference was also found between the two builds (p-value = 0.012, p-value = 0.032). All other variables and interactions were not significant (p-value > 0.05).

A second order regression model was fitted to the data, the variation in geometry is plotted as a function of speed and current in Figure 4.12. A summary of the fit for the model is included in Table 4.9. The model fitted the data well with an R^2 value of 93.9% and a standard deviation of $69\mu m$. The lack of fit for the model was not significant (p-value = 0.659).

The geometry response was plotted against the volumetric energy density as presented in Figure 4.13. The volumetric energy density was found to

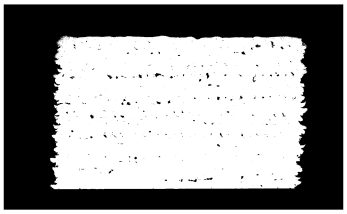

(a) Original sample image

(b) Fill any closed porosity

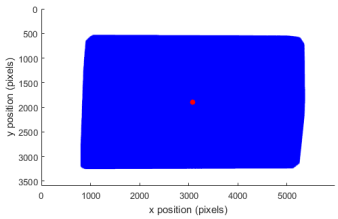

(c) Find the centroid

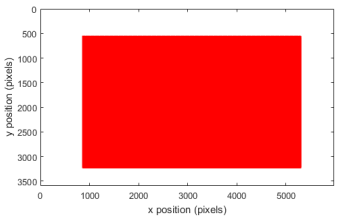

(d) Generate the ideal geometry

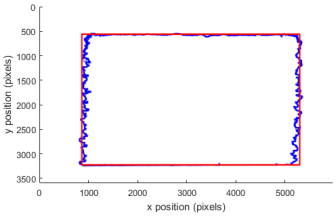

(e)Measure distance between perimeters

Figure 4.11: Geometry image processing method

Table 4.9: Regression model summary of fit the geometry response

Standard Deviation	R^2	$R^2(adj)$	$R^2(pred)$
69.16	93.9%	85.6%	57.1%

have a significant effect on the Geometry ($p-value = 6x10^{-}5$ $R^2 = 0.578$). Over the range of parameters investigated geometry tends to be less accurate with increasing energy density.

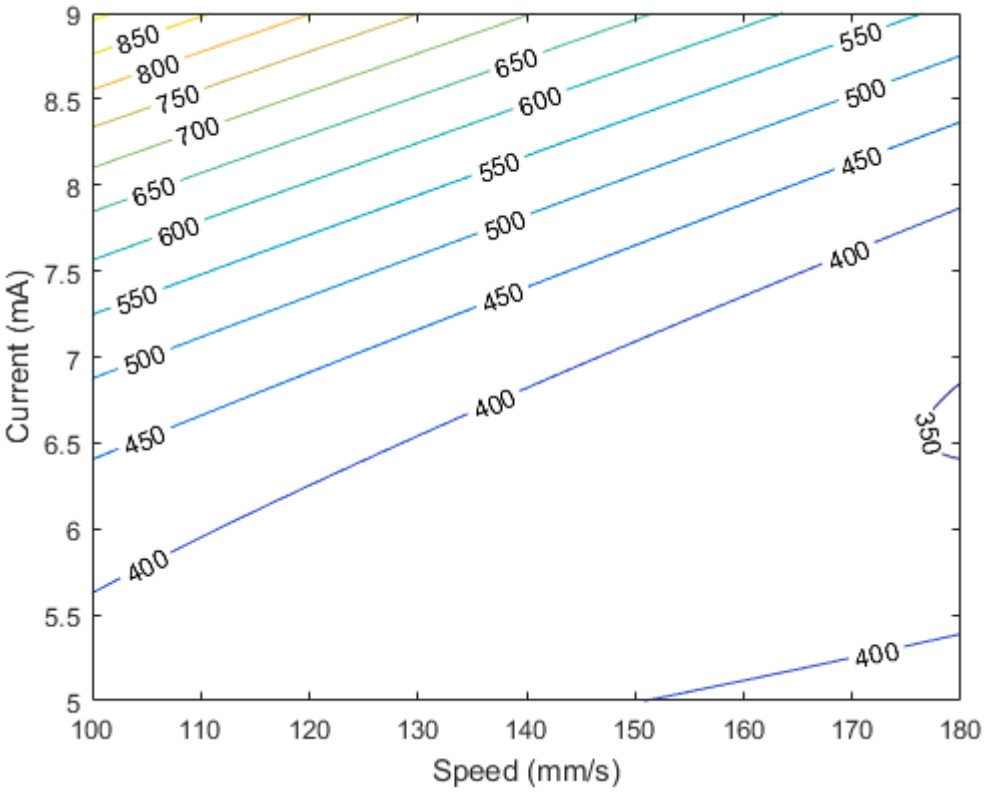

Figure 4.12: Contour plot variation in maximum cross section offset (µm) against speed and current based on second order regression model (Hatch 0.25mm)

4.4 DISCUSSION AND CONCLUSIONS

The experiment discussed in this chapter was carried out in order to asses the affect of process parameters on the porosity response. Upon removal of the samples from the substrate and following sample preparation an additional geometry response was identified.

Porosity in samples was observed in the range 0.04 to 11 and was significantly affected by the three variables investigated. The second order regression model fitted the data well and can be used to predict the response. This allows us to define a processing region as plotted in Figure 4.7 where porosity is predicted to be very low. Ideally processing of tungsten should

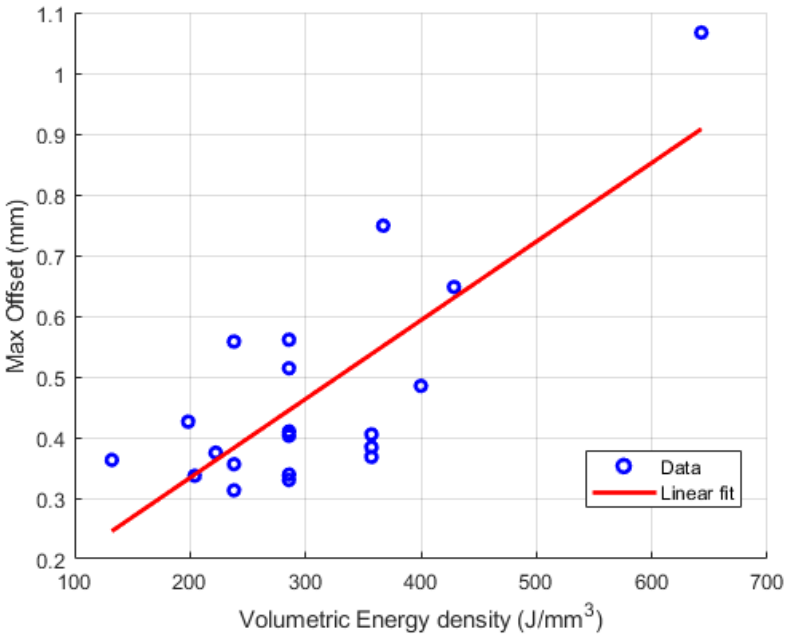

Figure 4.13: The effect of volumetric energy density on geometric accuracy with linear fit ($p-value = 6x10^{-}5$ $R^2 = 0.578$). Parameters given in Table 4.7

take place in the centre of this region at a current of approximately $8mA$, speed of $130mm/s$, and hatch offset $0.25mm$.

Porosity was found to decrease with increasing volumetric energy density. The minimum porosity was achieved at an energy density of $367J/mm^3$. However there is a high degree of scatter in the relationship between energy density and porosity ($R^2 = 0.33$) and energy density alone can't reliably be used to predict porosity levels.

The geometry response was significantly affected by the variables speed and current. A second order model fitted the data well but with an $R^2(pred)$ value of 57.1% can not be used as a reliable predictor. Within the range tested the lower energy density was found to result in a more accurate geometry. This is in conflict with the results for porosity which would suggest operating at the higher end of the energy densities tested. Parameter selection should therefore take both of these responses into account, operating along the contour of low porosity and low geometry offset. A significant difference was found in the geometrical accuracy between the two experimental builds, this suggests that additional external factors are likely to affect the geometry of components. Further work needs to be carried out to investigate the source of these differences.

The EBM process was found to eliminate the cracks that were present in samples prepared via SLM. The primary differences between the two systems are considered as a potential factors which lead to the elimination of cracks, these can be summarised as atmosphere, build temperature and energy source.

Firstly in the case of EBM the atmosphere is a high vacuum and in SLM an inert argon atmosphere is used which contains below 100ppm of oxygen. Relative to the EBM process SLM has a high concentration of oxygen and

other impurities. During melting the solubility of oxygen within tungsten is high. Upon cooling impurities will segregate to the grain boundaries which can embrittle the material and increase inter granular fracture [77].

Secondly the elevated build temperature's of the EBM system may act to prevent the formation of cracks as visible in samples produced via SLM. This is due to the fact that at higher build temperatures thermal gradients are lower. Lower temperature gradients produce slower cooling rates and therefore induce lower residual stresses. Additionally long build times at elevated temperature can act to stress relieve parts [174]. Temperatures of $900^{o}C$ for one hour have been found previously to be sufficient to relieve some stresses in worked tungsten [175, 176].Additionally operating above the DBTT may allow the material to elastically and plastically deform under any induced stress preventing brittle fracture.

It has previously been shown that dimensional inaccuracy in EBM can be significantly reduced via control of the melt functions [28]. A further investigation should therefore be carried out into the effect of these functions on the measured geometry.

5 CHARACTERISATION OF EBM TUNGSTEN

5.1 INTRODUCTION

Following the determination of process parameters outlined in the previous section a series of builds were carried out to create the samples necessary to characterise the resulting material. The material was characterised using a range of testing methods. Mechanical properties were evaluated via three-point bend testing and nano indentation. Thermal properties were measured using laser flash analysis (LFA) and thermomechanical analysis (TMA). Texture and gain structure were determined using electron backscatter diffraction (EBSD).

5.2 BUILD LAYOUT

Samples were manufactured via EBM with the required geometry for the various characterisation testing methods used, following each build EDM was used to remove supports and create flat and parallel surfaces where necessary. Two builds were carried out in order to generate all the samples necessary for testing Figures 5.1 and 5.2 show the build layout for these two builds. The height of all samples were kept constant to minimise the variation in energy input between layers. The exact sample geometry for each test specimen will be discussed in the relevant subsection.

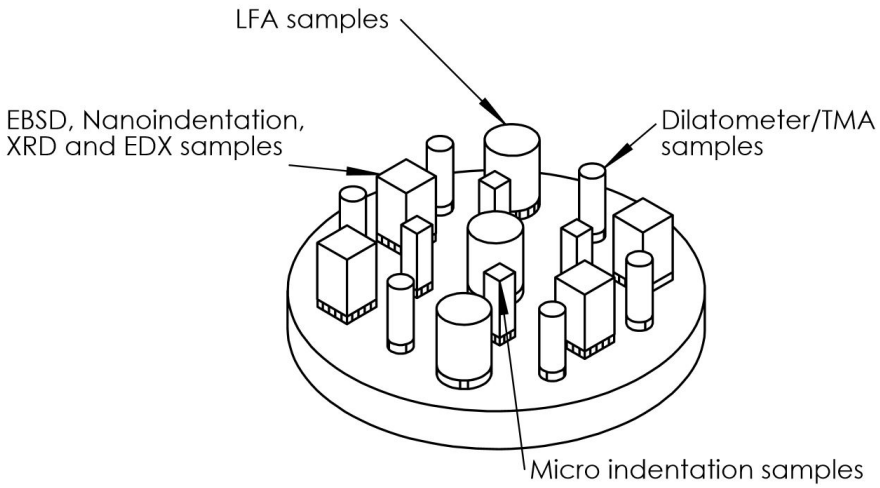

Figure 5.1: Build layout for first test sample build

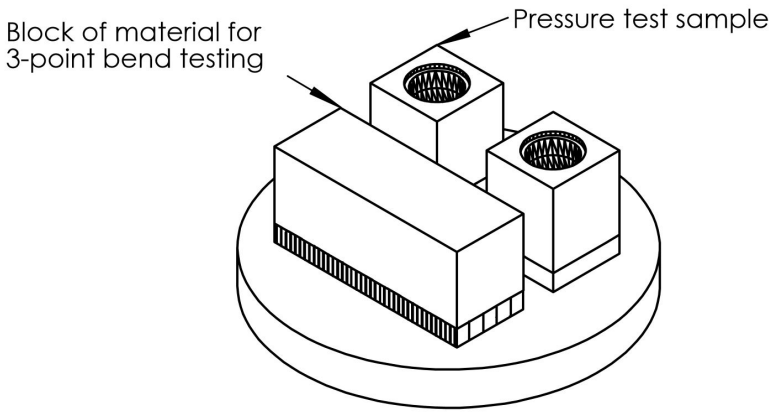

Figure 5.2: Build layout for second test sample build

Table 5.1: Melt Parameters selected for the two characterisation builds

Parameter	Value
Current (mA)	9
Speed (mm/s)	170
Speed Function	4.997
Hatch offset (mm)	0.25

5.2.1 Build Parameters

Plate heating, preheat, thickness function, and support parameters discussed in Chapter 4 were maintained. Melt parameters used are listed in Table 5.1 these parameters were selected based in the results in Chapter 4; speed was maximised within the range of speed and current which produced high density. Figure 5.3 plots the temperature profile for the first test build. Temperature data for the second build was not collected due to a thermocouple failure.

5.3 GRAIN STRUCTURE AND ORIENTATION

For EBSD analysis cuboid samples with dimensions of 10x10x5mm were used. These were cut from 10x10x15mm cuboids via EDM. Samples were cut both parallel and perpendicular to the build direction as illustrated in Figure 5.4. The samples were prepared and imaged using the methods outlined in Chapter 2.

5.3.1 Results

Figure 5.5 shows an orientation map of the sample surface prepared perpendicular to the build direction (XY plane). Figure 5.6 shows the orientation map of the sample in the build direction (XZ plane). Pole figures are presented in Figure 5.7, taken from the mapping shown in Figure 5.5.A strong

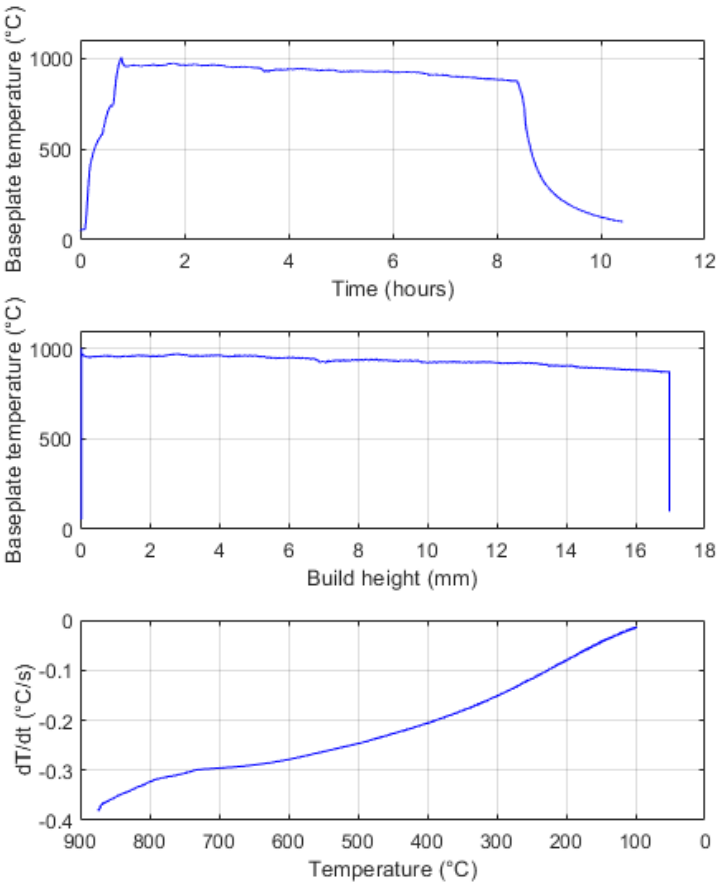

Figure 5.3: Base Temperature profiles for the first characterisation sample build. Top: Baseplate temperature for the entire build from plate heating to cooling. Middle: Baseplate temperature against build height. Bottom: Cooling rate after completion of build.

[111] fibre was shown relative to the plane of deposition with intensity 24 MUD.

The material shows a columnar grain structure, with large grains elongated in the build direction. Viewed perpendicular to the build direction the grains appear equiaxed. Grain size was measured using Oxford instruments HKL post processing software, grains were measured at a miss orientation of ten degrees and approximated to ellipses. The average grain diameter in the XZ plane was measured at 155 µm. In the XZ plane grains had an aspect ratio of 3.6 and were elongated in the build direction. The average grain diameter in the XY plane was measured at 97 µm.

Cubic materials have a [100] preferred growth direction [68]. Other alloys produced via EBM such as titanium show a [001] fiber texture [177]. This texture result is therefore somewhat unexpected. A similar result was found previously in the SLM of tantalum [178]. The authors of this tantalum study modelled the heat flux, in the process finding that the average heat flux was rotated around the scanning direction by 45 degrees and around the traverse direction (perpendicular to scanning and build directions) by 54 degrees. This resulted in a thermal gradient in approximately the [111] di-

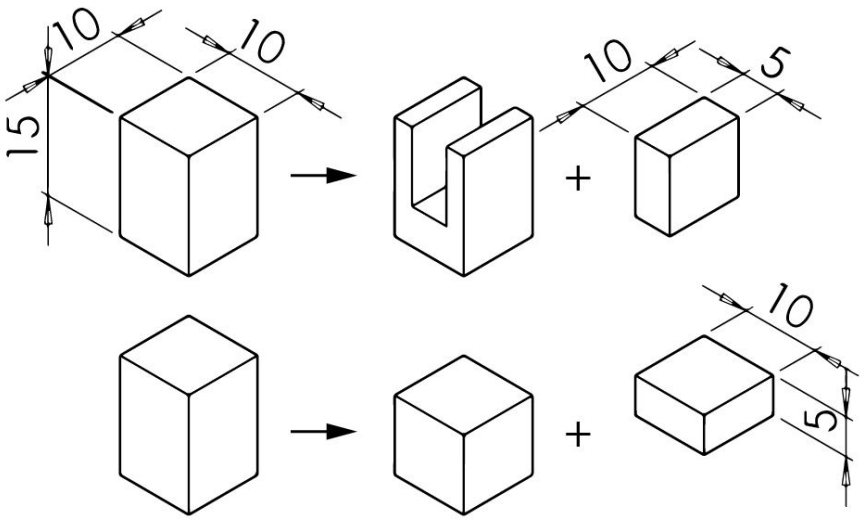

Figure 5.4: Diagram to illustrate the EDM cutting of EBSD samples, parallel (Top) and perpendicular (bottom) to the build direction. All dimensions given in mm

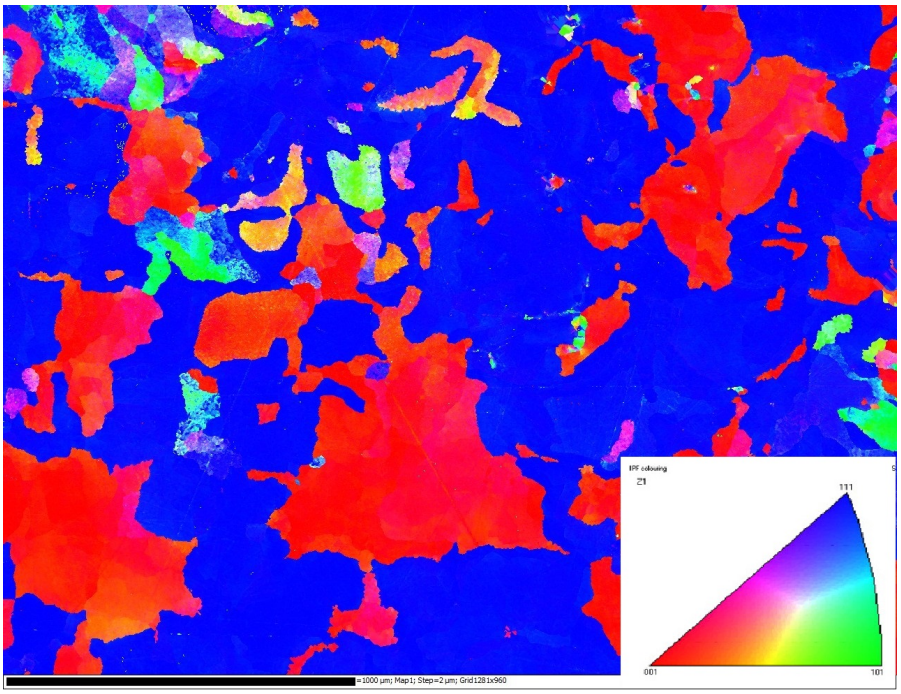

Figure 5.5: EBSD orientation map taken perpendicular to the build direction (XY Plane) with IPF colouring

rection producing this strong [111] texture due to the preferred [100] growth direction [178].

In a very recent study Sidambe et al observed a similar [111] orientation in SLM tungsten [169]. The authors came to a simillar conclusion suggesting that this was due to the shape of the melt pool which is more hemispherical than that of typical ALM alloys [169] [177]. Common ALM alloys are melted

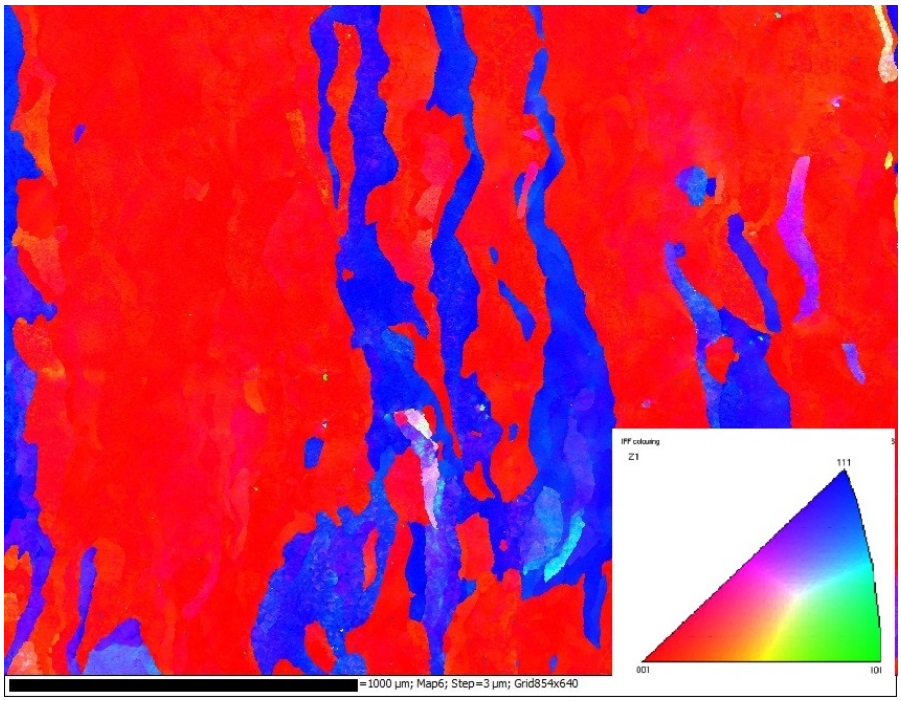

Figure 5.6: EBSD orientation map taken parallel to the build direction (XZ Plane) with IPF colouring

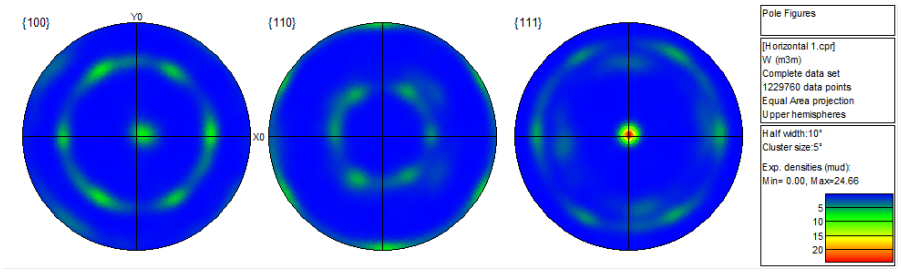

Figure 5.7: Orientation pole figure taken form EBSD map perpendicular to the build direction (XY Plane)

at high beam speeds and have low thermal conductivity. Titanium for example has a shallow elongated melt pool and the preferred growth direction is therefore not tilted much relative to the build direction [177]. As the melt pool becomes less elongated the angle between the build direction and that of preferred growth will increase. As the scanning directions change each layer a new preferred orientation could emerge [169].

It is likely that a similar effect is occurring here to that found in tantalum. Further thermal modelling or experimental measurement would be required to fully confirm the direction of thermal gradients during solidification. Further analysis of the texture at the edge of the samples could also demonstrate this effect as at this point the thermal conditions change and the texture would therefore be expected to become more random.

It should also be noted that the tantalum study by Thijs et al found that rotation of scanning direction between layers resulted in a rotation of this thermal gradient [178]. It is possible therefore that the thermal gradient in

the traverse direction will vary as a factor of the time between subsequent hatch lines. It is therefore possible that the texture could be modified to some extent by changing scanning strategies and the length of scan lines.

5.4 THREE-POINT BENDING

Sample Preparation and Surface Finish

The second test sample build (Figure 5.2) included a cuboid of material with dimensions 55mm x 20mm x 20mm. The long dimension ot the cuboid was aligned perpendicular to the build direction. The block was attached to the substrate with a combination of wafer and solid supports with a height of 5mm. Figure 5.8 shows an image of the manufactured block of material.

Figure 5.8: Photograph of manufactured cuboid used for 3-point bend tests

The manufactured cuboid was cut into test specimens via EDM in accordance with the British Standard EN 843-1 [164]. Sample type 'A' was selected from the standard with dimensions and tolerances listed in Table 5.2.

The block of material was cut via EDM, into two sets of samples denoted 'batch A' and 'batch B'. Samples in batch A were cut such that the test face was parallel to the XZ plane. Samples in B were cut such that the test face was parallel to the XY plane. +

An initial cut was made parallel to the top surface to remove support structures and the bottom 5mm of material where the thickness function was in effect. 1 to 2mm of material was then removed from all other surfaces to ensure the faces were flat and square. The material was sectioned across the longest face to create two cuboids of material which were labelled 'A' and 'B'. As many samples as possible were cut from these two blocks with dimensions listed in Table 5.2. Samples in batch A were cut such that the width of 2.5mm was aligned to the build direction. Samples in batch B were cut such that the 2mm sample thickness was aligned with the build direction. For clarity on this cutting process Figure 5.9 is included, detailing

Table 5.2: 3-point bending test piece dimensions and tolerances in accordance with BS EN 843-1 [164]

Sample Type	Surface Condition	Parameter	Dimensions (mm)		
			Length	Width	Thickness
A	All	Dimensional Range	$\geqslant 25$	2.5 ± 0.2	2.0 ± 0.2
	Machined	Parallelism Tollerence	-	± 0.02	± 0.02

this process. A total of 40 samples were cut from batch B and 31 from batch A.

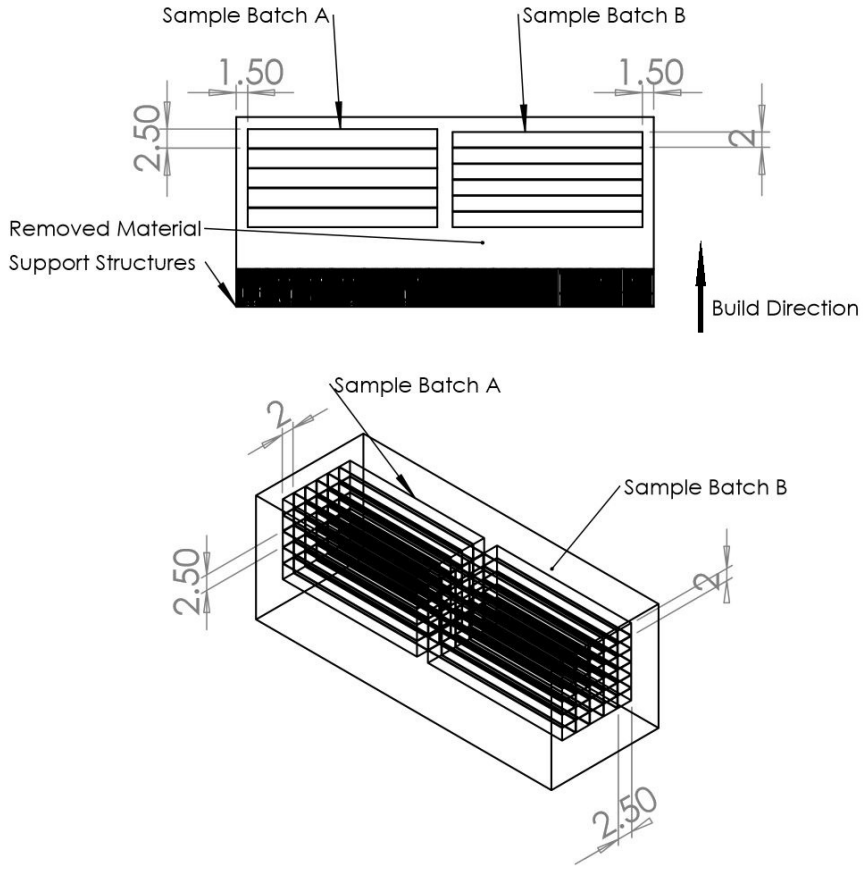

Figure 5.9: Photograph of manufactured cuboid used for 3-point bend tests

Following cutting of the samples, surface preparation was carried out to BS EN 843-1 [164]. The sample surface was prepared using a planar grinding wheel with a 120 grit resin bonded diamond wheel followed by a 500 grit wheel. Grinding was performed parallel to the length of each test piece. The two long edges of the samples along the test face were chamfered at an angle of 45 degrees by hand using 1000 grit silicon carbide papers. Figure 5.10 shows the surface of the samples following preparation.

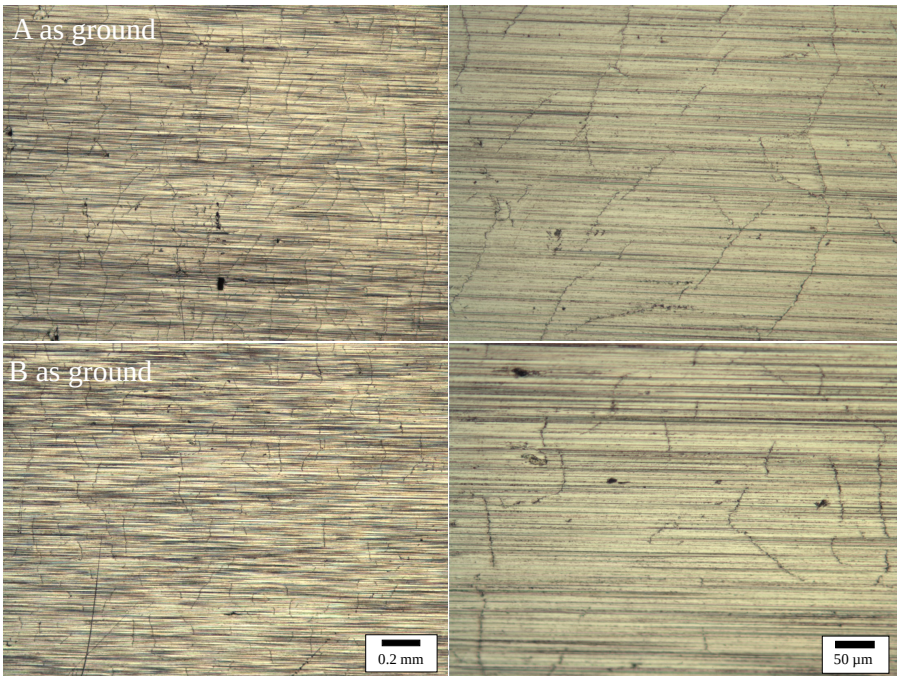

Figure 5.10: Example images of prepared sample surface for 3-point bend testing (Note lines on figures appear to show defects or cracks but these appear to be grain boundaries)

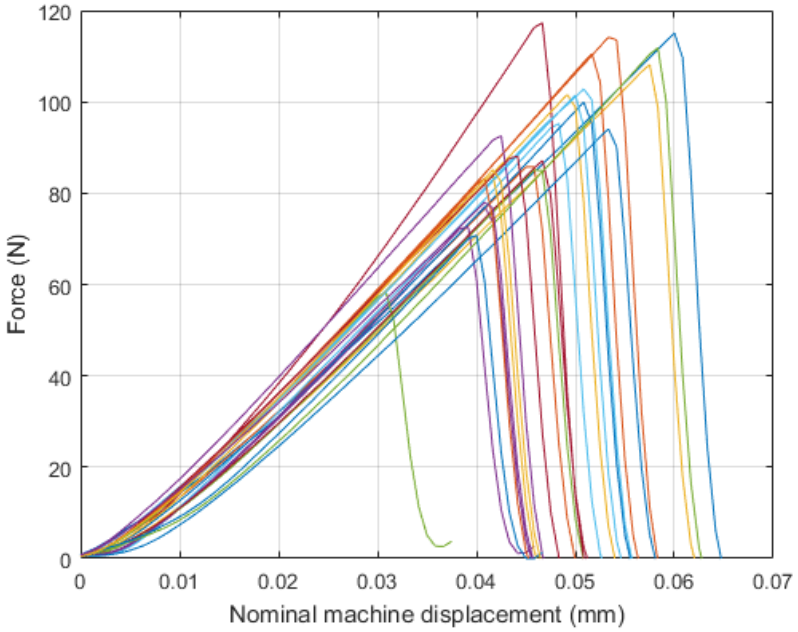

Figure 5.11: Force displacement response for samples from set A

5.4.1 Results

Dimensions for each sample along with the applied force and calculated fracture stress at failure are listed in Appendix G Tables G.1 and G.2. The mean fracture stress for batch A was 318.4MPa, with a standard deviation of 52. For batch B the mean fracture stress was 268.8MPa with a standard

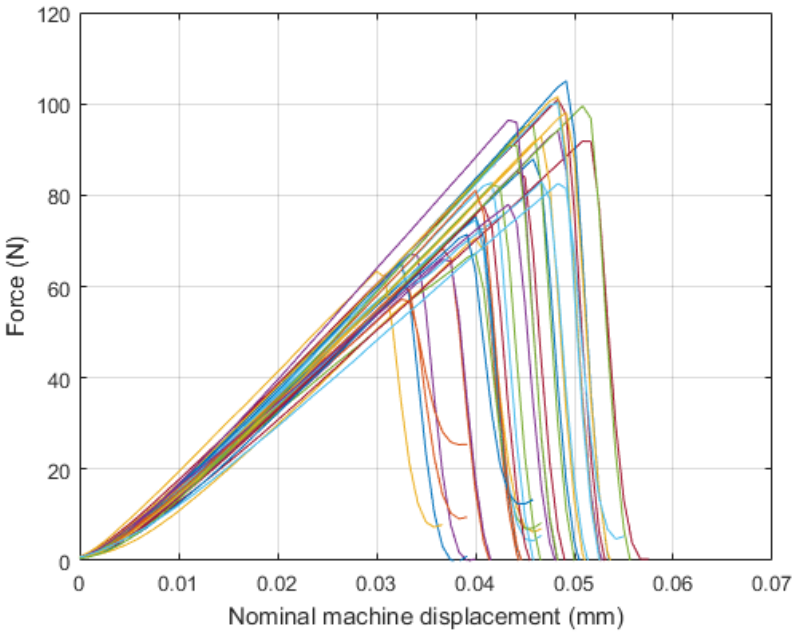

Figure 5.12: Force displacement response for samples from set B

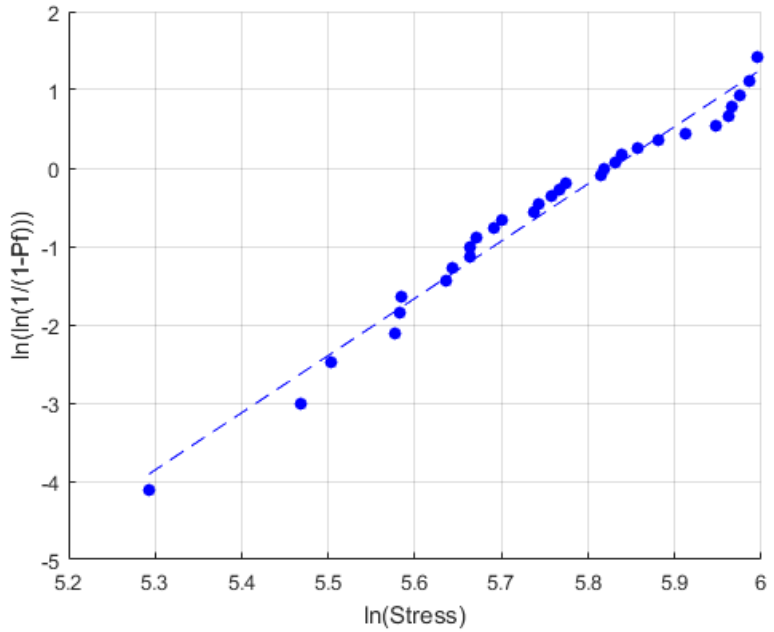

Figure 5.13: Linear Weibull plot for samples in batch A $R^2 = 97.7\%$

deviation of 63.3. A one way ANOVA was preformed to compare the means of the two batches. A significant difference was found between the two conditions (p-value = 0.001) with batch A on average having a higher failure stress.

Recorded force and displacement data is plotted in Figures 5.11 and 5.12. Force displacement data displayed no evidence of plastic deformation before failure. The degree of load drop at fracture was dependent on the peak

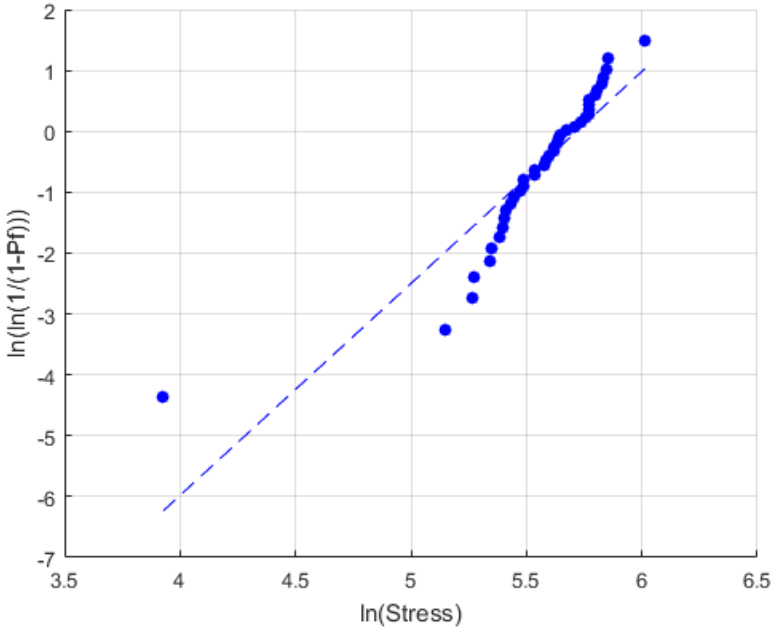

Figure 5.14: Linear Weibull plot for samples in batch B $R^2 = 82.1\%$

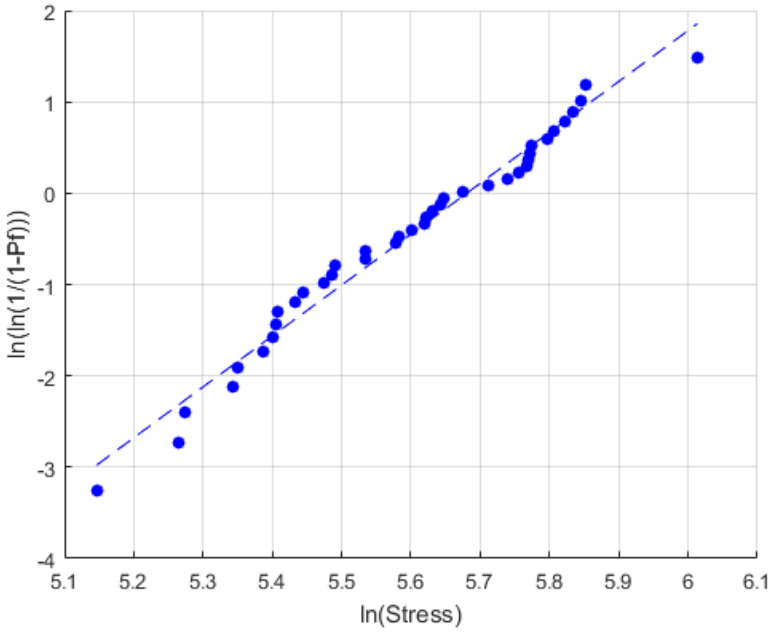

Figure 5.15: Linear Weibull plot for samples in batch B with low outlier removed $R^2 = 97.8$

force, with some test piece halves holding together. This implies samples had failed due to low energy brittle fracture. The majority of samples failed close to the centre, however a number of the samples failed away from the centre.

Weibull plots are shown in Figures 5.13 and 5.14. Sample 8 in batch B was judged to be a low anomaly and skewed the result, the Weibull plot

Table 5.3: Calculated estimate of Weibull parameters $\sigma_0(\eta)$ and β, 95% confidence intervals are shown in brackets

Condition	No. of samples	Characteristic strength σ_0 (MPa)	Shape parameter β
A	31	340 (322/358)	7.11 (5.40/9.37)
B	40	298 (279/341)	5.65 (4.46/7.15)

for batch B is replotted in Figure 5.15 with this data point removed. Least square linear regression fits were calculated for the plots. Calculated R^2 values show the fit accounts for 97.7% and 97.8% of the variance for batch A and the corrected batch B results respectively.

Table 5.3 lists the calculated Weibull parameters using the maximum likelihood estimate along with the 95% confidence intervals. Figure 5.16 plots the estimated distribution of failures based on these calculated values. Batch B showed a 12% reduction in characteristic strength when compared to batch A.

No fractography was carried on these samples.

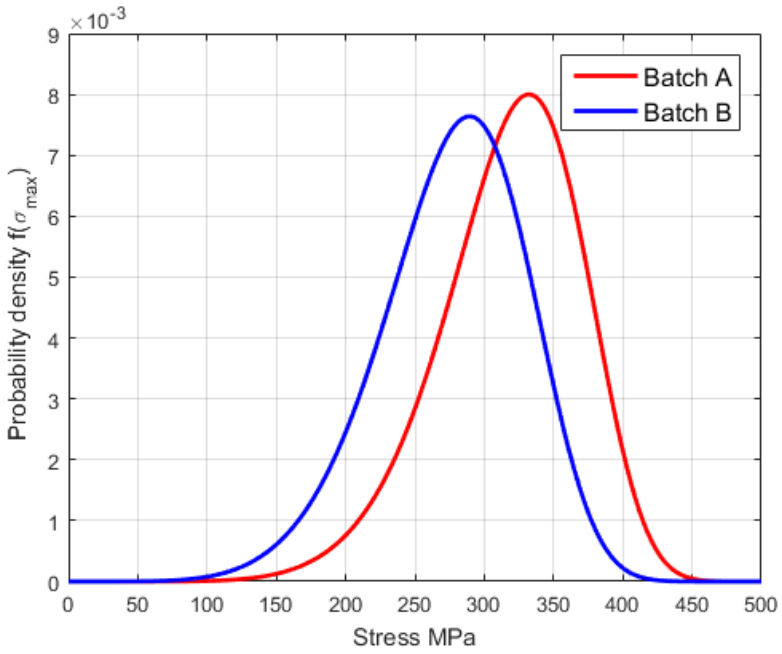

Figure 5.16: Estimated Weibull PDF for Batch A and B

Discussion

The characteristic strength can be used as a direct comparison between this work and the values reported in the literature as it is a material constant, independent of testing parameters. The characteristic strength calculated was found to be significantly lower than expected, values calculated by You et al [179] are listed in Table 5.4 for comparison. The tested material shows a 86% reduction in strength when compared to the warm rolled material tested by You et al.

The low strength values are likely explained by porosity within the samples. Areas containing large pores were identified on the test surface of samples as shown in Figure 5.17. It is therefore highly likely that these areas of porosity near the loading roller serve as origin points for fractures.

Porosity is likely a factor of the EBM parameters used and the part size. Chapter 4 discussed the need to maximise the speed and minimise current in order to minimise the amount of distortion in parts, however this in turn can increase the chance of porosity. An additional factor that is likely to influence the percentage of porosity in the test pieces is the size of the part from which samples were cut. When investigating the effect of the process parameters on the porosity in Chapter 4 the sample size and geometry remained constant. Scaling to much larger samples with differing geometries such as that used for this series of characterisation tests, may have a significant effect on the parts produced. It has been shown previously by Smith et al [28] that process parameters need to be varied as a function of the part geometry in order to produce defect free parts with the desired geometry. Geometry can have a significant effect on the heat dissipation in the part between subsequent passes of the beam. This is of particular importance when the parts are not attached directly to the substrate. Future work should therefore investigate the effect of sample geometry on porosity in EBM tungsten in order to evaluate the extent of this effect.

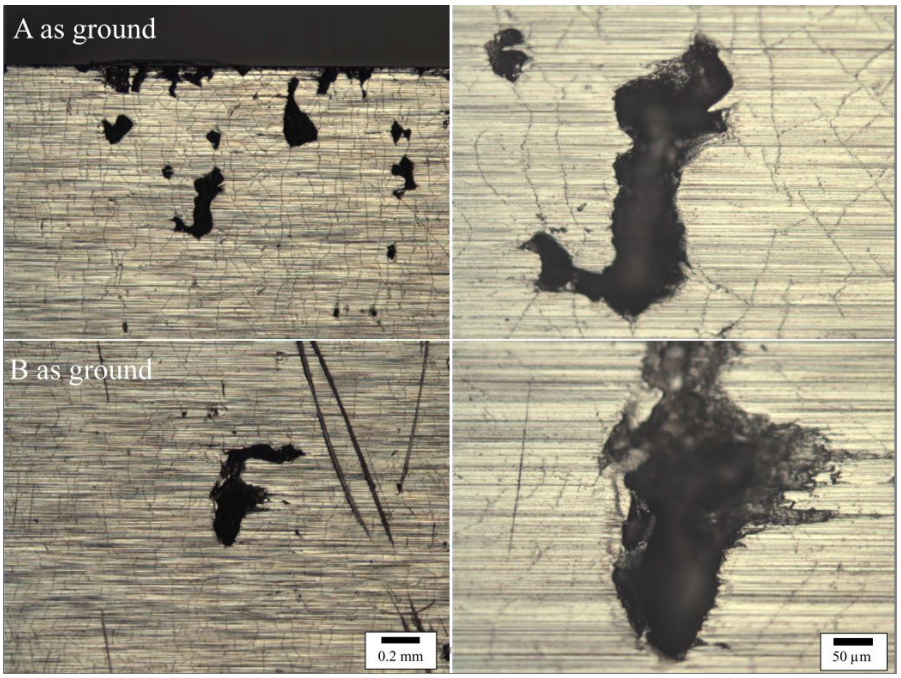

Figure 5.17: Example of porosity found on the sample surface

5.5 ULTRASONIC TESTING

Samples geometry for ultrasonic was the same as used for EBSD imaging as described in Section 5.3. The testing method was as outlined in Section 2.8. Testing was carried out on a total of four samples, two with surfaces prepared in the XY plane and two with surfaces in the XZ plane.

Table 5.4: Weibull parameters as measured by You et al [179]

Condition	**Characteristic Strength σ_0 (MPa)**	**Shape Parameter β**
As-received (warm rolled at 350°C)	2489	19
Heat treated (1000°C, 10h)	2353	31

5.5.1 Results

Table 5.5 lists the measurements for transverse and longitudinal wave velocities through the samples and the calculated moduli and Poisson's ratio. Young's modulus is calculated using the two methods discussed in Section 2.8 using purely experimental measurements as well as inference from Poisson's ratio reference values. A Poisson's ratio of 0.284 was used to calculate inferred values.

Table 5.5: Measurements taken for ultrasonic, transverse and longitudinal wave velocities in tungsten EBM samples. Also listed are the calculated values for Moduli and poisons ratio

	Measured					**Inferred**	
Sample	c_l **(m/s)**	c_t **(m/s)**	E **(GPa)**	G **(GPa)**	μ	B **(GPa)**	E **(GPa)**
XZ plane - 1	5,060	2,833	394	155	0.27	288	398
XZ plane - 2	4,798	2,850	385	157	0.23	235	402
XY plane - 1	4,720	2,766	366	148	0.24	233	379
XY plane - 2	4,592	2,902	380	163	0.17	190	417
Mean	4,792	2,838	381	155	0.23	237	399
Std Dev	197	56	12	6	0.04	40	16

5.6 NANOINDNENTATION

Samples were built and prepared for Nanoindentation using the same method and sample geometry used for EBSD analysis as outlined previously in Section 5.3. In summary two samples were prepared with dimensions 10mm x 10mm x 5mm in differing orientations; prepared 10mm x 10mm surfaces were oriented in the XZ plane and the XY plane. Samples were tested using the method fully outlined in Section 2.8. Indents were arranged in the layout shown in Figure 5.18 where the co-ordinate origin is located at the centre of the sample. In the XZ plane indent sets were arranged in a H pattern and in the XY plane in a line from the centre to edge along the Y axis. Each set of indents consisted of a total of nine indents arranged in a 3x3 grid with a spacing of 10µm. Indent locations were manually selected such that grain boundaries and defects were avoided.

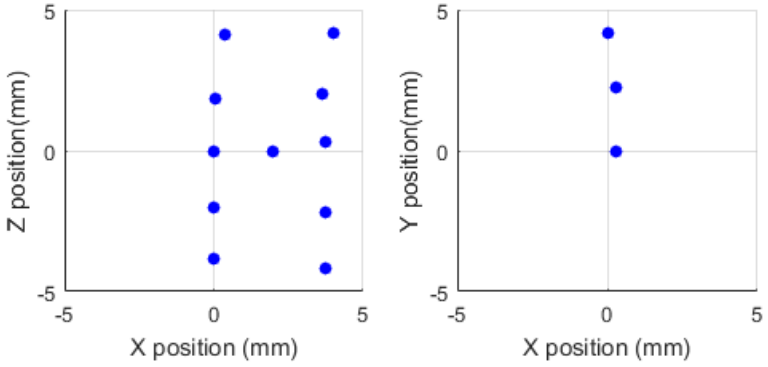

Figure 5.18: The arrangement of indents across the sample surfaces in the XZ and XY planes

5.6.1 Results

Following testing, results were arranged according to indent location and load. Liner regression and interpolation were then used to asses the effect of the indent location on the measured responses. In the XZ plane indents were analysed in the following three groups:

- $-4 < Z < 4$ at $X = 0$ - Representing the variation in the Z axis across the centre of the sample in X. Denoted 'Z centre'
- $-4 < Z < 4$ at $X = 4$ - The variation in the Z axis across the edge of the sample in X. Denoted 'Z edge'
- $0 < X < 4$ at $Z = 0$ -The variation in the X axis across the centre of the sample in Z. Denoted 'X centre'

In the XY plane the response was analysed for $0 < Y < 4$ at $X = 0$ representing the change across the centre of the sample in X. This response was denoted 'Y centre'

Linear regression was carried out across each group at each load to asses the effect of indent position on the responses of hardness and Young's modulus. The equation of the regression line was of the form $y = mx + c$ where m is the gradient, c is the intercept, y is the position variable, and x is the response variable. The results are tabulated in Appendix H Tables H.1 and H.2.

In general increased load was found to reduce the variance in results (R^2 values increased as load increased) providing a higher degree of significance. As a result, all further analysis was carried out for the maximum load.

At the maximum load the results show that there is a significant increase in modulus moving from the edge to the centre of the samples in the X and Y directions for $Z = 0$ (p-value < 0.001). A significant change in modulus was found in the Z direction across both the centre ($X = 0$) and edge ($X = 4$) of the sample (p-value < 0.001). The modulus was found to increase in the Z direction from the base of the sample to the top surface.

Hardness was found to significantly increase with Z direction across both the edge and centre of the sample (p-value < 0.001). A significant increase was found in hardness moving from the edge to centre of the sample in the Y direction (p-value = 0.002). No significant change was found in the hardness as a function of X position (p-value = 0.750).

For each of the four groups the main effects of position on hardness and modulus are plotted in Figures 5.19 and 5.20 respectively at the maximum load of 10mN.

Contour plots in Figures 5.21 and 5.22 display the expected variation in hardness and modulus based on linear regression and interpolation at maximum load in the ZY plane.

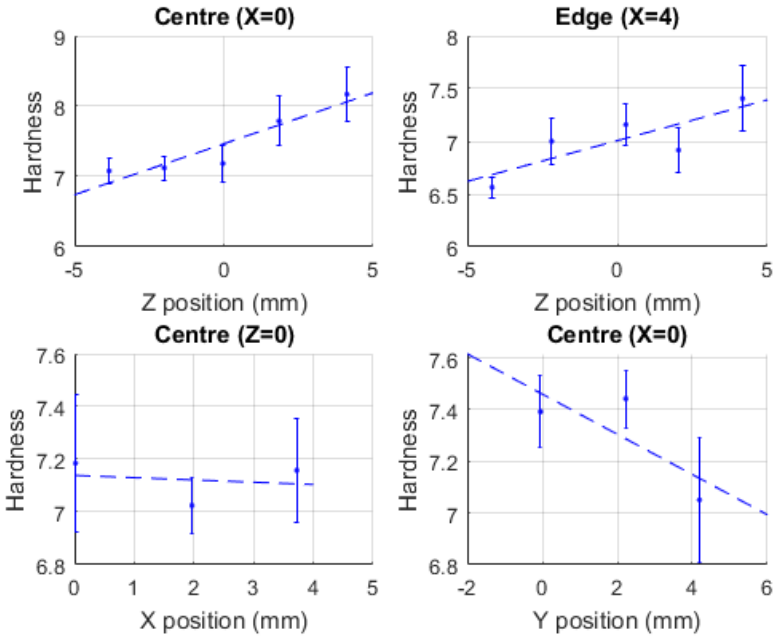

Figure 5.19: The variation in hardness data across samples for each of the four conditions investigated with linear fit. Error bars display one standard deviation from the mean Load = 10mN

5.6.2 Discussion

As early as 1932 it was demonstrated that the stress state of a material has an influence on hardness measurements. More recently Tsui et al showed that both elastic modulus measurements via Nanoindentation were also stress dependent[156]. A range of methods have since emerged for measurement of residual stress using indentation techniques [153] . It is likely that the observed variation in hardness and modulus across the samples are a representation of the variation in residual stress. To estimate the true values for hardness modulus and residual stress a stress free reference sample would be required.

The reduced hardness and modulus values in comparison to reference data and ultrasonic measurements imply a high compressive stress through the samples, from top to bottom and centre to edge. This result aligns well with stress distributions demonstrated previously through finite element and experimental modelling of both SLM and EBM processes [180] [181] [57] [182]. These models demonstrate an increase in stress with build height due to the temperature gradient mechanism (TGM) typically associated with laser bending of sheets[182]. As the top surface of a component is rapidly heated, a steep temperature gradient is formed. The expansion

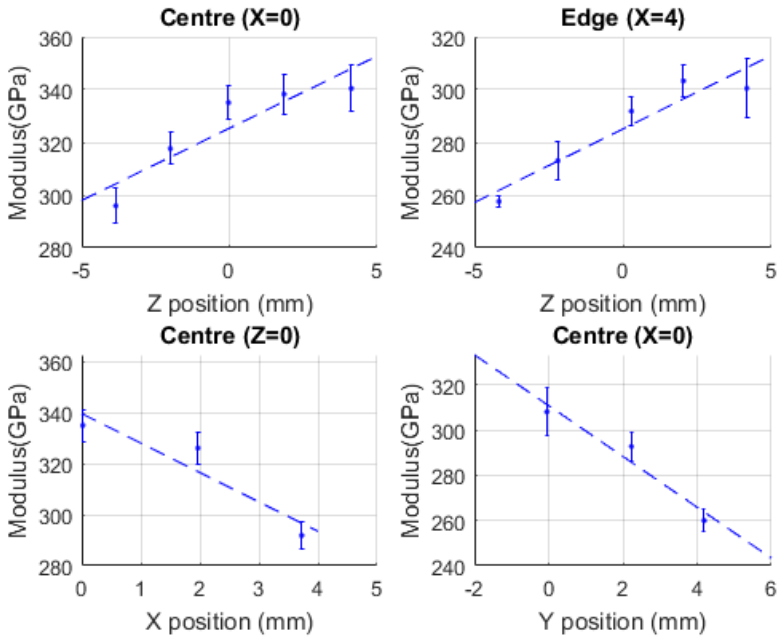

Figure 5.20: The variation in modulus data across samples for each of the four conditions investigated with linear fit. Error bars display one standard deviation from the mean. Load = 10mN

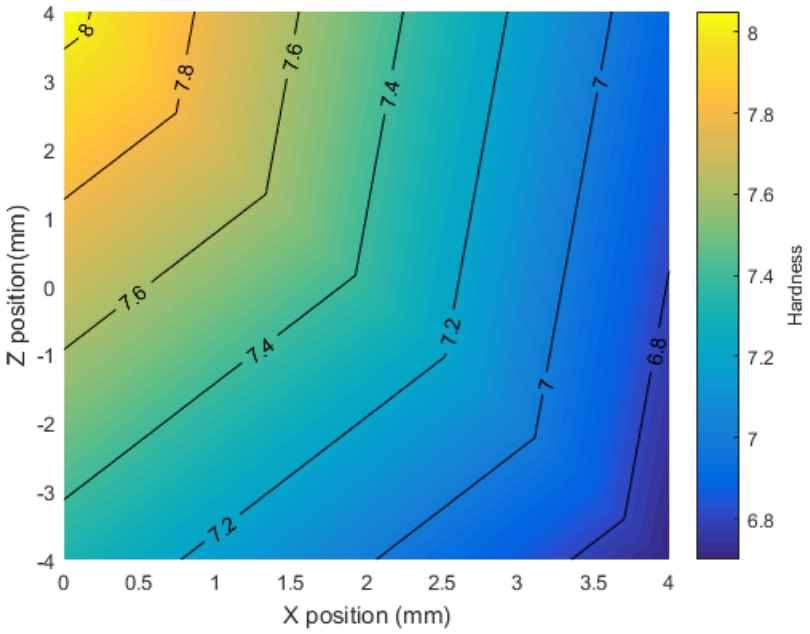

Figure 5.21: Contour plot of the predicted variation in hardness across samples in the XZ Plane

of the hot top surface is restricted by the underlying material and therefore compressive strains are induced. The increased temperature of the top surface leads to a reduced yield strength, when this strength is reached it will

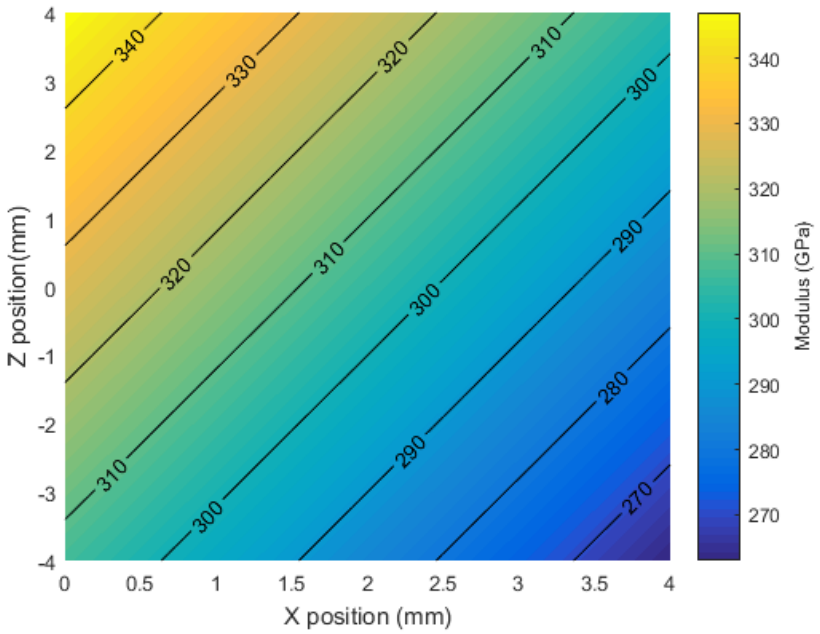

Figure 5.22: Contour plot of the predicted variation in modulus across samples in the XZ Plane

plastically compress. During subsequent cooling the compressed upper layers begin to shrink and a bending towards the beam develops. During the EBM and SLM process this stress builds on each layer[58]. The distribution of displacement as a result of these strains were observed by Prabhakar et al [58] during EBM of Inconel 718. The displacement measured match the observed geometry distortion discussed in the previous chapter.

The load dependence observed is likely due to the indentation size effect (ISE)[183]. The ISE effect occurs when the area sampled approaches the spacing between dislocations resulting in higher hardness at lower loads [184]. Another consideration is that low loads result in a low indenter penetration depth. This low penetration results in measurement of the top surface where residual stress imparted during sample preparation may skew results.

5.7 THERMAL PROPERTIES

Samples for LFA were built as cylinders with height 15mm and diameter 12mm. The samples were cut to form cylinders 5mm in length with parallel sides. Samples were cleaned using isopropyl alcohol before testing as outlined previously. Samples for TMA were built as cylinders with 15mm in height, the test samples were prepared in the same way as for LFA to form cylinders with a 5mm height.

5.7.1 Results and Discussion

Thermal conductivity results obtained via laser flash analysis are plotted in Figure 5.23. The results were fitted to a second order polynomial of the form $f(T) = p_1T^2 + p_2T + p_3$ in the range tested, the fit is plotted in Figure

Table 5.6: Coefficients of fitted polynomial with 95% confidence intervals

Coeff.	Value
p_1	$8.51x10^{-5}(5.70x10^{-5}, 11.32x10^{-5})$
p_2	$-0.22(-0.26, -0.17)$
p_3	$240(223, 256)$

5.23, along with the 95% confidence intervals. Table 5.6 lists the coefficients of the polynomial along with 95% confidence intervals.

Figure 5.24 plots same data along with reference data for annealed high purity tungsten as measured by Ho et al [63]. The reference data has an accuracy of 3% with in the range tested. A significant difference was not found between the reference data and the measurements taken, the reference data lies within the 95% confidence interval.

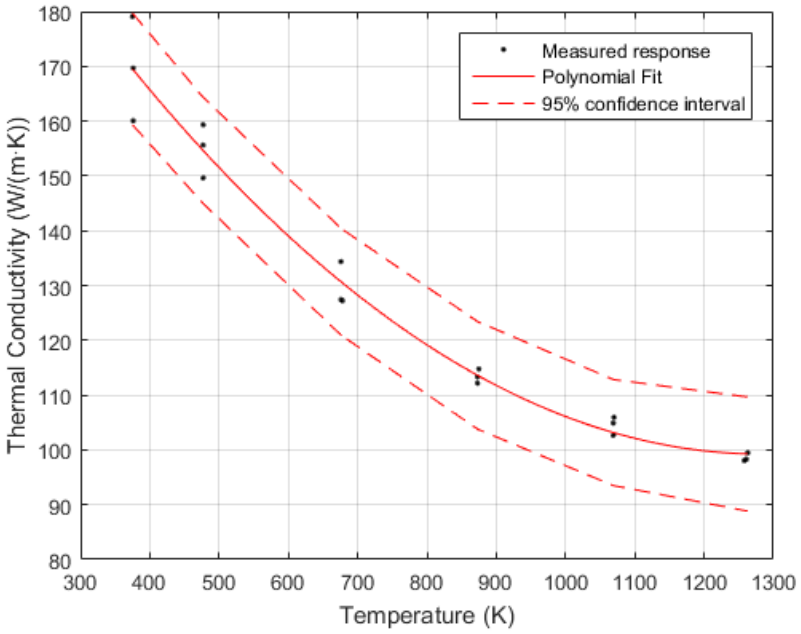

Figure 5.23: Plot of LFA data with polynomial fit and 95% confidence intervals

TMA data for each sample was fitted using linear regression to find the coefficient of thermal expansion. Figure 5.25 plots example data for the first sample along with the linear fit. Figure 5.26 plots the fit for all five samples, the results are summarised in Table 5.7. The mean coefficient of thermal expansion was $4.872x10^{-6}K^{-1}$ with a standard deviation of 0.241. The mean thermal expansion coefficient lies in the range reported in the literature of between 4.49 and $5.02x10^{-6}K^{-1}$ in the temperature range examined.

5.8 CHAPTER SUMMARY

This chapter investigated the properties of EBM tungsten.

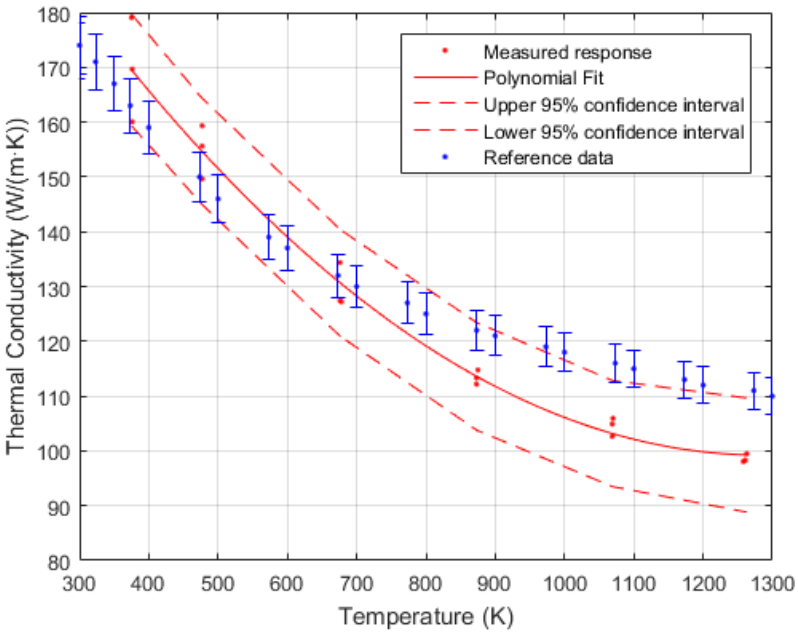

Figure 5.24: Plot of LFA data with polynomial fit and 95% confidence intervals and high purity tungsten reference data [63]

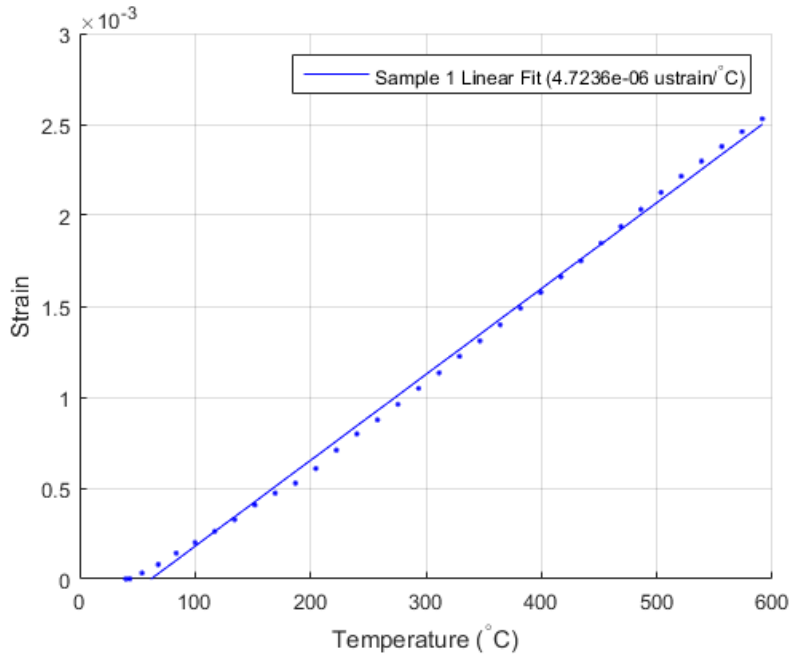

Figure 5.25: Plot of TMA data and linear fit for sample No.1

Microstructure analysis carried out using EBSD identified large columnar grains aligned elongated in the in the build direction. The material demonstrated a strong [111] fibre texture. This unexpected texture was attributed to the rotation of thermal gradients due to the high conductivity of tungsten

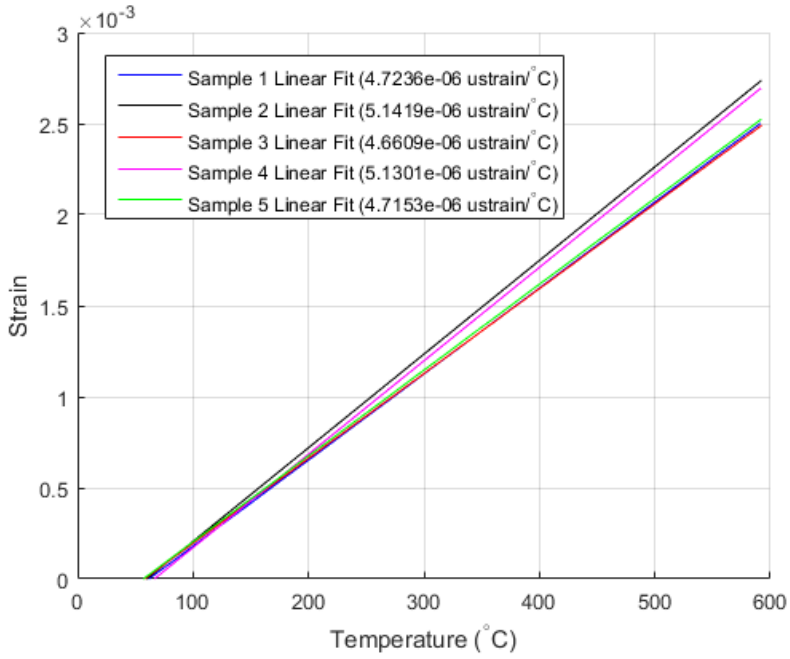

Figure 5.26: Linear fit of data for all TMA samples

Table 5.7: Summary of TMA regression analysis and calculated expansion coefficients

Sample No.	**Thermal expansion Coeff. ($10^{-6}K^{-1}$)**	R^2
1	4.72	0.97
2	5.14	0.97
3	4.66	0.97
4	5.13	0.96
5	4.71	0.97
Mean	**4.872**	
Standard Deviation	**0.241**	

and is a phenomenon that has been observed by a number of other authors [169, 178].

Mechanical testing was carried out using three-point bending and Weibull analysis. The characteristic strength of samples was significantly lower than values reported in literature and showed a high degree of scatter. The low characteristic strength was determined to be due to porosity visible on the surface of samples which will reduce the effective sample cross section and are likely to act as origin points for fracture.

Residual stress was inhered in EBM samples via nano indentation. A significant variation in hardness and modulus was found in samples, increasing towards centre of the top surface. Residual stress was caused by the TGM and the variation in mechanical properties matched experimental and modelled distributions. The magnitude of the residual stress however was not measured.

Thermal properties of expansion and conductivity were measured through TMA and LFA respectively. No significant difference was found between the measured properties and those reported in the literature.

Further work needs to be carried out to improve EBM tungsten for use in plasma facing components. The interactions between EBM parameters, geometry, residual stress, mechanical properties and porosity are not yet fully understood. Though significant progress has been made.

6 COMPONENTS AND APPLICATIONS

A number of additional components were manufactured as concepts, highlighting potential applications for ALM tungsten such as in MCF. These will briefly be covered in this section. No functional, mechanical or structural testing was carried out on these samples they simply serve as demonstrations of concept.

6.1 SLM LANGMUIR PROBE

A langmuir probe is a measurement device used to evaluate the electron temperature, electron density, and electric potential of a plasma [185]. Langmuir probes are used in magnetic confinement fusion (MCF) experiments such as the JET to monitor the properties of the plasma. Due to the extreme conditions on the plasma facing wall during magnetic confinement fusion, tungsten is the material of choice for this application. Current langmuir probes are machined, this is however very costly due to the relatively fine and complex geometry.

A set of langmuir probes were manufactured via SLM in order to assess the feasibility of using additive manufacturing for this application. Samples are currently in testing at CCFE. Images of these components are provided in Figures 6.1.

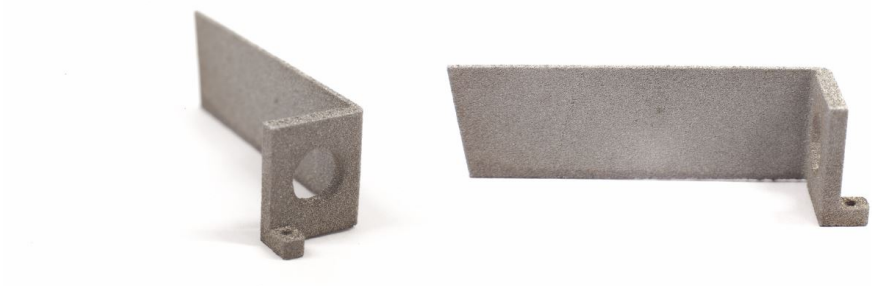

Figure 6.1: A tungsten Langmuir Probe manufactured via SLM. 25mm in length

6.2 EBM TUNGSTEN MONOBLOCK

A monoblock is a plasma facing component which acts as armour against neutron irradiation and provides the means for which coolant can be pumped near the reactors' inside surface. Typical monoblock designs consist of a simple cubic block of tungsten out of which a through-hole is machined. ALM has the potential to provide the ability to optimise this geometry for its application.

A set of tungsten monoblocks were included with the specimens manufactured in Chapter 7 via EBM, in order to assess the feasibility of using additive manufacturing for this application. These samples are currently in testing at CCFE as part of another project. The samples will be tested under a high rate of heat flux whilst containing a high pressure coolant mimicking the MCF environment.

Images of these components are provided in Figure 6.2

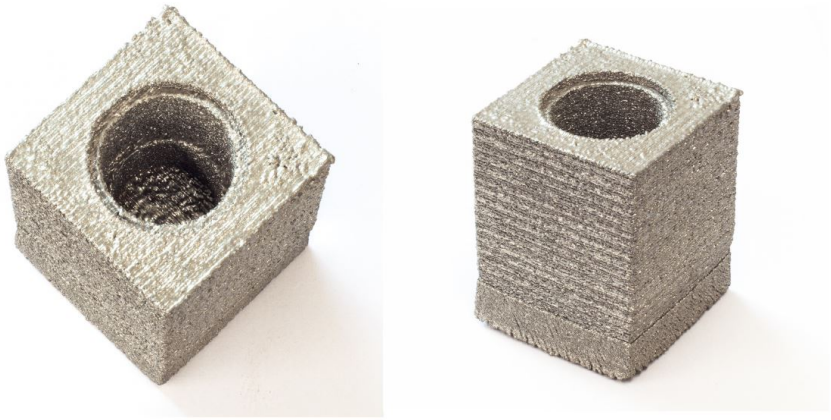

Figure 6.2: A tungsten mono-block manufactured via EBM. External dimensions of 20mm x 20mm x 25mm

6.3 EBM TUNGSTEN LATTICE

The final component which was manufactured was a tungsten lattice structure, produced via EBM (Figure 6.3). This structure was designed as a demonstration piece to show the capability of this technology. The structure was based on a repeating diamond lattice pattern and was created using Rhino3D and the plug-in grasshopper. The lattice geometry was modified into a cylindrical shape such that the 80mm diameter build area was maximised.

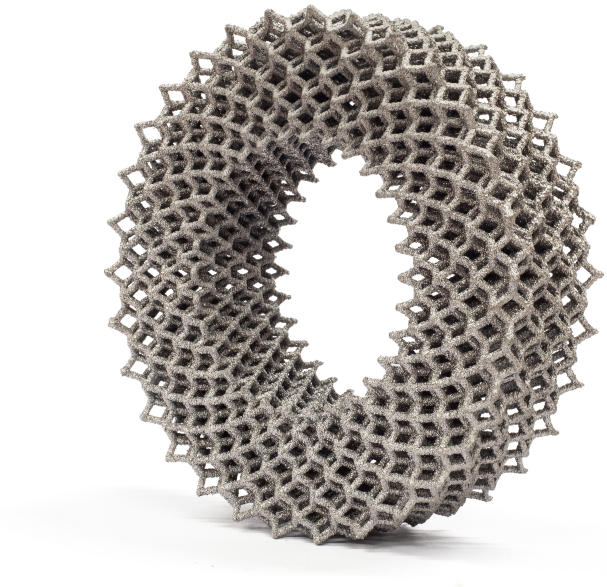

Figure 6.3: A tungsten lattice structure manufactured via EBM. External diameter: 80mm. Thickness 20mm

7 CONCLUSIONS

7.1 SELECTIVE LASER MELTING

The testing that was completed using SLM of tungsten produced the following conclusions:

- Defect free tungsten parts could not be produced via SLM.
- At 200W all samples had high porosity. Increasing energy density via reducing point distance and melting each layer twice was found to reduce porosity within the range tested.
- Beam power was found to be the significant factor effecting the measure of porosity in samples. The lowest porosity was achieved at 400*W*.
- As porosity in tungsten samples produced via SLM was reduced the number of cracks was found to increase, this was also therefore a function of beam power.

7.2 ELECTRON BEAM MELTING

The testing that was completed using EBM of tungsten produced the following conclusions:

- Optimal EBM process parameters were identified for the production of low defect tungsten samples. Speed, current, and hatch spacing were all found to have a significant effect on the occurrence of porosity.
- Geometric accuracy of EBM tungsten samples was found to be significantly reduced at increased line energy (low speed and high current). Optimal parameters for accurate geometry are found to be in conflict with those found for minimising defects.
- Mechanical properties were tested via three point bending; the characteristic strength of the material was found to be poor when compared to rolled tungsten. This was be attributed to large pores in samples and residual stress imparted during the process. The build direction also had a significant effect on material strength.
- Residual stresses were inferred in samples via nano-indentation. Stress is believed to vary as a function of position within the sample in all directions. With the highest residual stress occurred in the centre of the top surface of the sample
- Measured thermal properties were in agreement with values reported in the literature.

7.3 SUMMARY

Overall significant progress has been made towards the direction of creating usable tungsten components via ALM.

A full systematic investigation of process parameters on defects in SLM tungsten has been carried out. This provided a new insight into the dominant parameters which result in the formation of lack of fusion defects and cracks.

For the first time EBM of tungsten has been reported. Specifically, EBM was able to produce low porosity, crack free parts. EBM appears to the preferable manufacturing process due to its combination of a vacuum environment, high build temperatures and high beam power. Nonetheless, mechanical properties and geometric accuracy require further improvements before ALM can be used to manufacture tungsten for structural applications. For Applications where mechanical properties are non critical and complex geometry is required, such as in x-ray collimation, the ALM techniques outlined here could provide a viable processing route.

8 FURTHER WORK

8.1 SELECTIVE LASER MELTING

- Further work needs to be carried out on SLM of tungsten in order produce crack free parts. This may include an investigation of adding an external heat source. A heated environment is likely to reduce residual stresses and raise material above the DBTT.
- The presence and effect of oxygen and other impurities should be investigated. It is likely that impurities in powder or induced during processing lead to embrittlement through the weakening of grain boundaries. This embrittlement may be a source of the cracks observed in this study.
- The investigation of the effect of alloying elements such as rhenium could provide an insight into the effects of ductility on SLM processing tungsten.
- Mechanical, microstructural and thermal evaluation should be carried out in order to establish the properties of parts produced by SLM, as well as their constraints.

8.2 ELECTRON BEAM MELTING

- Alternative substrate materials to steel should be assessed allowing for direct melting of tungsten onto the surface.
- An investigation into the effect of sample geometry on dimensional accuracy and porosity should be carried out. Including validation of the second order model produced in Chapter 4. If a significant effect is found the Arcam geometry dependent melt functions should be developed in order to ensure properties are independent of sample size.
- The effect of process parameters on residual stress should be probed with the aim of reducing them. Post process heat treatment should also be investigated in order to stress relieve parts.
- Following model validation and stress relief mechanical properties could be re evaluated. Improving strength and decreasing the degree of scatter in mechanical properties is essential if ALM is to be viewed as a viable processing route for tungsten.

This study has not investigated the surface finish of parts. Surface roughness is particularly important for brittle materials as an uneven surfaces can serve as initiation points for fracture. For structural applications the surface roughness will need to be reduced through post processing. The effect of process parameters for both SLM and EBM and surface roughness should also be evaluated.

APPENDIX

A ARCAM MELT FUNCTIONS

A.1 CURRENT COMPENSATION FUNCTION

The length of hatch lines will affect the size of the melt pool. Longer hatch lines result in a greater time period between successive hatch lines, this results in an increased dissipation of heat. To account for this heat dissipation the Arcam control system uses a function known as current compensation to increase the beam current I for longer hatch lines. The current compensation function is outlined in Equation 24 where L_0 and b are a reference line length and constant respectively and assume the default values of 45mm and 0.9. L is the length of the hatch line being processed and I_0 is the current used at the reference length L_0. Figure A.1 plots the current compensation function over a range of scan lengths for default L_0 and b values.

$$\frac{I}{I_0} = \left(1 + \frac{b(L - L_0)}{L_0}\right) \tag{24}$$

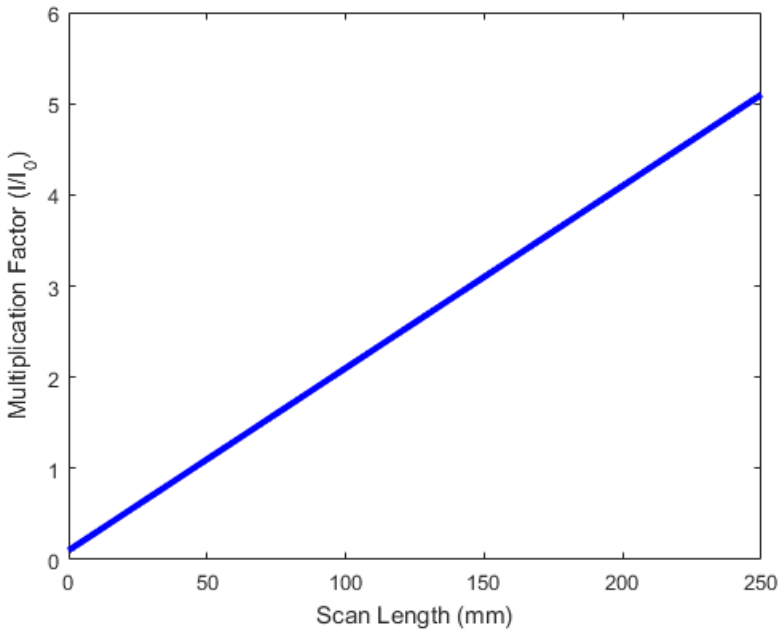

Figure A.1: Current compensation function at default b and L_0 values

A.2 SPEED FUNCTION

Following selection of an appropriate current, using current compensation, the speed at which the beam will travel is determined. The speed function

aims to maintain the size of the melt pool for any given current. This relationship has been determined by Arcam using finite element modelling (FEM) and is stored in the EBM control software. Plotted in Figure A.2 are the relationships between beam speed and current for a range of speed functions. Typically the EBM system will operate at a speed function of 36.

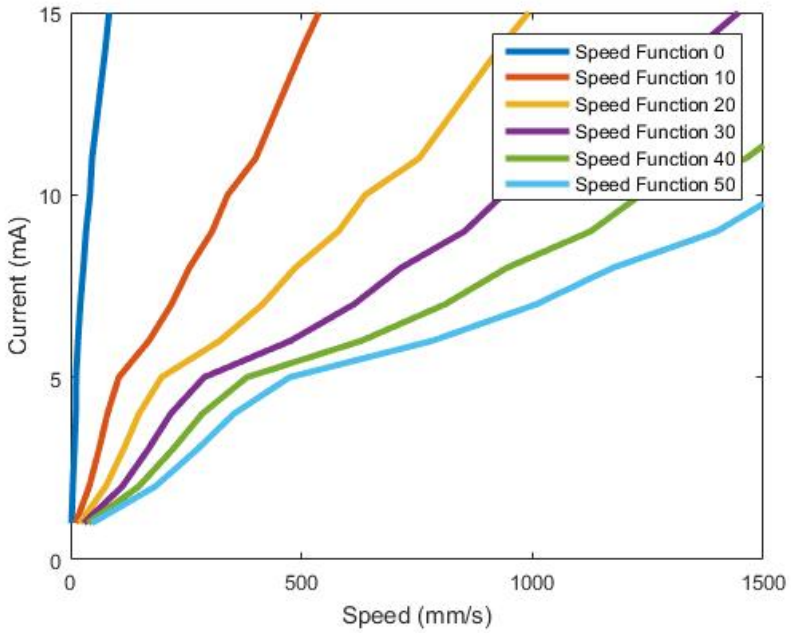

Figure A.2: Beam speed and current for a range of speed functions

A.3 THICKNESS FUNCTION

The thickness function is used to account for the difference in thermal conductivity between melted parts and sintered powder. To account for the reduced conductivity when melting overhanging surfaces the beam speed is increased in these areas. The beam speed is increased as opposed to varying the current as the electron gun cannot achieve the rapid variation in current that is required. The thickness function is stated in Equation 25 where v_0 is the initial velocity, as selected by the speed function, v is the velocity selected by the thickness function, and Z is the distance from the overhanging surface in the build direction. The profile of the thickness function can be controlled via three factors; the speed factor S_f the thickness factor Z_f and the exponent factor E_f. An additional parameter Z_{max} defines the maximum thickness to which the function is applied, after this thickness $v/v_0 = 1$. The thickness function is plotted in Figure A.3 at the default values used for processing Ti6AL4V.

$$\frac{V}{V_0} = 1 + \frac{S_f}{\exp(E_f(Z - Z_f)) + 1} \tag{25}$$

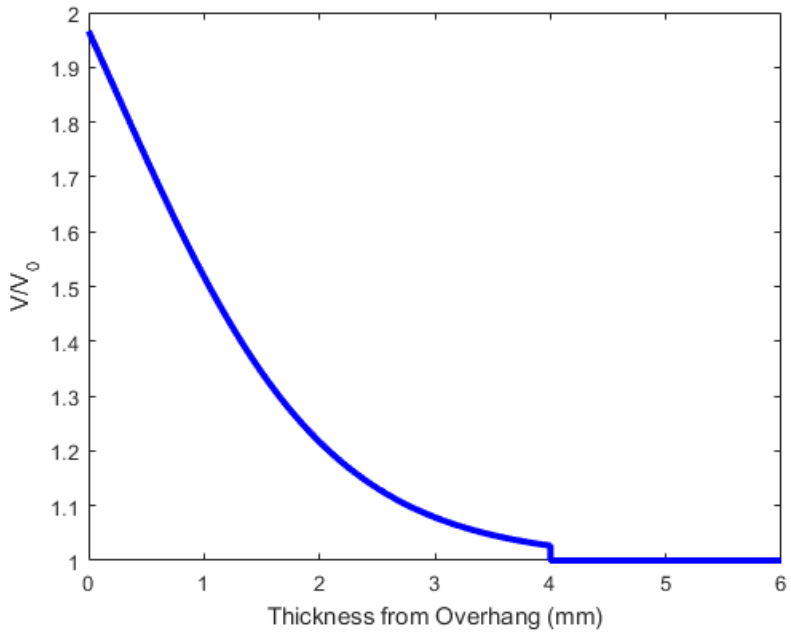

Figure A.3: Thickness function at default S_f, E_f, Z_f and Z_{max} values

A.4 TURNING POINT FUNCTION

At the end of each line, during melting, the beam turns 180 degrees to travel in the opposite direction. At these turning points there is little time for the heat to dissipate before the beam changes direction for the next pass. This results in a higher temperatures, causing variation in the melt pool size, at the edge of parts. To account for this short time period between subsequent passes the turning point function (Equation 26) is used. This function increases the beam speed V based on the distance d from the turning point. C_e, E_F, and E_{F2} are constants which can be used to alter the profile of the function.

$$V = V_0 \left(1 + C_e \exp\left(-(V_0(E_f d - E_{F2} V_0)^2\right)\right) \tag{26}$$

A.5 SOFTWARE

A number of software packages are required for the Arcam EBM system. Magics (Materialise) was used to generate simple geometries in the STL format, for more complex structures Rhino 3D (McNeel) along with the Grasshopper plugin was used. Magics was also used to check for and fix any errors within the STL file, add supports to overhanging surfaces and position parts within the build volume.

Build assembler (Arcam AB) is used to generate Arcam Build Files (ABF) from STL files. All parts and supports for a build are loaded into build assembler and given a layer thickness. The software will create two dimensional slices of each part to generate an ABF file. An ABF file does not contain any information about the process parameters, with the exception of layer thickness.

The user interface on the machine runs EBM control (Arcam AB). EBM control directly monitors and controls all aspects of the EBM hardware. EBM control reads ABF files and allows the user to apply the desired process parameters and functions to each part and layer before starting a build.

B TUNGSTEN AM PARAMETERS FROM LITERATURE TABULATED

Authour	**SLM system**	T (°C)	r_b (μm)	P (W)	Pdens W/m^2	P_{Max}	Pd (μm)	Et (/mus)	h (/mum)	l (μm)	v (mm/s)	Ed (J/mm^3)	Ed at $\rho_{(Max)}$ (J/mm^3)	$\rho_{(Max)}$ (/%)
Wang et al (2017)	Renishaw AM 400	Room	75	400	7.10E+04	400	70-150	200	75-150	30	350-750	119-508	380	96
Ivekovic et al (2017)	3d Systems Pro X DMP 320	Room	NS	500	NS	500	NA	NA	NS	NS	NS	>200	200	97.1
Ivekovic et al (2017)	In House System	400	90	300	3.70E+04	300	NA	NA	NS	NS	NS	475	475	94.4
Tan et al (2018)	EOS M290	50	100	200-370		370	NA	NA	NS	20	100-400	NS	NS	98.5
Sidambe et al	Renishaw AM125	Room	43	150, 200	8.10E+07	200	20,29	200	11.5	30	100-145	299-578	NS	
Enneti et al (2017)	Concept laser Mlab	Room	110	90	7.40E+03	90	NA	NA	15,30	30	200-1400	71-1000	1000	75
Nie et al	In House System	Room	NS	50		50	NA	NA	200	15	25	666	NS	
Deprez et al (2012)	NS	NS	NS	100-200	NS	200	NS	NS	NS	NS	NS	NS	NS	89.92
Zang et al (2012)	HRPM-IV	Room	NS	180-200	NS	200	NA	NA	50, 100	50, 70	25- 300	122-3200	NS	82
Zhou et al (2015)	Renishaw AM250	Room	75	200	3.60E+04	200	50	200 - 400	90	NS	125 - 250	NS	NS	82.9

C IMAGE J AND MATLAB SCRIPTS FOR POROSITY MEASUREMENT

C.1 IMAGE J

```
input = getDirectory("Input directory");
output = getDirectory("Output directory");

suffix = ".tif";

processFolder(input);

function processFolder(input) {
    list = getFileList(input);
    for (i = 0; i < list.length; i++) {
        if(File.isDirectory(input + list[i]))   //if it's a
            directory, go to subfolder
            processFolder("" + input + list[i]);
        if(endsWith(list[i], suffix))   //if it's a tiff image,
            process it
            processFile(input, output, list[i]);
        //if it's neither a tiff nor a directory, do nothing
    }
}

function processFile(input, output, file) {
    //here, you put the real processing
    print("Processing: " + input + file);

    open(input + file);  //open image

                run("8-bit");
                run("Set Scale...", "distance=1");
                setAutoThreshold("Default");
                //run("Threshold...");
                setAutoThreshold("Default dark");
                setOption("BlackBackground", false);
                run("Convert to Mask");

                run("Analyze Particles...", "size=100-Infinity
                    display exclude summarize");

    saveAs("results", output + file + "_results.csv");

           if (isOpen("Results")) {
       selectWindow("Results");
       run("Close");
   }
```

```
   run("Close");

    print("Saved to: " + output);
}
```

C.2 MATLAB

```
clc
close all
clear

numfiles = 31;


sampleResultsLocation = char('C:\Users\Jon\Google Drive\PhD\
    Results\SLM DOE\400W Clemex\SampleArea\');
porosityResultsLocation = char('C:\Users\Jon\Google Drive\PhD\
    Results\SLM DOE\400W Clemex\PorosityArea\');

% Import Sample area data and sum areas
totalSampleArea=[];

for k = 1:numfiles

    if k == 18 || k == 26
       totalSampleArea=[totalSampleArea 0];
    else

    filename = sprintf('Sample%d.tif_results.csv',k);
    file = strcat(sampleResultsLocation,filename);

    sampleResults = csvread(file,1,2);
    area = sum(sampleResults(:,1));
    totalSampleArea=[totalSampleArea area];

    end
end


% Import Porosity Measurments and Sum

totalPorosityArea = [];

for k = 1:numfiles

    if k == 18 || k == 26 || k == 28
       totalPorosityArea=[totalPorosityArea 0];
    else

    filename = sprintf('Sample%d.tif_results.csv',k);
```

```
    file = strcat(porosityResultsLocation,filename);

    sampleResults = csvread(file,1,2);
    area = sum(sampleResults(:,1));
    totalPorosityArea=[totalPorosityArea area];

    end
end

Density = 100-(totalPorosityArea./totalSampleArea*100);

% Import porosity measurments and seperate by aspect ratio

crackArea = [];
poreArea = [];
cracks=[];
pores=[];

for k = 1:numfiles

    cracks=[];
    pores=[];


  if k == 18 || k == 26

        crackArea = [crackArea 0];
        poreArea = [poreArea 0];

    else

        filename = sprintf('Sample%d.tif_results.csv',k);
        file = strcat(porosityResultsLocation,filename);

        sampleResults = csvread(file,1,2);

                for n = 1:length(sampleResults)

                    if sampleResults(n,12)<0.1

                    cracks = [cracks sampleResults(n,1)];

                    else

                    pores = [pores sampleResults(n,1)];

                    end
                end
      crackAreaSum = sum(cracks);
      crackArea = [crackArea crackAreaSum];

      poreAreaSum = sum(pores);
      poreArea = [poreArea poreAreaSum];
```

```
    end
end

scatter(poreArea, crackArea)
set(gca,'xscale','log')
set(gca,'yscale','log')

porosity = poreArea./totalSampleArea.*100
porosityTran = transpose(porosity)
crackisity  = crackArea./totalSampleArea.*100
crackisityTran = transpose(crackisity)

porosity./crackisity

totalPorosity = crackisityTran + porosityTran
```

D | POROSITY MEASUREMENTS FOR DOE CARRIED OUT ON THE SLM125

Table D.1: A summary of porosity measurements for the DOE carried out on the 200W SLM125 system - continued overleaf

Std Order	t_e	h	Pd	l	Remelt	Porosity (%)	Pore area (μm^2)
1	200	30	30	20	Yes	13.61	4.57E+03
2	600	30	30	20	Yes	9.30	3.76E+03
3	200	70	30	20	Yes	12.00	2.69E+03
4	600	70	30	20	Yes	6.46	2.08E+03
5	200	30	70	20	Yes	18.33	4.41E+03
6	600	30	70	20	Yes	7.49	2.55E+03
7	200	70	70	20	Yes	20.81	4.09E+03
8	600	70	70	20	Yes	8.73	2.52E+03
9	200	30	30	40	Yes		
10	600	30	30	40	Yes		
11	200	70	30	40	Yes		
12	600	70	30	40	Yes		
13	200	30	70	40	Yes		
14	600	30	70	40	Yes		
15	200	70	70	40	Yes		
16	600	70	70	40	Yes		
17	200	50	50	30	Yes	14.89	2.90E+03
18	600	50	50	30	Yes	12.50	3.97E+03
19	400	30	50	30	Yes	8.44	2.05E+03
20	400	70	50	30	Yes	9.51	1.80E+03
21	400	50	30	30	Yes	7.34	1.81E+03
22	400	50	70	30	Yes	10.87	2.21E+03
23	400	50	50	20	Yes	8.62	2.33E+03
24	400	50	50	40	Yes		
25	400	50	50	30	Yes	9.22	2.07E+03
26	400	50	50	30	Yes	8.40	1.81E+03
27	400	50	50	30	Yes	11.22	2.11E+03
28	400	50	50	30	Yes	13.41	3.67E+03
29	400	50	50	30	Yes	10.47	2.20E+03
30	400	50	50	30	Yes	8.90	1.56E+03

Std Order	t_e	h	Pd	l	Remelt	Porosity (%)	Pore area (μm^2)
31	400	50	50	30	Yes	13.07	1.92E+03
32	200	30	30	20	No	10.85	2.76E+03
33	600	30	30	20	No	6.88	2.02E+03
34	200	70	30	20	No	12.26	2.13E+03
35	600	70	30	20	No	8.01	1.91E+03
36	200	30	70	20	No	16.39	2.77E+03
37	600	30	70	20	No	10.49	2.63E+03
38	200	70	70	20	No	17.48	2.27E+03
39	600	70	70	20	No	13.79	2.41E+03
40	200	30	30	40	No		
41	600	30	30	40	No		
42	200	70	30	40	No		
43	600	70	30	40	No		
44	200	30	70	40	No		
45	600	30	70	40	No		
46	200	70	70	40	No		
47	600	70	70	40	No		
48	200	50	50	30	No	12.81	1.98E+03
49	600	50	50	30	No	11.36	3.53E+03
50	400	30	50	30	No	11.39	2.34E+03
51	400	70	50	30	No	14.30	2.81E+03
52	400	50	30	30	No	8.41	1.35E+03
53	400	50	70	30	No	14.52	3.34E+03
54	400	50	50	20	No	12.42	2.57E+03
55	400	50	50	40	No		
56	400	50	50	30	No	12.46	2.59E+03
57	400	50	50	30	No	16.45	3.86E+03
58	400	50	50	30	No	14.25	3.35E+03
59	400	50	50	30	No	12.19	2.69E+03
60	400	50	50	30	No	9.12	1.90E+03
61	400	50	50	30	No	13.42	2.93E+03
62	400	50	50	30	No	11.96	2.58E+03
					Mean	11.70	2.63E+03
					s	3.21	7.80E+02

Table D.2: A summary of the ANOVA investigating the effect of SLM125 process parameters on the size and percentage of porosity

	Porosity (%)		**Mean pore area (μm)**	
Source	P-Value	Coef.	P-Value	Coef.
Model	<0.001		0.013	
Constant		11.457		2470
Linear	0.039		0.072	
t_e	0.338	-0.960	0.039	655
h	0.320	0.997	0.857	55
Pd	0.021	2.410	0.058	597
l	0.826	0.240	0.791	-90
Remelt	0.022	-0.938	0.104	-199
Square	0.266		0.127	
t_e*t_e	0.060	1.779	0.021	678
h*h	0.826	-0.200	0.551	-167
Pd*Pd	0.370	-0.825	0.398	-237
2-Way Interaction	0.151		0.011	
t_e*h	0.948	-0.032	0.598	80
t_e*Pd	0.078	-0.902	0.673	-64
t_e*l	0.056	2.200	0.006	1017
t_e*Remelt	0.082	-0.796	0.117	-218
h*Pd	0.213	0.628	0.193	201
h*l	0.583	0.610	0.256	390
h*Remelt	0.290	-0.475	0.254	-157
Pd*l	0.804	0.280	0.158	489
Pd*Remelt	0.330	-0.436	0.385	-119
l*Remelt	0.219	-0.759	0.003	-617

E DEFECT MEASUREMENTS FOR DOE CARRIED OUT ON THE AM400

Table E.1: A summary of porosity measurements for the DOE carried out on the 400W AM400 system

Std Order	Q (W)	h (μm)	Pd (μm)	t_e (μs)	l (μm))	**Porosity (%)**	**Crack (%)**	**Total defect (%)**
1	200	30	30	100	30	24.03	1.62E-02	24.05
2	400	30	30	100	30	1.64	7.54E-01	2.39
3	200	70	30	100	30	14.83	1.40E-02	14.84
4	400	70	30	100	30	0.23	5.84E-01	0.82
5	200	30	70	100	30	20.48	2.00E-04	20.48
6	400	30	70	100	30	1.03	1.08E-01	1.13
7	200	70	70	100	30	17.49	5.90E-03	17.50
8	400	70	70	100	30	2.89	4.12E-02	2.93
9	200	30	30	600	30	10.31	1.33E-02	10.33
10	400	30	30	600	30	1.00	8.51E-02	1.09
11	200	70	30	600	30	17.17	2.92E-02	17.20
12	400	70	30	600	30	3.33	4.13E-01	3.74
13	200	30	70	600	30	24.91	7.10E-03	24.92
14	400	30	70	600	30	-	-	
15	200	70	70	600	30	8.16	9.30E-03	8.17
16	400	70	70	600	30	0.52	2.57E-01	0.78
17	200	50	50	350	30	15.66	2.62E-02	15.69
18	400	50	50	350	30	1.04	4.02E-01	1.44
19	300	30	50	350	30	1.35	3.86E-01	1.73
20	300	70	50	350	30	3.99	1.29E-01	4.12
21	300	50	30	350	30	1.80	3.63E-01	2.16
22	300	50	70	350	30	1.35	1.66E-01	1.51
23	300	50	50	100	30	0.99	7.12E-02	1.06
24	300	50	50	600	30	0.71	4.69E-01	1.17
25	300	50	50	350	30	6.32	5.25E-01	6.84
26	300	50	50	350	30	1.37	1.60E-01	1.53
27	300	50	50	350	30	-	-	
28	300	50	50	350	30	0.89	2.12E-01	1.10
29	300	50	50	350	30	1.09	7.53E-02	1.17
30	300	50	50	350	30	2.95	2.82E-01	3.23
31	300	50	50	350	30	2.83	1.38E-01	2.97
					Mean	6.56	1.98E-01	6.76
					s	7.83	2.06E-01	7.72

Table E.2: A summary of the ANOVA investigating the effect of AM400 process parameters on area percentage of porosity and cracks

	Porosity area (%)		**Crack area (%)**	
Source	p-Value	Coef.	p-Value	Coef.
Model	<0.001		0.173	
Blocks	0.336		0.690	
Constant		2.05E+00		2.54E-01
Linear	<0.001		0.013	
Q	<0.001	-7.67E+00	0.004	1.44E-01
h	0.258	-1.08E+00	0.956	2.40E-03
Pd	0.733	3.18E-01	0.053	-8.93E-02
t_e	0.400	-7.92E-01	0.754	-1.35E-02
Square	0.003		0.719	
Q*Q	0.009	6.82E+00	0.554	-6.30E-02
h*h	0.616	1.15E+00	0.855	-1.90E-02
Pd*Pd	0.983	5.00E-02	0.904	-1.30E-02
t_e*t_e	0.766	-6.80E-01	0.948	-7.00E-03
2-Way Interaction	0.475		0.304	
Q*h	0.178	1.38E+00	0.728	1.60E-02
Q*Pd	0.839	-2.02E-01	0.091	-8.19E-02
Q*t_e	0.254	1.16E+00	0.359	-4.28E-02
h*Pd	0.240	-1.20E+00	0.955	-2.60E-03
h*t_e	0.928	9.00E-02	0.306	4.79E-02
Pd*t_e	0.808	2.42E-01	0.181	6.35E-02

F

POROSITY AND GEOMETRY MEASUREMENTS FOR RESPONSE SURFACE DOE CARRIED OUT ON THE ARCAM S12

Table F.1: Summary of tungsten sample porosity measurements for RSM design. Carried out on Arcam S12 EBM system

Sample	v (mm/s)	I (mA)	Hatch (mm)	Speed Function	Porosity (%)
1	140	7	0.30	6.02	1.29
2	140	7	0.20	6.02	0.12
3	140	5	0.25	13.84	5.85
4	180	7	0.25	8.05	2.88
5	140	9	0.25	3.90	0.02
6	140	7	0.25	6.02	0.25
7	100	7	0.25	4.00	0.55
8	140	7	0.25	6.02	0.12
9	180	5	0.30	18.16	11.43
10	100	5	0.20	9.51	2.19
11	140	7	0.25	6.02	0.10
12	140	7	0.25	6.02	0.43
13	180	9	0.20	5.36	0.11
14	100	9	0.30	2.43	0.04
15	180	9	0.30	5.36	0.38
16	180	5	0.20	18.16	8.51
17	140	7	0.25	6.02	1.06
18	100	5	0.30	9.51	6.01
19	140	7	0.25	6.02	0.74
20	100	9	0.20	2.43	0.04

Table F.2: Results of ANOVA and regression analysis for the porosity response

	P-Value	Regres Coeff	Coeff
Model	<0.001		
Constant		6.91	0.570
Blocks	0.852		0.023
Linear	<0.001		
Speed(mm/s)	<0.001	0.0044	1.448
Current(mA)	<0.001	-4.77	-3.331
Hatch(mm)	<0.001	90.5	0.818
Square	<0.001		
Speed(mm/s)*Speed(mm/s)	0.009	0.000596	0.954
Current(mA)*Current(mA)	<0.001	0.5436	2.174
Hatch(mm)*Hatch(mm)	0.849	-22	-0.056
2-Way Interaction	<0.001		
Speed(mm/s)*Current(mA)	<0.001	-0.01770	-1.416
Speed(mm/s)*Hatch(mm)	0.623	-0.0452	-0.090
Current(mA)*Hatch(mm)	0.001	-8.09	-0.809
Lack-of-Fit	0.22		

Table F.3: The maximum offset from the input CAD geometry for all samples for Response surface DOE carried out on the ARCAM S12

Sample	v (mm/s)	I (mA)	Hatch(mm)	Porosity (%)	Max Offset µm
1	140	7	0.3	1.29	356
2	140	7	0.2	0.12	368
3	140	5	0.25	5.85	337
4	180	7	0.25	2.88	375
5	140	9	0.25	0.02	749
6	140	7	0.25	0.25	561
7	100	7	0.25	0.55	485
8	140	7	0.25	0.12	410
9	180	5	0.3	11.43	363
10	100	5	0.2	2.19	405
11	140	7	0.25	0.1	330
12	140	7	0.25	0.43	339
13	180	9	0.2	0.11	384
14	100	9	0.3	0.04	648
15	180	9	0.3	0.38	558
16	180	5	0.2	8.51	426
17	140	7	0.25	1.06	514
18	100	5	0.3	6.01	313
19	140	7	0.25	0.74	403
20	100	9	0.2	0.04	1067

Table F.4: Results of ANOVA and regression analysis for the geometry response

Term	Coef	p-Value
Constant	413	<0.001
Blocks		
1	-75	0.012
2	61	0.032
Speed(mm/s)	-81	0.006
Current(mA)	156	<0.001
Hatch(mm)	-41	0.096
Speed(mm/s).Speed(mm/s)	22	0.624
Current(mA).Current(mA)	135	0.013
Hatch(mm).Hatch(mm)	-47	0.303
Speed(mm/s).Current(mA)	-106	0.003
Speed(mm/s).Hatch(mm)	78	0.013
Current(mA).Hatch(mm)	-11	0.658

G | THREE POINT BEND RESULTS

Table G.1: Three-point bend test results for samples in Batch A

No.	Width (mm)	Thickness (mm)	Force (N)	Nom fracture stress (MPa)
1	2.442	1.922	115.1	382.8
2	2.379	1.928	94.8	321.6
3	2.424	1.927	118.1	393.6
4	2.403	1.923	92.4	311.9
5	2.395	1.923	118.5	401.4
6	2.429	1.917	86.4	290.4
7	2.401	1.94	107.9	358.2
8	2.383	1.905	76.8	266.4
9	2.434	1.932	85.5	282.3
10	2.429	1.921	95.4	319.3
11	2.429	1.928	117.3	389.7
12	2.44	1.913	99.8	335.3
13	2.421	1.924	110.4	369.6
14	2.429	1.919	101.7	341.1
15	2.437	1.919	79.5	265.8
16	2.434	1.912	72.82	245.5
17	2.392	1.897	98.5	343.3
18	2.392	1.914	58.1	198.9
19	2.417	1.934	101.3	336.2
20	2.396	1.915	86.7	296.0
21	2.437	1.913	94.2	316.9
22	2.401	1.899	114.9	398.1
23	2.423	1.92	83.4	280.1
24	2.426	1.923	92.7	310.0
25	2.385	1.904	111.9	388.3
26	2.385	1.923	102.9	350.0
27	2.389	1.926	88.4	299.3
28	2.437	1.918	70.8	236.9
29	2.378	1.907	83	287.9
30	2.394	1.924	85.1	288.1
31	2.39	1.927	78.2	264.3
			Mean	**318.4**
			Std dev	**52.0**

Table G.2: Three-point bend test results for samples in Batch B

No.	Width (mm)	Thickness (mm)	Force (N)	Nom fracture stress (MPa)
1	2.412	1.931	90.56	302.1
2	2.418	1.924	62.46	209.3
3	2.428	1.933	69.96	231.3
4	2.411	1.941	123.80	408.9
5	2.389	1.946	87.90	291.5
6	2.426	1.919	75.47	253.4
7	2.406	1.916	50.59	171.8
8	2.407	1.923	15.08	50.8
9	2.397	1.92	70.33	238.8
10	2.418	1.917	67.83	229.0
11	2.425	1.925	96.15	321.0
12	2.401	1.913	83.03	283.5
13	2.424	1.939	85.68	282.0
14	2.402	1.928	65.02	218.5
15	2.433	1.953	68.48	221.4
16	2.425	1.933	63.64	210.7
17	2.408	1.925	66.40	223.2
18	2.411	1.938	67.22	222.7
19	2.419	1.952	74.41	242.2
20	2.399	1.93	92.50	310.5
21	2.426	1.919	75.39	253.2
22	2.393	1.928	57.37	193.5
23	2.404	1.904	92.97	320.0
24	2.412	1.913	94.10	319.8
25	2.418	1.931	99.83	332.2
26	2.431	1.929	83.29	276.2
27	2.412	1.908	101.20	345.8
28	2.437	1.929	105.10	347.7
29	2.43	1.952	60.18	195.0
30	2.417	1.922	101.80	342.0
31	2.399	1.922	97.36	329.6
32	2.422	1.929	82.83	275.7
33	2.419	1.919	100.40	338.1
34	2.402	1.906	77.31	265.8
35	2.412	1.916	71.24	241.4
36	2.42	1.925	80.92	270.7
37	2.413	1.946	98.03	321.8
38	2.415	1.911	77.77	264.5
39	2.411	1.899	91.61	316.1
40	2.405	1.925	82.91	279.1
			Mean	**268.8**
			Std dev	**63.3**

H | NANOINDANTATION RESULTS

Table H.1: Summary of linear regression analysis on the effect of indent location on Young's Modulus

Load	Modulus in Z Centre (X = 0)				Modulus in Z Edge (X = 4)				Modulus in X Centre (Z = 0)				Modulus in Y Centre (X = 0)			
	m	c	R^2	α	m	c	R^2	α	m	c	R^2	α	m	c	R^2	α
4.98E+02	1.28	337	-0.01	0.519	1.60	327	0.00	0.373	1.92	330	-0.03	0.729	0.49	311	-0.04	0.896
6.62E+02	2.68	348	0.03	0.120	0.82	337	-0.02	0.605	-2.15	350	-0.03	0.595	-0.56	323	-0.04	0.873
8.92E+02	4.66	349	0.12	0.010	0.28	328	-0.02	0.829	-10.30	370	0.14	0.031	2.03	317	-0.02	0.550
1.16E+03	5.17	347	0.16	0.004	3.96	331	0.24	<0.001	-9.88	377	0.18	0.017	-0.33	328	-0.04	0.928
1.45E+03	3.75	348	0.09	0.023	2.88	324	0.13	0.009	-8.85	363	0.20	0.011	-4.55	334	0.04	0.153
1.79E+03	4.58	346	0.21	0.001	4.52	330	0.34	<0.001	-7.45	360	0.19	0.014	-1.98	327	-0.02	0.441
2.15E+03	3.80	354	0.17	0.003	4.39	326	0.25	<0.001	-10.75	368	0.32	0.001	-1.72	328	-0.02	0.525
2.55E+03	5.02	348	0.31	<0.001	4.95	321	0.40	<0.001	-6.90	360	0.16	0.022	-2.94	329	0.01	0.270
2.98E+03	3.30	343	0.19	0.002	4.11	319	0.26	<0.001	-3.95	352	0.03	0.201	-2.72	329	0.02	0.232
3.45E+03	5.07	343	0.28	<0.001	4.61	317	0.36	<0.001	-9.18	363	0.32	0.001	-7.44	332	0.39	0.000
3.95E+03	4.06	344	0.34	<0.001	4.45	315	0.31	<0.001	-8.07	354	0.34	0.001	-4.76	327	0.13	0.037
4.49E+03	3.91	343	0.31	<0.001	4.83	310	0.51	<0.001	-9.60	355	0.49	<0.001	-6.77	328	0.36	0.001
5.06E+03	3.57	341	0.31	<0.001	4.28	305	0.29	<0.001	-8.46	352	0.39	<0.001	-9.00	330	0.50	<0.001
5.66E+03	3.44	336	0.23	<0.001	5.54	304	0.57	<0.001	-11.50	353	0.52	<0.001	-8.87	324	0.49	<0.001
6.30E+03	3.78	335	0.42	<0.001	4.81	303	0.56	<0.001	-9.66	350	0.58	<0.001	-8.90	324	0.72	<0.001
6.97E+03	5.15	330	0.45	<0.001	5.05	299	0.53	<0.001	-13.37	354	0.68	<0.001	-10.22	320	0.73	<0.001
7.68E+03	4.26	330	0.50	<0.001	4.93	293	0.66	<0.001	-9.50	342	0.59	<0.001	-10.01	317	0.75	<0.001
8.42E+03	4.48	325	0.53	<0.001	5.51	289	0.60	<0.001	-8.36	336	0.48	<0.001	-11.03	313	0.68	<0.001
9.19E+03	5.59	324	0.69	<0.001	4.94	287	0.57	<0.001	-9.80	333	0.66	<0.001	-10.10	312	0.76	<0.001
1.00E+04	5.48	325	0.71	<0.001	5.58	285	0.78	<0.001	-11.54	340	0.80	<0.001	-11.23	311	0.83	<0.001

Table H.2: Summary of linear regression analysis on the effect of indent location on Hardness

Load	Hardness in Z Centre (X = 0)				Hardness in Z Edge (X = 4)				Hardness in X Centre (Z = 0)				Hardness in Y Centre (X = 0)			
	m	c	R^2	α	m	c	R^2	α	m	c	R^2	α	m	c	R^2	α
4.98E+02	1.46E-01	9.20	0.31	<0.001	5.73E-02	8.37	0.08	0.030	-2.48E-01	9.25	0.38	<0.001	7.97E-02	7.91	0.00	0.333
6.62E+02	1.57E-01	9.03	0.32	<0.001	5.48E-02	8.24	0.07	0.050	-1.50E-01	8.85	0.15	0.024	7.61E-02	7.90	0.01	0.252
8.92E+02	1.61E-01	8.78	0.36	<0.001	5.82E-02	8.05	0.14	0.007	-9.62E-02	8.47	0.05	0.128	3.58E-02	7.85	-0.02	0.523
1.16E+03	1.64E-01	8.55	0.37	<0.001	6.38E-02	7.79	0.20	0.001	-9.18E-02	8.20	0.08	0.088	3.44E-02	7.67	-0.02	0.443
1.45E+03	1.63E-01	8.35	0.43	<0.001	6.96E-02	7.74	0.28	<0.001	-7.09E-02	8.07	0.07	0.101	3.60E-02	7.60	0.00	0.358
1.79E+03	1.59E-01	8.25	0.47	<0.001	7.14E-02	7.64	0.24	<0.001	-6.20E-02	7.93	0.05	0.127	2.22E-02	7.59	-0.02	0.523
2.15E+03	1.61E-01	8.14	0.49	<0.001	7.69E-02	7.59	0.33	<0.001	-5.01E-02	7.84	0.03	0.185	1.22E-03	7.59	-0.04	0.969
2.55E+03	1.57E-01	8.09	0.47	<0.001	7.96E-02	7.52	0.37	<0.001	-5.56E-02	7.77	0.05	0.138	-1.89E-02	7.61	-0.02	0.506
2.98E+03	1.59E-01	8.03	0.50	<0.001	7.95E-02	7.46	0.33	<0.001	-4.53E-02	7.66	0.02	0.218	-2.99E-02	7.58	0.01	0.259
3.45E+03	1.56E-01	7.95	0.51	<0.001	7.94E-02	7.38	0.37	<0.001	-2.96E-02	7.56	-0.01	0.385	-2.73E-02	7.57	0.01	0.297
3.95E+03	1.58E-01	7.87	0.50	<0.001	8.45E-02	7.33	0.39	<0.001	-2.13E-02	7.51	-0.02	0.491	-5.09E-02	7.58	0.11	0.048
4.49E+03	1.57E-01	7.82	0.53	<0.001	8.34E-02	7.28	0.37	<0.001	-2.07E-02	7.47	-0.02	0.520	-5.51E-02	7.58	0.14	0.031
5.06E+03	1.57E-01	7.77	0.54	<0.001	8.46E-02	7.24	0.40	<0.001	-2.44E-02	7.42	-0.02	0.482	-5.55E-02	7.55	0.14	0.031
5.66E+03	1.57E-01	7.73	0.55	<0.001	8.12E-02	7.20	0.37	<0.001	-1.19E-02	7.37	-0.03	0.695	-6.23E-02	7.56	0.20	0.012
6.30E+03	1.53E-01	7.68	0.56	<0.001	8.56E-02	7.17	0.41	<0.001	-1.29E-02	7.32	-0.03	0.658	-7.25E-02	7.55	0.27	0.003
6.97E+03	1.48E-01	7.65	0.55	<0.001	8.27E-02	7.13	0.42	<0.001	-5.23E-03	7.26	-0.04	0.860	-6.73E-02	7.54	0.22	0.008
7.68E+03	1.49E-01	7.60	0.59	<0.001	8.09E-02	7.11	0.40	<0.001	-1.74E-02	7.25	-0.03	0.563	-7.48E-02	7.53	0.27	0.003
8.42E+03	1.47E-01	7.57	0.60	<0.001	7.92E-02	7.07	0.43	<0.001	-2.03E-02	7.22	-0.02	0.470	-7.36E-02	7.51	0.27	0.003
9.19E+03	1.44E-01	7.51	0.59	<0.001	7.97E-02	7.03	0.43	<0.001	-1.31E-02	7.19	-0.03	0.654	-8.02E-02	7.49	0.32	0.001
1.00E+04	1.45E-01	7.47	0.62	<0.001	7.73E-02	7.01	0.42	<0.001	-8.52E-03	7.14	-0.04	0.750	-7.76E-02	7.46	0.29	0.002

I MATLAB GEOMETRY MEASURMENT SCRIPT

```
clear; close all
clc

numfiles = 1;
maxdist = []


for k = 1:numfiles

filename = sprintf('Sample%d.tif',k);
x=10
y=6
pixelmm = 444
X=x*pixelmm
Y=y*pixelmm

imPerfect =im2bw(imread(filename));
imagesc(imPerfect)%255==rgb2gray(imread('Sample.tif'));

Filled= imfill(imPerfect,'holes');
iPP = bwperim(Filled);
%%
[xx, yy] = meshgrid(1:size(imPerfect,2),1:size(imPerfect,1));
bw2 = bwconvhull(imPerfect);

stats = regionprops(bw2,'centroid');
xmin = stats.Centroid(1,1) - (X/2)
xmax = stats.Centroid(1,1) + (X/2)
ymin = stats.Centroid(1,2) - (Y/2)
ymax = stats.Centroid(1,2) + (Y/2)

Perfect = and(yy>ymin,and(yy<ymax,and(xx>xmin,xx<xmax)));
PC = bwperim(Perfect);

% SE = strel('rectangle',[400 100])

DistanceMap = bwdist(Perfect)-bwdist(~Perfect);
%%
compared =DistanceMap.*iPP;
figure
subplot(2,2,1)
imagesc(imPerfect)
hold on
hold off
subplot(2,2,2)
imagesc(Perfect);
```

```
subplot(2,2,3)
imagesc(compared);
bins = min(compared(:)):max(compared(:));
binneddata = histc(compared(:),bins);
subplot(2,2,4)
binneddata(bins==0)=0;
plot(bins,binneddata)

maxdist =  [maxdist max(bins)]

figure
imshow(imPerfect)
figure
imshow(Filled)
figure
hold on
spy(bw2,'b')
scatter(stats.Centroid(1,1),stats.Centroid(1,2),'filled','r')
xlabel('x position (pixels)')
ylabel('y position (pixels)')
hold off

figure
spy(Perfect,'r')
xlabel('x position (pixels)')
ylabel('y position (pixels)')

figure
hold on
spy(iPP,'b')
spy(PC,'r')
xlabel('x position (pixels)')
ylabel('y position (pixels)')



end
```

J ARCAM S12 EBM SMALL BUILD TANK

- Corrections 4.1 - Remove Chapter to appendix/experimental

J.1 INTRODUCTION

ARCAM EBM systems are designed for commercial production and therefore have build volumes to allow for manufacturing of large components. This large build volume, though useful in the commercial environment, can make research and development of new materials challenging. The costs associated with the volume of material required are often difficult to justify. The EBM process is complex and there is no guarantee that a given powder can be successfully processed, this is particularly relevant for materials with high density such as Tungsten. Spherical tungsten powder is currently priced at around £200/Kg which is comparable to Ti6Al4V powder, however at a density of $19.2g/cm^3$ compared to $4.43g/cm^3$ for the Titanium powder, the cost per unit volume is over four times higher for tungsten powder. Furthermore large volumes of powder require material specific handling and processing equipment such as a PRS, pneumatic sieve, and a clean vacuum.

Reducing the volume of material used in the EBM process can significantly reduce the costs and challenges associated with material development. To address this issue, and facilitate processing of tungsten powder, a small build tank (SBT) was developed for the Arcam S12 EBM system. The SBT consists of an assembly of components forming a cylindrical build tank with a 110mm inner diameter. Figure J.1 shows a rendered CAD image of the SBT assembly. This chapter will discuss these components which create this new experimental apparatus.

A number of general considerations were made when creating components for the SBT. Firstly, material considerations were made, specifically the thermal and mechanical requirements along with the need to use non-magnetic materials. Components and fittings located near to the build area were manufactured from stainless steels due to the high temperatures they would experience. Components which were located further away from the build area were made using aluminium as it is lower cost and easier to machine. Considerations were also made for the movement of powder during operation; glass rope seals were used where necessary and fittings between components were made to a high tolerance preventing powder leaks. The number of fittings and components were minimised and made easy to disassemble ensuring that the machine could easily be cleaned when changing between materials.

Component drawings and assembly diagrams are provided in Appendix K for the components of the SBT described in this section for clarity.

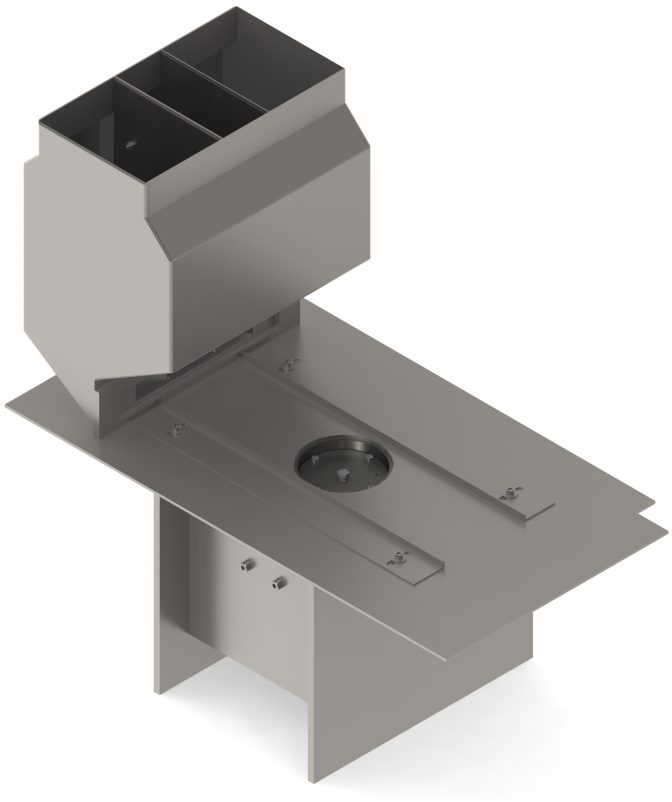

Figure J.1: Rendered CAD image of the Small Build Tank

J.2 COMPONENTS

J.2.1 Build Tank

The build tank is cylindrical and machined from one piece of stainless steel, it has an inner diameter of 110mm and a wall thickness of 10mm. There are four tapped M8 blind holes in the tank to a depth of 8mm. Through holes were drilled into the standard S12 tank and M8x 100mm bolts along with spacers are used to centre the small tank within the S12 Tank. A CAD image of the build tank sub assembly is provided in figure J.2

The build tank in the S12 provides a square build tank area of 250x250mm, with a height of 200mm giving a maximum build size of 200x200x180mm. The build tank in the SBT assembly, on the other hand provides a circular build area with a diameter 110mm and height 110mm, giving a maximum build area of 90mm in diameter and 80mm in height. This reduction in build tank size reduces the build area by a factor of 6.5.

J.2.2 Build Platform

Figure J.3 shows a diagram of the build platform assembly. The build platform assembly attaches directly to the standard S12 build platform which is in turn connected to the shaft and motor which allows for movement in the Z axis. The small build platform is circular with a diameter of 10mm pro-

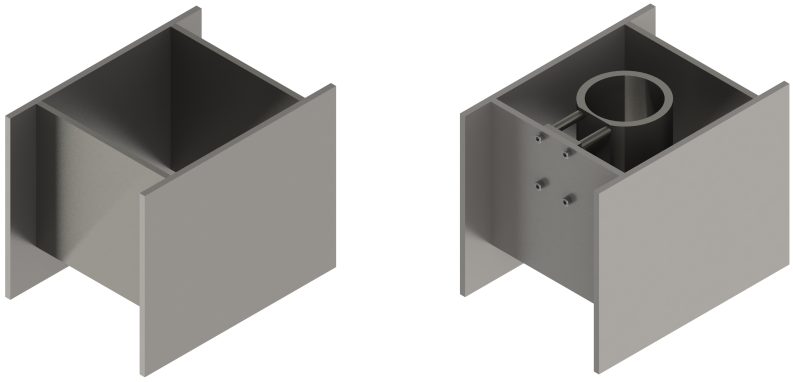

(a) Standard S12 Build Tank **(b)** Small Build Tank

Figure J.2: CAD renderings of the Standard and Small S12 Build Tanks

viding a 5mm clearance to the build tank when assembled. A 4mm by 4mm groove in the platform allows for fitting of a glass rope which acts as a seal between the platform and tank. The build platform attaches via a 20mm diameter, 120mm length steel rod, and a mounting bracket. Four through holes were drilled and tapped in the S12 build platform to a M5 sizing for attachment of the assembly. The platform has a 5mm diameter through hole located to one side providing a feed through for the thermocouple. Before operation the hole was plugged to prevent powder from leaking through it as shown in figure J.4.

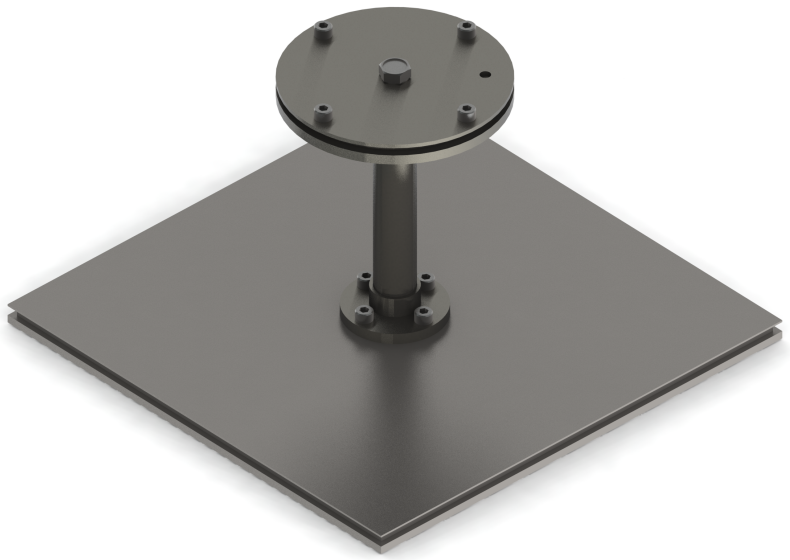

Figure J.3: Rendered CAD image of the small build platform

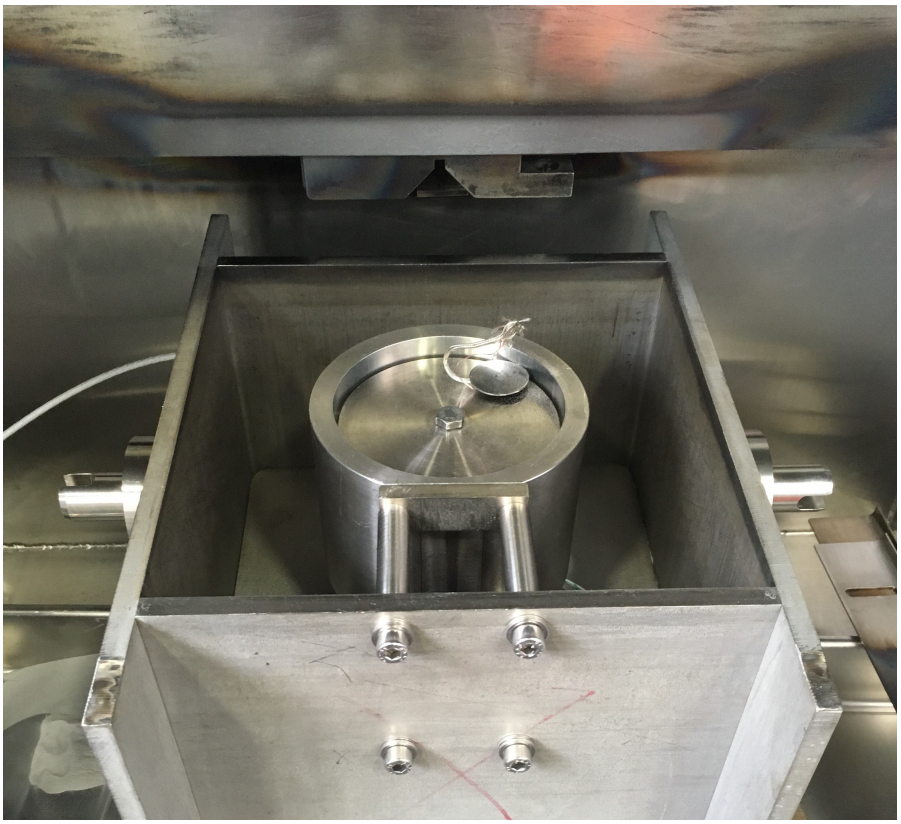

Figure J.4: Image of the SBT and build platform

J.2.3 Hoppers

Modifications were carried out to the hoppers in order to constrain the flow of powder to the area required. Figure J.5 shows CAD renderings of the unmodified and modified hopper. A set of four aluminium inserts were fabricated from 2mm thick sheets, to be fitted inside of the hopper. The insets were held in place against the internals of the hopper using a total of eight M3 bolts, nuts, and washers.

To further minimise the required powder only one hopper was used, this was located on the left hand side of the chamber.

J.2.4 Shelf and Rake

Many different terms are used to describe the flat area over which powder is spread, here it will be referred to as the shelf. A new shelf was fabricated to accommodate the SBT from 4mm thick steel.

To control the spreading of powder, lips with a height of 10mm were fabricated and attached perpendicular to the shelf, this helped to constrain powder to the area required. The rake was modified by simply reducing the number of teeth; the rake teeth which sat outside the two lips were removed. This ensured that powder was not spread outside of the build area.

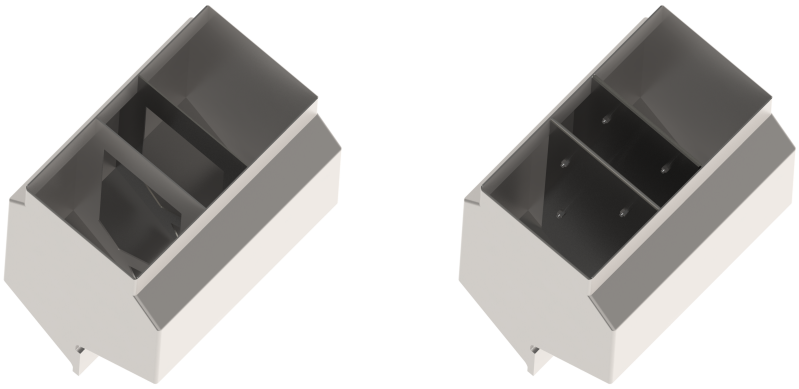

(a) Standard S12 Hopper **(b)** Small Build Tank Hopper

Figure J.5: CAD renderings of the Standard and Modified Hopper

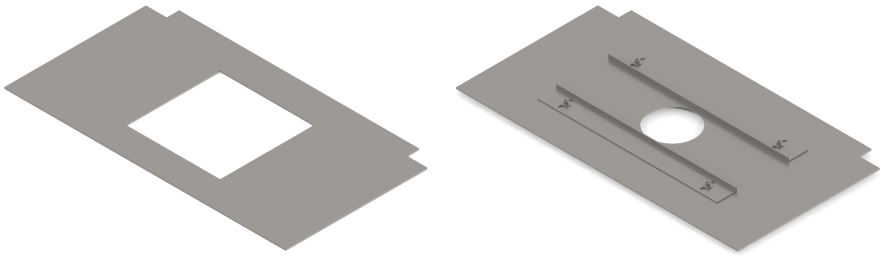

(a) Standard S12 Shelf **(b)** Small Build Tank Shelf

Figure J.6: CAD renderings of the Standard and Small S12 Build Shelves

J.2.5 Software

A number of minor adjustments were made to the EBM software to allow for the use of the SBT. Firstly the build area was restricted to a 90mm circular area ensuring that the beam would not be deflected outside of this. Secondly the raking settings were modified to allow for powder dosing from only one side of the hopper. Finally the powder sensors were disabled, fetch positions were set manually, and remained constant throughout all builds.

J.2.6 Substrates

Substrates were cut form the 210mm square stainless steel plates provided by ARCAM. The substrates were circular with a diameter of 90mm and thickness 10mm.

J.3 CHAPTER SUMMARY

The SBT was assembled to enable for materials development in the ARCAM S12 EBM system. The SBT provides a reduction in build tanks volume by a factor of 6.5. In addition to the reduction in build tank area the assembly

controls powder spreading with the addition of a reduced internal hopper volume, a lipped build shelf, and a modified rake. Set-up and operation for the SBT is identical to the normal S12 set-up procedure discussed in Chapter 2. It is important to consider how the small build volume affects the EBM process; this will be investigated in the next chapter.

K | SMALL BUILD TANK DRAWRINGS

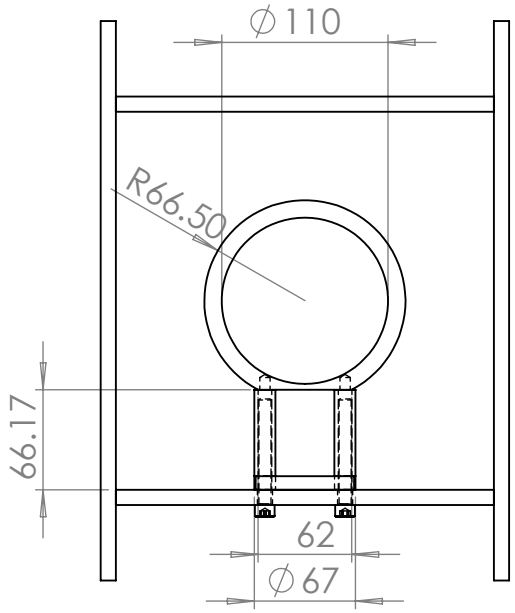

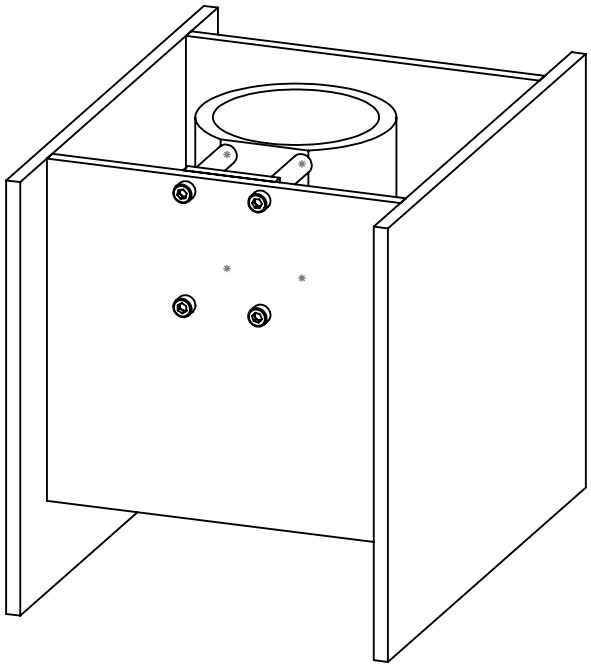

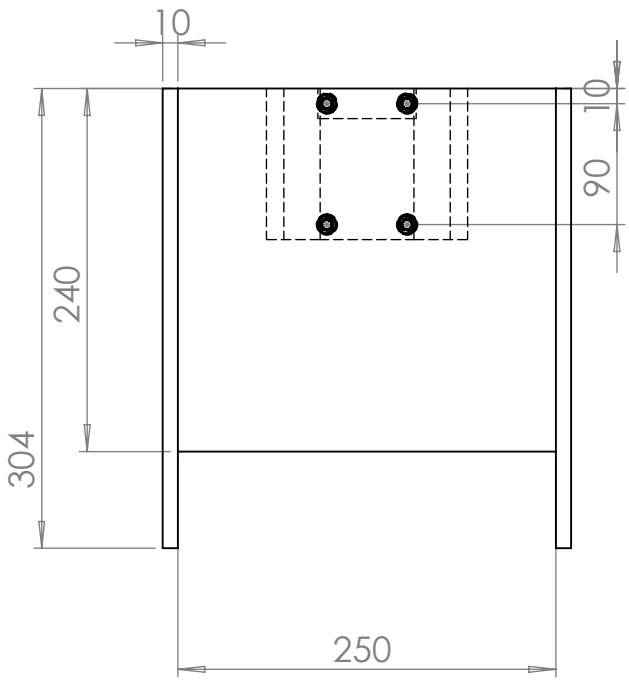

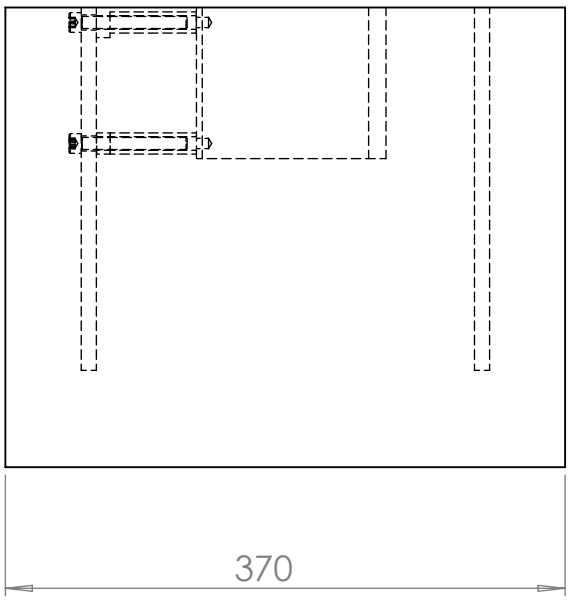

UNLESS OTHERWISE SPECIFIED: DIMENSIONS ARE IN MILLIMETERS SURFACE FINISH: TOLERANCES: LINEAR: ANGULAR:	FINISH:		DEBUR AND BREAK SHARP EDGES	DO NOT SCALE DRAWING	REVISION	
	NAME	SIGNATURE	DATE	TITLE:		
DRAWN				Small Build Tank Chamber Assembly		
CHK'D						
APPV'D						
MFG						
Q.A				MATERIAL:	DWG NO. 001	A4
				WEIGHT:	SCALE:1:5	SHEET 1 OF 1

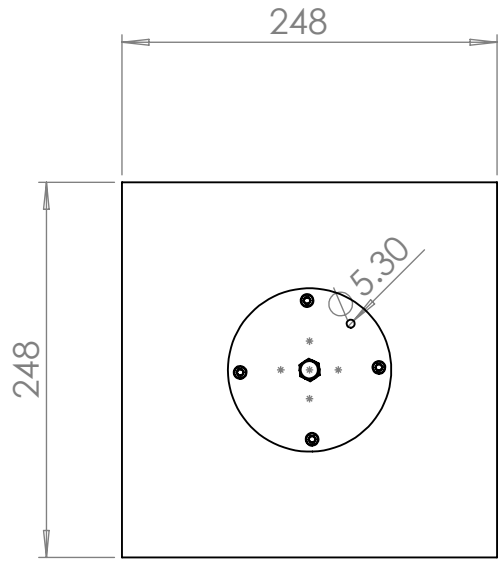

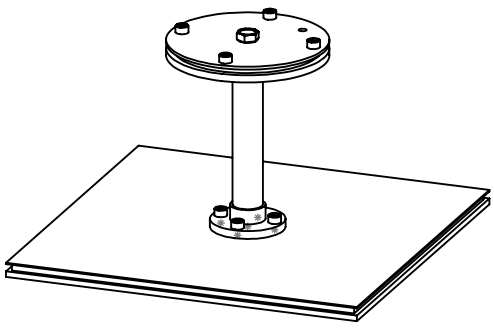

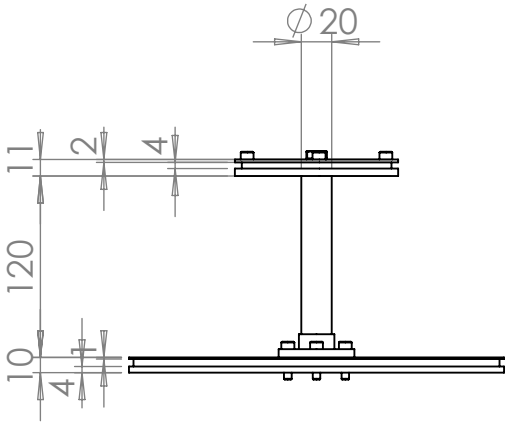

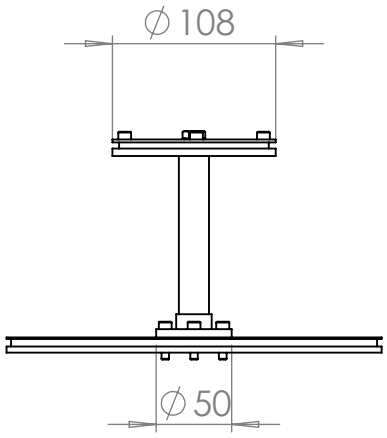

UNLESS OTHERWISE SPECIFIED: DIMENSIONS ARE IN MILLIMETERS SURFACE FINISH: TOLERANCES: LINEAR: ANGULAR:	FINISH:	DEBUR AND BREAK SHARP EDGES	DO NOT SCALE DRAWING / REVISION

	NAME	SIGNATURE	DATE
DRAWN			
CHK'D			
APPV'D			
MFG			
Q.A			

MATERIAL:

WEIGHT:

TITLE:

Small Platform Assembly

DWG NO. 002

A4

SCALE:1:5

SHEET 1 OF 1

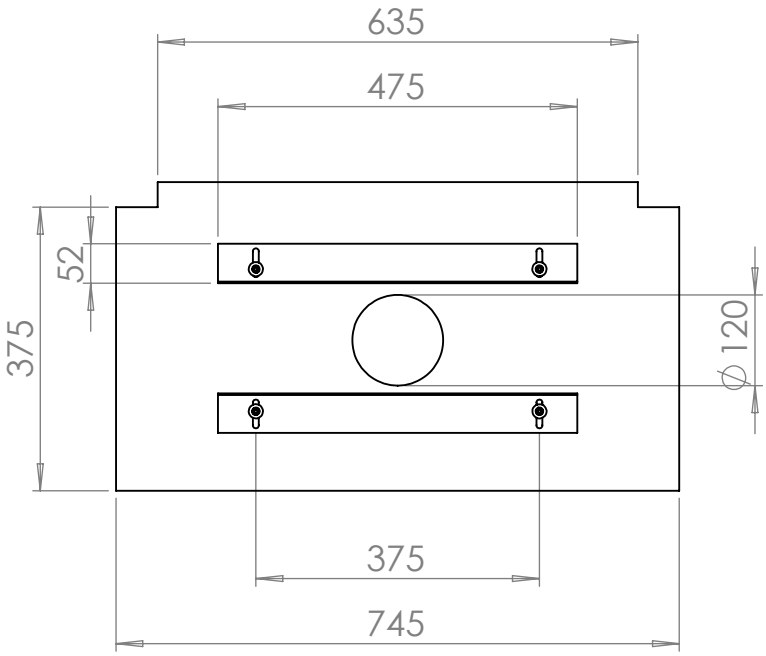

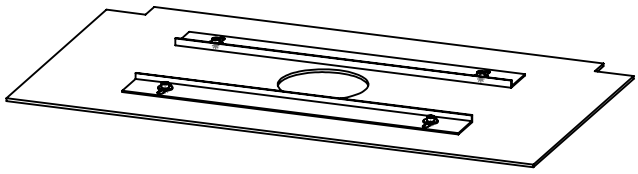

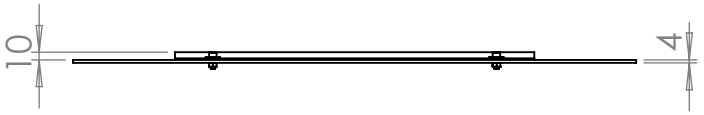

UNLESS OTHERWISE SPECIFIED: DIMENSIONS ARE IN MILLIMETERS SURFACE FINISH: TOLERANCES: LINEAR: ANGULAR:		FINISH:		DEBUR AND BREAK SHARP EDGES		
				DO NOT SCALE DRAWING		REVISION
	NAME	SIGNATURE	DATE			
DRAWN				TITLE:	Small Build Tank Shelf Assembly	
CHK'D						
APPV'D						
MFG						
Q.A				MATERIAL:	DWG NO. 003	A4
				WEIGHT:	SCALE:1:10	SHEET 1 OF 1

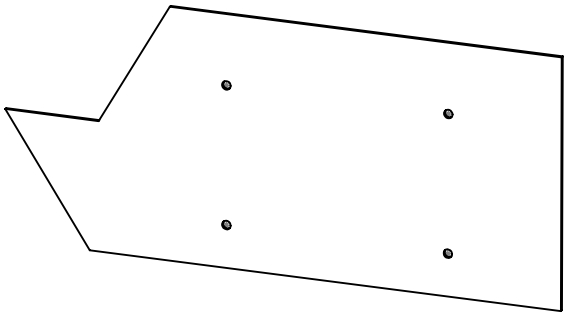

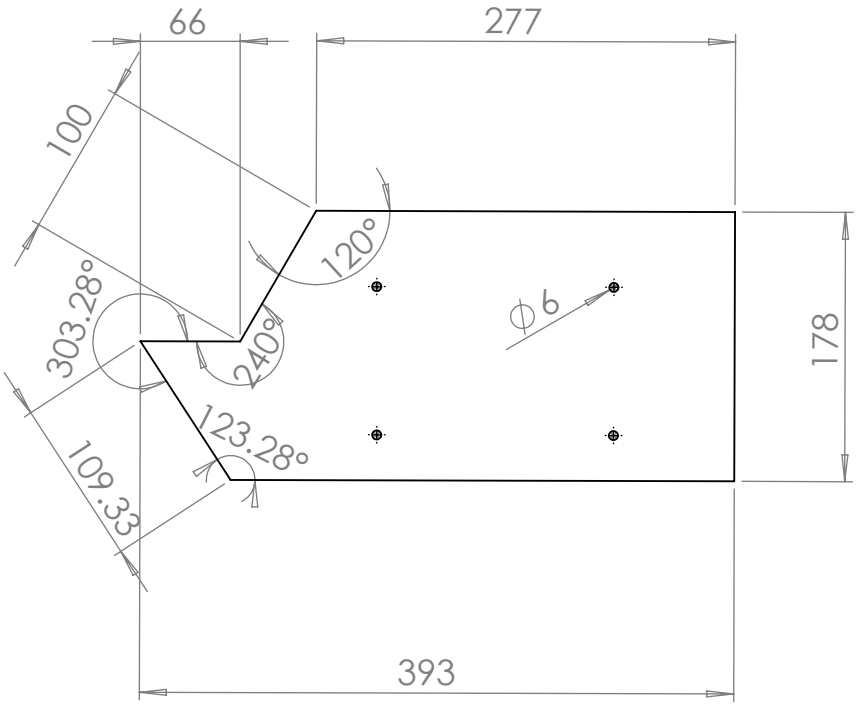

UNLESS OTHERWISE SPECIFIED: DIMENSIONS ARE IN MILLIMETERS SURFACE FINISH: TOLERANCES: LINEAR: ANGULAR:	FINISH:		DEBUR AND BREAK SHARP EDGES	DO NOT SCALE DRAWING	REVISION	
	NAME	SIGNATURE	DATE	TITLE:		
DRAWN				Hopper Divider		
CHK'D						
APPV'D						
MFG						
Q.A				MATERIAL:	DWG NO. 004	A4
				WEIGHT:	SCALE:1:5	SHEET 1 OF 1

L | 3-POINT BENDING

Figure L.2 shows a schematic free body diagram of a standard three point bend test. The test sample is supported on two points, a distance L_0 apart. A load P is applied between the supports. The test sample thickness is denoted h and width, b.

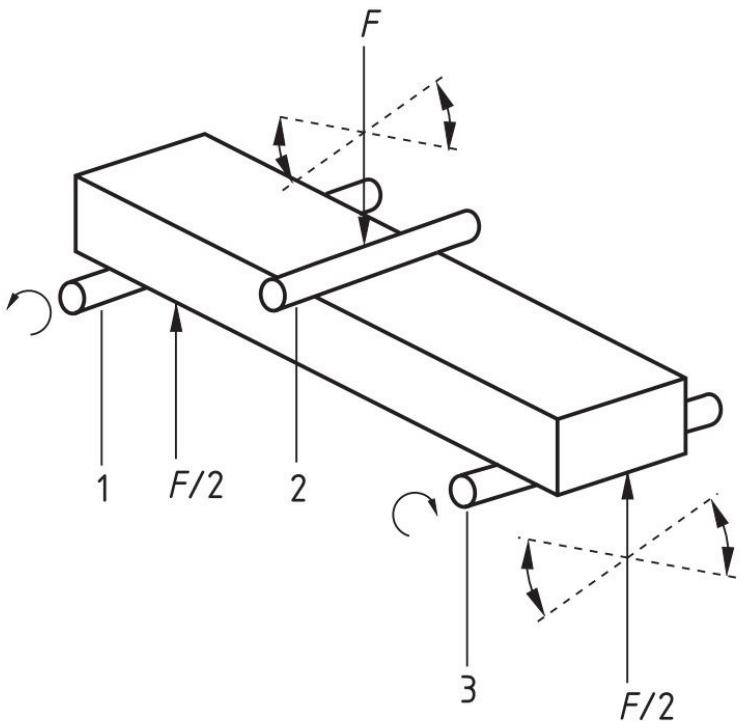

Key

1 Rolling but non articulating support roller 2 Articulating loading roller

3 Rolling and articulating support roller

Figure L.1: Degrees of freedom of the three-point bend rig [164]

The bending stress σ_x at any point within the beam can be determined using the formula in the following equation [186].

$$\sigma_x = \frac{M_z y}{I_x} \tag{27}$$

Where y is the perpendicular distance from the normal axis and I_x is the second moment of area about the neutral axis x. I_x for a square cross section is calculated as follows.

$$I_x = \iint_R y^2 \, dA = \int_{-\frac{b}{2}}^{\frac{b}{2}} \int_{-\frac{h}{2}}^{\frac{h}{2}} y^2 \, dy \, dx = \int_{-\frac{b}{2}}^{\frac{b}{2}} \frac{1}{3}\frac{h^3}{4} \, dx = \frac{bh^3}{12} \tag{28}$$

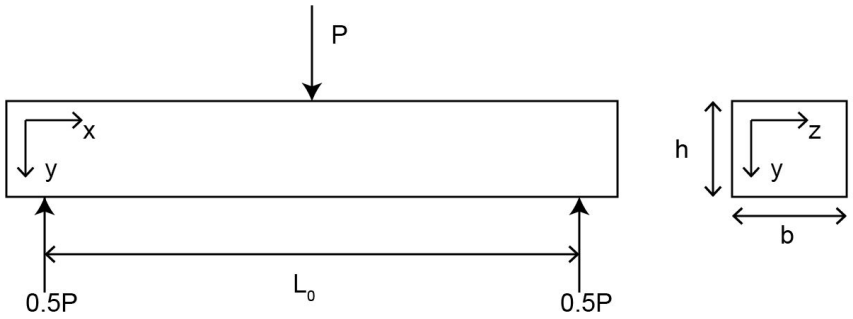

Figure L.2: Schematic free body diagram of a three-point bend test

M_z is the bending moment about the z axis, it can be shown that

$$M_z = \frac{1}{2}Px \quad \text{for } 0 \leqslant x \leqslant \frac{L_0}{2} \tag{29}$$

Substituting into Equation 27 the stress in the test sample can expressed as a function of the x and y positions.

$$\sigma(x, y) = \frac{6Pxy}{bh^3} \tag{30}$$

The maximum stress occurs on the bottom face of the sample in the centre such that:

$$\sigma_{max} = \frac{3PL_0}{2bh^2} \tag{31}$$

The displacement of the specimen δ at the point of load is given by Equation 32[186].

$$\delta = \frac{PL^3}{48EI} \tag{32}$$

Applying Hooke's Law and substituting it can be shown therefore that the maximum strain ϵ_{max} is:

$$\epsilon_{max} = \frac{6\delta h}{L^2} \tag{33}$$

L.0.1 Weibull Analysis

The Weibull distribution is a probability density function (PDF) named after Waloddi Weibull who described the function in detail in 1939 and 1951[187] [188]. The two parameter Weibull distribution has been shown to accurately represent the distribution of failures for brittle materials typically ceramics [189][190][191], it has also recently been shown that failure in tungsten samples follow this distribution [179]. The two parameter Weibull function f is given by:

$$f(t) = \frac{\beta}{\eta}\left(\frac{t}{\eta}\right)^{\beta-1} e^{-\left(\frac{t}{\eta}\right)^{\beta}} \tag{34}$$

Where η and β are known as the scale and shape parameters respectively. β is also often referred to as the Weibull modulus. The cumulative density function (CDF) F of this distribution is given by:

$$F(t) = 1 - e^{-\left(\frac{t}{\eta}\right)^{\beta}} \tag{35}$$

The function $F(t)$ describes the proportion of samples which would be expected to fail up to a given value of the condition t which in the case of static mechanical tests is the maximum stress (ϵ_{max}). The reliability function $R(t)$ which describes the chance of the surviving at or beyond at a given ϵ_{max} can be expressed as:

$$R(t) = e^{-\left(\frac{t}{\eta}\right)^{\beta}} \tag{36}$$

The failure rate function λ describes the frequency at which a material fails at a given value of t is given by:

$$\lambda(t) = \frac{f(t)}{R(t)} = \frac{\beta}{\eta}\left(\frac{t}{\eta}\right)^{\beta-1} \tag{37}$$

The effect of the shape and scale parameters

Figure L.3 plots the probability density function for a range of values of the shape parameter β. As shown β can have a significant effect on the behaviour of the distribution and at $\beta = 1$ the function reduces to an exponential distribution of the form $f(t) = \frac{1}{\eta}e^{\frac{t}{\eta}}$. Figures L.4 and L.5 plot the reliability and failure rate respectively for the same values of β. Figure L.5 shows that for values $\beta < 1$ the failure rate decreases as a function of t, where $\beta = 1$ the failure rate remains constant and for $\beta > 1$ the rate increases. The failure of brittle materials can be described by distributions of the form $\beta <$.

The parameter η can be said to describe the width of the distribution, Figure L.6 plots the PDF for a range of values of η where $\beta = 3$. As η increases the distribution is stretched and flattened, such that the area under the curve is maintained. An ideal material would have a low value of η and high values of β as this would describe a narrow distribution with a low probability of failing at small loads.

Data Analysis and Parameter estimation

Experimental failure data can be used to estimate the two parameters which define the distribution of results. Determination of the Weibull parameters can be summarised in the following steps:

- Linearise the cumulative density function (reliability) function.
- Estimate the cumulative failure for each data point.
- Plot the data in a linear form.
- Perform linear regression to find the linear equation of the line in order to asses if the results follow the distribution.
- Determine β and η using the maximum likelihood estimate.

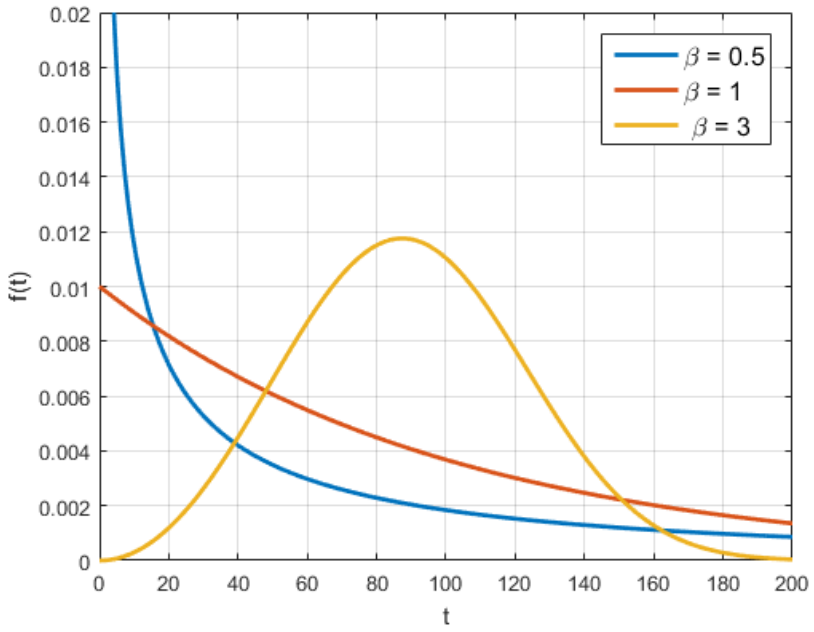

Figure L.3: The effect of β on the Weibull probability density function for $\eta = 100$

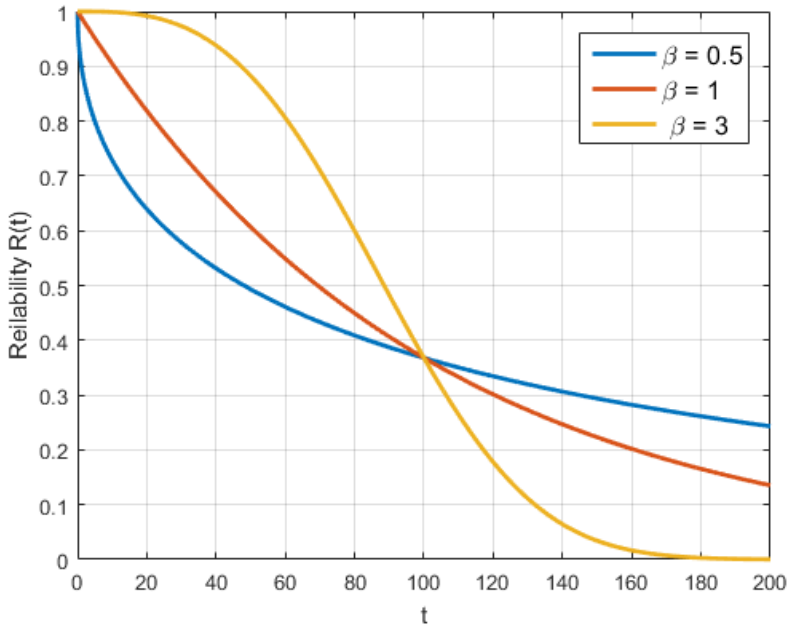

Figure L.4: The effect of β on the Weibull reliability function for $\eta = 100$

The cumulative density function (Equation L.5) can be linearised into the form $y = mx + c$ as follows:

$$F(t) = 1 - e^{-\left(\frac{t}{\eta}\right)^{\beta}}$$

$$\ln(1 - F(t)) = \ln\left(e^{-\left(\frac{t}{\eta}\right)^{\beta}}\right)$$

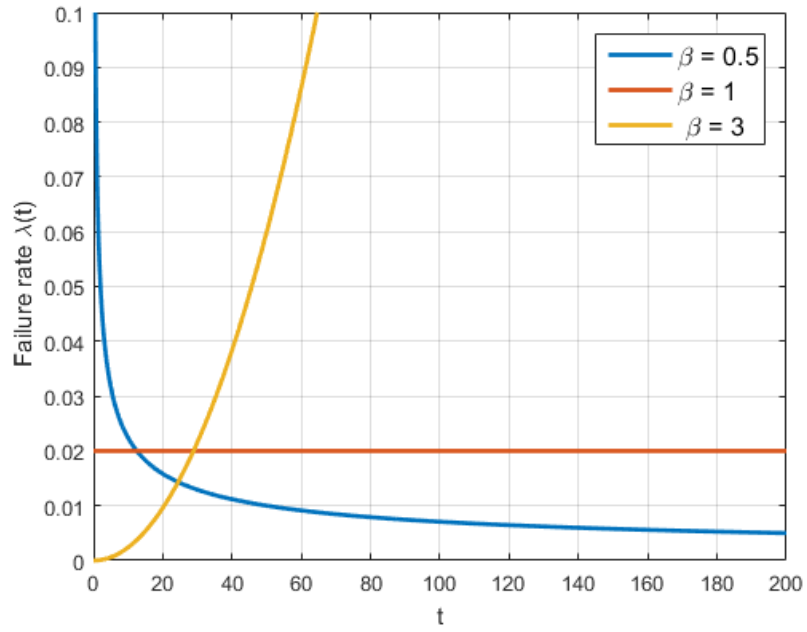

Figure L.5: The effect of β on the Weibull failure rate function for $\eta = 100$

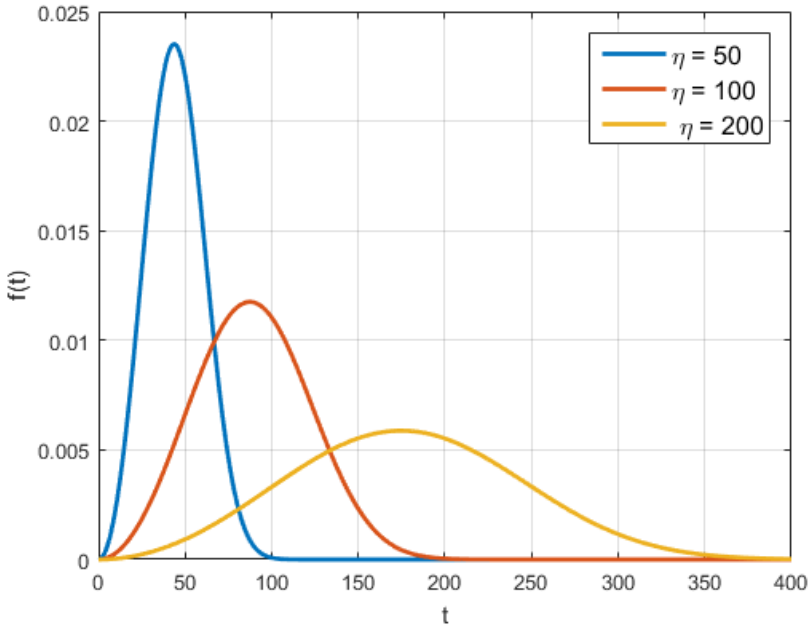

Figure L.6: The effect of η on the Weibull probability density function for $\beta = 3$

$$\ln(1 - F(t)) = -\left(\frac{t}{\eta}\right)^{\beta}$$

$$\ln(1 - F(t)) = -\left(\frac{t}{\eta}\right)^{\beta}$$

$$\ln(-\ln(1 - F(t))) = \beta\left(\ln\left(\frac{t}{\eta}\right)\right)$$

$$\ln\left(\ln\left(\frac{1}{1-F(t)}\right)\right) = \beta\ln(t) - \beta\ln(\eta)$$

Therefore in the form $y = mx + c$ we can set:

$$y = \ln\left(\ln\left(\frac{1}{1-F(t)}\right)\right) \tag{38}$$

$$x = \ln(t) \tag{39}$$

$$m = \beta \tag{40}$$

With intercept:

$$c = -\beta\ln(\eta) \tag{41}$$

In order to plot experimental data we need to estimate the CDF for test point. There are a number of statistical techniques which can be used to make this estimate but most commonly ranking methods are used[192]. To carry out all ranking methods test results are first ordered by the load at which they failed from lowest to highest. For the i-th failure at a load ti we then need to estimate the CDF. It would seem intuitive to calculate i/n however, in practice this is usually an overestimate, and as a result corrections are often used such as $(i-0.5)/n$. Here we will use what is known as an approximate median rank or Bernard's Approximation outlined in Equation 42[191].

$$F(t) \approx \frac{i-0.3}{n+0.4} \tag{42}$$

Once $F(t)$ has been estimated for each data point we can calculate our x and y data points using Equations 39 and 38 respectively. Liner regression can be used to find the best fit for the data, the fit can then be used along with Equations 38-41 in order to estimate the Weibull parameters defining the expected distribution of the failure response.

Once it has been determined that a valid Weibull distribution can be fitted to the data using linear methods the maximum likelihood method can be used to give a more accurate estimate for the Weibull parameters. The characteristic strength $sigma_0$ can be defined as the point at which $\sigma_{max} = \eta$ or $F(t) = 0.632$. The stress σ_{max} at failure for the i-th sample is denoted σfi. The likelihood function for a single critical flaw distribution is given by [164]:

$$L = \prod_{i=1}^{N}\left(\frac{\beta}{\sigma_0}\right)\left(\frac{\sigma_{fi}}{\sigma_0}\right)^{\beta-1} exp\left[-\left(\frac{\sigma_{fi}}{\sigma_0}\right)\right] \tag{43}$$

Taking logs and differentiation with respect to β and σ_0 and setting tro zero we find:

$$\frac{\sum_{i=1}^{N}\sigma_{fj}^{\beta}\ln\sigma_f j}{\sum_{i=1}^{N}\sigma_{fj}^{\beta}} - \frac{1}{N}\sum_{i=1}^{N}\ln\sigma_{fj} - \frac{1}{\beta} = 0 \tag{44}$$

and

$$\sigma_0 = \left[\left(\sum_{i=1}^{N} \sigma_{fj}^{\beta} \right) \frac{1}{N} \right]^{\frac{1}{\beta}} \tag{45}$$

Equation 44 can be solved numerically to find the estimate for β aolving Equation 45 the estimate of characteristic strength σ_0 can be found.

BIBLIOGRAPHY

[1] C W Hull. Apparatus for production of three-dimensional objects by stereolithography, 1986.

[2] Paulo Jorge Bártolo. Stereolithographic Processes. In *Stereolithography*. 2011.

[3] Neil Hopkinson, Richard J M Hague, and Phill M. Dickens. Introduction to Rapid Manufacturing. In *Rapid Manufacturing: An Industrial Revolution for the Digital Age*. 2006.

[4] Kwai S. Chan, Marie Koike, Robert L. Mason, and Toru Okabe. Fatigue life of titanium alloys fabricated by additive layer manufacturing techniques for dental implants. *Metallurgical and Materials Transactions A: Physical Metallurgy and Materials Science*, 44(2):1010–1022, 2013.

[5] N Hopkinson and P Dicknes. Analysis of rapid manufacturing,Äîusing layer manufacturing processes for production. *Proceedings of the Institution of Mechanical Engineers, Part C: Journal of Mechanical Engineering Science*, 217(1):31–39, 2003.

[6] Ben Redwood. Additive Manufacturing Technologies: An Overview, 2019.

[7] C.R.: Deckard, Joseph J.: Beaman, and James F. Darrah. Method and Apparatus for Producing Parts by Selective Sintering. *U.S. Patent 4,863,538*, page 12, 1992.

[8] William E. Frazier. Metal additive manufacturing: A review. *Journal of Materials Engineering and Performance*, 23(6):1917–1928, 2014.

[9] H. K. Rafi, N. V. Karthik, Haijun Gong, Thomas L. Starr, and Brent E. Stucker. Microstructures and mechanical properties of Ti6Al4V parts fabricated by selective laser melting and electron beam melting. *Journal of Materials Engineering and Performance*, 22(12):3872–3883, 2013.

[10] C. Y. Yap, C. K. Chua, Z. L. Dong, Z. H. Liu, D. Q. Zhang, L. E. Loh, and S. L. Sing. Review of selective laser melting: Materials and applications. *Applied Physics Reviews*, 2(4), 2015.

[11] Equipment - Aconity3d.

[12] Bugatti uses SLM Solutions' metal 3D printing to produce optimised functional components - TCT Magazine.

[13] Syed Zia Uddin, David Espalin, Jorge Mireles, Philip Morton, Cesar Terrazas, Shane Collins, Lawrence E Murr, and Ryan Wicker. Laser powder bed fusion fabrication and characterization of crack- free aluminum alloy 6061 using in-process powder bed induction heating. *Solid Freeform Fabrication Symposium*, pages 214–227, 2016.

[14] Bin Zhou, Jun Zhou, Hongxin Li, and Feng Lin. A study of the microstructures and mechanical properties of Ti6Al4V fabricated by SLM under vacuum. *Materials Science and Engineering A*, 2018.

[15] Tae Wook Na, Won Rae Kim, Seung Min Yang, Ohyung Kwon, Jong Min Park, Gun Hee Kim, Kyung Hwan Jung, Chang Woo Lee, Hyung Ki Park, and Hyung Giun Kim. Effect of laser power on oxygen and nitrogen concentration of commercially pure titanium manufactured by selective laser melting. *Materials Characterization*, 2018.

[16] PROCESSING OF TITANIUM ALUMINIDES (TIAL) WITH HIGH-TEMPERATURE SELECTIVE LASER MELTING (HT-SLM).

[17] Haider Ali, Le Ma, Hassan Ghadbeigi, and Kamran Mumtaz. In-situ residual stress reduction, martensitic decomposition and mechanical properties enhancement through high temperature powder bed preheating of Selective Laser Melted Ti6Al4V. *Materials Science and Engineering A*, 695(February):211–220, 2017.

[18] R. Mertens, B. Vrancken, N. Holmstock, Y. Kinds, J. P. Kruth, and J. Van Humbeeck. Influence of powder bed preheating on microstructure and mechanical properties of H13 tool steel SLM parts. In *Physics Procedia*, 2016.

[19] Bey Vrancken, Sam Buls, Jean-Pierre Kruth, and Jan Van Humbeeck. Preheating of Selective Laser Melted Ti6Al4V: Microstructure and Mechanical Properties. In *Proceedings of the 13th World Conference on Titanium*. 2016.

[20] Nikolay K. Tolochko, Sergei E. Mozzharov, Igor A. Yadroitsev, Tahar Laoui, Ludo Froyen, Victor I. Titov, and Michail B. Ignatiev. Balling processes during selective laser treatment of powders. *Rapid Prototyping Journal*, 10(2):78–87, 2004.

[21] J. P. Kruth, L. Froyen, J. Van Vaerenbergh, P. Mercelis, M. Rombouts, and B. Lauwers. Selective laser melting of iron-based powder. *Journal of Materials Processing Technology*, 149(1-3):616–622, 2004.

[22] Wayne E. King, Holly D. Barth, Victor M. Castillo, Gilbert F. Gallegos, John W. Gibbs, Douglas E. Hahn, Chandrika Kamath, and Alexander M. Rubenchik. Observation of keyhole-mode laser melting in laser powder-bed fusion additive manufacturing. *Journal of Materials Processing Technology*, 214(12):2915–2925, 2014.

[23] Umberto Scipioni Bertoli, Alexander J. Wolfer, Manyalibo J. Matthews, Jean Pierre R. Delplanque, and Julie M. Schoenung. On the limitations of Volumetric Energy Density as a design parameter for Selective Laser Melting. *Materials and Design*, 113:331–340, 2017.

[24] W. J. Suder and S. W. Williams. Investigation of the effects of basic laser material interaction parameters in laser welding. *Journal of Laser Applications*, 24(3):032009, 2012.

[25] Ahmed Hussein, Liang Hao, Chunze Yan, and Richard Everson. Finite element simulation of the temperature and stress fields in single layers built without-support in selective laser melting. *Materials and Design*, 52:638–647, 2013.

[26] M. Matsumoto, M. Shiomi, K. Osakada, and F. Abe. Finite element analysis of single layer forming on metallic powder bed in rapid prototyping by selective laser processing. *International Journal of Machine Tools and Manufacture*, 42(1):61–67, 2002.

[27] S. Haeri. Optimisation of blade type spreaders for powder bed preparation in Additive Manufacturing using DEM simulations. *Powder Technology*, 321:94–104, 2017.

[28] C. J. Smith, F. Derguti, E. Hernandez Nava, M. Thomas, S. Tammas-Williams, S. Gulizia, D. Fraser, and I. Todd. Dimensional accuracy of Electron Beam Melting (EBM) additive manufacture with regard to weight optimized truss structures. *Journal of Materials Processing Technology*, 229(May):128–138, 2016.

[29] Meurig Thomas, Gavin J. Baxter, and Iain Todd. Normalised model-based processing diagrams for additive layer manufacture of engineering alloys. *Acta Materialia*, 108(April):26–35, 2016.

[30] J. C. Ion, H. R. Shercliff, and M. F. Ashby. Diagrams for laser materials processing. *Acta Metallurgica Et Materialia*, 1992.

[31] T. Mukherjee, V. Manvatkar, A. De, and T. DebRoy. Dimensionless numbers in additive manufacturing. *Journal of Applied Physics*, 121(6), 2017.

[32] W. J. Suder and S. W. Williams. Investigation of the effects of basic laser material interaction parameters in laser welding. *Journal of Laser Applications*, 24(3):032009, 2012.

[33] A. Safdar, H.Z. He, Liu,ÄêYing Wei, A. Snis, and Luis E. Chavez de Paz. Effect of process parameters settings and thickness on surface roughness of EBM produced Ti,Äê6Al,Äê4V. *Rapid Prototyping Journal*, 18(5):401–408, 2012.

[34] C. Körner. Additive manufacturing of metallic components by selective electron beam melting - A review, 2016.

[35] Peter Heinl, Lenka Müller, Carolin Körner, Robert F. Singer, and Frank A. Müller. Cellular Ti-6Al-4V structures with interconnected macro porosity for bone implants fabricated by selective electron beam melting. *Acta Biomaterialia*, 2008.

[36] Nikolas Hrabe and Timothy Quinn. Effects of processing on microstructure and mechanical properties of a titanium alloy (Ti-6Al-4V) fabricated using electron beam melting (EBM), part 1: Distance from build plate and part size. *Materials Science and Engineering A*, 2013.

[37] Peter Mercelis and Jean,ÄêPierre Kruth. Residual stresses in selective laser sintering and selective laser melting. *Rapid Prototyping Journal*, 12(5):254–265, 2006.

[38] Bey Vrancken, Lore Thijs, Jean-Pierre Kruth, and Jan Van Humbeeck. Heat treatment of Ti6Al4V produced by Selective Laser Melting: Microstructure and mechanical properties. *Journal of Alloys and Compounds*, 541:177–185, 2012.

[39] S. S. Al-Bermani, M. L. Blackmore, W. Zhang, and I. Todd. The origin of microstructural diversity, texture, and mechanical properties in electron beam melted Ti-6Al-4V. *Metallurgical and Materials Transactions A: Physical Metallurgy and Materials Science*, 41(13):3422–3434, 2010.

[40] K. Kempen, B. Vrancken, L. Thijs, S. Buls, J. Van Humbeeck, and J.-P. Kruth. Lowering thermal gradients in Selective Laser melting by pre-heating the baseplate. *Solid Freeform Fabrication Proceedings*, 24, 2013.

[41] F Medina. *Reducing metal alloy powder costs for use in powder bed fusion additive manufacturing: Improving the economics for production*. PhD thesis, The University of Texas at El Paso, 2013.

[42] Clint Atwood, Michelle Gribth, Lane Harwell, Eric Schlienger, Mark Ensz, John Smugeresky, Tony Romero, Don Greene, and Daryl Reckaway. Laser Engineered Net Shaping (LENS): A Tool for Direct Fabrication of Metal Parts. *Proceedings of the International Congress on Applications of Lasers and Electro-Optics '98*, pages 1–7, 1998.

[43] Tomasz Durejko, Michał Zietala, Wojciech Polkowski, and Tomasz Czujko. Thin wall tubes with Fe3Al/SS316L graded structure obtained by using laser engineered net shaping technology. *Materials and Design*, 63:766–774, 2014.

[44] Tomasz Durejko, Michał Zietala, Magda Łazińska, Stanisław Lipiński, Wojciech Polkowski, Tomasz Czujko, and Robert A. Varin. Structure and properties of the Fe3Al-type intermetallic alloy fabricated by laser engineered net shaping (LENS). *Materials Science and Engineering A*, 650:374–381, 2016.

[45] Leijun Li. Repair of directionally solidified superalloy GTD-111 by laser-engineered net shaping. *Journal of Materials Science*, 41:7886–7893, 2006.

[46] Donghong Ding, Zengxi Pan, Dominic Cuiuri, and Huijun Li. Wire-feed additive manufacturing of metal components: technologies, developments and future interests. *International Journal of Advanced Manufacturing Technology*, 81(1-4):465–481, 2015.

[47] J.G Kaufman and Elwin Rooy. Aluminum Alloys Castings. pages 1–6, 2004.

[48] C. M. Sonsino and J. Ziese. Fatigue strength and applications of cast aluminium alloys with different degrees of porosity. *International Journal of Fatigue*, 15(2):75–84, 1993.

[49] Naoya Taniguchi, Shunsuke Fujibayashi, Mitsuru Takemoto, Kiyoyuki Sasaki, Bungo Otsuki, Takashi Nakamura, Tomiharu Matsushita, Tadashi Kokubo, and Shuichi Matsuda. Effect of pore size on bone ingrowth into porous titanium implants fabricated by additive manufacturing: An in vivo experiment. *Materials Science and Engineering C*, 59:690–701, 2016.

[50] A. Bauerei, T. Scharowsky, and C. Körner. Defect generation and propagation mechanism during additive manufacturing by selective beam melting. *Journal of Materials Processing Technology*, 214(11):2522–2528, 2014.

[51] Bi Zhang, Yongtao Li, and Qian Bai. Defect Formation Mechanisms in Selective Laser Melting: A Review. *Chinese Journal of Mechanical Engineering (English Edition)*, 30(3):515–527, 2017.

[52] Haijun Gong, Khalid Rafi, Hengfeng Gu, G. D. Janaki Ram, Thomas Starr, and Brent Stucker. Influence of defects on mechanical properties of Ti-6Al-4V components produced by selective laser melting and electron beam melting. *Materials and Design*, 86:545–554, 2015.

[53] Wayne E. King, Holly D. Barth, Victor M. Castillo, Gilbert F. Gallegos, John W. Gibbs, Douglas E. Hahn, Chandrika Kamath, and Alexander M. Rubenchik. Observation of keyhole-mode laser melting in laser powder-bed fusion additive manufacturing. *Journal of Materials Processing Technology*, 214(12):2915–2925, 2014.

[54] Haijun Gong, Khalid Rafi, Hengfeng Gu, Thomas Starr, and Brent Stucker. Analysis of defect generation in Ti-6Al-4V parts made using powder bed fusion additive manufacturing processes. *Additive Manufacturing*, 1:87–98, 2014.

[55] Xin Zhou, Xihe Liu, Dandan Zhang, Zhijian Shen, and Wei Liu. Balling phenomena in selective laser melted tungsten. *Journal of Materials Processing Technology*, 222:33–42, 2015.

[56] Ruidi Li, Jinhui Liu, Yusheng Shi, Li Wang, and Wei Jiang. Balling behavior of stainless steel and nickel powder during selective laser melting process. *International Journal of Advanced Manufacturing Technology*, 59(9-12):1025–1035, 2012.

[57] Peter Mercelis and Jean,ÄêPierre Kruth. Residual stresses in selective laser sintering and selective laser melting. *Rapid Prototyping Journal*, 12(5):254–265, 2006.

[58] P. Prabhakar, W.J. Sames, R. Dehoff, and S.S. Babu. Computational modeling of residual stress formation during the electron beam melting process for Inconel 718. *Additive Manufacturing*, 7:83–91, 2015.

[59] Bey Vrancken, Lore Thijs, Jean Pierre Kruth, and Jan Van Humbeeck. Heat treatment of Ti6Al4V produced by Selective Laser Melting: Microstructure and mechanical properties. *Journal of Alloys and Compounds*, 541(0):177–185, 2012.

[60] Devon Hagedorn-Hansen, Martin Bezuidenhout, Dimitar Dimitrov, and G A Oosthuizen. The Effects of Selective Laser Melting Scan Strategies on Deviation of Hybrid Parts. *South African Journal of Industrial Engineering*, 28, 2017.

[61] Erik (University of Technology Vienna) Lassner and Wolf-Dieter (University of Technology Vienna) Schubert. *Tungsten: properties, chemistry, technology of the element, alloys, and chemical compounds*. 2000.

[62] Raj P Singh Gaur. Modern hydrometallurgical production methods for tungsten. *Jom*, 58(9):45–49, 2006.

[63] Y. C. Ho, R. W. Powell, and P. E Liley. Thermal Conductivity of the Elements: A Comprehensive Review. *Journal of Physical and Chemical Reference Data*, 3(1972):810, 1974.

[64] K. Farrell, A.C. Schaffhauser, and J.O. Stiegler. Recrystallization, grain growth and the ductile-brittle transition in tungsten sheet. *Journal of the Less Common Metals*, 13(2):141–155, 1967.

[65] Nasa Technical Note. CO CM CO RECRYSTALLIZATION BEHAVIOR OF ELECTRON-BEAM-MELTED TUNGSTEN COMPARED WITH ARC-MELTED TUNGSTEN by William D . Klopp and Walter R . Witzke Cleveland , Ohio. (January), 1966.

[66] A. Alfonso, D. Juul Jensen, G. N. Luo, and W. Pantleon. Recrystallization kinetics of warm-rolled tungsten in the temperature range 1150-1350c. *Journal of Nuclear Materials*, 455(1):591–594, 2014.

[67] J R Davis and A.S.M.I.H. Committee. *ASM Specialty Handbook: Heat-Resistant Materials*. ASM Specialty Handbook. ASM International, 1997.

[68] Hsun Hu. Texture of Metals. *Texture*, 1(4):233–258, 1974.

[69] R E Honig and D A Kramer. *Vapor Pressure Data for the Solid and Liquid Elements*. RCA Laboratories, David Sarnoff Research Center, 1969.

[70] Plansee. Shieldings | Plansee.

[71] M. Rieth, S. L. Dudarev, S. M. Gonzalez De Vicente, J. Aktaa, T. Ahlgren, S. Antusch, D. E J Armstrong, M. Balden, N. Baluc, M. F. Barthe, W. W. Basuki, M. Battabyal, C. S. Becquart, D. Blagoeva, H. Boldyryeva, J. Brinkmann, M. Celino, L. Ciupinski, J. B. Correia, A. De Backer, C. Domain, E. Gaganidze, C. Garca-Rosales, J. Gibson, M. R. Gilbert, S. Giusepponi, B. Gludovatz, H. Greuner, K. Heinola, T. Hschen, A. Hoffmann, N. Holstein, F. Koch, W. Krauss, H. Li, S. Lindig, J. Linke, Ch Linsmeier, P. Lpez-Ruiz, H. Maier, J. Matejicek, T. P. Mishra, M. Muhammed, A. Muoz, M. Muzyk, K. Nordlund, D. Nguyen-Manh, J. Opschoor, N. Ords, T. Palacios, G. Pintsuk, R. Pippan, J. Reiser, J. Riesch, S. G. Roberts, L. Romaner, M. Rosiski, M. Sanchez, W. Schulmeyer, H. Traxler, A. Urea, J. G. Van Der Laan, L. Veleva, S. Wahlberg, M. Walter, T. Weber, T. Weitkamp, S. Wurster, M. A. Yar, J. H. You, and A. Zivelonghi. Recent progress in research on tungsten materials for nuclear fusion applications in Europe. *Journal of Nuclear Materials*, 432(1-3):482–500, 2013.

[72] Chai Ren, Z. Zak Fang, Mark Koopman, Brady Butler, James Paramore, and Scott Middlemas. Methods for improving ductility of tungsten - A review. *International Journal of Refractory Metals and Hard Materials*, 75(April):170–183, 2018.

[73] John Price Hirth and Jens Lothe. THEORY OF DISLOCATIONS Second Edition. Technical report.

[74] B. Gludovatz, S. Wurster, T. Weingartner, A. Hoffmann, and R. Pippan. Influence of impurities on the fracture behaviour of tungsten. *Philosophical Magazine*, 91(22):3006–3020, 2011.

[75] A. Joshi and D. F. Stein. Intergranular brittleness studies in Tungsten Using Auger Spectroscopy. *Metallurgical Transactions*, 1970.

[76] H. S. W. Yih and C. T. Wang. Tungsten Sources, Metallurgy and Applications, 1981.

[77] Nasa Tn and National Aeronautics. Technical note 0-1581. *Nasa Technical Note*, (April), 1963.

[78] G C Jr. Bodine. TUNGSTEN SHEET ROLLING PROGRAM. Final Report, June 1, 1960-March 1, 1963. Technical report, United States, 1963.

[79] Q Wei and L J Kecskes. Effect of low-temperature rolling on the tensile behavior of commercially pure tungsten. *Materials Science and Engineering: A*, 491(1):62–69, 2008.

[80] Jens Reiser, Jan Hoffmann, Ute Jäntsch, Michael Klimenkov, Simon Bonk, Carsten Bonnekoh, Michael Rieth, Andreas Hoffmann, and Tobias Mrotzek. Ductilisation of tungsten (W): On the shift of the brittle-to-ductile transition (BDT) to lower temperatures through cold rolling. *International Journal of Refractory Metals and Hard Materials*, 54:351–369, 2016.

[81] Rainer Birringer, Ulrich Herr, and Herbert Gleiter. *NANOCRYSTALLINE MATERIALS - A FIRST REPORT.*, volume 27. jan 1986.

[82] L J Kecskes, K C Cho, R J Dowding, B E Schuster, R Z Valiev, and Q Wei. Grain size engineering of bcc refractory metals: Top-down and bottom-up,ÄîApplication to tungsten. *Materials Science and Engineering: A*, 467(1):33–43, 2007.

[83] Simon Bonk, Jan Hoffmann, Andreas Hoffmann, and Jens Reiser. Cold rolled tungsten (W) plates and foils: Evolution of the tensile properties and their indication towards deformation mechanisms. *International Journal of Refractory Metals and Hard Materials*, 70:124–133, 2018.

[84] Q. Wei, T. Jiao, K. T. Ramesh, E. Ma, L. J. Kecskes, L. Magness, R. Dowding, V. U. Kazykhanov, and R. Z. Valiev. Mechanical behavior and dynamic failure of high-strength ultrafine grained tungsten under uniaxial compression. *Acta Materialia*, 54(1):77–87, 2006.

[85] Q. Wei, H. T. Zhang, B. E. Schuster, K. T. Ramesh, R. Z. Valiev, L. J. Kecskes, R. J. Dowding, L. Magness, and K. Cho. Microstructure and mechanical properties of super-strong nanocrystalline tungsten processed by high-pressure torsion. *Acta Materialia*, 54(15):4079–4089, 2006.

[86] J. R Geach, G. A. & Hughes. The alloys of rhenium and molybdenum or with tungsten and having good high temperature properties. *Plansee Proceedings*, F:245–253, 1955.

[87] W. D. Klopp, W. R. Witzke, and Peter L. Raffo. Mechanical Properties of Dilute Tungsten-Rhenium Alloys. *Nasa Technical Note*, 1966.

[88] William D. Klopp. A review of chromium, molybdenum, and tungsten alloys. *Journal of The Less-Common Metals*, 1975.

[89] William D Klopp. Review of Ductilizing of Group VIA Elements by Rhenium and Other Solutes, 1968.

[90] A. Luo, D. L. Jacobson, and K. S. Shin. Solution softening mechanism of iridium and rhenium in tungsten at room temperature. *International Journal of Refractory Metals and Hard Materials*, 1991.

[91] Mark R Gilbert and Robin A Forrest. Handbook of activation , transmutation , and radiation damage properties of the elements simulated using FISPACT-II & TENDL-2014 ;. (December), 2015.

[92] Chumphol Busabok and T Shikama. Temperature dependence of thermal conductivity in W and W ,Äì Re alloys from 300 to 1000 K Temperature dependence of thermal conductivity in W and W ,Äì Re alloys from 300 to 1000 K. (December 2017), 2003.

[93] Hong Li, Stefan Wurster, Christian Motz, Lorenz Romaner, Claudia Ambrosch-Draxl, and Reinhard Pippan. Dislocation-core symmetry and slip planes in tungsten alloys: Ab initio calculations and microcantilever bending experiments. *Acta Materialia*, 2012.

[94] T Massalski, P Submanian, and Hiroaki Okamoto. *ASM Handbook Volume 3: Alloy Phase Diagrams*, volume 1. ASTM International, 2016.

[95] Platinum Metals Review. Tungsten-Iridium Alloys at High Temperatures. *Platinum Metals Review*, 36(3):13, 1992.

[96] Stefan Wurster, Bernd Gludovatz, Andreas Hoffmann, and Reinhard Pippan. Fracture behaviour of tungsten-vanadium and tungsten-tantalum alloys and composites. *Journal of Nuclear Materials*, 413(3):166–176, 2011.

[97] M. V. Aguirre, A. Mart, J. Y. Pastor, J. Llorca, M. A. Monge, and R. Pareja. Mechanical behavior of W-Y_2O_3 and W-Ti Alloys from 25 to 1000C. *Metallurgical and Materials Transactions A: Physical Metallurgy and Materials Science*, 40(10):2283–2290, 2009.

[98] A. Patra, R. Saxena, and S. K. Karak. Combined effect of Ni and nano-Y_2O_3 addition on microstructure, mechanical and high temperature behavior of mechanically alloyed W-Mo. *International Journal of Refractory Metals and Hard Materials*, 60:131–146, 2016.

[99] Luca Costa. Welding with non-consumable thoriated tungsten electrodes. *Welding in the World*, 59(1):145–150, 2014.

[100] Peter L Raffo, William D Klopp, and Walter R Witzke. Mechanical Properties on Arc-Melted and Electron-Beam-Melted Tungsten-Base Alloys, 1965.

[101] Danqing Zhang, Qizhou Cai, and Jinhui Liu. Formation of Nanocrystalline by Selective Laser Melting of Tungsten Powder. *Materials and Manufacturing Processes*, 2(20 ml):120910120106002, 2012.

[102] Karel Deprez, Stefaan Vandenberghe, Karen Van Audenhaege, Jonas Van Vaerenbergh, and Roel Van Holen. Rapid additive manufacturing of MR compatible multipinhole collimators with selective laser melting of tungsten powder. *Medical physics*, 40(1):012501, 2013.

[103] Bai Nie, Huan Huang, Shuang Bai, and Jian Liu. Femtosecond laser melting and resolidifying of high-temperature powder materials. *Applied Physics A: Materials Science and Processing*, 118(1):37–41, 2014.

[104] Bai Nie, Lihmei Yang, Huan Huang, Shuang Bai, Peng Wan, and Jian Liu. Femtosecond laser additive manufacturing of iron and tungsten parts. *Applied Physics A: Materials Science and Processing*, 119(3):1075–1080, 2015.

[105] Dianzheng Wang, Chenfan Yu, Xin Zhou, Jing Ma, Wei Liu, and Zhijian Shen. Dense Pure Tungsten Fabricated by Selective Laser Melting. *Applied Sciences*, 7(4):430, 2017.

[106] A.T. Sidambe and P. Fox. Investigation of the Selective Laser Melting process with tungsten metal powder. *Additive Manufacturing*, 8:88–94, 2015.

[107] Ravi K. Enneti, Rick Morgan, and Thomas Wolfe. Direct Metal Laser Sintering (Dmls) / Selective Laser Melting (Slm) of Tungsten Powders. pages 9–13.

[108] Ravi K. Enneti, Rick Morgan, and Sundar V. Atre. Effect of process parameters on the Selective Laser Melting (SLM) of tungsten. *International Journal of Refractory Metals and Hard Materials*, 71(November 2017):315–319, 2018.

[109] Aljaž Iveković, Neda Omidvari, Bey Vrancken, Karel Lietaert, Lore Thijs, Kim Vanmeensel, Jef Vleugels, and Jean Pierre Kruth. Selective laser melting of tungsten and tungsten alloys. *International Journal of Refractory Metals and Hard Materials*, 72(February 2018):27–32, 2018.

[110] Dongdong Gu, Donghua Dai, Wenhua Chen, and Hongyu Chen. Selective Laser Melting Additive Manufacturing of Hard-to-Process Tungsten-Based Alloy Parts With Novel Crystalline Growth Morphology and Enhanced Performance. *Journal of Manufacturing Science and Engineering*, 138(8):081003, 2016.

[111] Eckart Uhlmann, André Bergmann, and Witalij Gridin. Investigation on Additive Manufacturing of Tungsten Carbide-cobalt by Selective Laser Melting. *Procedia CIRP*, 35:8–15, 2015.

[112] Wolfmet. Metal Additive Manufacturing - Tungsten 3d Printing | Wolfmet.

[113] Cardiff Road Newport NP10 8QQ. information@ipo.gov.uk Intellectual Property Office, Concept House. Intellectual Property Office - Patent document and information service (Ipsum).

[114] 3dprintingindustry.com. Smit Röntgen & EOS 3DP Tungsten - 3D Printing Industry.

[115] British Petroleum. BP Statistical Review of World Energy 2017. *British Petroleum*, (66):1–52, 2017.

[116] International Energy Agency. World Energy Outlook 2017. *INTERNATIONAL ENERGY AGENCY Together Secure Sustainable*, Executive:13, 2017.

[117] Short-term Energy Outlook. Short-Term Energy Outlook (STEO) Forecast highlights. (January 2019), 2020.

[118] Susan Solomon, Gian-Kasper Plattner, Reto Knutti, and Pierre Friedlingstein. Irreversible climate change due to carbon dioxide emissions. *Proceedings of the National Academy of Sciences*, 2009.

[119] Matthew Collins, Reto Knutti, Julie Arblaster, Jean-Louis Dufresne, Thierry Fichefet, Pierre Friedlingstein, Xuejie Gao, William J. Gutowski, Tim Johns, Gerhard Krinner, Mxolisi Shongwe, Claudia Tebaldi, Andrew J. Weaver, and Michael Wehner. Long-term Climate Change: Projections, Commitments and Irreversibility. *Climate Change 2013: The Physical Science Basis. Contribution of Working Group I to the Fifth Assessment Report of the Intergovernmental Panel on Climate Change*, pages 1029–1136, 2013.

[120] James Hansen, Makiko Sato, Paul Hearty, Reto Ruedy, Maxwell Kelley, Valerie Masson-Delmotte, Gary Russell, George Tselioudis, Junji Cao, Eric Rignot, Isabella Velicogna, Blair Tormey, Bailey Donovan, Evgeniya Kandiano, Karina Von Schuckmann, Pushker Kharecha, Allegra N. Legrande, and Michael Bauer. Ice melt, sea level rise and superstorms: Evidence from paleoclimate data, climate modeling, and modern observations that 2c global warming could be dangerous. *Atmospheric Chemistry and Physics*, 16(6):3761–3812, 2016.

[121] Tetsuji Noda, Fujio Abe, Hiroshi Araki, and Masatoshi Okada. Materials selection for reduced activation of fusion reactors. *Journal of Nuclear Materials*, 155-157(PART 2):581–584, 1988.

[122] R. A. CAIRNS. Tokamaks 3rd Edition by John Wesson, Oxford University Press 2004. *Journal of Plasma Physics*, 2005.

[123] CCFE. Fusion energy: Introduction to fusion, 2017.

[124] J P Freidberg. *Plasma physics and fusion energy*. 2007.

[125] W M Stacey. *Fusion: An Introduction to the Physics and Technology of Magnetic Confinement Fusion*. 2010.

[126] Jet Team. Fusion energy production from a deuterium-tritium plasma in the JET tokamak. *Nuclear Fusion*, 1992.

[127] H. Pero and S. Paidassi. The EU fusion programme and roadmap. *Fusion Engineering and Design*, 2013.

[128] F. Romanelli. Fusion Electricity: A roadmap to the realisation of fusion energy. *Efda*, pages 1–75, 2012.

[129] Controlled Fusion. Plasma Physics and Controlled Fusion Related content Energy confinement scaling in Tokamaks : some implications of recent experiments with Ohmic and strong auxiliary heating. 1984.

[130] A. Loarte, G. Saibene, R. Sartori, D. Campbell, M. Becoulet, L. Horten, T. Eich, A. Herrmann, G. Matthews, N. Asakura, A. Chankin, A. Leonard, G. Porter, G. Federici, G. Janeschitz, M. Shimada, and M. Sugihara. Characteristics of type I ELM energy and particle losses in existing devices and their extrapolation to ITER. *Plasma Physics and Controlled Fusion*, 45(9):1549–1569, 2003.

[131] Jochen Max Linke, Takeshi Hirai, Manfred Rödig, and Lorenz Anton Singheiser. Performance of Plasma-Facing Materials Under Intense Thermal Loads in Tokamaks and Stellarators. *Fusion Science and Technology*, 46(1):142–151, jul 2004.

[132] T. Hirai, F. Escourbiac, S. Carpentier-Chouchana, A. Fedosov, L. Ferrand, T. Jokinen, V. Komarov, A. Kukushkin, M. Merola, R. Mitteau, R. A. Pitts, W. Shu, M. Sugihara, B. Riccardi, S. Suzuki, and R. Villari. ITER tungsten divertor design development and qualification program. *Fusion Engineering and Design*, 88(9-10):1798–1801, 2013.

[133] D. Maisonnier, D. Campbell, I. Cook, L. Di Pace, L. Giancarli, J. Hayward, A. Li Puma, M. Medrano, P. Norajitra, M. Roccella, P. Sardain, M. Q. Tran, and D. Ward. Power plant conceptual studies in Europe. *Nuclear Fusion*, 2007.

[134] O. Crofts and J. Harman. Maintenance duration estimate for a DEMO fusion power plant, based on the EFDA WP12 pre-conceptual studies. *Fusion Engineering and Design*, 89(9-10):2383–2387, 2014.

[135] D. Maisonnier, I. Cook, Sardain Pierre, Boccaccini Lorenzo, Bogusch Edgar, Broden Karin, Di Pace Luigi, Forrest Robin, Giancarli Luciano, Hermsmeyer Stephan, Nardi Claudio, Norajitra Prachai, Pizzuto Aldo, Taylor Neill, and Ward David. The European power plant conceptual study. *Fusion Engineering and Design*, 75-79(SUPPL.):1173–1179, 2005.

[136] K. Brodén and G. Olsson. Categorisation of activated material from fusion power reactors and acceptability for final disposal. *Fusion Engineering and Design*, 75-79(SUPPL.):1229–1232, 2005.

[137] T. Loarer. Fuel retention in tokamaks. *Journal of Nuclear Materials*, 390-391(1):20–28, 2009.

[138] H. Bolt, V. Barabash, W. Krauss, J. Linke, R. Neu, S. Suzuki, and N. Yoshida. Materials for the plasma-facing components of fusion reactors. *Journal of Nuclear Materials*, 329-333(1-3 PART A):66–73, 2004.

[139] G. F. Matthews, M. Beurskens, S. Brezinsek, M. Groth, E. Joffrin, A. Loving, M. Kear, M. L. Mayoral, R. Neu, P. Prior, V. Riccardo, F. Rimini, M. Rubel, G. Sips, E. Villedieu, P. De Vries, and M. L. Watkins. JET ITER-like wall - Overview and experimental programme. *Physica Scripta T*, T145, 2011.

[140] H. Bolt, V. Barabash, G. Federici, J. Linke, A. Loarte, J. Roth, and K. Sato. Plasma facing and high heat flux materials - Needs for ITER and beyond. *Journal of Nuclear Materials*, 307-311(1 SUPPL.):43–52, 2002.

[141] S. Brezinsek, T. Loarer, V. Philipps, H. G. Esser, S. Grünhagen, R. Smith, R. Felton, J. Banks, P. Belo, A. Boboc, J. Bucalossi, M. Clever, J. W. Coenen, I. Coffey, S. Devaux, D. Douai, M. Freisinger, D. Frigione, M. Groth, A. Huber, J. Hobirk, S. Jachmich, S. Knipe, K. Krieger, U. Kruezi, S. Marsen, G. F. Matthews, A. G. Meigs, F. Nave, I. Nunes, R. Neu, J. Roth, M. F. Stamp, S. Vartanian, and U. Samm. Fuel retention studies with the ITER-Like Wall in JET. *Nuclear Fusion*, 53(8), 2013.

[142] Coenen Forschungszentrum. Tungsten As a Plasma Facing Component and Development of Advanced Materials for Fusion. pages 250–259.

[143] T. Hirai, F. Escourbiac, S. Carpentier-Chouchana, A. Fedosov, L. Ferrand, T. Jokinen, V. Komarov, A. Kukushkin, M. Merola, R. Mitteau, R. A. Pitts, W. Shu, M. Sugihara, B. Riccardi, S. Suzuki, and R. Villari. ITER tungsten divertor design development and qualification program. *Fusion Engineering and Design*, 88(9-10):1798–1801, 2013.

[144] T. Hirai, S. Panayotis, V. Barabash, C. Amzallag, F. Escourbiac, A. Durocher, M. Merola, J. Linke, Th Loewenhoff, G. Pintsuk, M. Wirtz, and I. Uytdenhouwen. Use of tungsten material for the ITER divertor. *Nuclear Materials and Energy*, 9(2016):616–622, 2016.

[145] Karol Kobiela, Irina Smolina, Mariusz Frankiewicz, and Edward Chlebus. Plasma spheroidisation of high melt point materials on example of tungsten. *Przegląd Spawalnictwa - Welding Technology Review*, 87(11):30–34, 2015.

[146] ASTM. B213-17: Standard Test Methods for Flow Rate of Metal Powders Using the Hall Flowmeter. *ASTM Standards*, pages 1–4, 2017.

[147] ASTM B212. Standard Test Method for Apparent Density of Free-Flowing Metal Powders Using the Hall Flowmeter Funnel, 2017.

[148] Douglas C. Montgomery and Douglas C. *Design and analysis of experiments*. 2001.

[149] Ralph Waldo Emerson and M Cavazzuti. *Deterministic optimization*. 2013.

[150] Mohammad M. Nasseri. Determination of Tungsten Target Parameters for Transmission X-ray Tube: A Simulation Study Using Geant4. *Nuclear Engineering and Technology*, 48(3):795–798, 2016.

[151] UK Parliament. The Ionising Radiations Regulations 2017. *2000*, (1075):1–68, 2017.

[152] W C Oliver and G M Pharr. An improved technique for determining hardness and elastic modulus using load and displacement sensing indentation experiments. *Journal of Materials Research*, 7(6):1564–1583, 1992.

[153] Jae Il Jang. Estimation of residual stress by instrumented indentation: A review. *Journal of Ceramic Processing Research*, 10(3):391–400, 2009.

[154] G Sines Carlson and R. Hardness measurment for determination of residual stresses. *ASTM Bulletin*, (180):35–37, 1952.

[155] M Chaudhri and Martin A. Phillips. *Quasi-Static Indentation Cracking of Thermally Tempered Soda-Lime Glass with Spherical and Vickers Indenters*, volume 62. jul 1990.

[156] T. Y. Tsui, W. C. Oliver, and G. M. Pharr. Influences of stress on the measurement of mechanical properties using nanoindentation: Part I. Experimental studies in an aluminum alloy. *Journal of Materials Research*, 11(03):752–759, 1996.

[157] A Bolshakov, W C Oliver, and G M Pharr. Influences of stress on the measurement of mechanical properties using nanoindentation: Part II. Finite element simulations. *Journal of Materials Research*, 11(3):760–768, 1996.

[158] Josef Kräutkramer and Herbert Kräutkramer. *Ultrasonic testing of materials*. 1987.

[159] G. V.S. Murthy, Sabita Ghosh, Mousumi Das, G. Das, and R. N. Ghosh. Correlation between ultrasonic velocity and indentation-based mechanical properties with microstructure in Nimonic 263. *Materials Science and Engineering A*, 2008.

[160] H. Bolt, V. Barabash, W. Krauss, J. Linke, R. Neu, S. Suzuki, and N. Yoshida. Materials for the plasma-facing components of fusion reactors. *Journal of Nuclear Materials*, 329-333(1-3 PART A):66–73, 2004.

[161] E1461. E1461. Standard test method for thermal diffusivity by the flash method. *ASTM, West Conshohocken, PA*, i:1–11, 2001.

[162] W. J. Parker, R. J. Jenkins, C. P. Butler, and G. L. Abbott. Flash method of determining thermal diffusivity, heat capacity, and thermal conductivity. *Journal of Applied Physics*, 32(9):1679–1684, 1961.

[163] Silica Dilatometer, Thermal Expansion, and Glass Transition Temperature. Standard Test Method for Linear Thermal Expansion of Solid Materials by. pages 1–5, 2016.

[164] B S En. Advanced technical ceramics ,Äî Mechanical properties of monolithic ceramics at room temperature ,Äî. *Measurement*, 3, 2006.

[165] V. Ankudinov, G. A. Gordeev, and M. D. Krivilyov. Numerical simulation of heat transfer and melting of Fe-based powders in SLM processing. *IOP Conference Series: Materials Science and Engineering*, 192(1), 2017.

[166] P Mercelis and J P Kruth. Residual stresses in selective laser sintering and selective laser melting. *Rapid Prototyping Journal*, 12(5):254–265, 2006.

[167] Dianzheng Wang, Chenfan Yu, Jing Ma, Wei Liu, and Zhijian Shen. Densification and crack suppression in selective laser melting of pure molybdenum. *Materials and Design*, 129(March):44–52, 2017.

[168] Libo Zhou, Tiechui Yuan, Ruidi Li, Jianzhong Tang, Guohua Wang, and Kaixuan Guo. Selective laser melting of pure tantalum: Densification, microstructure and mechanical behaviors. *Materials Science and Engineering A*, 707(September):443–451, 2017.

[169] A. T. Sidambe, Y. Tian, P. B. Prangnell, and P. Fox. Effect of processing parameters on the densification, microstructure and crystallographic texture during the laser powder bed fusion of pure tungsten. *International Journal of Refractory Metals and Hard Materials*, 78(July 2018):254–263, 2019.

[170] David Hancock, David Homfray, Michael Porton, Iain Todd, and Brad Wynne. Refractory metals as structural materials for fusion high heat flux components. *Journal of Nuclear Materials*, 512(18):169–183, 2018.

[171] D. Faidel, D. Jonas, G. Natour, and W. Behr. Investigation of the selective laser melting process with molybdenum powder. *Additive Manufacturing*, 8:88–94, 2015.

[172] Priyanshu Bajaj, Jonathan Wright, Iain Todd, and Eric A. Jägle. Predictive process parameter selection for Selective Laser Melting Manufacturing: Applications to high thermal conductivity alloys. *Additive Manufacturing*, 27(September 2018):246–258, 2019.

[173] Damien Buchbinder, Wilhelm Meiners, Norbert Pirch, Konrad Wissenbach, and Johannes Schrage. Investigation on reducing distortion by preheating during manufacture of aluminum components using selective laser melting. *Journal of Laser Applications*, 2014.

[174] Shunyu Liu and Yung C. Shin. Additive manufacturing of Ti6Al4V alloy: A review. *Materials and Design*, 164:107552, 2019.

[175] K. Sato, H. Yamashita, A. Hirosako, S. Komazaki, Q. Xu, M. Onoue, R. Kasada, K. Yabuuchi, and A. Kimura. Investigation of mechanical properties of stress-relieved and electron-irradiated tungsten after hydrogen charging. *Nuclear Materials and Energy*, 17(August):29–33, 2018.

[176] Kenta Sasaki, Shuhei Nogami, Makoto Fukuda, Yasuyuki Katakai, and Akira Hasegawa. Effect of heat treatment on bend stress relaxation of pure tungsten. *Fusion Engineering and Design*, 88(9-10):1735–1738, 2013.

[177] A. A. Antonysamy, J. Meyer, and P. B. Prangnell. Effect of build geometry on the β-grain structure and texture in additive manufacture of Ti6Al4V by selective electron beam melting. *Materials Characterization*, 84:153–168, 2013.

[178] Lore Thijs, Maria Luz Montero Sistiaga, Ruben Wauthle, Qingge Xie, Jean Pierre Kruth, and Jan Van Humbeeck. Strong morphological and crystallographic texture and resulting yield strength anisotropy in selective laser melted tantalum. *Acta Materialia*, 61(12):4657–4668, 2013.

[179] J. H. You and I. Komarova. Probabilistic failure analysis of a water-cooled tungsten divertor: Impact of embrittlement. *Journal of Nuclear Materials*, 375(3):283–289, 2008.

[180] Michael F. Zaeh and Gregor Branner. Investigations on residual stresses and deformations in selective laser melting. *Production Engineering*, 4(1):35–45, 2010.

[181] Jean-Pierre Kruth, Jan Deckers, Evren Yasa, and Ruben Wauthlé. Assessing and comparing influencing factors of residual stresses in selective laser melting using a novel analysis method. *Proceedings of the Institution of Mechanical Engineers, Part B: Journal of Engineering Manufacture*, 226(6):980–991, 2012.

[182] Yongjun Shi, Hong Shen, Zhenqiang Yao, and Jun Hu. Temperature gradient mechanism in laser forming of thin plates. *Optics and Laser Technology*, 39(4):858–863, 2007.

[183] George Voyiadjis and Mohammadreza Yaghoobi. Review of Nanoindentation Size Effect: Experiments and Atomistic Simulation. *Crystals*, 7(10):321, 2017.

[184] George M. Pharr, Erik G. Herbert, and Yanfei Gao. The Indentation Size Effect: A Critical Examination of Experimental Observations and Mechanistic Interpretations. *Annual Review of Materials Research*, 40(1):271–292, 2010.

[185] E. V. Shunko. Langmuir probe in theory and practice. *Journal of Education Policy*, pages 1–19, 1937.

[186] James M. Gere. *Mechanics of materials*. 2004.

[187] W. Weibull. A statistical distribution function of wide applicability, 1951.

[188] W. Weibull. A Statistical Theory of the Strength of Materials, 1939.

[189] R. Danzer, P. Supancic, J. Pascual, and T. Lube. Fracture statistics of ceramics - Weibull statistics and deviations from Weibull statistics. *Engineering Fracture Mechanics*, 74(18):2919–2932, 2007.

[190] Jianghong Gong. Correlation between Weibull moduli for tensile and bending strength of brittle ceramics: A numerical simulation analysis based on a three-parameter Weibull distribution. *Journal of Materials Science*, 38(11):2541–2545, 2003.

[191] Claudinei Dos Santos, Kurt Strecker, Francisco Piorino Neto, Olivério Moreira De Macedo Silva, Sandro Aparecido Baldacim, and Cosme Roberto Moreira Da Silva. Evaluation of the reliability of Si3N4-Al2O3 -CTR2O3 ceramics through Weibull analysis. *Materials Research*, 6(4):463–467, 2003.

[192] Antonio Fernández and Manuel Vázquez. Improved estimation of Weibull parameters considering unreliability uncertainties. *IEEE Transactions on Reliability*, 61(1):32–40, 2012.

[193] R. H. Myers and D. C. Montgomery. Response surface methodology. *Technometrics*, 31(2):137–157, 1971.

[194] Mario Merola, D. Loesser, A. Martin, P. Chappuis, R. Mitteau, V. Komarov, R. A. Pitts, S. Gicquel, V. Barabash, L. Giancarli, J. Palmer, M. Nakahira, A. Loarte, D. Campbell, R. Eaton, A. Kukushkin, M. Sugihara, F. Zhang, C. S. Kim, R. Raffray, L. Ferrand, D. Yao, S. Sadakov, A. Furmanek, V. Rozov, T. Hirai, F. Escourbiac, T. Jokinen, B. Calcagno, and S. Mori. ITER plasma-facing components. *Fusion Engineering and Design*, 2010.

[195] Linda Dr. Capuano. International Energy Outlook 2018 (IEO2018). 2018:21, 2018.

[196] Fu-Zhong Xia, Hai-Gen Wei, Ming-Pu Wang, and Dong-Hui Zhu. Investigation of normal recrystallization and abnormal recrystallization in pure tungsten sheet by EBSD. *Rmhm*, 52:98–103, 2015.

[197] J Pokluda and Pavel Sandera. Brittle and ductile fracture. *Micromechanisms of Fracture and Fatigue in a Multi-scale Context*, pages 69–98, 2010.

[198] G E P Box and D W Behnken. Some New Three Level Designs for the Study of Quantitative Variables. *Technometrics*, 2(4):455–475, nov 1960.

[199] M. Rieth and A. Hoffmann. Influence of microstructure and notch fabrication on impact bending properties of tungsten materials. *International Journal of Refractory Metals and Hard Materials*, 28(6):679–686, 2010.

[200] Joseph R. Stephens. A review of the deformation behavior of tungsten at temperatures less than 0.2 of the melting point. *Nasa Tm*, (X-2482):1–34, 1972.

[201] Source Journal, Royal Statistical, and Society Series. On the Experimental Attainment of Optimum Conditions Author (s): G . E . P . Box and K . B . Wilson Published by : Blackwell Publishing for the Royal Statistical Society Stable URL : http://www.jstor.org/stable/2983966. 13(1):1–45, 2008.

[202] PPD Mont. Alternatives to thorium additions to tungsten-based materials. *Jom*, 1996.

[203] Dejun MA, Ong Chung Wo, Jianmin Liu, and Jiawen HE. Determination of Youngs modulus by nanoindentation. *Science in China Series E*, 47(4):398, 2004.

[204] L L Lucas and M P Unterweger. Comprehensive review and critical evaluation of the half-life of tritium. *Journal Of Research Of The National Institute Of Standards And Technology*, 105(4):541–549, 2000.

[205] Ning Wei, Ting Jia, Xiaoli Zhang, Ting Liu, Z. Zeng, and Xiaoyu Yang. First-principles study of the phase stability and the mechanical properties of W-Ta and W-Re alloys. *AIP Advances*, 4(5), 2014.

[206] G. Miranda, S. Faria, F. Bartolomeu, E. Pinto, S. Madeira, A. Mateus, P. Carreira, N. Alves, F. S. Silva, and O. Carvalho. Predictive models for physical and mechanical properties of 316L stainless steel produced by selective laser melting. *Materials Science and Engineering A*, 657:43–56, 2016.

[207] Xin Zhou, Kailun Li, Dandan Zhang, Xihe Liu, Jing Ma, Wei Liu, and Zhijian Shen. Textures formed in a CoCrMo alloy by selective laser melting. *Journal of Alloys and Compounds*, 631:153–164, 2015.

[208] Marcos Almeida Bezerra, Ricardo Erthal Santelli, Eliane Padua Oliveira, Leonardo Silveira Villar, and Luciane Amélia Escaleira. Response surface methodology (RSM) as a tool for optimization in analytical chemistry. *Talanta*, 76(5):965–977, 2008.

[209] F. A. Holland and E. V. Zaretsky. Investigation of Weibull Statistics in Fracture Analysis of Cast Aluminum. *Nasa Tm 102000*, 1989.

[210] Q. Wei and L. J. Kecskes. Effect of low-temperature rolling on the tensile behavior of commercially pure tungsten. *Materials Science and Engineering A*, 491(1-2):62–69, 2008.

[211] A. Giannattasio and S. G. Roberts. Strain-rate dependence of the brittle-to-ductile transition temperature in tungsten. *Philosophical Magazine*, 87(17):2589–2598, 2007.

[212] Colombo Paolo. nited States Patent [191. pages 1–4, 1988.

[213] Yoshio UEDA. Status of Plasma Facing Material Studies and Issues toward DEMO. *Plasma and Fusion Research*, 5:S1009–S1009, 2010.

[214] R.A. Fisher. The Design of Experiments. *The American Mathematical Monthly*, 43(3):180, 1936.

[215] Galina Kasperovich, Jan Haubrich, Joachim Gussone, and Guillermo Requena. Correlation between porosity and processing parameters in TiAl6V4 produced by selective laser melting. *Materials and Design*, 105:160–170, 2016.

[216] I. Gibson, D. W. Rosen, and B. Stucker. *Additive manufacturing technologies: Rapid prototyping to direct digital manufacturing*. 2010.

[217] Mohamed Abdou, Neil B. Morley, Sergey Smolentsev, Alice Ying, Siegfried Malang, Arthur Rowcliffe, and Mike Ulrickson. Blanket/-first wall challenges and required R&D on the pathway to DEMO. *Fusion Engineering and Design*, 100:2–43, 2015.

[218] W.C. Oliver and G.M. Pharr. An improved technique for determining hardness and elastic modulus using load and displacement sensing indentation experiments, 1992.

[219] J Clifton Young. BLOCKING, REPLICATION, AND RANDOMIZATION,ÄîTHE KEY TO EFFECTIVE EXPERIMENTATION: A CASE STUDY. *Quality Engineering*, 9(2):269–277, jan 1996.

[220] Isiklar Yasar. a Numerical Study of Heat Transfer Behavior in Welding. 1998.

[221] Indah Rosidah Maymunah, Zaki Suud, and Putranto Ilham Yazid. Optimization of tritium breeding and shielding analysis to plasma in ITER fusion reactor. *AIP Conference Proceedings*, 1677, 2015.

[222] Edwin Martinez, Lawrence E. Murr, Jennifer Hernandez, Xuemin Pan, Krista Amato, Pedro Frigola, Cesar Terrazas, Sara Gaytan, Emmanuel Rodriguez, Francisco Medina, and Ryan B. Wicker. Microstructures of Niobium Components Fabricated by Electron Beam Melting. *Metallography, Microstructure, and Analysis*, 2(3):183–189, 2013.

[223] Kaufui V. Wong and Aldo Hernandez. A Review of Additive Manufacturing. *ISRN Mechanical Engineering*, 2012:1–10, 2012.

[224] J. Bruno, A. Rochman, and G. Cassar. Effect of Build Orientation of Electron Beam Melting on Microstructure and Mechanical Properties of Ti-6Al-4V. *Journal of Materials Engineering and Performance*, 26(2):692–703, 2017.

[225] Brady G. Butler, James D. Paramore, Jonathan P. Ligda, Chai Ren, Z. Zak Fang, Scott C. Middlemas, and Kevin J. Hemker. Mechanisms of deformation and ductility in tungsten ,Äì A review. *International Journal of Refractory Metals and Hard Materials*, 75(April):248–261, 2018.

[226] S. M. Gaytan, L. E. Murr, F. Medina, E. Martinez, M. I. Lopez, and R. B. Wicker. Advanced metal powder based manufacturing of complex components by electron beam melting. *Materials Technology*, 24(3):180–190, 2013.

[227] S Suresh and A E Giannakopoulos. A new method for estimating residual stresses by instrumented sharp indentation. *Acta Materialia*, 46(16):5755–5767, 1998.

[228] Å Björck. Numerical methods for least squares problems. *Gene*, 1996.

[229] Darya Ivanova. *Plasma-facing components in tokamaks : material modification and fuel retention*. 2012.

[230] J. H. Heo and J. D. Salas. Estimation of quantiles and confidence intervals for the log-Gumbel distribution. *Stochastic Hydrology and Hydraulics*, 10(3):187–207, 1996.

[231] T. Weber and J. Aktaa. Numerical assessment of functionally graded tungsten/steel joints for divertor applications. *Fusion Engineering and Design*, 86(2-3):220–226, 2011.

[232] P. Zhao, J. Riesch, T. Höschen, J. Almanstötter, M. Balden, J. W. Coenen, R. Himml, W. Pantleon, U. von Toussaint, and R. Neu. Microstructure, mechanical behaviour and fracture of pure tungsten wire after different heat treatments. *International Journal of Refractory Metals and Hard Materials*, 68(March):29–40, 2017.

[233] M Keilhacker, A Gibson, C Gormezano, and P H Rebut. The scientific success of JET. *Nuclear Fusion*, 41(12):1925, 2001.

[234] E. O. Olakanmi, R. F. Cochrane, and K. W. Dalgarno. A review on selective laser sintering/melting (SLS/SLM) of aluminium alloy powders: Processing, microstructure, and properties. *Progress in Materials Science*, 74:401–477, 2015.

[235] M Gilbert. Transmutation and He Production in W and W-alloys. *Culham Science Centre*, (10), 2010.

[236] R. Ferencz, J. Sanchez, B. Blümich, and W. Herrmann. AFM nanoindentation to determine Young's modulus for different EPDM elastomers. *Polymer Testing*, 31(3):425–432, 2012.

[237] M. T. Todinov. Is Weibull distribution the correct model for predicting probability of failure initiated by non-interacting flaws? *International Journal of Solids and Structures*, 46(3-4):887–901, 2009.

[238] K. F. Walker, Q. Liu, and M. Brandt. Evaluation of fatigue crack propagation behaviour in Ti-6Al-4V manufactured by selective laser melting. *International Journal of Fatigue*, 104:302–308, 2017.

[239] L.W. Packer, P. Batistoni, S.C. Bradnam, B. Colling, S. Conroy, Z. Ghani, M.R. Gilbert, S. Jednorog, E. Łaszyńska, D. Leichtle, I. Lengar, J.W. Mietelski, R. Misiak, C.R. Nobs, M. Pillon, S. Popovichev, V. Radulović, I.E. Stamatelatos, T. Vasilopoulou, and A. Wójcik-Gargula. Activation of ITER materials in JET: nuclear characterisation experiments for the long-term irradiation station. *Nuclear Fusion*, 58(9):096013, 2018.

[240] F.A. Maeda, M.S. Bello-Silva, C.P. Eduardo, P.F. Cesar, and W.G. Miranda. Effects of pre-sintered Y-TZP surface treatments on shear bond strength. *Dental Materials*, 27:e64, 2011.

[241] A. A F Tavassoli. Present limits and improvements of structural materials for fusion reactors - A review. *Journal of Nuclear Materials*, 302(2-3):73–88, 2002.

[242] Mathematical Statistics. A Generalization of the Gamma Distribution Author (s): E . W . Stacy Source : The Annals of Mathematical Statistics , Vol . 33 , No . 3 (Sep ., 1962), pp . 1187-1192 Published by : Institute of Mathematical Statistics Stable URL : http://www.jstor.org. 33(3):1187–1192, 2017.

[243] S. L. Sing, L. P. Lam, D. Q. Zhang, Z. H. Liu, and C. K. Chua. Interfacial characterization of SLM parts in multi-material processing: Intermetallic phase formation between AlSi10Mg and C18400 copper alloy. *Materials Characterization*, 107:220–227, 2015.

[244] A. V. Gusarov, I. Yadroitsev, Ph. Bertrand, and I. Smurov. Model of Radiation and Heat Transfer in Laser-Powder Interaction Zone at Selective Laser Melting. *Journal of Heat Transfer*, 131(7):072101, 2009.

[245] Nist/Sematech. Engineering statistics handbook. *National Institute Standart Tech*, 2001.

[246] A M Freudenthal. Statistical Approach to Brittle Fracture. *Fracture*, 2:591–619, 1968.

[247] Xi Chen, Jin Yan, and Anette M. Karlsson. On the determination of residual stress and mechanical properties by indentation. *Materials Science and Engineering A*, 416(1-2):139–149, 2006.

[248] Jing Qian, C.Y. Wu, J.L. Fan, and H.R. Gong. Effect of alloying elements on stacking fault energy and ductility of tungsten. *Journal of Alloys and Compounds*, 737:372–376, 2017.

[249] S. Tammas-Williams, H. Zhao, F. Léonard, F. Derguti, I. Todd, and P. B. Prangnell. XCT analysis of the influence of melt strategies on defect population in Ti-6Al-4V components manufactured by Selective Electron Beam Melting. *Materials Characterization*, 102(July 2016):47–61, 2015.

[250] Joel T. Mague. Gmelin Handbook of Inorganic Chemistry. 8th Edition Rh. *Organometallics*, 1984.

[251] O. El-Atwani, Sean Gonderman, Mert Efe, Gregory De Temmerman, Thomas Morgan, Kirill Bystrov, Daniel Klenosky, Tian Qiu, and J. P. Allain. Ultrafine tungsten as a plasma-facing component in fusion devices: Effect of high flux, high fluence low energy helium irradiation. *Nuclear Fusion*, 54(8), 2014.

[252] Gaia Franceschini and Sandro Macchietto. Model-based design of experiments for parameter precision: State of the art. *Chemical Engineering Science*, 63(19):4846–4872, 2008.

[253] Anna Warren, Anders Nylund, and Ingemar Olefjord. Oxidation of tungsten and tungsten carbide in dry and humid atmospheres. *International Journal of Refractory Metals and Hard Materials*, 14(5-6):345–353, 1996.

[254] Qume Drive and San Jose. Femtosecond Fiber Laser Additive Manufacturing of Tungsten. *Spie Lase*, 1(408):97380U–1–97380U–10, 2016.

[255] Jayasheelan Vaithilingam, Ruth D. Goodridge, Richard J.M. Hague, Steven D.R. Christie, and Steve Edmondson. The effect of laser remelting on the surface chemistry of Ti6al4V components fabricated by selective laser melting. *Journal of Materials Processing Technology*, 232:1–8, 2016.

[256] Ben Vandenbroucke and Jean,ÄêPierre Kruth. Selective laser melting of biocompatible metals for rapid manufacturing of medical parts. *Rapid Prototyping Journal*, 13(4):196–203, 2007.

[257] P. Wanjara, M. Brochu, and M. Jahazi. Electron beam freeforming of stainless steel using solid wire feed. *Materials and Design*, 28(8):2278–2286, 2007.

[258] ASTM. ASTM E384-2016: Standard Test Method for Knoop and Vickers Hardness of Materials. *ASTM Standards*, i:1–43, 2016.

[259] G. Taguchi (Asian productivity organization). Introduction to quality engineering: Designing quality into products and processes. *Quality and Reliability Engineering International*, 1986.

[260] M. Kaufmann and R. Neu. Tungsten as first wall material in fusion devices. *Fusion Engineering and Design*, 2007.

[261] William J Hill and William G Hunter. A Review of Response S R , eethod 1 A Literature u :. 8(4):571–590, 2012.

[262] Chaolin Tan, Kesong Zhou, Min Liu, Tongchun Kuang, and Engineering Technology. Selective laser melting of high-performance pure tungsten : parameter design , d ensification behavior and mechanical property. *Science and Technology of Advanced Materials*, 6996:1–21, 2018.

[263] J. W. Davis and P. D. Smith. ITER material properties handbook. *Journal of Nuclear Materials*, 233-237(Pt B):1593–1596, 1996.

[264] C Eschey, S Lutzmann, and M F Zaeh. Examination of the powder spreading effect in Electron Beam Melting (EBM). *Proceedings of the 20th Solid Freeform Fabrication Symposium (SFF)*, pages 308–319, 2009.

[265] Daniel Scheiber. Theoretical Study of Grain Boundaries in Tungsten and Molybdenum. 2016.

[266] Animesh Bose, Christopher A. Schuh, Jay C. Tobia, Nihan Tuncer, Nicholas M. Mykulowycz, Aaron Preston, Alexander C. Barbati, Brian Kernan, Michael A. Gibson, Dana Krause, Tomek Brzezinski, Jan Schroers, Ricardo Fulop, Jonah S. Myerberg, Mark Sowerbutts, Yet Ming Chiang, A. John Hart, Emanuel M. Sachs, Ester E. Lomeli, and Alan C. Lund. Traditional and additive manufacturing of a new Tungsten heavy alloy alternative. *International Journal of Refractory Metals and Hard Materials*, 73(January):22–28, 2018.

[267] Loong Ee Loh, Chee Kai Chua, Wai Yee Yeong, Jie Song, Mahta Mapar, Swee Leong Sing, Zhong Hong Liu, and Dan Qing Zhang. Numerical investigation and an effective modelling on the Selective Laser Melting (SLM) process with aluminium alloy 6061. *International Journal of Heat and Mass Transfer*, 80:288–300, 2015.

[268] S. J. Zinkle and N. M. Ghoniem. Operating temperature windows for fusion reactor structural materials. *Fusion Engineering and Design*, 51-52(2000):55–71, 2000.

[269] Douglas C Montgomery. *Design and Analysis of Experiments Eighth Edition*, volume 2. 2012.

[270] Y. Ueda, J. W. Coenen, G. De Temmerman, R. P. Doerner, J. Linke, V. Philipps, and E. Tsitrone. Research status and issues of tungsten plasma facing materials for ITER and beyond. *Fusion Engineering and Design*, 89(7-8):901–906, 2014.

[271] I. A. Roberts, C. J. Wang, R. Esterlein, M. Stanford, and D. J. Mynors. A three-dimensional finite element analysis of the temperature field during laser melting of metal powders in additive layer manufacturing. *International Journal of Machine Tools and Manufacture*, 49(12-13):916–923, 2009.

[272] L. Eriksson, E. Johansson, N. Kettaneh-Wold, C. Wikström, and S. Wold. Design of Experiments. 2008.

[273] M. Rieth, J. L. Boutard, S. L. Dudarev, T. Ahlgren, S. Antusch, N. Baluc, M. F. Barthe, C. S. Becquart, L. Ciupinski, J. B. Correia, C. Domain, J. Fikar, E. Fortuna, C. C. Fu, E. Gaganidze, T. L. Galán, C. García-Rosales, B. Gludovatz, H. Greuner, K. Heinola, N. Holstein, N. Juslin, F. Koch, W. Krauss, K. J. Kurzydlowski, J. Linke, Ch Linsmeier, N. Luzginova, H. Maier, M. S. Martínez, J. M. Missiaen, M. Muhammed, A. Muñoz, M. Muzyk, K. Nordlund, D. Nguyen-Manh, P. Norajitra, J. Opschoor, G. Pintsuk, R. Pippan, G. Ritz, L. Romaner, D. Rupp, R. Schäublin, J. Schlosser, I. Uytdenhouwen, J. G. Van Der Laan, L. Veleva, L. Ventelon, S. Wahlberg, F. Willaime, S. Wurster, and M. A. Yar. Review on the EFDA programme on tungsten materials technology and science. *Journal of Nuclear Materials*, 417(1-3):463–467, 2011.

[274] Joy Gockel, Jack Beuth, and Karen Taminger. Integrated control of solidification microstructure and melt pool dimensions in electron beam wire feed additive manufacturing of ti-6al-4v. *Additive Manufacturing*, 1:119–126, 2014.

[275] S. Wurster, N. Baluc, M. Battabyal, T. Crosby, J. Du, C. García-Rosales, A. Hasegawa, A. Hoffmann, A. Kimura, H. Kurishita, R. J. Kurtz, H. Li, S. Noh, J. Reiser, J. Riesch, M. Rieth, W. Setyawan, M. Walter, J. H. You, and R. Pippan. Recent progress in R&D on tungsten alloys for divertor structural and plasma facing materials. *Journal of Nuclear Materials*, 442(1-3 SUPPL.1):181–189, 2013.

[276] Natalia Semioshkina and Gabrielle Voigt. An overview on ... *Journal Of Radiation Research*, 47 Suppl A(2):A95–A100, 2006.

[277] V. P. Budaev, Yu V. Martynenko, A. V. Karpov, N. E. Belova, A. M. Zhitlukhin, N. S. Klimov, V. L. Podkovyrov, V. A. Barsuk, A. B. Putrik, A. D. Yaroshevskaya, R. N. Giniyatulin, V. M. Safronov, and L. N. Khimchenko. Tungsten recrystallization and cracking under ITER-relevant heat loads. *Journal of Nuclear Materials*, 463:237–240, 2015.

[278] C. Thomser, V. Bailescu, S. Brezinsek, J. W. Coenen, H. Greuner, T. Hirai, J. Linke, C. P. Lungu, H. Maier, G. Matthews, P. H. Mertens, R. Neu, V. Philipps, V. Riccardo, M. Rubel, C. Ruset, A. Schmidt, and I. Uytdenhouwen. Plasma facing materials for the jet iter-like wall. *Fusion Science and Technology*, 62(1):1–8, 2012.

[279] W C Oliver and G M Pharr. experiments. (1), 1992.

[280] R. A. Pitts, S. Carpentier, F. Escourbiac, T. Hirai, V. Komarov, S. Lisgo, A. S. Kukushkin, A. Loarte, M. Merola, A. Sashala Naik, R. Mitteau, M. Sugihara, B. Bazylev, and P. C. Stangeby. A full tungsten divertor for ITER: Physics issues and design status. *Journal of Nuclear Materials*, 438(SUPPL):S48–S56, 2013.

[281] S. N. Mathaudhu, A. J. DeRosset, K. T. Hartwig, and L. J. Kecskes. Microstructures and recrystallization behavior of severely hot-deformed tungsten. *Materials Science and Engineering A*, 503(1-2):28–31, 2009.

[282] S. L C Ferreira, R. E. Bruns, H. S. Ferreira, G. D. Matos, J. M. David, G. C. Brandão, E. G P da Silva, L. A. Portugal, P. S. dos Reis, A. S. Souza, and W. N L dos Santos. Box-Behnken design: An alternative for the optimization of analytical methods. *Analytica Chimica Acta*, 597(2):179–186, 2007.

[283] Richard F. Gunst. Response surface methodology: process and product optimization using designed experiments. *Technometrics*, 38(3):284–286, 1996.

[284] J. M. Montes, F. G. Cuevas, and J. Cintas. Electrical resistivity of metal powder aggregates. *Metallurgical and Materials Transactions B: Process Metallurgy and Materials Processing Science*, 38(6):957–964, 2007.